frontiers | Research Topics

Dynamics at surfaces: Understanding energy dissipation and physicochemical processes at the atomic and molecular level

Edited by
Marco Sacchi, Helen Chadwick, Barbara A. J. Lechner, Glauco Bauerfeldt and Anton Tamtögl

Published in
Frontiers in Chemistry
Frontiers in Physics

ISSN 1664-8714
ISBN 978-2-8325-4846-2
DOI 10.3389/978-2-8325-4846-2

About Frontiers

Frontiers is more than just an open access publisher of scholarly articles: it is a pioneering approach to the world of academia, radically improving the way scholarly research is managed. The grand vision of Frontiers is a world where all people have an equal opportunity to seek, share and generate knowledge. Frontiers provides immediate and permanent online open access to all its publications, but this alone is not enough to realize our grand goals.

Frontiers journal series

The Frontiers journal series is a multi-tier and interdisciplinary set of open-access, online journals, promising a paradigm shift from the current review, selection and dissemination processes in academic publishing. All Frontiers journals are driven by researchers for researchers; therefore, they constitute a service to the scholarly community. At the same time, the *Frontiers journal series* operates on a revolutionary invention, the tiered publishing system, initially addressing specific communities of scholars, and gradually climbing up to broader public understanding, thus serving the interests of the lay society, too.

Dedication to quality

Each Frontiers article is a landmark of the highest quality, thanks to genuinely collaborative interactions between authors and review editors, who include some of the world's best academicians. Research must be certified by peers before entering a stream of knowledge that may eventually reach the public - and shape society; therefore, Frontiers only applies the most rigorous and unbiased reviews. Frontiers revolutionizes research publishing by freely delivering the most outstanding research, evaluated with no bias from both the academic and social point of view. By applying the most advanced information technologies, Frontiers is catapulting scholarly publishing into a new generation.

What are Frontiers Research Topics?

Frontiers Research Topics are very popular trademarks of the *Frontiers journals series*: they are collections of at least ten articles, all centered on a particular subject. With their unique mix of varied contributions from Original Research to Review Articles, Frontiers Research Topics unify the most influential researchers, the latest key findings and historical advances in a hot research area.

Find out more on how to host your own Frontiers Research Topic or contribute to one as an author by contacting the Frontiers editorial office: frontiersin.org/about/contact

Dynamics at surfaces: Understanding energy dissipation and physicochemical processes at the atomic and molecular level

Topic editors

Marco Sacchi — University of Surrey, United Kingdom
Helen Chadwick — Swansea University, United Kingdom
Barbara A. J. Lechner — Technical University of Munich, Germany
Glauco Bauerfeldt — Federal Rural University of Rio de Janeiro, Brazil
Anton Tamtögl — Graz University of Technology, Austria

Citation

Sacchi, M., Chadwick, H., Lechner, B. A. J., Bauerfeldt, G., Tamtögl, A., eds. (2024). *Dynamics at surfaces: Understanding energy dissipation and physicochemical processes at the atomic and molecular level*. Lausanne: Frontiers Media SA.
doi: 10.3389/978-2-8325-4846-2

Table of contents

frontiers | Frontiers in Chemistry

TYPE Editorial
PUBLISHED 18 April 2024
DOI 10.3389/fchem.2024.1411748

OPEN ACCESS

EDITED AND REVIEWED BY
Malgorzata Biczysko,
Shanghai University, China

*CORRESPONDENCE
Anton Tamtögl,
tamtoegl@tugraz.at

RECEIVED 03 April 2024
ACCEPTED 10 April 2024
PUBLISHED 18 April 2024

CITATION
Tamtögl A, Chadwick H, Lechner BAJ and Sacchi M (2024), Editorial: Dynamics at surfaces: understanding energy dissipation and physicochemical processes at the atomic and molecular level.
Front. Chem. 12:1411748.
doi: 10.3389/fchem.2024.1411748

Editorial: Dynamics at surfaces: understanding energy dissipation and physicochemical processes at the atomic and molecular level

Anton Tamtögl[1]*, Helen Chadwick[2], Barbara A. J. Lechner[3] and Marco Sacchi[4]

[1]Institute of Experimental Physics, Graz University of Technology, Graz, Austria, [2]Department of Chemistry, Faculty of Science and Engineering, Swansea University, Swansea, United Kingdom, [3]Department of Chemistry, Functional Nanomaterials Group and Catalysis Research Center, School of Natural Sciences, Technical University of Munich, Munich, Germany, [4]School of Chemistry and Chemical Engineering, University of Surrey, Guildford, United Kingdom

KEYWORDS

surface chemistry, catalysis, Ab initio (calculations), energy transfer, scattering spectroscopy, nanotechnology/nanomaterials, thin film growth and stability, surface diffusion

Editorial on the Research Topic
Dynamics at surfaces: understanding energy dissipation and physicochemical processes at the atomic and molecular level

The processes of energy dissipation at solid interfaces (see Figure 1) are integral to numerous physical phenomena ranging from catalytic reactions and astrochemistry to lubrication and materials science including the development of nanostructures (Ertl, 2009; Yang and Wodtke, 2016; Park et al., 2019; Ollier et al., 2023). Despite its ubiquity and importance in both technological applications and natural systems these surface dynamical processes remain poorly understood (Yang and Wodtke, 2016; Park et al., 2019; Sacchi and Tamtögl, 2023; Yu et al., 2023). For advancements in fields like catalysis, electrochemistry, and photoactivated processes, a comprehensive understanding, including energy transfer from gas or liquid phase molecules to surfaces and how energy is further dissipated through various means, such as phonons and via electron-phonon coupling, is essential (Chadwick and Beck, 2017; Tamtögl et al., 2020). Over recent decades, both experimental and theoretical advancements have significantly enriched the field, enabling more detailed investigations of surface structures and surface dynamical processes (Meyer and Reuter, 2014; Nattino et al., 2016; Alducin et al., 2017; Maurer et al., 2019; Dou and Subotnik, 2020; Holst et al., 2021).

Within the current Research Topic a diverse editorial team with different approaches to the topic, including molecular and state-to-state scattering (H. Chadwick), scanning probe techniques (B. A. J. Lechner) theoretical methods (M. Sacchi) and atom/beam scattering (A. Tamtögl) collected a total of 10 original articles and one mini review including the recent progress in understanding energy dissipation in surface dynamical processes (see Figure 1 for a few illustrated examples).

The study by Sabik et al. investigates the surface dynamical motion of cobalt phthalocyanine molecules on silver using helium spin-echo (HeSE) spectroscopy,

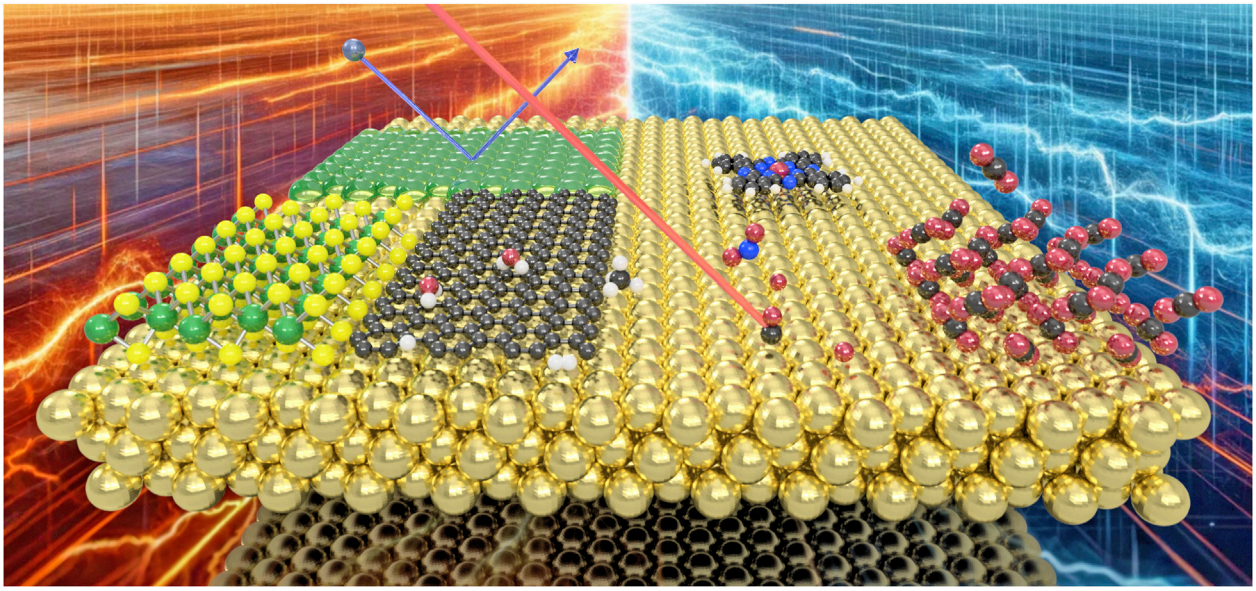

FIGURE 1
Energy dissipation processes are ubiquitous on surfaces and interfaces, from molecular motion to the formation of thin-films, determining adsorption, desorption and dissociation processes of molecules as well as the energetics upon molecular scattering from surfaces.

revealing that the activation energy for lateral diffusion decreases with temperature, leading to a transition from single jumps to predominantly long jumps at higher temperatures. It highlights the importance of considering a wide temperature range to capture the complete dynamics of molecular motion on surfaces.

Using the same method, Kyrkjebø et al. illustrate a stark contrast in water mobility across graphene-covered and bare Ir(111) surfaces. On graphene-covered Ir(111), water molecules exhibit significantly hindered diffusion, attributed to the trapping at specific sites within the surface's corrugated structure. Their findings not only advance our understanding of water-surface interactions but also implicate potential impacts on the development of anti-icing and anti-corrosion materials.

Via atom-surface scattering, Maier et al. study the surface properties of 1T-TaS_2 and $TlBiTe_2$, contrasting electron-phonon coupling between these materials, and potential implications for phase transitions driven by phonons. The study of thermal expansion and interaction potentials offers valuable insights into the complex behaviour of these compounds, contributing to a broader knowledge of charge-density wave systems and topological insulators.

The scattering of keV protons through graphene is studied by Bühler et al. who challenge prior assumptions of the process. By incorporating the lattice thermal motion in simulations, they uncover that previously observed phenomena, such as the outer rainbow scattering, are artefacts of statistical averaging. At the same time, they illustrate new avenues for detailed studies of proton-graphene interactions and the orientations of graphene membranes.

Dorst et al. study the recombinative desorption of O atoms from Ag(111) by combining ion imaging techniques with temperature-programmed desorption. The hyperthermal velocity distribution of the resulting O_2 is consistent with activated recombinative desorption but lower than state-of-the-art calculations currently predict. These results, therefore, provide a valuable benchmark for refining theoretical models of metal oxidation processes.

The influence of vibrational excitation on the sublimation of CO_2 is investigated by Jansen and Juurlink, where they use a laser to excite the antisymmetric stretch vibration (ν_3) of the CO_2 impinging on the CO_2 ice. They report that exciting ν_3 has a negligible effect on either the sticking of CO_2 to the ice, or the resulting structure of the CO_2 ice despite the additional vibrational energy being greater than the CO_2 desorption energy.

Floß et al. studied the surface-induced vibrational energy redistribution of methane scattering from Ni(111) and Au(111). Quantum state and angle-resolved measurements reveal a stark contrast in the vibrational energy conversion from ν_3 to ν_1 modes of methane, underlining the catalytic superiority of Ni(111) over the more inert Au(111). It thus shows a direct correlation between surface-induced vibrational energy redistribution efficiency and catalytic activity.

Tetenoire et al. elucidated the complex interplay between electrons and phonons in driving the photoinduced desorption and oxidation of CO on ruthenium surfaces. They demonstrate that phononic excitations play a pivotal role in CO desorption, while both electronic and phononic excitations significantly contribute to CO oxidation. Their research opens new avenues for optimising photochemical reactions on metal surfaces.

Xavier Jr and co-workers investigate graphene nanoribbons (GNRs) as potential catalysts for catalytic methane decomposition using density functional theory. They find that armchair edges offer lower energy barriers for hydrogen desorption, compared to zizag edges on GNRs, indicating a better regeneration potential. Highlighting GNRs as comparable to metallic catalysts for methane decomposition, their research may pave the way for sustainable hydrogen production and emphasises the significance of nanomaterials in catalytic processes for green technology.

The study by Prabhu and Groot demonstrates direct synthesis of metallic 1T Co-promoted MoS_2 without intercalating agents via growth in a highly reducing environment. High-pressure *in-situ* reactor scanning tunnelling microscopy measurements, reveal the transformation from a disordered $CoMoS_x$ phase at low temperatures to crystalline 1T slabs at around 600 K. It highlights the importance of reducing conditions in materials growth thus avoiding the need of additional chemicals.

In their mini review, Ueta et al. summarise recent studies on ortho-para conversion of hydrogen in molecular chemisorption and isolated matrix systems. These have found that nuclear-spin conversion can occur on a timescale of seconds, even for non-magnetic surfaces, and that the surface can provide a pathway for dissipating the accompanying change in rotational energy.

The collection of 11 articles within this Research Topic, though only a fraction of the extensive work in the field, highlights that understanding energy dissipation and transfer at interfaces is an extremely active area of research being studied with state-of-the-art methods both experimentally and theoretically. The importance of understanding these surface dynamical processes at the molecular level, focusing on phenomena such as photoinduced reactions, vibrational energy redistribution, and molecular diffusion on surfaces cannot be overstated. Advancements in both experimental setups and theoretical models have opened up new avenues. For example, experiments include the dynamics of larger and more complex molecules and studies of more complex surfaces compared to flat metal substrates, including two-dimensional materials and heterostructures. Similarly, enhanced computing power and the utilisation of computational clusters have enabled more sophisticated *ab initio* calculations, incorporating phenomena like non-adiabatic effects and quantum friction (Alducin et al., 2017; Chadwick and Beck, 2017; Yu et al., 2023). Furthermore, the integration of machine learning approaches promises to refine theoretical analysis further (Jiang et al., 2016; Kapil et al., 2022). Thus, the studies do not only shed light on the underlying atomic-level interactions but also pave the way for optimising materials for specific technological applications, from optoelectronics to hydrogen production.

However, challenges remain, e.g., in extending *ab initio* methods to larger systems and longer timescales and in conducting experiments under conditions that more closely mimic "real-life" parameters in catalysis to name a few (Yang and Wodtke, 2016). Moreover, while theory does well in studying specific nanosystems, there is still a need for experimental development to measure dynamical processes at tailored nanostructures or in confinement (Sacchi and Tamtögl, 2023; Yu et al., 2023). By overcoming these challenges and unravelling the mechanisms governing energy dissipation at interfaces, our community can unlock a new era of material fabrication and device control. For example, imagine designing catalysts with unparalleled efficiency, tailoring self-assembly processes for nanomaterial fabrication, or even manipulating environmental interactions on a molecular level. Future research will thus be pivotal for advancing various applications, including catalysis, energy production, and materials science by providing insights into the interaction mechanisms between molecules and surfaces, the influence of surface properties on these interactions, and the development of novel materials with enhanced functionalities.

Author contributions

AT: Writing–original draft, Writing–review and editing. HC: Writing–original draft, Writing–review and editing. BL: Writing–review and editing. MS: Writing–original draft, Writing–review and editing.

Funding

The author(s) declare that financial support was received for the research, authorship, and/or publication of this article. This research was funded in whole, or in part, by the Austrian Science Fund (FWF): https://doi.org/10.55776/P34704.

Conflict of interest

The authors declare that the research was conducted in the absence of any commercial or financial relationships that could be construed as a potential conflict of interest.

Publisher's note

References

Alducin, M., Díez Muiño, R., and Juaristi, J. I. (2017). Non-adiabatic effects in elementary reaction processes at metal surfaces. *Prog. Surf. Sci.* 92, 317–340. doi:10.1016/j.progsurf.2017.09.002

Chadwick, H., and Beck, R. D. (2017). Quantum state–resolved studies of chemisorption reactions. *Annu. Rev. Phys. Chem.* 68, 39–61. doi:10.1146/annurev-physchem-052516-044910

Dou, W., and Subotnik, J. E. (2020). Nonadiabatic molecular dynamics at metal surfaces. *J. Phys. Chem. A* 124, 757–771. doi:10.1021/acs.jpca.9b10698

Ertl, G. (2009). *Reactions at solid surfaces*. United States: John Wiley and Sons, Ltd.

Holst, B., Alexandrowicz, G., Avidor, N., Benedek, G., Bracco, G., Ernst, W. E., et al. (2021). Material properties particularly suited to be measured with helium scattering: selected examples from 2D materials, van der Waals heterostructures, glassy materials, catalytic substrates, topological insulators and superconducting radio frequency materials. *Phys. Chem. Chem. Phys.* 23, 7653–7672. doi:10.1039/D0CP05833E

Jiang, B., Li, J., and Guo, H. (2016). Potential energy surfaces from high fidelity fitting of *ab initio* points: the permutation invariant polynomial - neural network approach. *Int. Rev. Phys. Chem.* 35, 479–506. doi:10.1080/0144235X.2016.1200347

Kapil, V., Schran, C., Zen, A., Chen, J., Pickard, C. J., and Michaelides, A. (2022). The first-principles phase diagram of monolayer nanoconfined water. *Nature* 609, 512–516. doi:10.1038/s41586-022-05036-x

Maurer, R. J., Freysoldt, C., Reilly, A. M., Brandenburg, J. G., Hofmann, O. T., Björkman, T., et al. (2019). Advances in density-functional calculations for materials modeling. *Annu. Rev. Mater. Res.* 49, 1–30. doi:10.1146/annurev-matsci-070218-010143

Meyer, J., and Reuter, K. (2014). Modeling heat dissipation at the nanoscale: an embedding approach for chemical reaction dynamics on metal surfaces. *Angew. Chem. Int. Ed.* 53, 4721–4724. doi:10.1002/anie.201400066

Nattino, F., Migliorini, D., Kroes, G.-J., Dombrowski, E., High, E. A., Killelea, D. R., et al. (2016). Chemically accurate simulation of a polyatomic molecule-metal surface reaction. *J. Phys. Chem. Lett.* 7, 2402–2406. doi:10.1021/acs.jpclett.6b01022

Ollier, A., Kisiel, M., Lu, X., Gysin, U., Poggio, M., Efetov, D. K., et al. (2023). Energy dissipation on magic angle twisted bilayer graphene. *Commun. Phys.* 6, 344–349. doi:10.1038/s42005-023-01441-4

Park, G. B., Krüger, B. C., Borodin, D., Kitsopoulos, T. N., and Wodtke, A. M. (2019). Fundamental mechanisms for molecular energy conversion and chemical reactions at surfaces. *Rep. Prog. Phys.* 82, 096401. doi:10.1088/1361-6633/ab320e

Sacchi, M., and Tamtögl, A. (2023). Water adsorption and dynamics on graphene and other 2D materials: computational and experimental advances. *Adv. Phys. X* 8, 2134051. doi:10.1080/23746149.2022.2134051

Tamtögl, A., Sacchi, M., Avidor, N., Calvo-Almazán, I., Townsend, P. S. M., Bremholm, M., et al. (2020). Nanoscopic diffusion of water on a topological insulator. *Nat. Commun.* 11, 278. doi:10.1038/s41467-019-14064-7

Yang, X., and Wodtke, A. M. (2016). Surface reaction dynamics. *Chem. Soc. Rev.* 45, 3573–3575. doi:10.1039/C6CS90049F

Yu, X., Principi, A., Tielrooij, K.-J., Bonn, M., and Kavokine, N. (2023). Electron cooling in graphene enhanced by plasmon–hydron resonance. *Nat. Nanotechnol.* 18, 898–904. doi:10.1038/s41565-023-01421-3

frontiers | Frontiers in Chemistry

TYPE Original Research
PUBLISHED 01 June 2023
DOI 10.3389/fchem.2023.1172687

OPEN ACCESS

EDITED BY
Oriele Palumbo,
National Research Council (CNR), Italy

REVIEWED BY
Celine Leonard,
Université Paris Est Marne la Vallée, France
Allan Abraham Padama,
University of the Philippines Los Baños, Philippines

*CORRESPONDENCE
Marco Sacchi,
m.sacchi@surrey.ac.uk

RECEIVED 23 February 2023
ACCEPTED 15 May 2023
PUBLISHED 01 June 2023

CITATION
Xavier NF Jr., Payne AJR, Bauerfeldt GF and Sacchi M (2023), Theoretical insights into the methane catalytic decomposition on graphene nanoribbons edges.
Front. Chem. 11:1172687.
doi: 10.3389/fchem.2023.1172687

Theoretical insights into the methane catalytic decomposition on graphene nanoribbons edges

Neubi F. Xavier Jr.[1], Anthony J. R. Payne[1], Glauco F. Bauerfeldt[2] and Marco Sacchi[1]*

[1]School of Chemistry and Chemical Engineering, University of Surrey, Guildford, United Kingdom, [2]Instituto de Química, Universidade Federal Rural Do Rio de Janeiro, Seropédica, Brazil

Catalytic methane decomposition (CMD) is receiving much attention as a promising application for hydrogen production. Due to the high energy required for breaking the C-H bonds of methane, the choice of catalyst is crucial to the viability of this process. However, atomistic insights for the CMD mechanism on carbon-based materials are still limited. Here, we investigate the viability of CMD under reaction conditions on the zigzag (12-ZGNR) and armchair (AGRN) edges of graphene nanoribbons employing dispersion-corrected density functional theory (DFT). First, we investigated the desorption of H and H_2 at 1200 K on the passivated 12-ZGNR and 12-AGNR edges. The diffusion of hydrogen atom on the passivated edges is the rate determinant step for the most favourable H_2 desorption pathway, with a activation free energy of 4.17 eV and 3.45 eV on 12-ZGNR and 12-AGNR, respectively. The most favourable H_2 desorption occurs on the 12-AGNR edges with a free energy barrier of 1.56 eV, reflecting the availability of bare carbon active sites on the catalytic application. The direct dissociative chemisorption of CH_4 is the preferred pathway on the non-passivated 12-ZGNR edges, with an activation free energy of 0.56 eV. We also present the reaction steps for the complete catalytic dehydrogenation of methane on 12-ZGNR and 12-AGNR edges, proposing a mechanism in which the solid carbon formed on the edges act as new active sites. The active sites on the 12-AGNR edges show more propensity to be regenerated due lower free energy barrier of 2.71 eV for the H_2 desorption from the newly grown active site. Comparison is made between the results obtained here and experimental and computational data available in the literature. We provide fundamental insights for the engineering of carbon-based catalysts for the CMD, showing that the bare carbon edges of graphene nanoribbons have performance comparable to commonly used metallic and bi-metallic catalysts for methane decomposition.

KEYWORDS

methane, DFT, carbon catalysis, graphene edges and nanoribbons, hydrogen

1 Introduction

In the last 3 decades, catalytic methane decomposition (CMD) has received great attention as a promising highly-efficient hydrogen production process (Pinaeva et al., 2017; Alves et al., 2021; Fan et al., 2021; Hamdan et al., 2022). Much of the interest in this process is motivated by the promising potential of the 'turquoise' (Hermesmann and Müller, 2022) hydrogen obtained by CMD to replace fossil fuels, without obtaining CO_x as by-products (Pomerantseva et al., 2019; Russell et al., 2021; Hamdan et al., 2022; Jiang et al.,

2022; Yang and Gao, 2022). The research effort regarding CMD has dramatically increased since the beginning of the 1990s (Alves et al., 2021), however only techniques like autothermal reforming (ATR), steam methane reforming (SRM), dry reforming of methane (DRM) and partial oxidation (POX) into synthesis gas (also called 'syngas' - consisting in a mixture of CO and H_2) have been shown maturity for industrial applications (Pinaeva et al., 2017; Tong et al., 2022). In fact, SMR accounts for more than 90% of the global H_2 supply, leading to an emission of 830 Mt of CO_2 per year (Tong et al., 2022). Therefore, low-temperature cracking of methane performed through CMD is a promising solution to tackle CO_x production, since its main products are pure hydrogen gas and solid carbon ($CH_4 \rightarrow 2H_2 + C$; $\Delta H = 75$ kJ mol^{-1}) (Alves et al., 2021; Yang and Gao, 2022).

The main challenge of CMD is that methane is a very inactive precursor with a strong C-H bond energy of 440 kJ mol^{-1}. For this reason, the most widely employed methane cracking processes require very high temperatures (above 1473 K) (Abánades et al., 2016; Qian et al., 2020) and the usage of a metal-based catalyst is necessary to achieve lower temperatures (773 K-1073 K) for efficient conversion (Ashik et al., 2015). In this aspect, considerable efforts have been made in designing more efficient and sustainable heterogeneous catalysts for methane cracking. Currently, metal-based catalysts are the most commonly employed for this reaction and, among those, nickel and iron-based catalysts stand out for their economic viability, practicality and for possessing high selectivity to produce hydrogen from methane decomposition (Reshetenko et al., 2004; Fan et al., 2021; Hamdan et al., 2022; Rattanaamonkulchai et al., 2022). On the other hand, as other metal catalysts, their performance suffers from rapid deactivation by carbon poisoning during the CMD (Hadian et al., 2021; Jiang et al., 2022; Rattanaamonkulchai et al., 2022; Yan et al., 2022).

Graphitic carbon materials such as graphite (3D) and carbon nanotubes (1D) have been investigated as alternative materials for methane cracking since they have higher resistance to carbon poisoning (Hamdan et al., 2022; Yang and Gao, 2022). For the latter, recent works (Wang et al., 2021; Rattanaamonkulchai et al., 2022) have reported carbon growth on the catalyst surface alongside H_2 production by methane decomposition (Chai et al., 2006; Ni et al., 2006; Pudukudy et al., 2018; Esteves et al., 2020). Among the novel carbon-based materials that have been investigated as CMD catalysts, graphene has generated considerable interest (Suelves et al., 2008; Guil-Lopez et al., 2011; Szymańska et al., 2015). Graphene is the 2D monolayer of graphite and is the fundamental building block for other carbon allotropes (Geim and Novoselov, 2007). The catalytic performances of graphene can be improved by tuning its surface properties, e.g., by heteroatomic substitution (Rao et al., 2014; Lawrence et al., 2021), adatoms (Castro Neto et al., 2009; Pizzochero and Kaxiras, 2022), defects (Han et al., 2019; Brooks et al., 2022) and inclusion of functional groups (Kuila et al., 2012; Wood et al., 2012; He et al., 2022). Graphene nanoribbon (GNR) are < 10 nm wide strips of graphene and can be obtained by cutting the graphene layer in one specific dimension (Li et al., 2008; Kosynkin et al., 2009; Dutta and Pati, 2010). The properties of GNRs are mainly defined by their edges (Jia et al., 2011; Fujii and Enoki, 2013), making them tunable and promising materials for catalysis (Zhang et al., 2018; Peng et al., 2021), for sensors (Wood et al., 2012; Suman et al., 2020; He et al., 2022) and all-carbon spintronics (Pizzochero and Kaxiras, 2022).

The CMD mechanism is expected to be initiated by the adsorption and dissociation of methane molecules on the catalyst active sites, followed by a series of surface deprotonation reactions. However, there is a considerable lack of agreement regarding the viability of the main decomposition mechanism and relevant intermediates structures on carbonaceous catalysts (Zhang et al., 2017; Fan et al., 2021). Although atomistic insights for methane cracking on metallic and bi-metallic catalysts have been widely reported in the literature (Li et al., 2014; Calderón et al., 2016; Arevalo et al., 2017; Salam and Abdullah, 2017; Palmer et al., 2019), the reaction mechanism of CMD on different surface structures (e.g., free valence sites, edges and vacancies) of carbon-based catalysts, elucidating the hydrogen formation channels, are limited to the reverse steps of the methanation reactions (Calderón et al., 2016; Zhang et al., 2017; Fan et al., 2021). To the best of our knowledge, this is the first time that the methane decomposition steps are investigated on graphene edges through first-principles methodologies under the reaction conditions of the CMD process. In this work, we presented a computational investigation of graphene nanoribbons edges as a catalyst for the CMD. We started our investigation by analysing the dehydrogenation mechanisms over the two distinct edge morphologies: zigzag nanoribbons (12-ZGNRs) and armchair nanoribbons (12-AGNRs). We report the Gibbs free energy profile for the formation of bare carbon active sites at 1200 K. We analyse of the CH_4 reactivity on the edges starting by the physisorption of methane on the zigzag and armchair edges. After, we focused on the mechanism of methane decomposition on 12-ZGNRs and 12-AGNRs, i.e., the deprotonation steps and H_2 formation. Our results were compared with literature reports, aiming to provide a full assessment of GNRs as catalysts for methane dissociation and hydrogen evolution and to provide insights for future works on the catalyst engineering of graphene-based materials. In our previous work (Xavier et al., 2023), we found that decoration of non-metallic heteroatoms on the nanocarbons edges can dramatically increase the regeneration of carbonaceous catalysts, however, the performance for methane decomposition reported here on the pure carbon edges was found to be superior. We expect that the insights provided here aid the engineering of carbon-based catalysts for the catalytic methane decomposition.

2 Computational details

In this work, calculations were carried out adopting periodic boundary conditions, within the density functional theory (DFT) framework, as implemented in the CASTEP package (Segall et al., 2002; Clark et al., 2005). The generalized gradient approximation (GGA) exchange-correlation functional devised by Perdew, Burke and Ernzerhof (Perdew et al., 1996) was adopted. Core electrons of atoms were treated by ultrasoft pseudopotentials of Vanderbilt (Vanderbilt, 1990). Non-covalent interactions were accounted for through the adoption of the TS dispersion correction method (Tkatchenko and Scheffler, 2009). The more robust Many-Body Dispersion correction scheme (Tkatchenko et al., 2012) was adopted

in selected cases, for comparison purpose, and discussed throughout the manuscript. Convergence tests of the kinetic energy cut-off and k-point sampling were made and a value of 550 eV and a 2 × 1 × 1 Monkhorst-Pack (Monkhorst and Pack, 1976) grid were adopted, respectively. A geometry optimization scheme based on the Broyden-Fletcher-Goldfarb-Shanno (BFGS) algorithm (Pfrommer et al., 1997) was adopted, as implemented in CASTEP. Transition states were obtained by adopting the Linear-Quadratic-Synchronous Transit (LST/QST) algorithm (Govind et al., 2003). In this double-ended methodology, the starting points for the calculations are the reactants and products of each reaction step. Therefore, the workflow for locating the transition states is to first perform the optimization of the local minima points under a force tolerance of 0.025 eV $Å^{-1}$ and SCF energy tolerance of 1×10^{-6} eV. In the second step of the workflow, we adopt the previously optimized stationary points as starting structures for the LST/QST calculation. Transition states were confirmed by the presence of a single imaginary frequency respective to the reaction coordinate in the vibrational analysis. The surface, adsorbate and isolate molecules were allowed to move during geometry optimisation and transition state searches. Adsorption energies (E_{ads}) were estimated as shown in Eq. 1.

$$E_{ads} = E_{g+GNR} - E_{GNR} - E_g \quad (1)$$

where $E_{g,}$ is the total energy of the isolated gas species. The E_{GNR} and $E_{g,+GNR}$ terms are related to graphene nanoribbons and the adsorbed system, respectively. The gas-phase species investigated here, i.e., CH_4, H_2 and the isolated hydrogen atom, H, were assumed as reference for the calculation of adsorption energies. Vibrational properties were obtained by phonons calculations at the Γ-point adopting the partial Hessian vibrational analysis (Li and Jensen, 2002). In this approach, we only considered the normal modes of the adsorbate and the two atomic rows closest to adsorbate and low-frequency vibrational modes were treated as 200 cm^{-1}, similar to the approach adopted in our previous work (Xavier et al., 2023). The partition functions of the adsorbates were estimated with the lattice gas approach. (Campbell et al., 2016; Knopf and Ammann, 2021) The Gibbs free energy was calculated for the reaction conditions of 1200 K and 1 bar with the fundamental equation $G = H - TS$, in which H is the enthalpy, comprising the DFT energy, the zero-point energy correction and thermal contributions, and S is the entropy. For the gas-phase molecule, the translational, rotational and vibrational partition functions were considered, accordingly to conventional statistical thermodynamic expressions. The isolated molecules were optimised inside a box of 20 Å and we assumed the experimental vibrational data retrieved from the NIST database (Johnson et al., 2020). The Gibbs free energy of activation was estimated as $\Delta G_a = G_{TS} - G_{IS}$, in which G_{TS} is the free energy of the transition state and G_{IS} is the free energy of the initial state, calculated at 1200 K. This temperature was chosen due to the slight endothermic character of methane decomposition over carbonaceous surfaces, in which the process is generally conducted at temperatures between 800 °C and 1,000 °C (Xie et al., 2018; ? Chang et al., 2021; Fan et al., 2021; Pinilla et al., 2008).

As defined before, GNRs can be classified depending on their edges, being defined as zigzag-edged GNR or armchair-edged GNR. Regarding their width, we adopted models consisting of 12 carbon atoms along the zigzag (12-ZGNR) and armchair (12-AGNR) lines between the edges of the non-periodic lattice as can be seen in Figure 1A, B, respectively. Furthermore, we constructed supercells comprising 72 carbon atoms for 12-ZGNR and 96 carbon atoms for the 12-AGNR, with a vacuum region of 20 Å in the direction perpendicular to the GNRs plane to avoid spurious interaction with adjacent periodic images. As further discussed in the following section, we adopted models consisting of hydrogen-passivated (H-terminated) and hydrogen-free (open-edge) GNRs, as catalysts for the dehydrogenation of methane. Therefore, the width of 12 carbon atom lines for the nanoribbon was adopted, since previous experimental work reported the observation of two hydrogen adatoms on the same zigzag-edge site, after the synthesis of H-terminated 12-ZGNRs (Ruffieux et al., 2016). Furthermore, a similar width of nanoribbons was adopted in previous theoretical works (He et al., 2022; Pizzochero and Kaxiras, 2022), from which adsorption energy values were suggested to be slightly altered in nanoribbons wider than 12-GNRs (He et al., 2022) Finally, previous studies showed that zigzag edges in graphene exhibit antiferromagnetic aligned edges (Son et al., 2006), therefore, spin-polarized DFT calculations were performed for 12-ZGNR.

3 Results

3.1 Physisorption of CH_4

Pristine zigzag edges exhibit a metallic behavuour whereas pristine armchair edges behave as a semiconductor. Their band structures can be altered by atomic or molecular doping, functionalisation and adsorbed molecules (López-Urías et al., 2020; 2021; Suman et al., 2020; He et al., 2022). The band structure and total density of states (DoS) plots for the 12-ZGNR and 12-AGNR were calculated and were found to compare well with those reported in the literature as shown in Supplementary Figure S1. A uniform (10 × 1 × 1) k-point sampling grid was adopted for the band structure calculations. The metallic behaviour of the 12-ZGNR was evidenced by the crossing of conduction and valence bands on the Fermi level (Supplementary Figure S1), in agreement with previous works (Suman et al., 2020; López-Urías et al., 2021). A semiconducting character was observed for the 12-AGNR, with a calculated band gap of 0.58 eV, which is comparable to the values of 0.83 eV obtained in the work of López-Urías et al. (2020).

We began our investigations with the first step of the reaction mechanism, i.e., the physisorption of CH_4 on the graphene nanoribbon. In summary, four unique-symmetry adsorptions sites in a surface normal, i.e., the out-of-plane (OP) direction of 12-ZGNR, were studied here and reported in Figure 1A. The adsorption sites were labelled as Z1, Z2, Z3 and Z4, with the former indicating the carbon atom on the edge itself. Adopting the same pattern, three unique-symmetry adsorption sites, in the OP direction, were studied for the 12-AGNR: A1, A3 and A3 (Figure 1B). Furthermore, we considered the physisorption of CH_4 in the in-plane (IP) direction of the graphene nanoribbon, which was labelled Z1-IP and Z2-IP, with respect to 12-ZGNR (Figure 1D), and A1-IP and A2-IP for the 12-AGNR. For the investigation of the CH_4 physisorption, we adopted the 12-ZGNR fully passivated with hydrogen atoms (Barone et al., 2006).

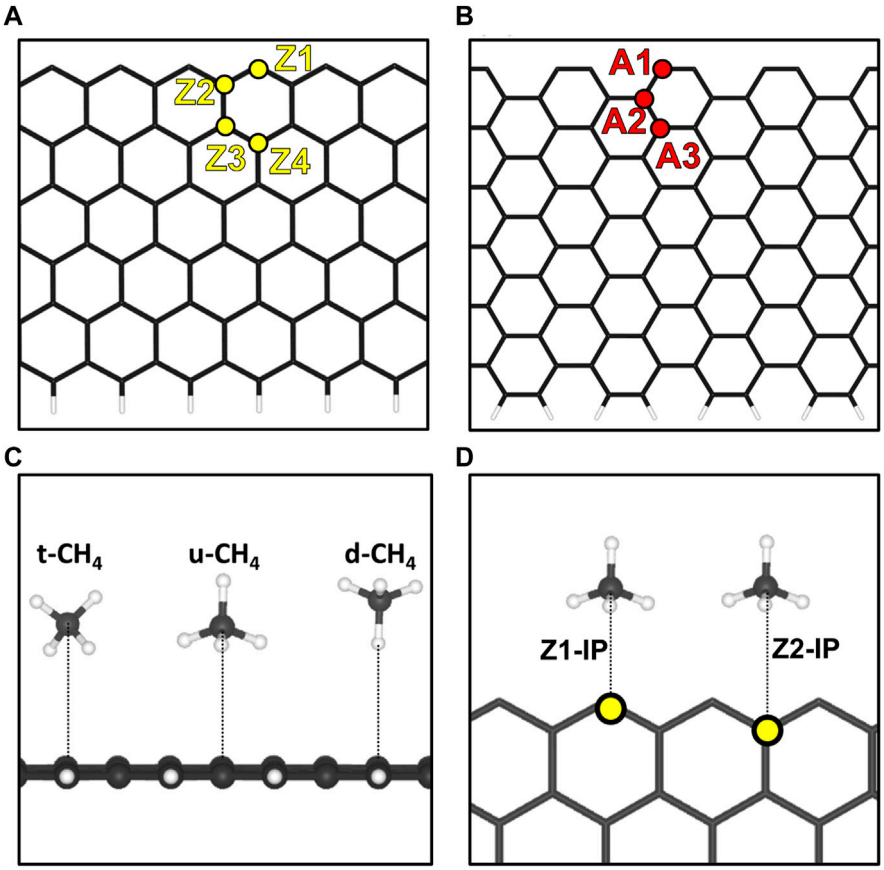

FIGURE 1
Representation of the **(A)** 12-ZGNR model and the unique-symmetry adsorption sites, Z1, Z2, Z3 and Z4 and the **(B)** 12-AGNR model and the unique-symmetry adsorption sites A1, A2, A3 and A4, investigated in this work. To better illustrate, the upper edge are hydrogen free whereas the lower edge is passivated with hydrogen. **(C)** Depictions of the orientations of methane with respect to the graphene nanoribbons, considered in this work. **(D)** Adsorptions sites for the methane in the same plane of the 12-ZGNR.

We performed a series of electronic energy calculations, with methane initially positioned at 6 Å from the Z1 site (12-ZGNR) and decreasing the distance by 0.25 Å until a distance of 2 Å from the adsorption site was reached. It is noteworthy that the distances between CH_4 and the GNR were measured between the atom of methane positioned the closest to the GNR surface, for each CH_4 conformation. We considered three possible orientations of methane for the construction of the potential energy surface: methane with one hydrogen atom oriented in the opposite direction from the surface (u-CH_4—Figure 1C), methane with one hydrogen atom pointing towards the surface, in a perpendicular orientation (d-CH_4—Figure 1C) and CH_4 in a tilted orientation in respect to the surface (t-CH_4—Figure 1C). Weak dispersion forces due to long-range electron correlation are expected to be the predominant interaction in the physisorption of methane (Sacchi et al., 2011; Sacchi et al., 2012a; Sacchi et al., 2012b). Therefore, we constructed potential energy surface curves for the d-CH_4, u-CH_4, t-CH_4 conformations, adopting the TS and MBD dispersion corrections. Curves are reported in Supplementary Figure S2.

The distances between each methane orientation and the surface, at the minimum energy configuration of the constructed PES, were adopted as starting points for geometry optimizations on the Z1 and Z1-IP adsorption sites of 12-ZGNRs. Adsorption energy values, adopting the TS and MBD dispersion corrections, were obtained as described in Eq. 1 and the results reported in Figure 2A. Overall, the u-CH_4 configuration was the most favourable physisorption configuration on the out-of-plane Z1 site, with adsorption energy values of −0.120 eV and −0.088 eV, obtained by adoption of the TS and MBD corrections, respectively. Only the u-CH_4 conformation was considered in investigations with respect to the Z1-IP sites, since it is the most favorable conformation in the OP adsorption sites. Adsorption energies were determined as −0.073 eV and −0.070 eV, adopting the TS and MBD corrections, respectively. Equilibrium distances between u-CH_4 and the carbon from the Z1 site were of 3.51 Å and 3.79 Å, obtained with the TS and MBD schemes, respectively.

With respect to the different dispersion corrections considered in this study, the MBD scheme yielded the same adsorption stability order of methane on the Z1 site of the 12-ZGNR as the TS correction, although we observed a divergence in the equilibrium distance between the methane and the out-of-plane adsorption site, as shown in Supplementary Table S1. The

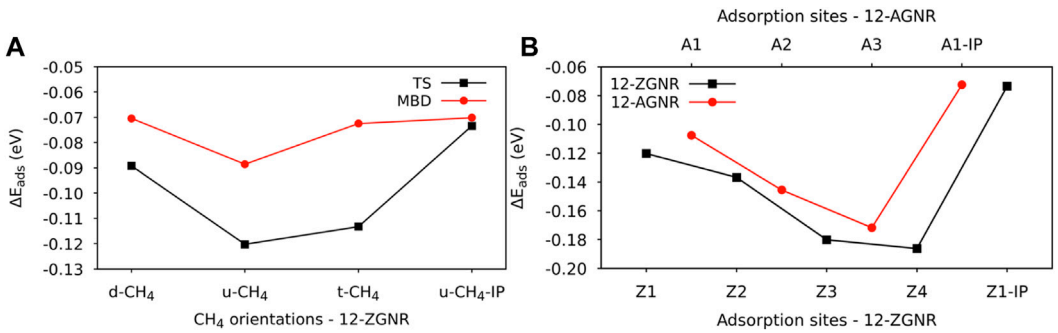

FIGURE 2
(A) Adsorption energy values for the CH_4 orientations on the Z1 adsorption site of the 12-ZGNR, adopting the TS and MBD dispersion correction. **(B)** Adsorption energy values for the most favourable adsorption orientation of methane (u-CH_4) on the adsorption sites of 12-ZGNR and 12-AGNR, investigated here.

largest deviation for the adsorption energy was obtained for the t-CH_4, from which PBE-TS calculations predicted a value 41 meV more negative, in comparison with PBE-MBD. The equilibrium physisorption distance values, obtained from MBD corrections, were 0.21 Å, 0.28 Å and 0.34 Å higher than values obtained from at the PBE-TS level, for the d-CH_4, u-CH_4 and t-CH_4 conformations, respectively. A negligible difference in the equilibrium distance was obtained when comparing the physisorption of u-CH_4 on the Z1-IP site, from which both methods resulted in roughly 2.80 Å. Therefore, due to the higher computational cost of the MBD methodology, resulting in similar results obtained when adopting the TS dispersion correction, the latter was adopted in further calculations.

Further investigations were made for the d-CH_4, u-CH_4 and t-CH_4 physisorbed conformations on the Z2, Z3 and Z4 adsorption sites. The adsorption energy values for the methane on the u-CH_4 and t-CH_4 orientations remained similar among all adsorption sites, varying between 4 meV and 7 meV. The u-CH_4 was the most stable orientation on the Z1, Z3 and Z4 sites by 7 meV, 3 meV and 6 meV, respectively, whereas t-CH_4 was the more stable at the Z2 site by 4 meV, as can be seen in Supplementary Table S2. Due to the u-CH_4 being the most stable physisorbed conformation on the majority of the adsorption sites studied here, on 12-ZGNR, it was adopted as a reference for comparison of the adsorption energies among the Z1, Z2, Z3, Z4 and Z1-IP sites, on the 12-ZGNR, and among A1, A2, A3 and A1-IP sites on the 12-AGNR. As shown in Figure 2B, the physisorption of methane was more favourable on the Z4 (12-ZGNR) and A3 (12-AGNR) sites, with E_{ads} values of −0.186 eV and −0.171 eV, respectively and equilibrium distances of 3.38 Å and 3.47 Å, respectively. In fact, the CH_4 physisorption energy on non-edge sites rapidly approached the adsorption energy value of methane on pristine graphene as the distance between the site and the edge grows, as evidenced by the comparison of our results with literature reports (Wood et al., 2012; Anithaa et al., 2017; Vekeman et al., 2018). In the work of Anithaa et al. (2017), the adsorption energy obtained for the physisorption of methane in the middle of a pristine graphene layer was of −0.183 eV. Wood et al. (2012) reported values of −0.175 eV for the physisorption of methane at the middle of graphene, obtained from van der Waals corrected DFT. We perform calculations for methane physisorbed at the middle of the 12-ZGNR and 12-AGNR, and we obtained values of −0.183 eV and −0.187 eV, which are similar to the adsorption energy values for the physisorption of CH_4 on the sites Z4 and A3 (−0.180 eV and −0.186 eV, respectively). Therefore, it is possible to assume that methane can also be physisorbed on the edges under the reaction conditions of CMD, due to the physisorption of CH_4 in the middle of graphene being only 0.08 eV and 0.06 eV more stable than the adsorption on the Z1 and A1 sites, respectively, which are lower than the thermal energy at 1200 K (0.1 eV).

The adsorption of methane on the out-of-plane adsorption sites were at least 46 meV more stable than the in-plane Z1-IP adsorption site, from which an E_{ads} value of −0.070 eV was obtained, in excellent agreement with previous DFT results (Wood et al., 2012). However, when adopting the same computational methodology, Wood et al. (2012) reported that no stable minimum was found for out-of-plane adsorption sites of 12-ZGNR. The adsorption energy of methane over the in-plane sites of 12-ZGNR and 12-AGNR was roughly the same, diverging by about 1 meV, which is likely due the zigzag and armchair edges being passivated with hydrogen. Depiction of the most favourable physisorption configurations of CH_4 on the Z4 (Figure 3A) and Z1-IP (Figure 3C) sites, as well as their equilibrium distances, were reported in Figure 2A, C, respectively. Chemical insights were gained about the preference for physisorption of methane on OP sites of graphene nanoribbons, in comparison with the IP site, by plotting the charge density difference between the adsorbed system, isolated molecule and GNR. Figure 3 shows the positive charge accumulation (yellow region) and charge depletion (blue region) of the methane physisorption on Z4 and Z1-IP sites of 12-ZGNR. The lower stability of the IP site can be attributed to the presence of a stronger repulsive electrostatic component in the bonding, suggested by the charge accumulation from the in-plane methane physisorbed mode and charge depletion on the edges, showed in Figure 3D. It can be seen in Figure 3B that the surface is polarised with positive charge density in the 12-ZGNR backbone whereas a stronger charge depletion region is observed in the edge sites. Therefore, we can infer that more intense dispersion interactions are present between methane and the Z4 physisorption site.

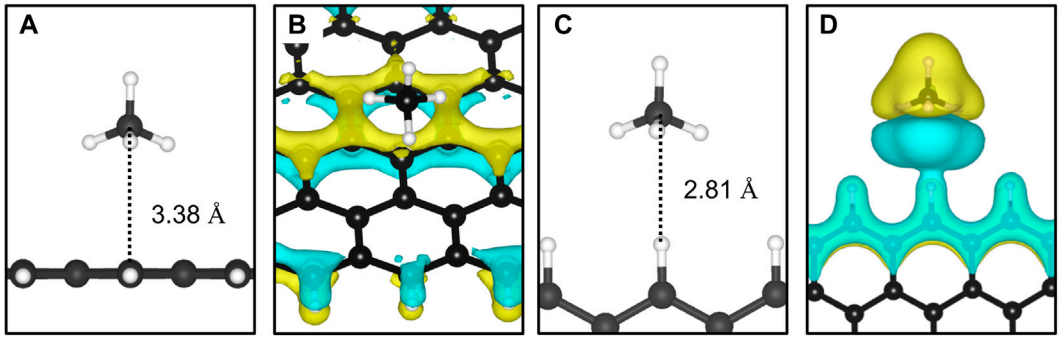

FIGURE 3
The most favourable physisorption mode of CH_4 in respect to the **(A)** out-of-plane 12-ZGNR (Z4 site) and **(C)** in-plane 12-ZGNR. Charge density difference plots for each respective adsorption site are shown in **(B)** and **(D)**. Charge depletion is represented by blue isosurfaces and positive charge accumulation is depicted in yellow isosurfaces. The adopted isosurface cut-off value was 0.04 e $Å^{-3}$.

TABLE 1 Chemisorption energy (eV) for the CH_3 and H, calculated for the Z1, Z2, Z3 and Z4 sites of 12-ZGNR and for the A1, A2 and A3 sites of 12-AGNR.

12-ZGNR			12-AGNR		
	E_{ads,CH_3} (eV)	$E_{ads,H}$ (eV)		E_{ads,CH_3} (eV)	$E_{ads,H}$ (eV)
Z1	−2.463	−2.830	A1	−1.010	−1.421
Z2	−0.251	−0.447	A2	−0.587	−0.931
Z3	−1.284	−1.622	A3	−0.277	−0.613
Z4	−0.561	−0.885			

3.2 First deprotonation of CH_4

The first deprotonation step of CMD ($CH_4 \rightarrow CH_3 + H$) was investigated for two possible mechanisms: the direct (dissociative) and precursor-mediated (non-dissociative) methane adsorption (Alves et al., 2021; Fan et al., 2021; Wang et al., 2021; Pan et al., 2022). For the former, CH_3 and H are expected to chemisorb at the surface of the catalyst while the first C-H bond of methane cleavage occurs simultaneously. For the precursor-mediated mechanism, the chemisorption and the C-H dissociation occurs in separate steps. The mechanism of methane adsorption over a solid catalyst is crucial for identifying the rate-limiting step of the catalytic methane decomposition (Hamdan et al., 2022; Tong et al., 2022). Therefore, a detailed investigation is presented in this section. Hereafter, the active site on the edge in which the species is chemisorbed is defined by "/Z1", for the 12-ZGNR and "/A1" for the 12-AGNR.

3.3 Dehydrogenation on H-terminated 12-ZGNR and 12-AGNR edges

To investigate the first reaction mechanism step of the catalytic dehydrogenation of CH_4, forming CH_3 and H on the 12-ZGNR and 12-AGNR edges, it is necessary to elucidate the most favourable chemisorption sites of CH_3 and H among the sites detailed in Figure 1 and correlate with the methane adsorption on edges. Adsorption energy values on the hydrogen-passivated edges of 12-ZGNR and 12-AGNR range from −2.463 eV (Z1) to −0.251 eV (Z2) for the methyl chemisorption on the 12-ZGNR. Adsorption energy values between −1.421 eV (A1) and −0.277 eV (A3) were observed for the CH_3 chemisorption on 12-AGNR (see Table 1). We investigated the adsorption of CH_4 into CH_3* and H* (the star index indicates chemisorbed species) at 1200 K on the hydrogen-terminated Z1 and A1 sites (Supplementary Figure S3) obtaining a free energy of activation of 3.76 eV and 3.95 eV, respectively. The high ΔG_a values for methane adsorption are likely due to deactivation by the strong chemisorption of hydrogen atoms on the passivated edges, evidenced by the E_{ads} value of −2.830 eV and −1.421 eV (Table 1) on the Z1 and A1 sites respectively, in agreement with previous theoretical results (Pizzochero and Kaxiras, 2022). Finally, the investigation of the dehydrogenation on the 12-ZGNR and 12-AGNR passivated edges is necessary to evaluate the availability of the bare carbon active site and the viability of the CMD process.

We investigated the H_2 formation reactions from the passivated Z1 and A1 sites by analysing the combination of hydrogen atoms chemisorbed on the edges. For the former, we labelled as 2H/Z1 and 2H/A1 when the hydrogen atoms are chemisorbed on different edge sites, as shown in Figure 4C. Following the same approach, we labelled as HH/Z1 and HH/A1 when both hydrogen atoms are chemisorbed on the same edge site (Figure 4C). We also made calculations for hydrogen diffusion on 12-ZGNR and 12-AGNR edges. Furthermore, we analyse the hydrogen atom desorption from the graphene edges and the results are reported in Figure 4. Overall, the combination of chemisorbed hydrogen on different sites into H_2 have activation free energy of 5.23 eV and 6.32 eV, respectively. Similar results are obtained for the atomic hydrogen desorption on 12-ZGNR and AGRN due to high ΔG_a values of 5.01 eV and 5.58 eV. The most feasible pathway for a bare carbon active site formation is from the recombination of the hydrogen adatom from the edges (HH/Z1 and HH/A1) forming H_2. On the 12-ZGNR, the $HH/Z_1 \rightarrow TS \cdot HH/Z_1 \rightarrow H_2$ reaction proceeds through a barrier of 2.92 eV, whereas a ΔG_a of only 1.56 eV is necessary on the 12-AGNR. Hydrogen diffusion on the 12-ZGNR and AGNR passivated

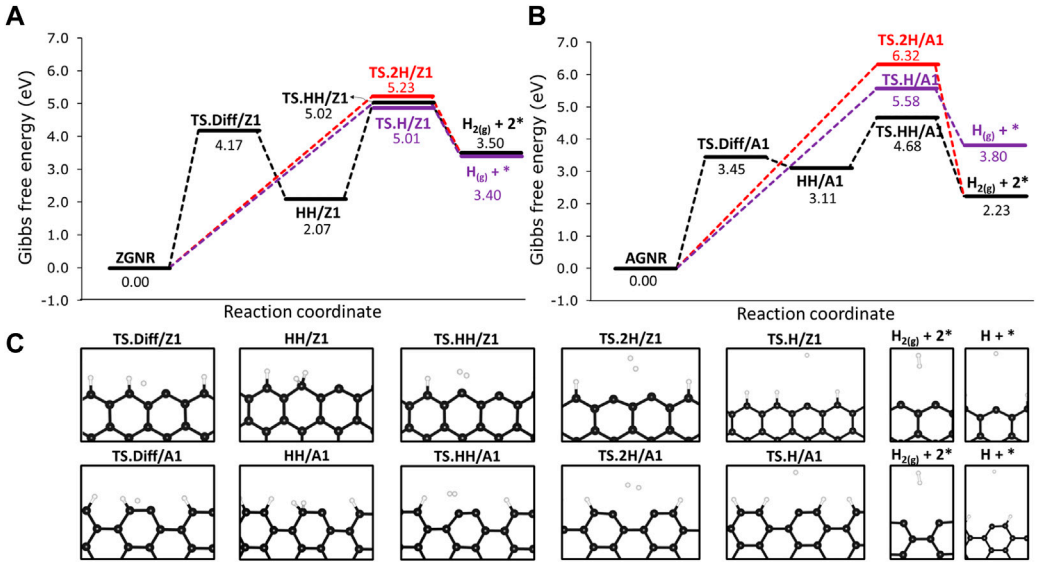

FIGURE 4
Free energy reaction profile, at 1200 K, of the dehydrogenation on H-passivated **(A)** zigzag edges and **(B)** armchair edges. **(C)** Depiction of the stationary point located in the reaction mechanisms and their respective labels. Reaction coordinate is in arbitrary units.

edges can occur by forming an hydrogen adatom with a ΔG_a of 4.17 eV and 3.45 eV, respectively, being the rate determinant step for the H_2 desorption from HH/Z1 and HH/A1. It is noteworthy that the barriers of methane adsorption on passivated edges have free energy of activation values 0.41 eV lower on 12-ZGNR and 0.50 eV higher on 12-ZGNR and 12-AGNR, respectively, being possible to occur at higher temperatures in which the process is conducted. However, further dehydrogenation steps of methane on passivated edges are unlikely to occur to the deactivation by hydrogen atoms and this scenario was not considered in the following investigations.

3.4 Methane deprotonation on H-free (open edge) 12-ZGNR and 12-AGNR

As it was stated in the last section, the availability of unpassivated carbon active sites is likely at the high temperatures in which the CMD process is conducted, with the H_2 desorption from armchair edges being the most kinetically feasible, therefore, we have investigated the CMD steps on the bare carbon active sites of the edges of 12-ZGNR and 12-AGNR, i.e., adopting a fully dehydrogenated edge (open edge). Experimental evidence confirms that hydrogen-free graphene edges are expected to exist even in vacuum conditions (He et al., 2014).). In fact, hydrogen-free edges have been adopted for the investigations of the growth of epitaxial graphene (Wu et al., 2019), and the reconstruction of the bare graphene zigzag and armchair edges (Gao et al., 2012; Li et al., 2013; Soldano et al., 2014). Moreover, it is expected that the non-hydrogenated edge reactive sites exist at high temperatures, at which the CMD process takes place (Calderón et al., 2016). A similar model, adopting dangling carbon atoms on edge, was adopted for the investigation of methane formation (Calderón et al., 2016) and CO_2 adsorption (Montoya et al., 2003; Noei, 2016) on edges of carbonaceous surfaces, with good agreement with experimental data (Montoya et al., 2003). For completeness, we also investigated the stability of the H-passivated and H-free ZGNR and AGNR, by performing *ab initio* molecular dynamics (AIMD) simulations at 1200 K and results are presented in Supplementary Figure S4 of the Supplementary Material. After 1 ps simulations, all the structures remained stable and no deformation or Stone-Wales transformation were observed, showing that the catalyst model is appropriate for further investigations of the deprotonation of methane. We added in Supplementary Figure S5 a snapshot of the AIMD simulations at different time steps of the simulation, and we observed a equilibrium distance between 6.04 Å and 6.81 Å obtained at 500 fs and 1,000 fs, respectively.

Two possible pathways for methane deprotonation were proposed on the 12-ZGNR and 12-AGNR edges: the first reaction pathway leads to the production of CH_3 and H chemisorbed on different Z1 (12-ZGNR) or A1 (12-AGNR) adsorption sites, while the second pathway leads to CH_3 and H chemisorbed on the same Z1 (or A1) site, as depicted in Figure 5B, C, respectively. The chemisorption of the methyl moiety and the hydrogen atom on the edges occurs in the plane of the nanoribbon (Figure 5). In this regard, the physisorption of CH_4 on the Z2 site (bridge site—Figure 1) is more favourable than the adsorption on Z1 by only 4 meV. Similarly, we observe that the physisorption of CH_4 on the A2 site of the 12-AGNR is energetically more favourable than on the A1 site by 21 meV. Depiction of the physisorption structure over the Z2 site is shown in Figure 5A.

We investigated two reaction pathways connecting the physisorbed CH_4 to the CH_3 and H chemisorbed on the same Z1 edges via: 1) a two-step mechanism, from which hydrogen is chemisorbed on Z1 in the first step, followed by the chemisorption of CH_3 on the same Z1 site (precursor-mediated mechanism) and a 2) one-step mechanism from which CH_3 and H are chemisorbed in the

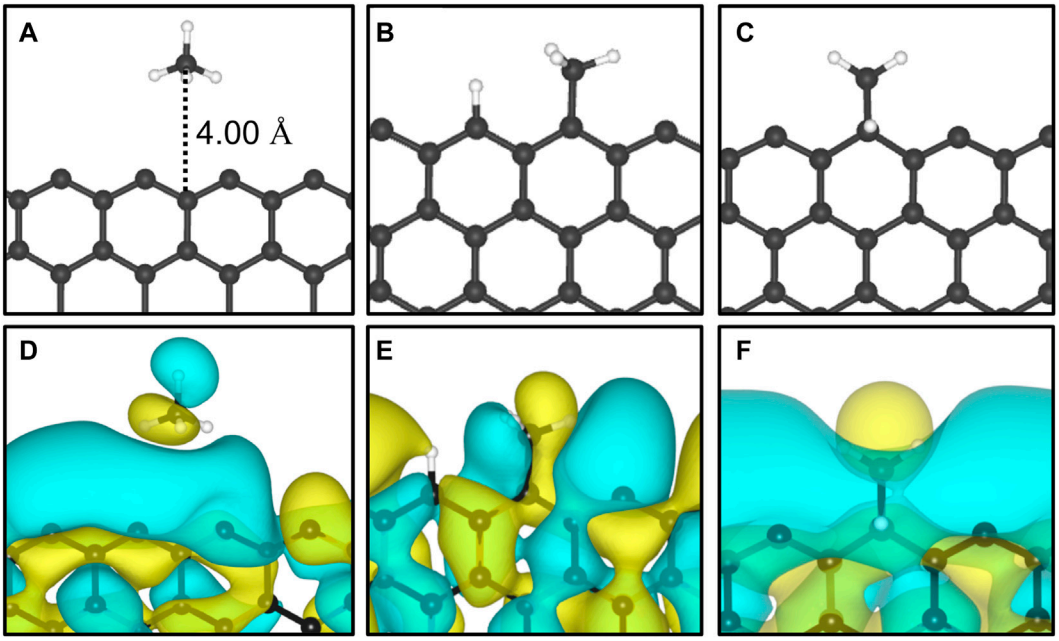

FIGURE 5
Representation of **(A)** CH_4 adsorbed on the Z2; **(B)** CH_3 and H chemisorbed on different Z1 sites; **(C)** CH_3 and H chemisorbed on the same Z1 site and their HOMO represented in **(D, E)** and **(F)**, respectively. The yellow and cyan colors represent the positive and negative phases, respectively, of the HOMO. The adopted isosurface cut-off value was 0.01 e $Å^{-3}$.

same step (direct dissociative mechanism). Reaction profiles of the 1) and 2) mechanisms are presented in Figure 6A, as well as labels for each of the stationary points of the reaction mechanism. The reaction mechanism 1) consists of two parts: firstly, the migration of H from CH_4 to the Z1 site through a free energy barrier of 1.41 eV (TS1-1). Here the methyl radical is stabilized by the hydrogen atom migrated to the edge of the int-CH_4 structure. Secondly, the TS1-2 connects int-CH_4 to the CH_3 and H chemisorbed onto the same Z1 site (hereafter referred to as CH_3-H/Z1) through a ΔG_a of 0.50 eV.

Our study suggests that the precursor-mediated i) and direct ii) mechanisms of methane deprotonation occur competitively (Figure 6A). For the latter, a one-step mechanism was proposed, passing through the transition state TS2 and forming CH_3–H/Z1 with an activation free energy of activation of 0.56 eV. Due to the lower ΔG_a value, it is expected that mechanism ii) is preferred over i) and the C-H bond cleavage is followed by the symmetric chemisorption of methyl and hydrogen. We also investigated the chemisorption of the methyl moiety and the hydrogen atom in different Z1 sites iii), as shown in Figure 6A. In this pathway, we found that the chemisorption of CH_3 and H proceeds synchronously, with u-CH_4/Z2 reacting through TS3, with a ΔG_a of 0.97 eV.

The reaction mechanism ii) is the more favourable reaction pathway, with a ΔG_a 0.41 eV lower than iii) and 0.85 eV lower than the rate-determining step (migration of the hydrogen atom to the edge) of mechanism i). Therefore, a thermodynamically controlled reaction is possible, from which the reaction pathway iii) is expected to be more relevant at higher temperatures. This possibility is suggested by the very exothermic character of the dehydrogenation reactions of methane on the graphene nanoribbon edges (ΔG = −3.92 on 12-ZGNR edges and ΔG = −3.04 on 12-AGNR edges), as presented in Figure 6. A better picture of the thermodynamic control of reaction pathway iii) can be seen in Supplementary Figure S6, from which the concentration of the thermodynamic product, CH_3/Z1-IP + H/ZI-IP was obtained as a function of time, at different temperatures. As expected, the formation rate of the product CH_3/Z1-IP + H/ZI-IP is heavily influenced by the temperature and the complete conversion was achieved, roughly 130 times faster at 900 K, in comparison with conversion time at 800 K and 60 times faster at 1000 K, in comparison with the conversion time at 900 K. Further insights were obtained by inspection of the HOMO orbitals of both products, CH_3/Z1 + H/Z1 and CH_3-H/Z1, as reported in Figure 5. It is possible to observe a greater overlap between the orbitals of the methyl and hydrogen fragments on different sites (CH_3/Z1 + H/Z1) in Figure 5E, in comparison with the HOMO orbitals in CH_3-H/Z1 (Figure 5F). For the latter, the π system formed by the dangling bonds of the GNR edge are the most dominant in the adsorbed system, contributing to its lower stability in comparison with CH_3/Z1 + H/Z1. Therefore, the interactions between the products and the dangling bonds result in an overall better stability of the CH_3 and H chemisorbed on different Z1 sites, in agreement with the experimental findings of the structural stability of graphene nanoribbons (Barone et al., 2006).

The reaction mechanism for the CH_4 dehydrogenation on the 12-AGNR is summarised in Figure 6B. Here, two competing one-step mechanisms for CH_4 deprotonation on the 12-AGNR edges lead either to the synchronous chemisorption of CH_3 and H on adjacent A1 sites (mechanism iv) or to the chemisorption of the

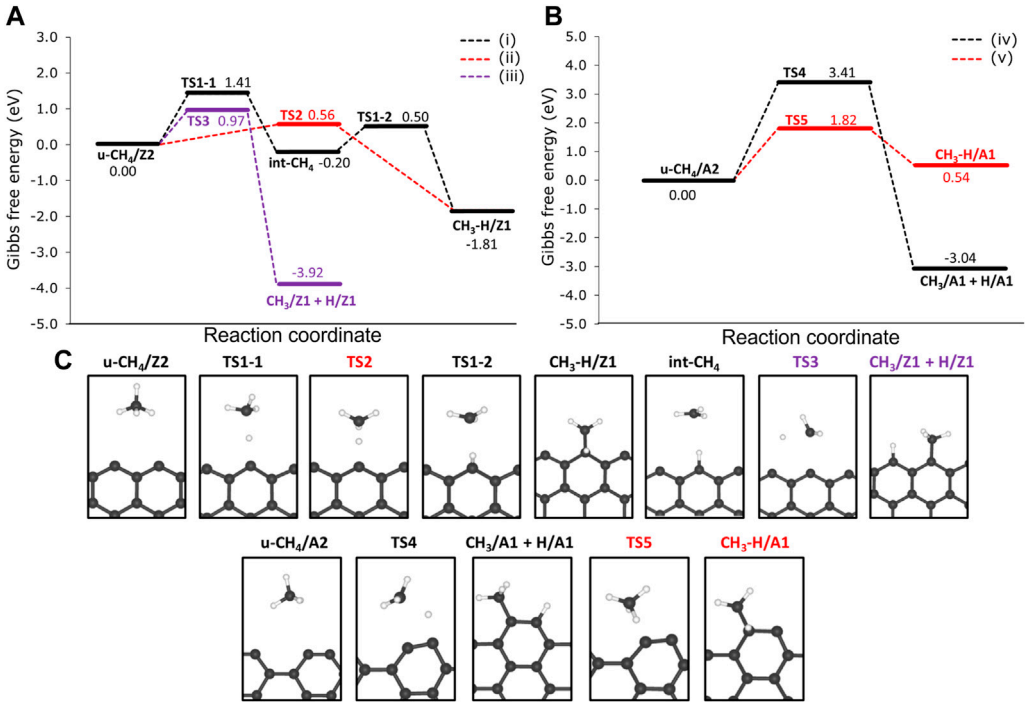

FIGURE 6
Free energy reaction profiles at 1200 K for the dehydrogenation of methane on the non-passivated edges of **(A)** 12-ZGNR and the **(B)** 12-AGNR. The zero energy is relative to the most stable physisorbed methane conformation on the 12-ZGNR and 12-AGNR edges. In **(A)**, the black line refers to the mechanism i), which is the precursor-mediated mechanism of CH_4 adsorption into CH_3 and H, onto 12-ZGNR edges; The red and purple lines represent the direct mechanism ii) of CH_4 deprotonation on the same Z1 site and different Z1 sites iii) of 12-ZGNR edges, respectively. In **(B)**, black lines and red lines represent the direct mechanisms of methane adsorption on different A1 sites and on the same A1 sites of 12-AGNR edges, respectively. Reaction coordinate is in arbitrary units. The stationary points of the reaction mechanism and their labels are depicted in **(C)**.

TABLE 2 The DFT energy barrier heights and activation free energy values at 1200 K (inside parenthesis) obtained here and compared with theoretical values and experimental apparent activation energy available in the literature, in eV, for the reaction steps of CMD mechanism (S1: $CH_4 \rightarrow CH_3^* + H^*$; S2: $CH_3^* \rightarrow CH_2^* + H^*$; S3: $CH_2^* \rightarrow CH^* + H^*$; and S4: $CH^* \rightarrow C^* + H^*$. The catalyst adopted in the respective work is indicated.

Catalyst	S1	S2	S3	S4
12-ZGNR edges (this work)	0.45 (0.56)	1.16 (1.24)	1.57 (1.53)	1.1 (1.06)
Ni(111) (Li et al., 2014)	1.23	0.85	0.29	1.36
ZGNR edges w/vacancy[a] (Calderón et al., 2016)	2.82	1.69	3.322[b]	0.45
Ni-γAl_2O_3 (Salam and Abdullah, 2017)	0.98	0.63	1.15	0.63
Pd-γAl_2O_3 (Salam and Abdullah, 2017)	0.003	0.34	0.33	0.21
Mo-γAl_2O_3 (Salam and Abdullah, 2017)	0.048	3.82	1.99	5.98
Stepped-Ru (0001) (Arevalo et al., 2017)	1.02	-	-	1.10
Cu-Bi (Palmer et al., 2019)	2.80	-	-	-

[a]Reaction steps were retrieved from the inverse reactions of the methane formation mechanism.
[b]Occurs concomitant with H_2 formation.

products on the same A1 site (mechanism v). It is expected that the adsorption of methane proceeds through TS4 iv), with an energy barrier height of 3.41 eV and forming CH_3/A1 + H/A1. We note that the carbon atom of the A1 site slightly relaxes towards the direction of the nanoribbon, as can be seen in Figure 6B. This occurs to minimise the steric hindrance between the methyl and the carbon from the A1 site during chemisorption. A more kinetically favourable reaction, in comparison with iv), was suggested through the v) mechanism, which is characterised by a rate-determining-step with a barrier height of 1.82 eV for the synchronous chemisorption of CH_3 and H on the same A1 site. As elucidated before, the synchronous chemisorption of CH_3 and H on different adsorption sites on the edge is expected to provide more thermodynamically stable products. Therefore, the formation of

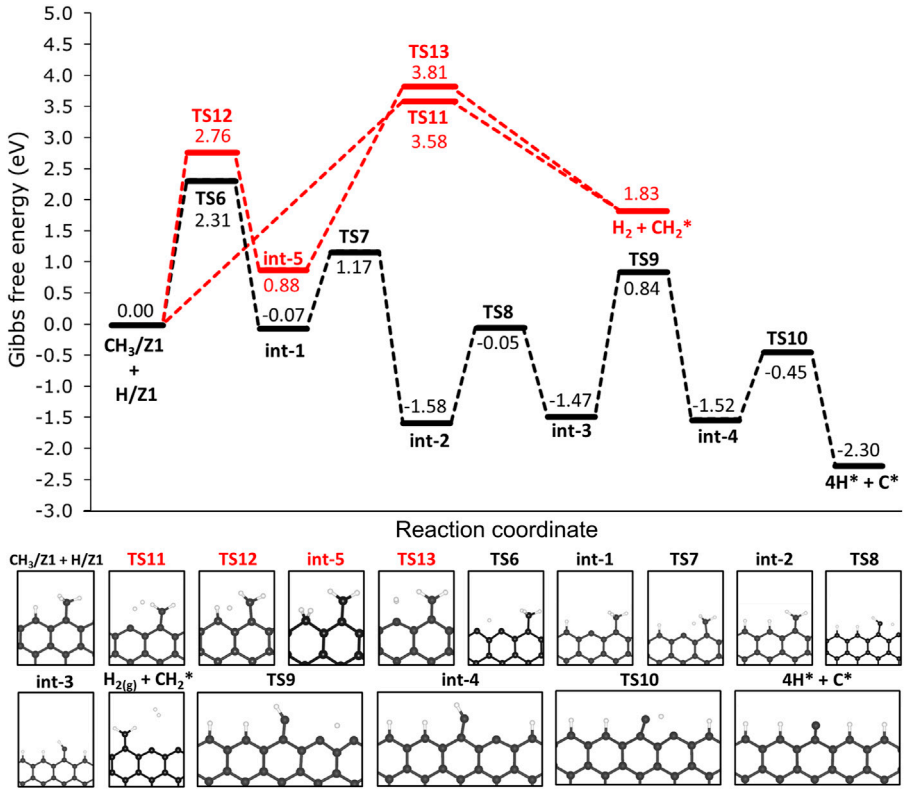

FIGURE 7
Free energy profiles for the consecutive dehydrogenation of CH_3/Z1 + H/Z1 on the non-passivated edges of 12-ZGNR (upper panel). Lower panel: depiction of the stationary points presented in the reaction profile Gibbs free energy values are relative to methyl and hydrogen chemisorbed on Z1 sites. Reaction coordinate is in arbitrary units.

CH_3/A1 and H/A1 products is exothermic, being 2.50 eV more stable than the chemisorption of the same moieties on the same adsorption site.

From the results presented in this section, we conclude that the first step of methane decomposition on the edges of graphene nanoribbons proceeds through a direct dissociation pathway and occurs more favourably on GNRs with zigzag edges. The discussion presented in this paragraph is based on the DFT energy values obtained here, detailed in Table 2, and reported in the literature. The dissociative chemisorption mechanism of CH_4 presented here, proceeds through a barrier of 0.45 eV ($\Delta G_{a,1200K}$ = 0.56 eV), which is significantly lower than what is reported (in the 0.54 eV–1.80 eV range) for the decomposition of methane over transition metal surfaces such as Ni, Fe and Ru (KOERTS, 1992; Salam and Abdullah, 2017). Several molecular beam studies combined with first-principle calculations have been reported for the direct dissociation of CH_4 on single-crystal metal surface such as Pt (111) (Bisson et al., 2007; Guo and Jackson, 2016), Pt (110) (Sacchi et al., 2011; Bisson et al., 2010a; b) and Ni(111) (Bisson et al., 2007; Nave and Jackson, 2009). There is generally an excellent agreement between the prediction of DFT calculations and the experimental barrier heights, 1.1 eV for Ni(111) (Shen et al., 2015) and 0.8 eV for Pt (111) (Guo and Jackson, 2016). Therefore we are confident that the most favourable calculated chemisorption barrier for methane over GNR is about 0.35–0.65 eV lower than both metal surfaces. The stretched C-H bond length at the transition state of methane dissociation into CH_3 and H on Ni(111), Ni(100) and Pt (110) surface was predicted to be 1.63 Å, 1.66 Å and 1.67 Å, respectively Shen et al. (2015); Sacchi et al. (2011); Anghel et al. (2005). Here, we obtained a stretched C-H bond length of 1.27 Å for the most favourable transition state on 12-ZGNR, meaning that the dissociation of CH_4 over GNRs has a much "earlier" barrier, using a Polanyi framework (Ebrahimi et al., 2010), than over Pt and Ni metal surfaces. The lower energy calculated for the methane adsorption on 12-ZGNR edges is likely due to the C-H bond length from the transition state being closer to the equilibrium C-H bond length of gas-phase methane of 1.09 Å, in comparison with the transition state of methane adsorption on Ni (111). Due to the consistency between experimental and computational results for the chemisorption of methane, we are confident in our proposed mechanisms. The barrier for methane chemisorption on GNR is lower than for Ni and Pt by 0.35–0.65, which may have catalytic implications.

3.5 Further steps in the dehydrogenation of CH_4 on the 12-ZGNR edges

As elucidated before, the most thermodynamically favourable products of the deprotonation of methane are CH_3/Z1 and H/Z1. Consecutive deprotonation steps were investigated and the reaction

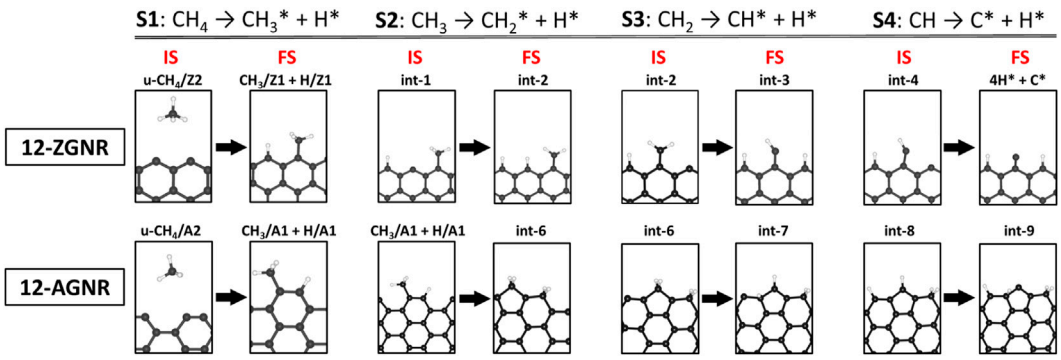

FIGURE 8
Schematic of geometries and their respective labels adopted in this work for the initial states (IS) and final states (FS) of the four steps of the CMD steps on 12-ZGNR and 12-AGNR. S1, S2, S3 and S4 stand for steps 1-4 of the CMD process.

profile is presented in Figure 7. Hereafter, the species chemisorbed on the edges are being represented by a star index '*', since we are referring to the same active site on the 12-ZGNR (Z1) and on 12-AGNR (A1). In the first step, the chemisorbed hydrogen on the edge (H/Z1) diffuses to the next Z1, passing through TS6 with an activation free energy of 2.31 eV, and forming int-1 CH_3/Z1 + H/Z1 → TS7 → int-1. Following the diffusion of H, the cleavage of the C-H bond from CH_2 is expected to occur through TS7 (int-1 → TS7 → int-2 with a ΔG_a value of 1.24 eV. The consecutive steps of hydrogen diffusion and CH_2 deprotonation, occur from int-2 and pass through two consecutive transition states: int-2 → TS8 → int-3 and int-3 → TS9 → int-4 with free energy barriers of 1.63 eV and 2.31 eV, respectively. An activation free energy of 1.07 eV was calculated for the last step of the reaction mechanism (int-4 → TS10 → 4H* + C*), resulting in a carbon atom and four hydrogen atoms chemisorbed on the edges. The final dehydrogenation products on the 12-ZGNR edges (4H* + C*) are predicted to be 2.30 eV more stable than the initial chemisorbed CH_3/Z1 and H/Z1. Overall, the free energy barriers of the diffusion reactions were higher than deprotonation barriers by an average of 1.03 eV, therefore, the diffusion of H is the rate-determining step of the dehydrogenation mechanism of methane on 12-ZGNR edges.

The mechanisms for H_2 formation were investigated, and three possible pathways were obtained. From CH_3/Z1 + H/Z1, H_2 is expected to be formed through the transition state TS11 (CH_3/Z1 + H/Z1 → TS11 → H_2 + CH_2*). In this pathway, one hydrogen atom from the chemisorbed CH_3/Z1 and the hydrogen atom chemisorbed on the edge reacted forming H_2, with a ΔG_a of 3.58 eV. Another possible reaction pathway was obtained from CH_3/Z1 + H/Z1, in which a s C-H bond cleavage occurs and the hydrogen atom migrates to the edge site already occupied with a proton (CH_3/Z1 + H/Z1 → TS12 → int-5). This process proceeds through TS12, with a ΔG_a of 2.76 eV. The H_2 is formed from int-5, from the two hydrogen atoms chemisorbed on the same edge, with a barrier height of 2.93 eV. Based on the results reported in Section 3.2.1, the most likely scenario of the bare carbon active sites regeneration under reaction conditions, i.e., the desorption of H_2 from the edges, is through the diffusion of H, forming HH/Z1 (12-ZGNR → TS. DIff/Z1 → HH/Z1, ΔG_a = 4.17 eV) followed by the H_2 formation (HH/Z1 → TS. HH/Z1 → H_2 + *, ΔG_a = 2.95 eV) leaving only solid carbon on the edges which remains as an active site for further methane dehydrogenation reactions.

The barrier heights (at 0 K) and activation free energy values at 1200 K of the reaction pathway proposed here, and a comparison with literature reports for the reaction steps S1 (dissociative: CH_4 → CH_3* + H*), S2 (CH_3* → CH_2* + H*), S3 (CH_2* → CH* + H*) and S4 (CH* → C* + H*), are presented in Table 2. We have shown in Figure 8 a schematic of the initial states (IS) and final states (FS) of each CMD step (S1—S4) and the respective labels adopted in this work, aiming to facilitate the comparison with the literature data presented in Table 2. Li et al. (2014) investigated the decomposition of methane on a Ni(111) clean surface, utilizing DFT coupled with STO-3G basis set. The authors reported that methane adsorption proceeds through a dissociative mechanism (S1) with a barrier height of 1.23 eV and suggested barrier heights of 0.85 eV, 0.29 eV and 1.36 eV for the consecutive dehydrogenation reactions (S2, S3 and S4, respectively). In the work of Calderón et al. (2016), a mechanism for methane formation on the zigzag edges was proposed in an aromatic cluster consisting of five benzene rings with two edges dangling carbon atoms as reactive sites. Calculations were made at the B3LYP/6–311++G (d,*p*) level and activation energies were proposed for the temperature range between 298 K and 1500 K. The processes relevant to CMD were taken as the reversible reaction steps of the proposed mechanism and reported in Table 2. Based on their reports, the dissociative mechanism of CH_4 adsorption (S1) occurred on a carbon vacancy on the zigzag edge, with a barrier height of 2.82 eV, whereas the H_2 formation was suggested to occur concomitant to step S2 (see Table 2) of CMD with an energetic barrier of 3.32 eV.

In the work of Salam and Abdullah (2017), the CMD mechanism was studied for Ni, Pd and Mo-promoted γ-alumina, from which methane was suggested to decompose through a direct mechanism. The barrier for the most kinetically-favourable dissociation mechanism obtained here (S1, 0.45 eV), was lower than barrier height values reported for the Ni-γAl_2O_3 (0.98 eV). When adopting other transition metals (Pd and Mo) promoting the γ-alumina catalyst, the direct mechanism of methane (S1) was suggested to proceed with a barrier height of 0.003 eV and

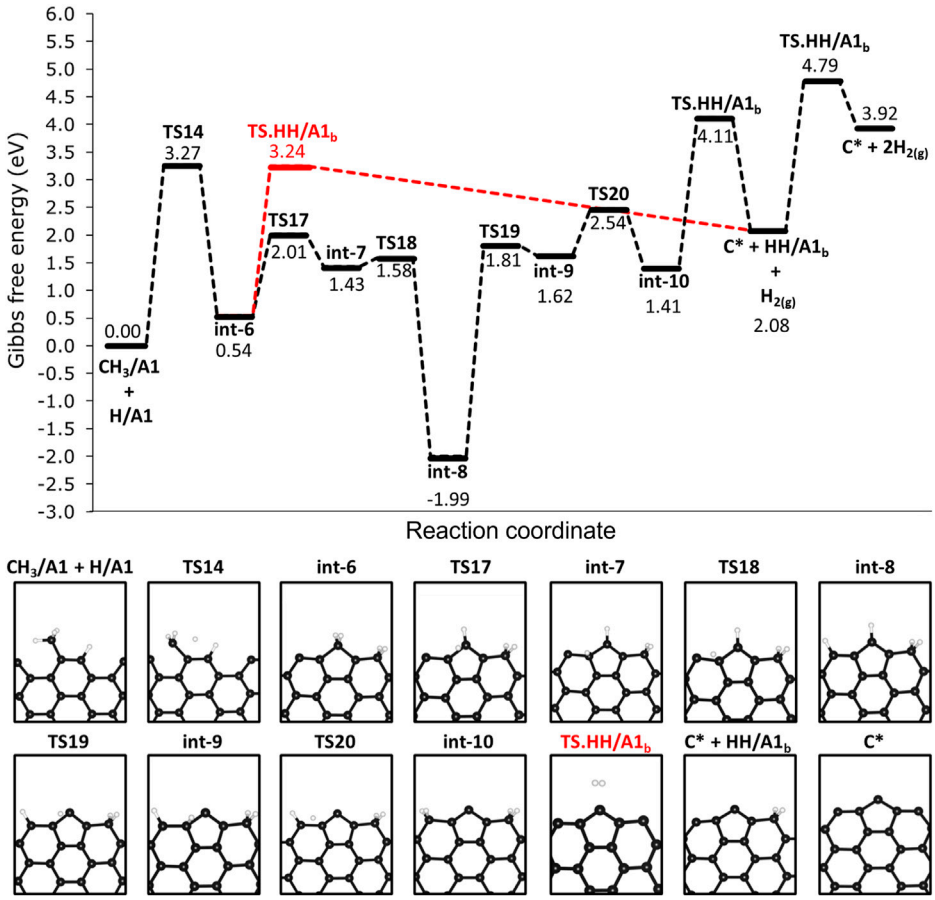

FIGURE 9
Free energy reaction profile, at 1200 K, for the deprotonation steps of methane on H-free edges of 12-AGNR (upper panel). The stationary points presented in the reaction profile are depicted in the lower panel. Gibbs free energy values are relative to methyl and hydrogen chemisorbed on A1 adsorption sites. Reaction coordinate is in arbitrary units.

0.048 eV, respectively (Salam and Abdullah, 2017). Arevalo et al. (2017) studied the dissociative adsorption of methane (S1) and the step S4 of the CMD mechanism on a stepped Ru (0001) surface, adopting the PBE-D2/PAW methodology, reporting values of 1.02 eV and 1.1 eV, respectively. In the work of Palmer et al. (2019), the mechanism of methane decomposition was investigated on a Cu-Bi alloy catalyst by AIMD simulations. Activation energy of 2.8 eV was obtained for the dissociative mechanism (S1). The results were in good agreement with the experimental measured apparent activation energy of 2.3 eV, in the temperature range of 1123 K and 1253 K for the same reaction step.

Overall we found that the reactions occurring at the 12-ZGNR edges are comparable, in terms of activation energies and thermodynamic requirements, with metallic catalysts, based on the literature reports presented in Table 2. Only a few metal-based catalysts, such as the Pd-promoted and the Mo-promoted γ-alumina have lower CH_4 dissociation barriers than 12-ZGNRs (0.44 eV and 0.40 eV lower, respectively). With respect to the entire CMD mechanism, the rate-determining step obtained on the 12-ZGNR edges was S3, with a barrier of 1.57 eV, which is higher than for the rate-determining step on Ni(111) (S1, 1.23 eV) (Li et al., 2014), Ni-γAl_2O_3 (S3, 1.15) eV and Pd-γAl_2O_3 (S2, 0.34 eV) (Salam and Abdullah, 2017).

3.6 Growth and active site regeneration on the 12-AGNR edges

We investigated the steps following the adsorption of methane on 12-AGNR edges and the results are shown in Figure 9. The deprotonation of CH_3/A1 proceeds with an activation free energy of 3.27 eV, forming int-6, which is a label for the CH_2/A1 and HH/A1 (CH_3/A1 + H/A1 → TS14 → int-6). The deprotonation of the methyl is followed by the bonding of CH_2/A1 into two rows of carbon atoms on the armchair edges, resulting in a grown active site on the edges hereafter labelled as $A1_b$ (Figure 9). The H_2 formation from HH/$A1_b$ proceeds with a higher activation free energy barrier of 2.70 eV (HH/$A1_b$ → TS. HH/$A1_b$ → C* + H_2) in comparison with the pristine carbon site on the armchair edge (HH/A1 → TS. HH/A1 → * + H_2, ΔG_a = 1.57 eV), detailed in Figure 4B. It is noteworthy that the same activation free energy value is expected for the H_2 formation on the carbon row containing the C* and, therefore, it is defined as the same active site and also labelled as $A1_b$. The ΔG_a

value of 2.70 eV is expected in the final step of the catalyst regeneration forming only a carbon atom on the surface (C^* + $HH/A1_b \rightarrow$ TS. $HH/A1_b \rightarrow C^* + H_2$) and remaining as an active site for further methane decomposition steps. An alternative pathway for the regeneration of the 12-AGNR active sites on edges proceeds from int-6 through low free energy barriers of 1.47 eV (int-6 → TS17 → int-7) and 0.15 eV (int-7 → TS18 → int-8), respective to the hydrogen atom migration among adjacent $A1_b$ sites until reaching the last carbon on the atom row (int-8, Figure 9). The intermediate formed (int-8) is more thermodynamic stable than the previous minimum energy structures in the mechanism (int-7), by 3.42 eV. The ΔG_a values of 3.80 eV (int-8 → TS19 → int-9) and 0.92 eV (int-9 → TS20 → int-10) are expected for the migration of a hydrogen atom from the grown carbon site to forming the $HH/A1_b$ (int-10, Figure 9). Finally, a consecutive reaction of H_2 formation is expected to occur from int-10 with ΔG_a of 2.70 eV ($HH/A1_b \rightarrow$ TS. $HH/A1_b \rightarrow C^* + H_2$), regenerating the $A1_b$ active sites.

4 Conclusion

Much effort has been made to design an efficient and environment-friendly catalyst for producing hydrogen from methane, and nanocarbons have been proposed as one of the most suited materials for this reaction. In this work, we presented a detailed reaction mechanism, obtained through first-principles DFT calculations, for the process of methane catalytic decomposition on the edges of graphene nanoribbons. The dehydrogenation of the zigzag and armchair edges was investigated and we concluded that the bare carbon active site is mainly available due to H_2 desorption from two hydrogen atoms chemisorbed on the sabe edge site, in which we estimated free energy activation values of 2.95 eV and 1.56 eV for the 12-AGNR and 12-ZGNR. Furthermore, we found that the direct mechanism of CH_4 dissociation into CH_3 and H was the preferred mechanism for catalysing the breaking of the first C-H bond of methane.

Several competing reaction mechanisms for methane dehydrogenation on 12-ZGNR and 12-AGNR were investigated. Our results show that the deprotonation of methane proceeds *via* a synchronous mechanism, in which the cleavage of the C-H bond and chemisorption of the methyl and hydrogen atom occur in the same step, i. e., direct reaction mechanism. Furthermore, the minimum reaction pathway proceeds through a small activation free energy of 0.56 eV on the 12-ZGNR edge. An alternative pathway connecting the physisorbed methane to the methyl and hydrogen chemisorbed on different sites was proposed. This reaction pathway proceeds through a barrier height of 0.97 eV and forming a more thermodynamically stable product. The highest free energy of activation among the deprotonation reactions was 1.53 eV whereas the highest ΔG_a value among the diffusion reactions was 2.32 eV. On the 12-AGNR edges, the deprotonation of CH_3 generates a carbon bonded with the atom row on the armchair edges. Molecular hydrogen is desorbed from the grown active sites with an activation free energy of 2.70 eV, being easier for catalyst regeneration in comparison with the zigzag edges.

Our theoretical results compare favorably with other literature reports, providing a justification for employing pristine graphene nanoribbons as a catalyst for the CMD process since these nanocarbons show a remarkably small barrier for the dissociation of methane, comparable to the values between 0.54 eV and 1.80 eV for commonly used metal catalysts. It is noteworthy that the zigzag edges are more susceptible to deactivation from the chemisorption of hydrogen atom whereas the growth of the armchair edges acts as the regeneration of the active sites.

The results presented here provide insights for the autocatalytic activity of graphene nanoribbons, enlightening the reactivity of graphene nanoribbons edges on the methane decomposition. To the best of our knowledge, this is the first time in which the CMD reaction steps were carefully evaluated under reaction conditions by addressing the deactivation of the edges by hydrogen passivation or solid carbon formation. Although we found that the armchair edges were the most promising edge morphology for promoting the autocatalytic effect on CMD, due to the low free energy barrier needed for the desorption of H_2, a high activation free energy is needed for the diffusion of H into the edges, being the rate determinant step for the dehydrogenation on the edges. The free energy of activation for hydrogen formation on the deposited carbon sites was higher in comparison with the reaction occurring on pristine armchair edges, showing that the H_2 formation decreases during the CMD process, mainly due to the non-ordered growth of the armchair edges. With respect to the CMD steps on 12-ZGNR edges, we found an excellent performance for the methane decomposition, however, structural and electronic modification on the zigzag edges should be considered in order to increase the activity for H_2 formation. We believe that the results presented in this work can provide fundamental insights for the design and synthesis of graphene-based catalysts for the activation and decomposition of methane and hydrogen production.

Data availability statement

Original datasets are available in a publicly accessible repository: The original contributions presented in the study are publicly available. This data can be found here: https://doi.org/10.15126/surreydata.900725.

Author contributions

NX performed the computational simulations and wrote the first draft of the manuscript. AP assisted in the computational simulations. GB contributed with the discussion and conceptualisation. MS contributed with the conception and design of the research. All authors contributed to the article and approved the submitted version.

Funding

The authors acknowledge the Royal Society for funding through the grants URF\R\191029 and RF\ERE\210215. We are grateful for computational support from the UK national high-performance

computing service, ARCHER2, for which access was obtained via the UKCP consortium and funded by EPSRC grant ref EP/P022561/1.

Acknowledgments

The authors acknowledge the University of Surrey for funding the open access publication fees

Conflict of interest

The authors declare that the research was conducted in the absence of any commercial or financial relationships that could be construed as a potential conflict of interest.

Publisher's note

Supplementary material

The Supplementary Material for this article can be found online at: https://www.frontiersin.org/articles/10.3389/fchem.2023.1172687/full#supplementary-material

References

Abánades, A., Rathnam, R. K., Geißler, T., Heinzel, A., Mehravaran, K., Müller, G., et al. (2016). Development of methane decarbonisation based on liquid metal technology for CO2-free production of hydrogen. *Int. J. Hydrogen Energy* 41, 8159–8167. doi:10.1016/j.ijhydene.2015.11.164

Alves, L., Pereira, V., Lagarteira, T., and Mendes, A. (2021). Catalytic methane decomposition to boost the energy transition: Scientific and technological advancements. *Renew. Sustain. Energy Rev.* 137, 110465. doi:10.1016/j.rser.2020.110465

Anghel, A. T., Wales, D. J., Jenkins, S. J., and King, D. A. (2005). Pathways for dissociative methane chemisorption on. *Phys. Rev. B* 71, 113410. doi:10.1103/PhysRevB.71.113410

Anithaa, V. S., Shankar, R., and Vijayakumar, S. (2017). DFT-based investigation on adsorption of methane on pristine and defected graphene. *Struct. Chem.* 28, 1935–1952. doi:10.1007/s11224-017-0988-x

Arevalo, R. L., Aspera, S. M., Sison Escaño, M. C., Nakanishi, H., and Kasai, H. (2017). First principles study of methane decomposition on B5 step-edge type site of Ru surface. *J. Phys. Condens. Matter* 29, 184001. doi:10.1088/1361-648X/aa66c7

Ashik, U. P., Wan Daud, W. M., and Abbas, H. F. (2015). Production of greenhouse gas free hydrogen by thermocatalytic decomposition of methane – a review. *Renew. Sustain. Energy Rev.* 44, 221–256. doi:10.1016/j.rser.2014.12.025

Barone, V., Hod, O., and Scuseria, G. E. (2006). Electronic structure and stability of semiconducting graphene nanoribbons. *Nano Lett.* 6, 2748–2754. doi:10.1021/nl0617033

Bisson, R., Sacchi, M., and Beck, R. D. (2010a). Mode-specific reactivity of CH4 on Pt(110)-(1× 2): The concerted role of stretch and bend excitation. *Phys. Rev. B* 82, 121404. doi:10.1103/PhysRevB.82.121404

Bisson, R., Sacchi, M., and Beck, R. D. (2010b). State-resolved reactivity of CH4 on Pt(110)-(1× 2): The role of surface orientation and impact site. *J. Chem. Phys.* 132, 094702. doi:10.1063/1.3328885

Bisson, R., Sacchi, M., Dang, T. T., Yoder, B., Maroni, P., and Beck, R. D. (2007). State-Resolved reactivity of CH 4 (2*v* 3) on Pt(111) and Ni(111): Effects of barrier height and transition state location. *J. Phys. Chem. A* 111, 12679–12683. doi:10.1021/jp076082w

Brooks, A., Jenkins, S. J., Wrabetz, S., McGregor, J., and Sacchi, M. (2022). The dehydrogenation of butane on metal-free graphene. *J. Colloid Interface Sci.* 619, 377–387. doi:10.1016/j.jcis.2022.03.128

Calderón, L. A., Chamorro, E., and Espinal, J. F. (2016). Mechanisms for homogeneous and heterogeneous formation of methane during the carbon–hydrogen reaction over zigzag edge sites. *Carbon* 102, 390–402. doi:10.1016/j.carbon.2016.02.052

Campbell, C. T., Sprowl, L. H., and Árnadóttir, L. (2016). Equilibrium constants and rate constants for adsorbates: Two-dimensional (2D) ideal gas, 2D ideal lattice gas, and ideal hindered translator models. *J. Phys. Chem. C* 120, 10283–10297. doi:10.1021/acs.jpcc.6b00975

Castro Neto, A., Kotov, V., Nilsson, J., Pereira, V., Peres, N., and Uchoa, B. (2009). Adatoms in graphene. *Solid State Commun.* 149, 1094–1100. doi:10.1016/j.ssc.2009.02.040

Chai, S.-P., Zein, S. H. S., and Mohamed, A. R. (2006). Preparation of carbon nanotubes over cobalt-containing catalysts via catalytic decomposition of methane. *Chem. Phys. Lett.* 426, 345–350. doi:10.1016/j.cplett.2006.05.026

Chang, C. R., Huang, Z. Q., Chen, Y. T., and Li, J. (2021). Theoretical insights into dual-metal-site catalysts for the nonoxidative coupling of methane. *ACS Catal.* 11, 13149–13159. doi:10.1021/acscatal.1c02597

Clark, S. J., Segall, M. D., Pickard, C. J., Hasnip, P. J., Probert, M. I. J., Refson, K., et al. (2005). First principles methods using CASTEP. *Z. für Kristallogr. - Cryst. Mater.* 220, 567–570. doi:10.1524/zkri.220.5.567.65075

Dutta, S., and Pati, S. K. (2010). Novel properties of graphene nanoribbons: A review. *J. Mater. Chem.* 20, 8207. doi:10.1039/c0jm00261e

Ebrahimi, M., Guo, S. Y., McNab, I. R., and Polanyi, J. C. (2010). Early and "late" barriers in dissociative attachment: Steering surface reaction. *J. Phys. Chem. Lett.* 1, 2600–2605. doi:10.1021/jz100868n

Esteves, L. M., Daás, A. A., Oliveira, H. A., and Passos, F. B. (2020). Influence of space velocity and catalyst pretreatment on COx free hydrogen and carbon nanotubes production over CoMo/MgO catalyst. *Int. J. Hydrogen Energy* 45, 27299–27311. doi:10.1016/j.ijhydene.2020.07.133

Fan, Z., Weng, W., Zhou, J., Gu, D., and Xiao, W. (2021). Catalytic decomposition of methane to produce hydrogen: A review. *J. Energy Chem.* 58, 415–430. doi:10.1016/j.jechem.2020.10.049

Fujii, S., and Enoki, T. (2013). Nanographene and graphene edges: Electronic structure and nanofabrication. *Accounts Chem. Res.* 46, 2202–2210. doi:10.1021/ar300120y

Gao, J., Zhao, J., and Ding, F. (2012). Transition metal surface passivation induced graphene edge reconstruction. *J. Am. Chem. Soc.* 134, 6204–6209. doi:10.1021/ja2104119

Geim, A. K., and Novoselov, K. S. (2007). The rise of graphene. *Nat. Mater.* 6, 183–191. doi:10.1038/nmat1849

Govind, N., Petersen, M., Fitzgerald, G., King-Smith, D., and Andzelm, J. (2003). A generalized synchronous transit method for transition state location. *Comput. Mater. Sci.* 28, 250–258. doi:10.1016/S0927-0256(03)00111-3

Guil-Lopez, R., Botas, J., Fierro, J., and Serrano, D. (2011). Comparison of metal and carbon catalysts for hydrogen production by methane decomposition. *Appl. Catal. A General* 396, 40–51. doi:10.1016/j.apcata.2011.01.036

Guo, H., and Jackson, B. (2016). Mode-selective chemistry on metal surfaces: The dissociative chemisorption of CH 4 on Pt(111). *J. Chem. Phys.* 144, 184709. doi:10.1063/1.4948941

Hadian, M., Buist, K., Bos, A., and Kuipers, J. (2021). Single catalyst particle growth modeling in thermocatalytic decomposition of methane. *Chem. Eng. J.* 421, 129759. doi:10.1016/j.cej.2021.129759

Hamdan, M., Halawy, L., Abdel Karim Aramouni, N., Ahmad, M. N., and Zeaiter, J. (2022). Analytical review of the catalytic cracking of methane. *Fuel* 324, 124455. doi:10.1016/j.fuel.2022.124455

Han, P., Yu, X., Yuan, D., Kuang, M., Wang, Y., Al-Enizi, A. M., et al. (2019). Defective graphene for electrocatalytic CO2 reduction. *J. Colloid Interface Sci.* 534, 332–337. doi:10.1016/j.jcis.2018.09.036

He, K., Lee, G.-D., Robertson, A. W., Yoon, E., and Warner, J. H. (2014). Hydrogen-free graphene edges. *Nat. Commun.* 5, 3040. doi:10.1038/ncomms4040

He, M., Liu, X. Q., Li, M., Yang, Y., Chen, Z., Jiang, W., et al. (2022). Multiple hydrogen bonds enhancing formaldehyde adsorption on functionalized zigzag graphene nanoribbons. *Appl. Surf. Sci.* 586, 152834. doi:10.1016/j.apsusc.2022.152834

Hermesmann, M., and Müller, T. (2022). Green, turquoise, blue, or grey? Environmentally friendly hydrogen production in transforming energy systems. *Prog. Energy Combust. Sci.* 90, 100996. doi:10.1016/j.pecs.2022.100996

Jia, X., Campos-Delgado, J., Terrones, M., Meunier, V., and Dresselhaus, M. S. (2011). Graphene edges: A review of their fabrication and characterization. *Nanoscale* 3, 86–95. doi:10.1039/C0NR00600A

Jiang, C., Wang, I. W., Bai, X., Balyan, S., Robinson, B., Hu, J., et al. (2022). Methane catalytic pyrolysis by microwave and thermal heating over carbon nanotube-supported catalysts: Productivity, kinetics, and energy efficiency. *Industrial Eng. Chem. Res.* 61, 5080–5092. doi:10.1021/acs.iecr.1c05082

Johnson, R. D., III, Richter, U., Manichaikul, A., Schneider, B., Acevedo, C., Cockrell, B., et al. (2020). *NIST computational Chemistry comparison and benchmark database*. Maryland, United States: National Institute Of Standards And Technology.

Knopf, D. A., and Ammann, M. (2021). Technical note: Adsorption and desorption equilibria from statistical thermodynamics and rates from transition state theory. *Atmos. Chem. Phys.* 21, 15725–15753. doi:10.5194/acp-21-15725-2021

Koerts, T. (1992). Hydrocarbon formation from methane by a low-temperature two-step reaction sequence. *J. Catal.* 138, 101–114. doi:10.1016/0021-9517(92)90010-F

Kosynkin, D. V., Higginbotham, A. L., Sinitskii, A., Lomeda, J. R., Dimiev, A., Price, B. K., et al. (2009). Longitudinal unzipping of carbon nanotubes to form graphene nanoribbons. *Nature* 458, 872–876. doi:10.1038/nature07872

Kuila, T., Bose, S., Mishra, A. K., Khanra, P., Kim, N. H., and Lee, J. H. (2012). Chemical functionalization of graphene and its applications. *Prog. Mater. Sci.* 57, 1061–1105. doi:10.1016/j.pmatsci.2012.03.002

Lawrence, R. A., Gante, N., and Sacchi, M. (2021). Reduction of NO on chemically doped, metal-free graphene. *Carbon Trends* 5, 100111. doi:10.1016/j.cartre.2021.100111

Li, H., and Jensen, J. H. (2002). Partial hessian vibrational analysis: The localization of the molecular vibrational energy and entropy. *Theor. Chem. Accounts Theory, Comput. Model. Theor. Chimica Acta)* 107, 211–219. doi:10.1007/s00214-001-0317-7

Li, J., Croiset, E., and Ricardez–Sandoval, L. (2014). Effect of carbon on the Ni catalyzed methane cracking reaction: A DFT study. *Appl. Surf. Sci.* 311, 435–442. doi:10.1016/j.apsusc.2014.05.081

Li, X., Wang, X., Zhang, L., Lee, S., and Dai, H. (2008). Chemically derived, ultrasmooth graphene nanoribbon semiconductors. *Science* 319, 1229–1232. doi:10.1126/science.1150878

Li, Y., Zhang, W., Morgenstern, M., and Mazzarello, R. (2013). Electronic and magnetic properties of zigzag graphene nanoribbons on the (111) surface of Cu, Ag, and Au. *Phys. Rev. Lett.* 110, 216804. doi:10.1103/PhysRevLett.110.216804

López-Urías, F., Fajardo-Díaz, J. L., Cortés-López, A. J., Rodríguez-Corvera, C. L., Jiménez-Ramírez, L. E., and Muñoz-Sandoval, E. (2020). Understanding the electrochemistry of armchair graphene nanoribbons containing nitrogen and oxygen functional groups: DFT calculations. *Phys. Chem. Chem. Phys.* 22, 4533–4543. doi:10.1039/c9cp05857e

López-Urías, F., Martínez-Iniesta, A. D., Morelos-Gómez, A., and Muñoz-Sandoval, E. (2021). Tuning the electronic and magnetic properties of graphene nanoribbons through phosphorus doping and functionalization. *Mater. Chem. Phys.* 265, 124450. doi:10.1016/j.matchemphys.2021.124450

Monkhorst, H. J., and Pack, J. D. (1976). Special points for Brillouin-zone integrations. *Phys. Rev. B* 13, 5188–5192. doi:10.1103/PhysRevB.13.5188

Montoya, A., Mondragón, F., and Truong, T. N. (2003). CO2 adsorption on carbonaceous surfaces: A combined experimental and theoretical study. *Carbon* 41, 29–39. doi:10.1016/S0008-6223(02)00249-X

Nave, S., and Jackson, B. (2009). Methane dissociation on Ni(111) and Pt(111): Energetic and dynamical studies. *J. Chem. Phys.* 130, 054701. doi:10.1063/1.3065800

Ni, L., Kuroda, K., Zhou, L.-P., Kizuka, T., Ohta, K., Matsuishi, K., et al. (2006). Kinetic study of carbon nanotube synthesis over Mo/Co/MgO catalysts. *Carbon* 44, 2265–2272. doi:10.1016/j.carbon.2006.02.031

Noei, M. (2016). DFT study on the sensitivity of open edge graphene toward CO2 gas. *Vacuum* 131, 194–200. doi:10.1016/j.vacuum.2016.06.018

Palmer, C., Tarazkar, M., Kristoffersen, H. H., Gelinas, J., Gordon, M. J., McFarland, E. W., et al. (2019). Methane pyrolysis with a molten Cu-Bi alloy catalyst. *ACS Catal.* 9, 8337–8345. doi:10.1021/acscatal.9b01833

Pan, Y., Lo, V., Cao, L., Roy, A., Chivers, B., Noorbehesht, N., et al. (2022). Graphitic carbon from catalytic methane decomposition as efficient conductive additives for zinc-carbon batteries. *Carbon* 192, 84–92. doi:10.1016/j.carbon.2022.02.049

Peng, H., Duan, D., Liu, S., Liu, J., Sun, L., Huang, P., et al. (2021). A graphene-like nanoribbon for efficient bifunctional electrocatalysts. *J. Mater. Chem. A* 9, 26688–26697. doi:10.1039/d1ta06078c

Perdew, J. P., Ernzerhof, M., and Burke, K. (1996). Rationale for mixing exact exchange with density functional approximations. *J. Chem. Phys.* 105, 9982–9985. doi:10.1063/1.472933

Pfrommer, B. G., Côté, M., Louie, S. G., and Cohen, M. L. (1997). Relaxation of crystals with the quasi-Newton method. *J. Comput. Phys.* 131, 233–240. doi:10.1006/jcph.1996.5612

Pinaeva, L. G., Noskov, A. S., and Parmon, V. N. (2017). Prospects for the direct catalytic conversion of methane into useful chemical products. *Catal. Industry* 9, 283–298. doi:10.1134/S2070050417040067

Pinilla, J. L., Suelves, I., Lázaro, M. J., and Moliner, R. (2008). Kinetic study of the thermal decomposition of methane using carbonaceous catalysts. *Chem. Eng. J.* 138, 301–306. doi:10.1016/j.cej.2007.05.056

Pizzochero, M., and Kaxiras, E. (2022). Hydrogen atoms on zigzag graphene nanoribbons: Chemistry and magnetism meet at the edge. *Nano Lett.* 22, 1922–1928. doi:10.1021/acs.nanolett.1c04362

Pomerantseva, E., Bonaccorso, F., Feng, X., Cui, Y., and Gogotsi, Y. (2019). Energy storage: The future enabled by nanomaterials. *Science* 366, eaan8285. doi:10.1126/science.aan8285

Pudukudy, M., Yaakob, Z., Jia, Q., and Sobri Takriff, M. (2018). Catalytic decomposition of undiluted methane into hydrogen and carbon nanotubes over Pt promoted Ni/CeO2 catalysts. *New J. Chem.* 42, 14843–14856. doi:10.1039/c8nj02842g

Qian, J. X., Chen, T. W., Enakonda, L. R., Liu, D. B., Basset, J. M., and Zhou, L. (2020). Methane decomposition to pure hydrogen and carbon nano materials: State-of-the-art and future perspectives. *Int. J. Hydrogen Energy* 45, 15721–15743. doi:10.1016/j.ijhydene.2020.04.100

Rao, C., Gopalakrishnan, K., and Govindaraj, A. (2014). Synthesis, properties and applications of graphene doped with boron, nitrogen and other elements. *Nano Today* 9, 324–343. doi:10.1016/j.nantod.2014.04.010

Rattanaamonkulchai, R., Kludpantanapan, T., Nantapong, P., Srifa, A., Koo-Amornpattana, W., Chaiwat, W., et al. (2022). Simultaneous production of hydrogen and carbon nanotubes from biogas: On the design of combined process. *Int. J. Hydrogen Energy* 47, 14432–14452. doi:10.1016/j.ijhydene.2022.02.179

Reshetenko, T., Avdeeva, L., Ushakov, V., Moroz, E., Shmakov, A., Kriventsov, V., et al. (2004). Coprecipitated iron-containing catalysts (Fe-Al2O3, Fe-Co-Al2O3, Fe-Ni-Al2O3) for methane decomposition at moderate temperatures. *Appl. Catal. A General* 270, 87–99. doi:10.1016/j.apcata.2004.04.026

Ruffieux, P., Wang, S., Yang, B., Sánchez-Sánchez, C., Liu, J., Dienel, T., et al. (2016). On-surface synthesis of graphene nanoribbons with zigzag edge topology. *Nature* 531, 489–492. doi:10.1038/nature17151

Russell, J. C., Posey, V. A., Gray, J., May, R., Reed, D. A., Zhang, H., et al. (2021). High-performance organic pseudocapacitors via molecular contortion. *Nat. Mater.* 20, 1136–1141. doi:10.1038/s41563-021-00954-z

Sacchi, M., Wales, D., and Jenkins, S. (2012a). Bond-selective energy redistribution in the chemisorption of CH3D and CD3H on Pt{110}-(1× 2): A first-principles molecular dynamics study. *Comput. Theor. Chem.* 990, 144–151. doi:10.1016/j.comptc.2011.11.048

Sacchi, M., Wales, D. J., and Jenkins, S. J. (2011). Mode-specific chemisorption of CH 4 on Pt{110}-(1 × 2) explored by first-principles molecular dynamics. *J. Phys. Chem. C* 115, 21832–21842. doi:10.1021/jp207746q

Sacchi, M., Wales, D. J., and Jenkins, S. J. (2012b). Mode-specificity and transition state-specific energy redistribution in the chemisorption of CH4 on Ni{100}. *Phys. Chem. Chem. Phys.* 14, 15879. doi:10.1039/c2cp42345f

Salam, M. A., and Abdullah, B. (2017). Catalysis mechanism of Pd-promoted γ-alumina in the thermal decomposition of methane to hydrogen: A density functional theory study. *Mater. Chem. Phys.* 188, 18–23. doi:10.1016/j.matchemphys.2016.12.022

Segall, M. D., Lindan, P. J. D., Probert, M. J., Pickard, C. J., Hasnip, P. J., Clark, S. J., et al. (2002). First-principles simulation: Ideas, illustrations and the CASTEP code. *J. Phys. Condens. Matter* 14, 2717–2744. doi:10.1088/0953-8984/14/11/301

Shen, X., Chen, J., Zhang, Z., Shao, K., and Zhang, D. H. (2015). Methane dissociation on Ni(111): A fifteen-dimensional potential energy surface using neural network method. *J. Chem. Phys.* 143, 144701. doi:10.1063/1.4932226

Soldano, G., Juarez, M., Teo, B., and Santos, E. (2014). Structure and stability of graphene edges in O2 and H2 environments from *ab initio* thermodynamics. *Carbon* 78, 181–189. doi:10.1016/j.carbon.2014.06.070

Son, Y.-W., Cohen, M. L., and Louie, S. G. (2006). Half-metallic graphene nanoribbons. *Nature* 444, 347–349. doi:10.1038/nature05180

Suelves, I., Pinilla, J., Lázaro, M., and Moliner, R. (2008). Carbonaceous materials as catalysts for decomposition of methane. *Chem. Eng. J.* 140, 432–438. doi:10.1016/j.cej.2007.11.014

Suman, H., Srivastava, R., Shrivastava, S., Srivastava, A., Jacob, A. P., and Malvi, C. S. (2020). DFT analysis of H2S adsorbed zigzag and armchair graphene nanoribbons. *Chem. Phys. Lett.* 745, 137280. doi:10.1016/j.cplett.2020.137280

Szymańska, M., Malaika, A., Rechnia, P., Miklaszewska, A., and Kozłowski, M. (2015). Metal/activated carbon systems as catalysts of methane decomposition reaction. *Catal. Today* 249, 94–102. doi:10.1016/j.cattod.2014.11.025

Tkatchenko, A., DiStasio, R. A., Car, R., and Scheffler, M. (2012). Accurate and efficient method for many-body van der Waals interactions. *Phys. Rev. Lett.* 108, 236402. doi:10.1103/PhysRevLett.108.236402

Tkatchenko, A., and Scheffler, M. (2009). Accurate molecular van der Waals interactions from ground-state electron density and free-atom reference data. *Phys. Rev. Lett.* 102, 073005. doi:10.1103/PhysRevLett.102.073005

Tong, S., Miao, B., Zhang, L., and Chan, S. H. (2022). Decarbonizing natural gas: A review of catalytic decomposition and carbon formation mechanisms. *Energies* 15, 2573. doi:10.3390/en15072573

Vanderbilt, D. (1990). Soft self-consistent pseudopotentials in a generalized eigenvalue formalism. *Phys. Rev. B* 41, 7892–7895. doi:10.1103/PhysRevB.41.7892

Vekeman, J., Cuesta, G., Faginas-Lago, N., Wilson, J., Sánchez-Marín, J., and Sánchez de Merás, A. (2018). Potential models for the simulation of methane adsorption on graphene: Development and CCSD(T) benchmarks. *Phys. Chem. Chem. Phys.* 20, 25518–25530. doi:10.1039/C8CP03652G

Wang, I., Dagle, R. A., Khan, T. S., Lopez-Ruiz, J. A., Kovarik, L., Jiang, Y., et al. (2021). Catalytic decomposition of methane into hydrogen and high-value carbons: Combined experimental and DFT computational study. *Catal. Sci. Technol.* 11, 4911–4921. doi:10.1039/d1cy00287b

Wood, B. C., Bhide, S. Y., Dutta, D., Kandagal, V. S., Pathak, A. D., Punnathanam, S. N., et al. (2012). Methane and carbon dioxide adsorption on edge-functionalized graphene: A comparative DFT study. *J. Chem. Phys.* 137, 054702. doi:10.1063/1.4736568

Wu, R., Ding, Y., Yu, K. M., Zhou, K., Zhu, Z., Ou, X., et al. (2019). Edge-epitaxial growth of graphene on Cu with a hydrogen-free approach. *Chem. Mater.* 31, 2555–2562. doi:10.1021/acs.chemmater.9b00147

Xavier, N. F., Bauerfeldt, G. F., and Sacchi, M. (2023). First-principles microkinetic modeling unravelling the performance of edge-decorated nanocarbons for hydrogen production from methane. *ACS Appl. Mater. Interfaces* 15, 6951–6962. doi:10.1021/acsami.2c20937

Xie, P., Pu, T., Nie, A., Hwang, S., Purdy, S. C., Yu, W., et al. (2018). Nanoceria-supported single-atom platinum catalysts for direct methane conversion. *ACS Catal.* 8, 4044–4048. doi:10.1021/acscatal.8b00004

Yan, W.-Q. Q., Zhu, Y.-A. A., Zhou, X.-G. G., and Yuan, W.-K. K. (2022). Rational design of heterogeneous catalysts by breaking and rebuilding scaling relations. *Chin. J. Chem. Eng.* 41, 22–28. doi:10.1016/j.cjche.2021.10.025

Yang, Z., and Gao, W. (2022). Applications of machine learning in alloy catalysts: Rational selection and future development of descriptors. *Adv. Sci.* 9, 2106043. doi:10.1002/advs.202106043

Zhang, J., Li, X., Chen, H., Qi, M., Zhang, G., Hu, H., et al. (2017). Hydrogen production by catalytic methane decomposition: Carbon materials as catalysts or catalyst supports. *Int. J. Hydrogen Energy* 42, 19755–19775. doi:10.1016/j.ijhydene.2017.06.197

Zhang, J., Sun, Y., Zhu, J., Gao, Z., Li, S., Mu, S., et al. (2018). Ultranarrow graphene nanoribbons toward oxygen reduction and evolution reactions. *Adv. Sci.* 5, 1801375. doi:10.1002/advs.201801375

frontiers | Frontiers in Chemistry

TYPE Original Research
PUBLISHED 14 July 2023
DOI 10.3389/fchem.2023.1235176

OPEN ACCESS

EDITED BY
Anton Tamtögl,
Graz University of Technology, Austria

REVIEWED BY
Emanuele Coccia,
University of Trieste, Italy
Federico Palazzetti,
University of Perugia, Italy

*CORRESPONDENCE
Maite Alducin,
maite.alducin@ehu.eus
Auguste Tetenoire,
auguste.tetenoire@dipc.org

RECEIVED 05 June 2023
ACCEPTED 03 July 2023
PUBLISHED 14 July 2023

CITATION
Tetenoire A, Juaristi JI and Alducin M (2023), Disentangling the role of electrons and phonons in the photoinduced CO desorption and CO oxidation on (O,CO)-Ru(0001). *Front. Chem.* 11:1235176. doi: 10.3389/fchem.2023.1235176

Disentangling the role of electrons and phonons in the photoinduced CO desorption and CO oxidation on (O,CO)-Ru(0001)

Auguste Tetenoire[1]*, J. Iñaki Juaristi[1,2,3] and Maite Alducin[1,3]*

[1]Donostia International Physics Center (DIPC), Donostia-San Sebastian, Spain, [2]Departamento de Polímeros y Materiales Avanzados: Física, Química y Tecnología, Facultad de Química (UPV/EHU), Donostia-San Sebastian, Spain, [3]Centro de Física de Materiales CFM/MPC (CSIC-UPV/EHU), Donostia-San Sebastian, Spain

The role played by electronic and phononic excitations in the femtosecond laser induced desorption and oxidation of CO coadsorbed with O on Ru(0001) is investigated using *ab initio* molecular dynamics with electronic friction. To this aim, simulations that account for both kind of excitations and that only consider electronic excitations are performed. Results for three different surface coverages are obtained. We unequivocally demonstrate that CO desorption is governed by phononic excitations. In the case of oxidation the low statistics does not allow to give a categorical answer. However, the analysis of the adsorbates kinetic energy gain and displacements strongly suggest that phononic excitations and surface distortion also play an important role in the oxidation process.

KEYWORDS

photoinduced reactions, CO oxidation, CO desorption, femtochemistry, *ab initio* molecular dynamics with electronic friction, Ru(0001), electron-mediated reactions, phonon-mediated reactions

1 Introduction

The use of intense femtosecond laser pulses in the near infrared, visible, and ultraviolet regime constitutes an efficient tool to promote adsorbate reactions at metal surfaces that are forbidden or less likely under thermal conditions (Cavanagh et al., 1993; Guo et al., 1999; Frischkorn and Wolf, 2006; Saalfrank, 2006). The laser excites the electrons of the metal and energy is subsequently transferred to the surface atoms by means of electron-phonon coupling. As a consequence, the adsorbates can gain energy from both the excited electronic and phononic systems. Experimentally, two-pulse correlation measurements have been used to disentangle which the timescale for the energy transfer to the adsorbates is (Budde et al., 1991; Busch et al., 1995; Bonn et al., 1999; Funk et al., 2000; Denzler et al., 2003; Frischkorn and Wolf, 2006; Szymanski et al., 2007; Hong et al., 2016). In this way, the reaction is ascribed to be a dominant electron-assisted process when its timescale is of few picoseconds or less and to be a dominant phonon-assisted process when its timescale is longer.

From the theoretical side, a proper understanding of this kind of experiments and of their outcome requires a proper characterization of the reaction dynamics. The excitation generated by the laser on the surface is accounted for using a two temperature model (2TM) in which the electronic and phononic excitations are described in terms of time-dependent electronic (T_e) and phononic (T_l) temperatures (Anisimov et al., 1974). Subsequently, the dynamics of the adsorbates in the highly excited environment are simulated (Springer et al.,

1994; Springer and Head-Gordon, 1996; Vazhappilly et al., 2009; Füchsel et al., 2010; 2011; Lončarić et al., 2016a; Lončarić et al., 2016b; Scholz et al., 2016). In this respect, the extension of the *ab initio* molecular dynamics with electronic friction method (Novko et al., 2015; Novko et al., 2016a; Novko et al., 2017) to incorporate the effect of time-dependent electronic and phononic temperatures in the adsorbate dynamics [hereafter denoted as (T_e, T_l)-AIMDEF] (Alducin et al., 2019; Scholz et al., 2019; Tetenoire et al., 2022; Tetenoire et al., 2023) constitutes a way of treating the multidimensional dynamics of the adsorbates and surface atoms at the density functional theory (DFT) level, incorporating the coupling of the adsorbates to both the excited electronic and phononic systems.

An important reaction that cannot be thermally activated under ultrahigh vacuum conditions (Kostov et al., 1992; Bonn et al., 1999) but can be propelled by femtosecond laser pulses (Bonn et al., 1999; Öberg et al., 2015; Öström et al., 2015) is CO oxidation when coadsorbed with atomic O on the Ru(0001) surface. Still, even in these conditions, CO desorption is around 30 times more probable than CO oxidation (Bonn et al., 1999; Öberg et al., 2015). In two previous works (Tetenoire et al., 2022; Tetenoire et al., 2023), we have applied the (T_e, T_l)-AIMDEF method to this system. Different surface coverages, for which the reaction paths under equilibrium conditions for CO desorption and oxidation had been previously studied (Tetenoire et al., 2021), were taken into account. Our results reproduced the experimental fact regarding the CO desorption to oxidation branching ratio being larger than one order of magnitude. Additionally, our dynamics simulations showed the reason for this behavior. We observed that CO desorption is a direct process only limited by the energy the CO molecules need to gain to overcome the desorption energy barrier. In contrasts, the oxidation dynamics is much more complex, the configurational space to oxidation is very restricted, and the fact that the O and CO adsorbates gain energy enough to overcome the energy barrier to oxidation does not guarantee their recombination. Our simulations also reproduced the changes in the O K-edge XAS experimental spectra attributed to the initial stage of the oxidation process (Öström et al., 2015), further confirming the robustness of the theoretical model.

An important question that was not studied in the previous works is the relative importance of electronic and phononic excitations in both CO desorption and CO oxidation reactions. In the present paper we aim to elucidate this question. We perform the so-called T_e-AIMDEF simulations (Juaristi et al., 2017), in which the Ru surface atoms are kept frozen in their equilibrium positions, so that the adsorbates are uniquely coupled to the excited electrons. In this way, we gain information about the CO desorption and oxidation probabilities, and about the dynamics of these processes, when only electronic excitations are considered. Comparison of these results with those obtained in the (T_e, T_l)-AIMDEF simulations, in which the effect of both electronic and phononic excitations is accounted for, allows us to answer the question about which channel dominates each reaction on each of the studied surface coverages.

The paper is organized as follows. The theoretical model and computational settings are described in the Theoretical Methods section. The results of both the T_e-AIMDEF and the (T_e, T_l)-AIMDEF simulations for the CO desorption and oxidation probabilities, kinetic energy gains, and adsorbate displacements are presented in the Results and Discussions section. Finally, the main conclusions of the paper are summarized in the Conclusions section.

2 Theoretical methods

2.1 Photoinduced desorption model

The photoinduced desorption and oxidation of CO from the (O,CO)-covered Ru(0001) surface was simulated in (Tetenoire et al., 2022; Tetenoire et al., 2023) with the *ab initio* classical molecular dynamics with electronic friction method (T_e, T_l)-AIMDEF that allows to include the effect of both the laser-induced hot electrons and concomitant electron-excited phonons (Alducin et al., 2019). As described in detail elsewhere (Alducin et al., 2019; Tetenoire et al., 2022), the electronic and ensuing phononic excitations created in the metal surface by near infrared laser pulses are described within a two-temperature model (2TM) (Anisimov et al., 1974) in terms of two coupled heat thermal baths. The time-dependent temperatures that are associated to the electron and phonon baths, $T_e(t)$ and $T_l(t)$, are obtained by solving the following differential equations:

$$C_e\frac{\partial T_e}{\partial t} = \frac{\partial}{\partial z}\kappa\frac{\partial T_e}{\partial z} - g\,(T_e - T_l) + S(z,t), \quad (1)$$

$$C_l\frac{\partial T_l}{\partial t} = g\,(T_e - T_l), \quad (2)$$

where C_e and C_l are the electron and phonon heat capacities, respectively, κ is the electron thermal conductivity, g is the electron-phonon coupling constant, and $S(z, t)$ is the absorbed laser power per unit volume that depends on the shape, wavelength, and fluence of the applied pulse. According to the above equations, the laser pulse is responsible of heating directly the electron system that subsequently transfers part of its energy into either the bulk electrons or the lattice phonons [first and second terms in the r.h.s. of Equation 1, respectively]. The diameter of the laser beam, on the one hand, and the time scale of few tens of picoseconds of interest, on the other hand, justify neglecting lateral heat diffusion by electrons in Equation 1 and heat diffusion by phonons in Equation 2 (Frischkorn and Wolf, 2006). All the simulations performed in the present work as well as those in (Tetenoire et al., 2022; Tetenoire et al., 2023) correspond to irradiating the surface with the experimental pulse of ref. (Bonn et al., 1999), i.e., a 800 nm Gaussian pulse of 110 fs duration. Figure 1 shows the results for $T_e(t)$ and $T_l(t)$ as obtained from 2TM for the experimental absorption fluences F = 200 and 300 J/m^2. As input parameters for the Ru(0001) surface in Equations 1, 2, we use those of refs. (Vazhappilly et al., 2009; Scholz et al., 2016; Juaristi et al., 2017; Tetenoire et al., 2022).

Next, the effect of the laser-excited electrons on each adsorbate is described through the following Langevin equation:

$$m_i\frac{d^2\mathbf{r}_i}{dt^2} = -\nabla_{\mathbf{r}_i}V(\mathbf{r}_1,\ldots,\mathbf{r}_N) - \eta_{e,i}(\mathbf{r}_i)\frac{d\mathbf{r}_i}{dt} + \mathbf{R}_{e,i}\left[T_e(t),\eta_{e,i}(\mathbf{r}_i)\right], \quad (3)$$

where m_i, $\mathbf{r}_i$, and $\eta_{e,i}$ are the mass, position vector, and electronic friction coefficient of the *ith* atom conforming the set of adsorbates. The adiabatic force [first term in the r.h.s. of Equation 3] depends on the position of all atoms in the system (i.e., adsorbates and surface

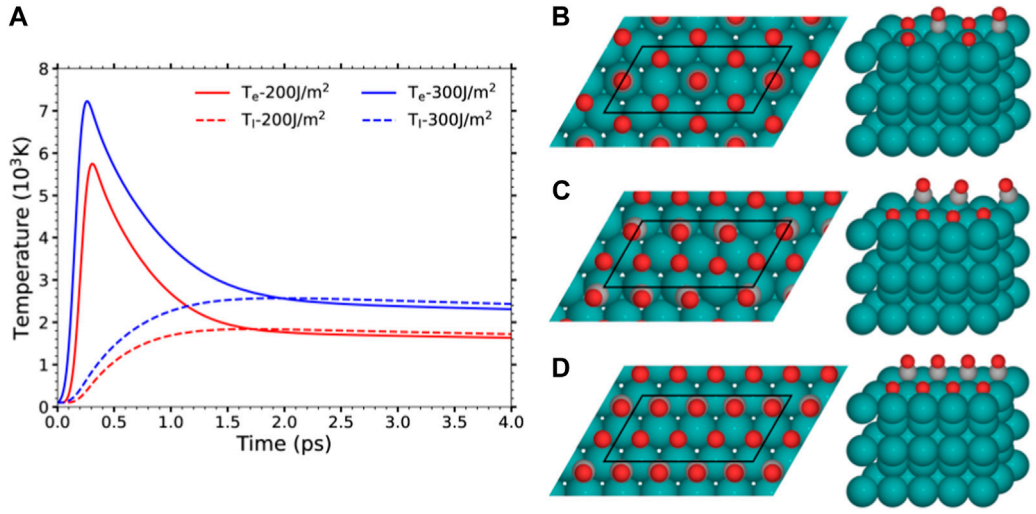

FIGURE 1
(A) 2TM-calculated electronic (solid) and lattice (dashed) temperatures induced by a 800 nm laser pulse with 110 fs FWHM and F = 200 and 300 J/m^2. **(B–D)** Top and perspective views of the energetically favored structures found in (Tetenoire et al., 2021) for Ru(0001) covered by: **(B)** 0.5 ML O+ 0.25 ML CO, **(C)** 0.5 ML O+ 0.375 ML CO, and **(D)** 0.5 ML O+ 0.5 ML CO. The black parallelograms depict the (4 × 2) surface unit cell used in the AIMDEF calculations for each coverage. Color code: O atoms in red, C in gray, and Ru in blue. For clarity, the periodic images of the O and CO adsorbates in the perspective view are not shown. Images prepared with ASE (Larsen et al., 2017).

atoms). The electronic friction force (second term) and the electronic stochastic force (third term), which are related by the fluctuation-dissipation theorem, describe the effect of the electronic excitations and deexcitations on the adsorbate dynamics. In particular, $\mathbf{R}_{e,i}$ is modeled by a Gaussian white noise with variance, $\mathrm{Var}[\mathbf{R}_{e,i}(T_e,\ \eta_{e,i})] = (2k_BT_e(t)\eta_{e,i}(\mathbf{r}_i))/\Delta t$, with k_B the Boltzmann constant and Δt the time-integration step. For each atom i, the electronic friction coefficient $\eta_{e,i}(\mathbf{r}_i)$ is calculated with the local density friction approximation (LDFA) (Juaristi et al., 2008; Alducin et al., 2017). Within this approximation, the friction coefficient is assumed to be equal to the friction coefficient that the same atom i would experience in case of moving within a homogeneous free electron gas (FEG) of density $n_0 = n_{\mathrm{sur}}(\mathbf{r}_i)$, with $n_{\mathrm{sur}}(\mathbf{r}_i)$ being the electron density of the bare metal surface at the position $\mathbf{r}_i$. As proposed by Novko *et al.* (Novko et al., 2015; 2016a), an efficient method to extract on-the-fly the bare surface electron density from the self-consistent DFT electron density of the whole system (adsorbates and surface), which is calculated at each integration step in AIMDEF, consists in applying the Hirshfeld partitioning scheme (Hirshfeld, 1977). Specifically, the latter is used to subtract the contribution of the adsorbates from the self-consistent electronic density in order to obtain the bare surface electron density.

In the (T_e, T_l)-AIMDEF simulations also the heating of the surface lattice due to the laser-induced electronic excitations is included. The latter is achieved by coupling the surface atoms to a Nosé-Hoover thermostat (Nosé, 1984; Hoover, 1985) that follows the temperature $T_l(t)$ obtained from 2TM. In contrast, in the T_e-AIMDEF simulations that we perform in this work all the surface atoms are kept fixed at their equilibrium positions and only the adsorbates are allowed to move as dictated by the T_e-dependent Langevin dynamics [Equation 3]. These dynamics-restricted simulations are an attempt to single out the direct effect of the laser-excited electrons on the adsorbates from the effect due to energy transfer between the adsorbates and the surface atoms, which are also vibrationally excited by the electrons.

2.2 General DFT computational settings

The new T_e-AIMDEF simulations presented here were performed with VASP (Kresse and Furthmüller, 1996a; Kresse and Furthmüller, 1996b) (version 5.4) and the AIMDEF module (Blanco-Rey et al., 2014; Saalfrank et al., 2014; Novko et al., 2015; Novko et al., 2016a; Novko et al., 2016b, Novko et al., 2017; Juaristi et al., 2017) using the same computational settings that we used in our previous (T_e, T_l)-AIMDEF simulations of the desorption and oxidation of CO on different covered Ru(0001) surfaces (Tetenoire et al., 2022; 2023). Figure 1 shows the supercells used to characterized the three coverages under study:

- The low coverage (0.5 ML O+0.25 ML CO), in which each atop CO is surrounded by six O atoms that adsorb on the nearest hcp and fcc sites forming a honeycomb arrangement.
- The intermediate coverage (0.5 ML O+0.375 ML CO), in which the O atoms adsorb at hcp sites forming a p(1 × 2) structure, while the CO molecules occupy the empty space left between the O arrays.
- The high coverage (0.5 ML O+0.5 ML CO), in which both the O and CO adsorb on hcp sites forming two inserted p(1 × 2) structures.

As seen in the figure, the three coverages are modeled with the same supercell that consists of a (4 × 2) surface unit cell and a vector length along the surface normal of 30.22 Å. Within this supercell, each covered Ru(0001) surface is described by five layers of Ru atoms

and the corresponding (O,CO) overlayer. The Ru topmost layer and the bottom of the nearest periodic Ru slab are separated by about 19 Å of vacuum. The employed (4 × 2) surface cell contains various adsorbates and, hence, it will provide a reasonable description of the interadsorbate interactions and their effect in the adsorbate dynamics, which become important at sufficiently large coverages (Denzler et al., 2003; Xin et al., 2015; Hong et al., 2016; Juaristi et al., 2017; Alducin et al., 2019; Serrano-Jiménez et al., 2021; Lidner et al., 2023). Let us remark that the low and intermediate coverages have been found in experiments (Kostov et al., 1992), while the high coverage is predicted to be stable by DFT (Tetenoire et al., 2021) but has not been experimentally observed.

In the T_e-AIMDEF simulations, the adiabatic forces are calculated with non spin-polarized DFT using the van der Waals exchange-correlation functional proposed by (Dion et al., 2004) and the same computational parameters that were used in our previous studies on the energetics (Tetenoire et al., 2021) and (T_e, T_l)-AIMDEF dynamics of the O + CO-Ru(0001) system (Tetenoire et al., 2022; Tetenoire et al., 2023). Specifically, the electronic ground state energy is determined at each integration step within a precision of 10^{-6} eV. Integration in the Brillouin zone is performed using a Γ-centered 3 × 6 × 1 Monkhorst-Pack grid of special k points (Monkhorst and Pack, 1976) and the Methfessel and Paxton scheme of first order with a broadening of 0.1 eV (Methfessel and Paxton, 1989). The Kohn-Sham orbitals are expanded in a plane-wave basis set with an energy cutoff of 400 eV. The projector augmented wave (PAW) method (Blöchl, 1994) that is implemented in VASP (Kresse and Joubert, 1999) is used to describe the electron-core interaction. Integration of the Langevin equation is performed with the Beeman method implemented in our AIMDEF module (Blanco-Rey et al., 2014). Each trajectory starts with the adsorbates at rest at their equilibrium position and is propagated up to 4 ps using a time step of 1 fs. For each coverage and absorbed fluence we run 100 trajectories.

2.3 Calculation of observables

Following (Tetenoire et al., 2022; Tetenoire et al., 2023), a CO molecule is counted as desorbed if its center of mass height reaches the distance Z_{cm} = 6.5 Å from the Ru(0001) topmost layer with positive momentum along the surface normal ($P_z > 0$). After analyzing all the trajectories, the CO oxidation (i.e., the O + CO recombinative desorption as CO_2) and CO desorption probabilities per CO molecule are calculated for each coverage as

$$P_{\mathrm{des}}(A) = \frac{N_{\mathrm{des}}(A)}{N_t N_{\mathrm{CO}}} \tag{4}$$

with $N_{des}(A)$ the number of the desorbing molecules under consideration (i.e., A stands for CO or CO_2), N_t the total number of trajectories, and N_{CO} the number of CO molecules in the simulation cell (2, 3, and 4, respectively, for low, intermediate, and high coverages).

The mean total kinetic energy $\langle E_{kin}\rangle(t)$ and mean center-of-mass kinetic energy $\langle E_{cm}\rangle(t)$ per adsorbate type are calculated at each instant t as

$$\langle E_{\mathrm{kin\ (cm)}}\rangle(t) = \sum_{i=1}^{N_t}\sum_{j=1}^{N_a}\frac{E^j_{\mathrm{kin\ (cm)}}(t)}{N_t N_a} \tag{5}$$

where N_a is the total number of the specific species under consideration (e.g., nondesorbing CO molecules that remain adsorbed on the surface at the end of the simulation, CO molecules that desorb, nondesorbing O adatoms. . .) and $E^j_{\mathrm{kin\ (cm)}}$ is the kinetic (center-of-mass) energy of adsorbate j at instant t.

3 Results and discussion

The CO desorption and CO oxidation probabilities obtained from the T_e-AIMDEF and (T_e, T_l)-AIMDEF simulations at the same absorbed fluence of 200 J/m^2 are compared for each coverage in Table 1. The CO desorption probabilities in the intermediate and high coverages are reduced by a factor 33.8 and 34.5, respectively, when only the direct effect of the excited electrons are included (T_e-AIMDEF). Assuming that a similar factor of ~34 stands for the low coverage, we consider that the predicted desorption probability of ~ 0.5% is compatible with the lack of CO desorption events we obtain within our limited statistics. As found in the (T_e, T_l)-AIMDEF simulations (Tetenoire et al., 2023), the P_{des}(CO) values correlate well with the CO desorption barriers calculated with DFT-vdW for each coverage (Tetenoire et al., 2021). That is, the number of CO desorption events increases as the barrier decreases. Let us remark that the drastic reduction we obtain in the T_e-AIMDEF desorption probabilities aligns with the two-pulse correlation measurements suggesting that the photoinduced desorption of CO on the O + CO-Ru(0001) surface is a phonon-dominated process (Bonn et al., 1999). Interestingly, this feature, the importance of the excited phonons in the photodesorption of CO, is not exclusive of the (O,CO)-covered surface, as it has been observed in diverse experiments in which Ru(0001) is covered with CO (Funk et al., 2000) and in molecular dynamics calculations motivated by those experiments (Scholz et al., 2016), which included the effect of $T_e(t)$ and $T_l(t)$ following the model by (Lončarić et al., 2016a).

In respect of the CO oxidation process, there are no events in the case of the T_e-AIMDEF simulations. Nevertheless, the statistics is insufficient to exclude that the laser-excited electrons are the dominant driving mechanism, as proposed in (Bonn et al., 1999). The analysis of the kinetic energy and displacements below will show however that there are distinct features in the (T_e, T_l)-AIMDEF adsorbate dynamics as compared to the T_e-AIMDEF adsorbate dynamics suggesting that not only electrons but also the highly excited phonons are contributing to the oxidation process, similarly to what was obtained for the laser-induced desorption of CO from Pd(111) (Alducin et al., 2019).

In order to confirm the above idea and gain further insights into the role of the excited electrons and phonons we also calculated for illustrative purposes an additional set of 100 T_e-AIMDEF trajectories assuming a extreme absorption fluence F = 300 J/m^2 for one of the covered surfaces, namely, the high coverage. As shown in Figure 1A, the maximum of the electronic temperature for the new fluence is about 1600 K higher than for F = 200 J/m^2. After reaching the maximum, a difference of about 800 K is still

TABLE 1 T_e-AIMDEF CO desorption probability $P_{des}(CO)$ and CO oxidation probability $P_{des}(CO_2)$ calculated for the low, intermediate, and high (O,CO)-Ru(0001) coverages at an absorbed fluence $F = 200$ J/m^2. For the high coverage also results at $F = 300$ J/m^2 are shown (last row). For comparison, the probabilities obtained from (T_e, T_l)-AIMDEF simulations with $F = 200$ J/m^2 in ref (Tetenoire et al., 2023) are reproduced within parenthesis. Activation energies (in eV) for CO desorption E_{TS}^{CO} and CO oxidation $E_{TS}^{CO_2}$ are from ref (Tetenoire et al., 2021).

Coverage	Fluence (J/m^2)	$P_{des}(CO)$ (%)	$P_{des}(CO_2)$ (%)	E_{TS}^{CO} (eV)	$E_{TS}^{CO_2}$ (eV)
0.5 ML O+0.250 ML CO	200	0.00 (18.25)	0.00 (0.50)	1.57	1.19
0.5 ML O+0.375 ML CO	200	1.33 (45.06)	0.00 (0.67)	0.58,0.73	0.80
0.5 ML O+0.5 ML CO	200	1.00 (34.53)	0.00 (1.26)	0.88	2.01
0.5 ML O+0.5 ML CO	300	15.25 (–)	0.00 (–)	0.88	2.01

maintained during the rest of the integration time used in our calculations. The purpose of these new simulations is to increase the energy provided to the adsorbates but excluding effects due to the lattice distortions inherent to phonon excitations. The results in Table 1 show that $P_{des}(CO)$ increases from 1% to 15.25% because of the fluence. The latter value is still about a factor 2 smaller than in the (T_e, T_l)-AIMDEF simulations for $F = 200$ J/m^2. Lastly, neither at this high fluence there are oxidation events, although the analysis of the adsorbate displacements below will show that in a few cases the adsorbates can eventually abandon their adsorption well.

3.1 Kinetic energy gain

The time evolution of the mean kinetic energy of the adsorbates along the T_e-AIMDEF (thick solid lines) and (T_e, T_l)-AIMDEF dynamics (dotted lines) is compared in Figure 2 for each adsorbate type and each coverage. In both simulations the absorbed laser fluence is $F = 200$ J/m^2. For simplicity, only the results of the nondesorbing species, i.e., the adsorbates that remain on the surface at the end of our simulations, will be discussed. A detailed analysis of the kinetic energy gained by the desorbed CO in the (T_e, T_l)-AIMDEF simulations can be found elsewhere (Tetenoire et al., 2023). A common observation in Figure 2 is that irrespective of the coverage the adsorbates gain less kinetic energy in the T_e-AIMDEF simulations than in (T_e, T_l)-AIMDEF. There exist some interesting features worth mentioning. As discussed in (Tetenoire et al., 2023) in the case of (T_e, T_l)-AIMDEF simulations a quasithermalized state was obtained at the end of the simulations, and even more rapidly for the intermediate and high coverages. This is shown by the fact that the average total kinetic energy of the CO molecules is twice the average kinetic energy of their center of mass, and that this coincides, roughly, with the average kinetic energy of the O atoms. This is what is expected when there exists equipartition of the energy among the different degrees of freedom. This is clearly not the case in the T_e-AIMDEF simulations. For instance, we observe that for all coverages the average kinetic energy of the atomic O is larger than the average kinetic energy of the center of mass of the CO molecules. This can be rationalized by the fact that the O atoms are more strongly bound than the CO molecules and therefore their coupling to the electronic system is stronger. Note, finally, that even though this statement is generally true for all the coverages, in the high coverage case the difference between these two energies is much smaller and that tends to disappear at the end of the simulation time. This may be due to an increased importance of interadsorbate energy exchange that favors the thermalization of the system when the concentration of adsorbates at the surface is larger.

Nevertheless, note that the energy gain when only electronic excitations are considered is roughly one-half of the energy gain when both electronic and phononic excitations are taken into account. It is difficult to rationalize reduction factors larger than 30 in the CO desorption probabilities such as those presented in Table 1 in terms of this reduction in the energy gain. This suggests that not only the increased energy gain but also other effects are playing a role in the increased CO desorption and oxidation probabilities when phononic excitations are considered. In order to strengthen this point further, in Figure 3 we show the results for the kinetic energy gain of the adsorbates in T_e-AIMDEF simulations in the high coverage case for a larger fluence, namely, $F = 300$ J/m^2. In this case, albeit a slightly different time dependence, the energy gain is very similar to that obtained with $F = 200$ J/m^2 in the (T_e, T_l)-AIMDEF simulations. Nevertheless, even with similar energy gains desorption and oxidation probabilities are, as shown in Table 1, much lower when only electronic excitations are accounted for. This constitutes a definitive proof of the fact that the role played by phononic excitations in the desorption and oxidation probabilities is not limited to being a energy source channel. This important point is further analyzed in the next subsection.

3.2 Adsorbate displacements

Evidence of the important role of the excited phonons in the photoinduced reactions on (O+CO)-Ru(0001) is provided by comparing the in-plane displacement of the adsorbed species between both types of calculations, T_e-AIMDEF and (T_e, T_l)-AIMDEF. As in the previous section, only the diffusion of the nondesorbing species will be discussed.

The displacement data is presented in terms of colored density plots, which correspond to two-dimensional histograms of the adsorbates (x, y) positions over the surface (Figures 4–6). For each kind of adsorbate and simulation type, each density plot is constructed using the in-plane positions along the whole trajectory (4 ps, *i.e.*, 4,000 steps) of all the adsorbates of that kind and of all the simulated trajectories. Thus, the density color code gives qualitatively an idea of the amount of time the adsorbates have spent in a given position (higher densities will correspond to longer times). Let us also remark that in each plot the atoms are allowed to go out of the unit cell (enclosed by a black solid line in the figures).

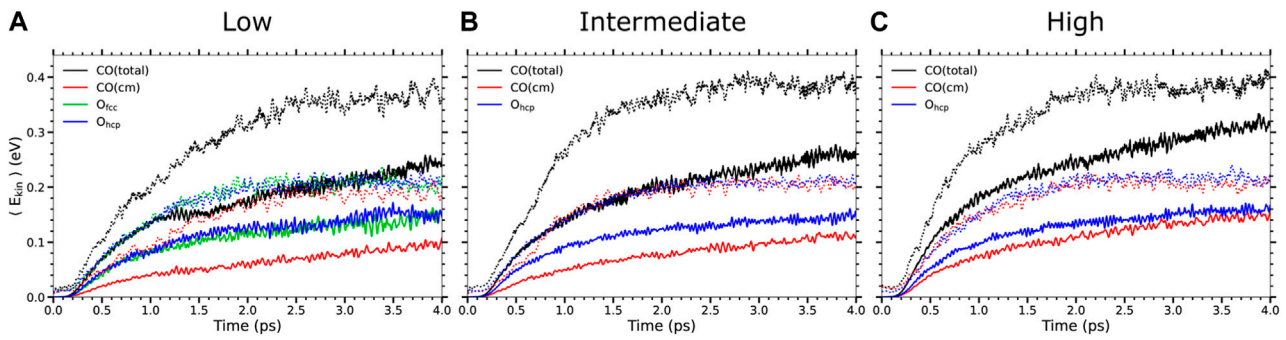

FIGURE 2
Time evolution of the adsorbate mean kinetic energy in the low **(A)**, intermediate **(B)**, and high **(C)** coverages as obtained in T_e-AIMDEF (solid lines) and (T_e, T_l)-AIMDEF (dotted lines) for an absorbed laser fluence F = 200 J/m^2. Shown for each coverage are: the mean total kinetic energy $\langle E_{kin} \rangle$ (black) and mean center-of-mass kinetic energy $\langle E_{cm} \rangle$ (red) of nondesorbing CO and the mean total kinetic energy of nondesorbing O_{hcp} (blue) and O_{fcc} (green).

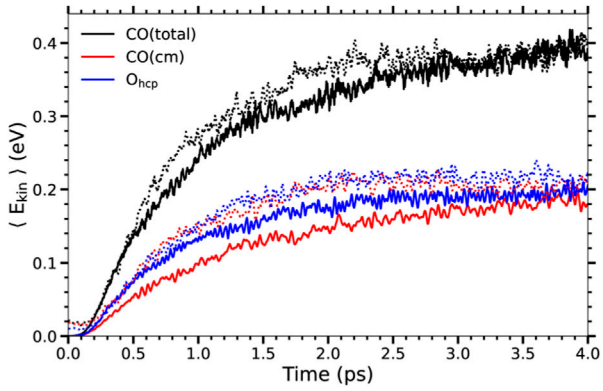

FIGURE 3
Same as Figure 2 for the high coverage. The results from T_e-AIMDEF at F = 300 J/m^2 (solid lines) are compared to those from (T_e, T_l)-AIMDEF at F = 200 J/m^2 (dotted lines).

The reason is that we are using a extended coordinate representation in order to show the continuous path followed by the adsorbates.

The adsorbate displacements in the low coverage case are plotted in Figure 4. In the T_e-AIMDEF simulations (left panels of Figure 4), the O adatoms stay on (or very close to) their respective adsorption sites. Something similar is observed for the CO molecules. They remain in top/near-top sites, showing no preference to move neither towards fcc sites nor towards hcp sites. The CO molecules explore an ellipse centered on the top position with a long axis of ~1.3 Å and a short axis of ~1 Å. These short displacements are clearly insufficient for CO oxidation to occur because the CO and O adsorbates cannot get close enough to recombine.

The in-plane mobility of all the adsorbates increases much when the Ru lattice excitation is incorporated with the (T_e, T_l)-AIMDEF simulations (right panels of Figure 4). The O adatoms can now abandon their initial adsorption site and cross the surrounding bridge sites. In particular, O atoms initially located at the fcc sites (O_{fcc}) show a tendency to move to the nearest hcp sites, whereas the ones initially located at the hcp sites (O_{hcp}) show a tendency to move to the closest fcc sites. We also observe that O_{hcp} shows a slightly smaller mobility than O_{fcc}. This is consistent with the larger adsorption energy of the former (5.62 eV) as compared to the latter (4.95 eV) (Tetenoire et al., 2023). Although less probable, note that there also exist events in which the O atoms move beyond the nearest neighbor adsorption sites. The mobility of the CO molecules is also much increased in the (T_e, T_l)-AIMDEF simulations. Now they explore a circle of radius ~2.3 Å centered at their equilibrium position. In some cases, the excited CO may even move beyond their first neighboring site.

Figure 5 shows that the adsorbate mobility is drastically reduced also in the intermediate coverage when the effect of the hot Ru lattice is not included. In the T_e-AIMDEF simulations (left column of Figure 5), the CO molecules basically move within an ellipse centered at their corresponding adsorption site as in the low coverage case, although the explored area is larger (long and short axis lengths of ~2.5 Å and ~1.3 Å, respectively). We also observe a few cases in which the CO diffuses either along the x direction or to a nearest top site. The O adatoms mostly remain in their hcp adsorption sites, although there exist a few events in which O diffuses towards the nearest fcc site that is located farther from the other adatoms. Furthermore, these diffusing atoms are the ones that have not a CO molecule adsorbed on the near-top site that is located above them in the density plot. We checked that the displacement of the second left O occurs once the nearest CO above it desorbs.

The mobility of both kind of adsorbates increases considerably in the (T_e, T_l)-AIMDEF simulations (right column of Figure 5). In fact, the difference respect to the T_e-AIMDEF simulations is even more pronounced than in the low coverage because in the intermediate coverage basically every spot in the simulation cell is at some instant occupied by either O or CO. Still, we observe that in the case of CO molecules, the O row acts as a barrier that prohibits the CO molecules to access the lower part of the simulation cell, except for very few rare events. In contrast, the O adatoms can move all over the cell albeit it is less probable to find them at top sites than on hcp or fcc sites. These features provide, in a qualitative manner, indirect information on the properties of the potential energy surface and were already discussed in detail elsewhere (Tetenoire et al., 2023).

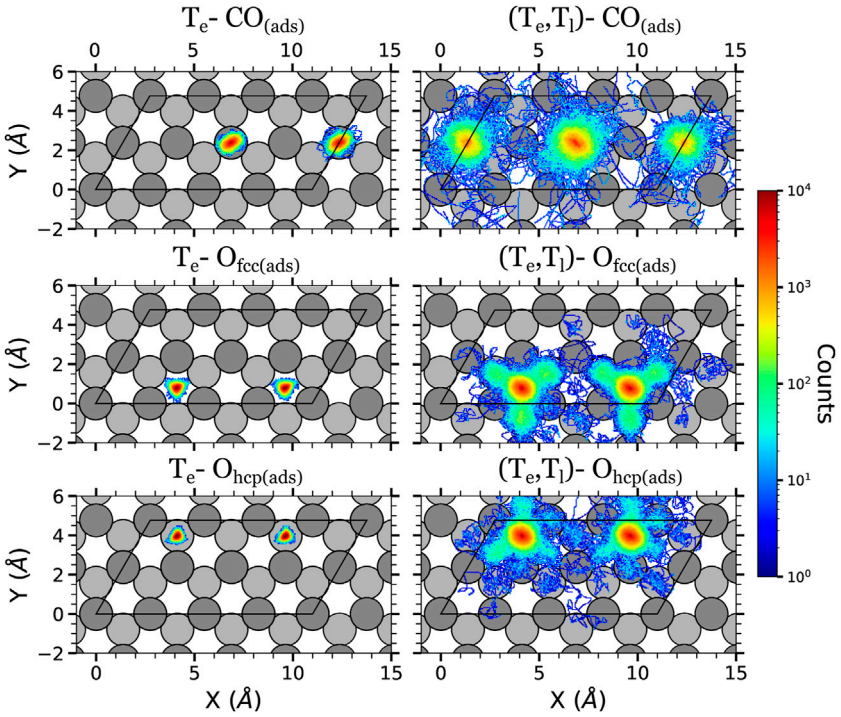

FIGURE 4
Density plots of the (*x*, *y*) positions over the surface of the adsorbates at the low surface coverage in the AIMDEF simulations. Only the positions of the adsorbates that remain adsorbed on the surface at the end of the simulation are shown. Left (right) column shows the results of the T_e-AIMDEF [(T_e, T_l)-AIMDEF] simulations. Top panels correspond to the center of mass of CO molecules, middle panels to the position of O atoms initially on fcc sites, and bottom panels to the position of O atoms initially on hcp sites. The black line encloses the simulation cell. For clarity, the position of the adsorbates is shown in an extended coordinate representation.

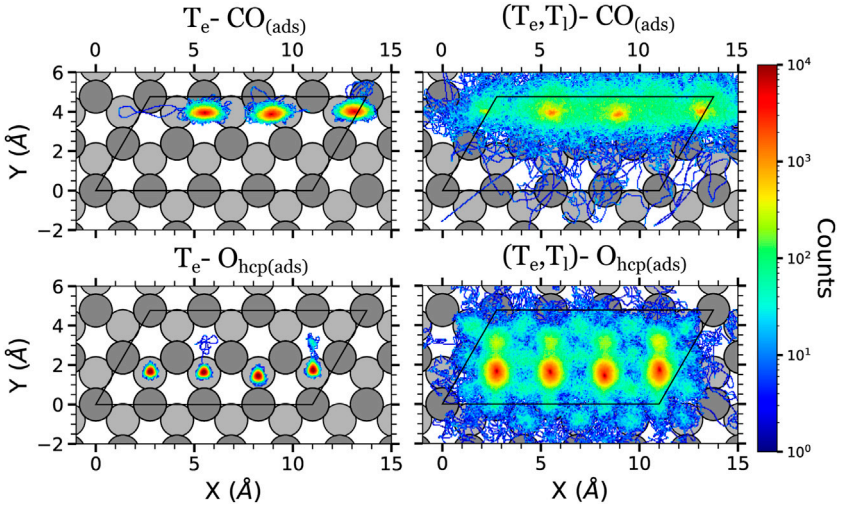

FIGURE 5
Density plots of the (*x*, *y*) positions over the surface of the adsorbates at the intermediate surface coverage in the AIMDEF simulations. Only the positions of the adsorbates that remain adsorbed on the surface at the end of the simulation are shown. Left (right) column shows the results of the T_e-AIMDEF [(T_e, T_l)-AIMDEF] simulations. Top panels correspond to the center of mass of CO molecules and bottom panels to the position of O atoms. The black line encloses the simulation cell. For clarity, the position of the adsorbates is shown in an extended coordinate representation.

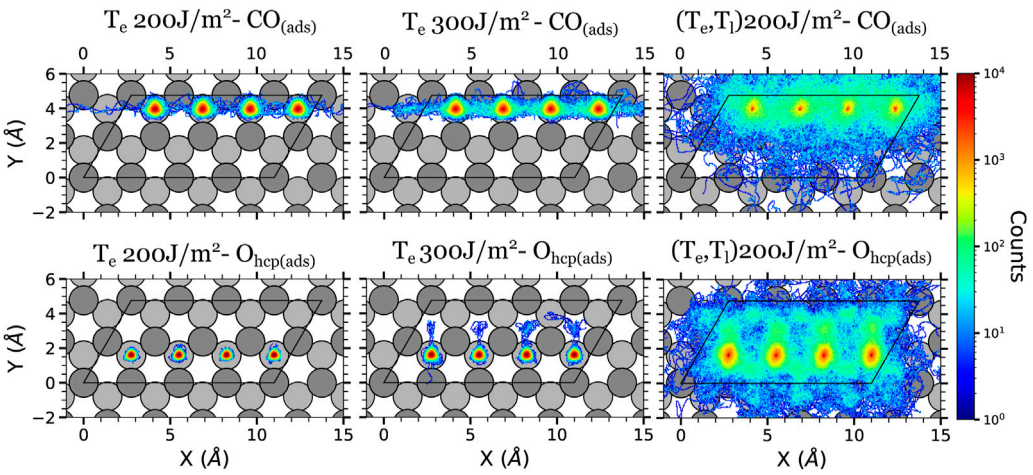

FIGURE 6
Density plots of the (x, y) positions over the surface of the adsorbates at the high surface coverage in the AIMDEF simulations. Only the positions of the adsorbates that remain adsorbed on the surface at the end of the simulation are shown. Left, center, and right columns show the results of the T_e-AIMDEF with F = 200 J/m^2, T_e-AIMDEF with F = 300 J/m^2, and (T_e, T_l)-AIMDEF with F = 200 J/m^2 simulations, respectively. Top panels correspond to the center of mass of CO molecules and bottom panels to the position of O atoms. The black line encloses the simulation cell. For clarity, the position of the adsorbates is shown in an extended coordinate representation.

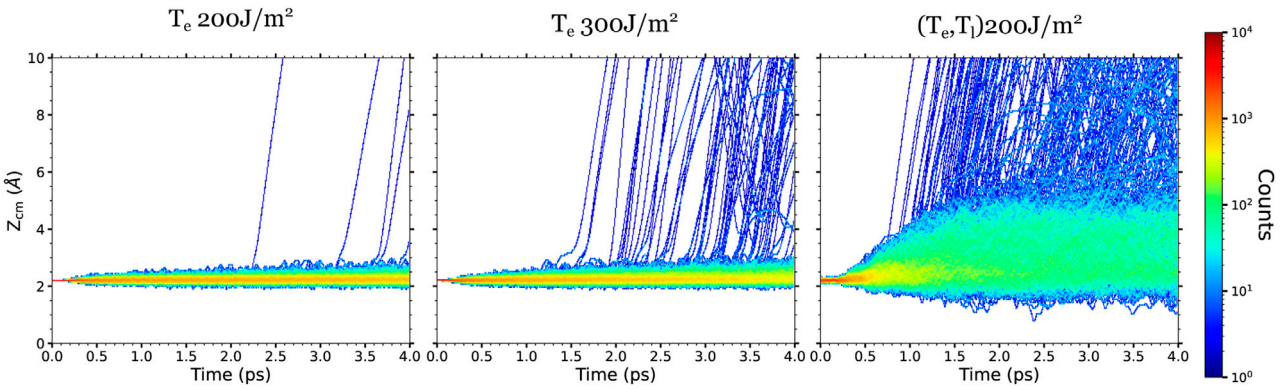

FIGURE 7
Density plots of the CO center-of-mass height Z_{CM} respect to the surface topmost layer obtained for the high surface coverage in the AIMDEF simulations. Left, center, and right columns show the results of the T_e-AIMDEF with F = 200 J/m^2, T_e-AIMDEF with F = 300 J/m^2, and (T_e, T_l)-AIMDEF with F = 200 J/m^2 simulations, respectively.

The in-plane displacement of the adsorbates in the high coverage are shown in Figure 6. Recall that in this case, the T_e-AIMDEF simulations were performed for two different fluences, namely, F = 200 and 300 J/m^2. In T_e-AIMDEF simulations with a laser fluence of 200 J/m^2 (left column of Figure 6), the in-plane motion of the CO molecules is mostly restricted to a circle of radius ~1 Å. Still, we observe some events that involve lateral displacement of the CO molecules from one hcp site to another along the row in which they are located. However, since O atoms hardly move away from their corresponding adsorption sites, no CO oxidation event is expected to take place under these conditions.

As in the intermediate coverage, all adsorbates become extremely mobile when we also include the effect of the excited phonons [right column of Figure 6, (T_e, T_l)-AIMDEF simulations]. In fact the pattern of the density plots for both coverages, which share the same $p(1 \times 2)$ arrangement of the O adatoms, is very similar. Specifically, the CO molecules move predominantly along the row in which they are adsorbed, while the O adatoms end moving all over the surface.

The comparison of the O and CO displacements in the T_e-AIMDEF simulations with F = 300 J/m^2 (middle column of Figure 6) and in the (T_e, T_l)-AIMDEF simulations with F = 200 J/m^2 (right column of Figure 6) is probably the most clear evidence of the importance that the hot phonons created indirectly by the laser pulse has on the reaction dynamics. As shown in the previous section, the energy gained by both O and CO is very similar in the two simulations (see Figure 3). In spite of it, we show here that the mobility of the adsorbates is still very limited in the high fluence T_e-AIMDEF simulations as compared to the displacements obtained in the (T_e, T_l)-AIMDEF simulations at lower laser fluence. For example, the in-plane motion of the CO molecules is mostly restricted to a circle of

radius ~1.2 Å in the former, while it basically occupies the whole surface in the latter. Nonetheless, it is also worth noticing that compared to T_e-AIMDEF with $F = 200$ J/m^2, the lateral displacement along the y-axis in between the two nearest rows of Ru atoms is clearly much more probable in the high fluence simulations. In the case of the O adatoms, even if they remain mostly at their adsorption site, we observe some events in which they go through bridge sites, toward the nearest fcc sites. Clearly, the adsorbates have an increased mobility when the laser fluence is increased that could allow them to eventually recombine, even if there is no motion of the surface, but with a much smaller probability.

All in all, the present analysis shows that, for all coverages, the inclusion of lattice motion and phononic excitations increase the mobility of the adsorbates and allow them to explore larger regions of the configurational space. Therefore, though the low statistics does not allow us to categorically establish whether electronic or phononic excitations govern the CO oxidation process, these results strongly suggest that the role of phononic excitations cannot be neglected.

Regarding the CO desorption process, it is also interesting to compare the displacements along the surface normal with and without including the effect of the phonon excitations. Similar to the in-plane displacements, the CO mobility along the z-axis is higher in (T_e, T_l)-AIMDEF than in T_e-AIMDEF for each coverage. As an example, we show in Figure 7 the time evolution of the CO center of mass height Z_{CM} for the high coverage. Comparing the results calculated for the same absorbed fluence ($F = 200$ J/m^2), we observe that the Z_{CM} displacements of the nondesorbing CO increase from about 0.5–1 Å in T_e-AIMDEF to 2–3 Å in (T_e, T_l)-AIMDEF. Increasing the fluence in the T_e-AIMDEF simulations also implies an increase in the Z_{CM} displacements and, importantly, in the number of desorption events, but still significantly smaller than in the (T_e, T_l)-AIMDEF simulations at 200 J/m^2.

4 Conclusion

The photoinduced desorption and oxidation of CO coadsorbed with O on Ru(0001) has been simulated with *ab initio* molecular dynamics with electronic friction that include the effect of the laser-induced hot electrons but neglects that of the phonon excitations (T_e-AIMDEF). Comparison of these new results with those we obtained previously with simulations that incorporated in the adsorbate dynamics both the effect of the hot electrons and hot phonons [(T_e, T_l)-AIMDEF)] allows us to discern the role of electrons and phonons in the oxidation and desorption of CO from the covered surface. The probability of both reactions are drastically reduced when only the coupling to electrons is included. As suggested by two pulse correlation experiments in this system, CO desorption is dominated by the transient high temperature that is indirectly created by the laser pulse. Unfortunately, the statistics for CO oxidation is insufficient to determine the relative importance of the electronic and phononic mechanisms. Nonetheless, the comparative analysis of various dynamical properties such as the adsorbate kinetic energy and adsorbate displacements indicates that energy exchange with the hot lattice and the associated strong surface distortions are important ingredients to understand the CO oxidation reaction. This conclusion is supported by T_e-AIMDEF simulations performed at a high laser fluence. The kinetic energy gain is similar to that obtained in (T_e, T_l)-AIMDEF at a lower fluence but the adsorbate displacements are still insufficient to facilitate recombination.

Data availability statement

The raw data supporting the conclusion of this article will be made available by the authors, without undue reservation.

Author contributions

All authors listed have made a substantial, direct, and intellectual contribution to the work and approved it for publication.

Funding

The authors acknowledge financial support by the Gobierno Vasco-UPV/EHU Project No. IT1569-22 and by the Spanish MCIN/AEI/10.13039/501100011033 (Grant No. PID2019-107396GB-I00).

Acknowledgments

Computational resources were provided by the DIPC computing center. This research was conducted in the scope of the Transnational Common Laboratory (LTC) "QuantumChemPhys–Theoretical Chemistry and Physics at the Quantum Scale".

Conflict of interest

The authors declare that the research was conducted in the absence of any commercial or financial relationships that could be construed as a potential conflict of interest.

Publisher's note

All claims expressed in this article are solely those of the authors and do not necessarily represent those of their affiliated organizations, or those of the publisher, the editors and the reviewers. Any product that may be evaluated in this article, or claim that may be made by its manufacturer, is not guaranteed or endorsed by the publisher.

References

Alducin, M., Camillone, N., Hong, S.-Y., and Juaristi, J. I. (2019). Electrons and phonons cooperate in the laser-induced desorption of CO from Pd(111). *Phys. Rev. Lett.* 123, 246802. doi:10.1103/PhysRevLett.123.246802

Alducin, M., Díez Muiño, R., and Juaristi, J. I. (2017). Non-adiabatic effects in elementary reaction processes at metal surfaces. *Prog. Surf. Sci.* 92, 317–340. doi:10.1016/j.progsurf.2017.09.002

Anisimov, S. I., Kapeliovich, B. L., and Perel'man, T. L. (1974). Electron emission from metal surfaces exposed to ultrashort laser pulses. *Sov. Phys.-JETP* 39, 375.

Blanco-Rey, M., Juaristi, J. I., Díez Muiño, R., Busnengo, H. F., Kroes, G. J., and Alducin, M. (2014). Electronic friction dominates Hydrogen hot-atom relaxation on Pd(100). *Phys. Rev. Lett.* 112, 103203. doi:10.1103/PhysRevLett.112.103203

Blöchl, P. E. (1994). Projector augmented-wave method. *Phys. Rev. B* 50, 17953–17979. doi:10.1103/PhysRevB.50.17953

Bonn, M., Funk, S., Hess, C., Denzler, D. N., Stampfl, C., Scheffler, M., et al. (1999). Phonon-versus electron-mediated desorption and oxidation of CO on Ru(0001). *Science* 285, 1042–1045. doi:10.1126/science.285.5430.1042

Budde, F., Heinz, T. F., Loy, M. M. T., Misewich, J. A., de Rougemont, F., and Zacharias, H. (1991). Femtosecond time-resolved measurement of desorption. *Phys. Rev. Lett.* 66, 3024–3027. doi:10.1103/PhysRevLett.66.3024

Busch, D. G., Gao, S., Pelak, R. A., Booth, M. F., and Ho, W. (1995). Femtosecond desorption dynamics probed by time-resolved velocity measurements. *Phys. Rev. Lett.* 75, 673–676. doi:10.1103/PhysRevLett.75.673

Cavanagh, R. R., King, D. S., Stephenson, J. C., and Heinz, T. F. (1993). Dynamics of nonthermal reactions: Femtosecond surface chemistry. *J. Phys. Chem.* 97, 786–798. doi:10.1021/j100106a002

Denzler, D. N., Frischkorn, C., Hess, C., Wolf, M., and Ertl, G. (2003). Electronic excitation and dynamic promotion of a surface reaction. *Phys. Rev. Lett.* 91, 226102. doi:10.1103/PhysRevLett.91.226102

Dion, M., Rydberg, H., Schröder, E., Langreth, D. C., and Lundqvist, B. I. (2004). Van der Waals density functional for general geometries. *Phys. Rev. Lett.* 92, 246401. doi:10.1103/PhysRevLett.92.246401

Frischkorn, C., and Wolf, M. (2006). Femtochemistry at metal surfaces: Nonadiabatic reaction dynamics. *Chem. Rev.* 106, 4207–4233. doi:10.1021/cr050161r

Füchsel, G., Klamroth, T., Monturet, S., and Saalfrank, P. (2011). Dissipative dynamics within the electronic friction approach: The femtosecond laser desorption of H_2/D_2 from Ru(0001). *Phys. Chem. Chem. Phys.* 13, 8659–8670. doi:10.1039/C0CP02086A

Füchsel, G., Klamroth, T., Tremblay, J. C., and Saalfrank, P. (2010). Stochastic approach to laser-induced ultrafast dynamics: The desorption of H_2/D_2 from Ru(0001). *Phys. Chem. Chem. Phys.* 12, 14082–14094. doi:10.1039/C0CP00895H

Funk, S., Bonn, M., Denzler, D. N., Hess, C., Wolf, M., and Ertl, G. (2000). Desorption of co from ru(001) induced by near-infrared femtosecond laser pulses. *J. Chem. Phys.* 112, 9888–9897. doi:10.1063/1.481626

Guo, H., Saalfrank, P., and Seideman, T. (1999). Theory of photoinduced surface reactions of admolecules. *Prog. Surf. Sci.* 62, 239–303. doi:10.1016/S0079-6816(99)00013-1

Hirshfeld, F. L. (1977). Bonded-atom fragments for describing molecular charge densities. *Theor. Chim. Acta* 44, 129–138. doi:10.1007/BF00549096

Hong, S.-Y., Xu, P., Camillone, N. R., White, M. G., and Camillone, N., III (2016). Adlayer structure dependent ultrafast desorption dynamics in carbon monoxide adsorbed on Pd(111). *J. Chem. Phys.* 145, 014704. doi:10.1063/1.4954408

Hoover, W. G. (1985). Canonical dynamics: Equilibrium phase-space distributions. *Phys. Rev. A* 31, 1695–1697. doi:10.1103/PhysRevA.31.1695

Juaristi, J. I., Alducin, M., Díez Muiño, R., Busnengo, H. F., and Salin, A. (2008). Role of electron-hole pair excitations in the dissociative adsorption of diatomic molecules on metal surfaces. *Phys. Rev. Lett.* 100, 116102. doi:10.1103/PhysRevLett.100.116102

Juaristi, J. I., Alducin, M., and Saalfrank, P. (2017). Femtosecond laser induced desorption of H_2, D_2, and HD from Ru(0001): Dynamical promotion and suppression studied with *ab initio* molecular dynamics with electronic friction. *Phys. Rev. B* 95, 125439. doi:10.1103/PhysRevB.95.125439

Kostov, K. L., Rauscher, H., and Menzel, D. (1992). Adsorption of CO on oxygen-covered Ru(001). *Surf. Sci.* 278, 62–86. doi:10.1016/0039-6028(92)90584-S

Kresse, G., and Furthmüller, J. (1996a). Efficiency of *ab-initio* total energy calculations for metals and semiconductors using a plane-wave basis set. *Comput. Mat. Sci.* 6, 15–50. doi:10.1016/0927-0256(96)00008-0

Kresse, G., and Furthmüller, J. (1996b). Efficient iterative schemes for *ab initio* total-energy calculations using a plane-wave basis set. *Phys. Rev. B* 54, 11169–11186. doi:10.1103/PhysRevB.54.11169

Kresse, G., and Joubert, D. (1999). From ultrasoft pseudopotentials to the projector augmented-wave method. *Phys. Rev. B* 59, 1758–1775. doi:10.1103/PhysRevB.59.1758

Larsen, A. H., Mortensen, J. J., Blomqvist, J., Castelli, I. E., Christensen, R., Dułak, M., et al. (2017). The atomic simulation environment—A python library for working with atoms. *J. Phys-Condes. Mat.* 29, 273002. doi:10.1088/1361-648x/aa680e

Lidner, S., Lončarić, I., Alducin, M., Saalfrank, P., and Juaristi, J. I. (2023). Femtosecond laser-induced desorption of hydrogen molecules from Ru(0001): A systematic study based on machine-learned potentials. *ChemRxiv*. doi:10.26434/chemrxiv-2023-34g9n

Lončarić, I., Alducin, M., Saalfrank, P., and Juaristi, J. I. (2016b). Femtosecond laser pulse induced desorption: A molecular dynamics simulation. *Nucl. Instrum. Methods B* 382, 114–118. doi:10.1016/j.nimb.2016.02.051

Lončarić, I., Alducin, M., Saalfrank, P., and Juaristi, J. I. (2016a). Femtosecond-laser-driven molecular dynamics on surfaces: Photodesorption of molecular Oxygen from Ag(110). *Phys. Rev. B* 93, 014301. doi:10.1103/PhysRevB.93.014301

Methfessel, M., and Paxton, A. T. (1989). High-precision sampling for Brillouin-zone integration in metals. *Phys. Rev. B* 40, 3616–3621. doi:10.1103/PhysRevB.40.3616

Monkhorst, H. J., and Pack, J. D. (1976). Special points for Brillouin-zone integrations. *Phys. Rev. B* 13, 5188–5192. doi:10.1103/PhysRevB.13.5188

Nosé, S. (1984). A unified formulation of the constant temperature molecular dynamics methods. *J. Chem. Phys.* 81, 511–519. doi:10.1063/1.447334

Novko, D., Blanco-Rey, M., Alducin, M., and Juaristi, J. I. (2016a). Surface electron density models for accurate *ab initio* molecular dynamics with electronic friction. *Phys. Rev. B* 93, 245435. doi:10.1103/PhysRevB.93.245435

Novko, D., Blanco-Rey, M., Juaristi, J. I., and Alducin, M. (2015). *Ab initio* molecular dynamics with simultaneous electron and phonon excitations: Application to the relaxation of hot atoms and molecules on metal surfaces. *Phys. Rev. B* 92, 201411. doi:10.1103/PhysRevB.92.201411

Novko, D., Blanco-Rey, M., Juaristi, J. I., and Alducin, M. (2016b). Energy loss in gas-surface dynamics: Electron-hole pair and phonon excitation upon adsorbate relaxation. *Nucl. Instrum. Methods B* 382, 26–31. doi:10.1016/j.nimb.2016.02.031

Novko, D., Lončarić, I., Blanco-Rey, M., Juaristi, J. I., and Alducin, M. (2017). Energy loss and surface temperature effects in *ab initio* molecular dynamics simulations: N adsorption on Ag(111) as a case study. *Phys. Rev. B* 96, 085437. doi:10.1103/PhysRevB.96.085437

Öberg, H., Gladh, J., Marks, K., Ogasawara, H., Nilsson, A., Pettersson, L. G. M., et al. (2015). Indication of non-thermal contribution to visible femtosecond laser-induced CO oxidation on Ru(0001). *J. Chem. Phys.* 143, 074701. doi:10.1063/1.4928646

Öström, H., Öberg, H., Xin, H., LaRue, J. b., Beye, M. b., Dell'Angela, M., et al. (2015). Probing the transition state region in catalytic CO oxidation on Ru. *Science* 347, 978–982. doi:10.1126/science.1261747

Saalfrank, P., Juaristi, J. I., Alducin, M., Blanco-Rey, M., and Díez Muiño, R. (2014). Vibrational lifetimes of Hydrogen on Lead films: An *ab initio* molecular dynamics with electronic friction (AIMDEF) study. *J. Chem. Phys.* 141, 234702. doi:10.1063/1.4903309

Saalfrank, P. (2006). Quantum dynamical approach to ultrafast molecular desorption from surfaces. *Chem. Rev.* 106, 4116–4159. doi:10.1021/cr0501691

Scholz, R., Floß, G., Saalfrank, P., Füchsel, G., Lončarić, I., and Juaristi, J. I. (2016). Femtosecond-laser induced dynamics of CO on Ru(0001): Deep insights from a hot-electron friction model including surface motion. *Phys. Rev. B* 94, 165447. doi:10.1103/PhysRevB.94.165447

Scholz, R., Lindner, S., Lončarić, I., Tremblay, J. C., Juaristi, J. I., Alducin, M., et al. (2019). Vibrational response and motion of carbon monoxide on Cu(100) driven by femtosecond laser pulses: Molecular dynamics with electronic friction. *Phys. Rev. B* 100, 245431. doi:10.1103/PhysRevB.100.245431

Serrano-Jiménez, A., Muzas, A. P. S., Zhang, Y., Ovčar, J., Jiang, B., Lončarić, I., et al. (2021). Photoinduced desorption dynamics of CO from Pd(111): A neural network approach. *J. Chem. Theory Comput.* 17, 4648–4659. doi:10.1021/acs.jctc.1c00347

Springer, C., and Head-Gordon, M. (1996). Simulations of the femtosecond laser-induced desorption of CO from Cu(100) at 0.5 Ml coverage. *Chem. Phys.* 205, 73–89. doi:10.1016/0301-0104(95)00316-9

Springer, C., Head-Gordon, M., and Tully, J. C. (1994). Simulations of femtosecond laser-induced desorption of CO from Cu(100). *Surf. Sci.* 320, L57–L62. doi:10.1016/0039-6028(94)00569-9

Szymanski, P., Harris, A. L., and Camillone, N. (2007). Adsorption-state-dependent subpicosecond photoinduced desorption dynamics. *J. Chem. Phys.* 126, 214709. doi:10.1063/1.2735594

Tetenoire, A., Ehlert, C., Juaristi, J. I., Saalfrank, P., and Alducin, M. (2022). Why ultrafast photoinduced co desorption dominates over oxidation on ru(0001). *J. Phys. Chem. Lett.* 13, 8516–8521. doi:10.1021/acs.jpclett.2c02327

Tetenoire, A., Juaristi, J. I., and Alducin, M. (2021). Insights into the coadsorption and reactivity of O and CO on Ru(0001) and their coverage dependence. *J. Phys. Chem. C* 125, 12614–12627. doi:10.1021/acs.jpcc.1c01618

Tetenoire, A., Juaristi, J. I., and Alducin, M. (2023). Photoinduced CO desorption dominates over oxidation on different O + CO covered Ru(0001) surfaces. *J. Phys. Chem. C* 127, 10087–10096. doi:10.1021/acs.jpcc.3c01192

Vazhappilly, T., Klamroth, T., Saalfrank, P., and Hernandez, R. (2009). Femtosecond-laser desorption of $H_2(D_2)$ from Ru(0001): Quantum and classical approaches. *J. Phys. Chem. C* 113, 7790–7801. doi:10.1021/jp810709k

Xin, H., LaRue, J., Öberg, H., Beye, M., Dell'Angela, M., Turner, J. J., et al. (2015). Strong influence of coadsorbate interaction on CO desorption dynamics on Ru(0001) probed by ultrafast X-Ray spectroscopy and *ab initio* simulations. *Phys. Rev. Lett.* 114, 156101. doi:10.1103/PhysRevLett.114.156101

frontiers | Frontiers in Chemistry

TYPE Original Research
PUBLISHED 25 July 2023
DOI 10.3389/fchem.2023.1238711

OPEN ACCESS

EDITED BY
Marco Sacchi,
University of Surrey, United Kingdom

REVIEWED BY
Bret Jackson,
University of Massachusetts Amherst, United States
Hirokazu Ueta,
Japan Atomic Energy Agency, Japan

*CORRESPONDENCE
Rainer D. Beck,
rainer.beck@epfl.ch

†These authors have contributed equally to this work and share first authorship

RECEIVED 12 June 2023
ACCEPTED 05 July 2023
PUBLISHED 25 July 2023

CITATION
Floß P, Reilly CS, Auerbach DJ and Beck RD (2023), Surface-induced vibrational energy redistribution in methane/surface scattering depends on catalytic activity.
Front. Chem. 11:1238711.
doi: 10.3389/fchem.2023.1238711

Surface-induced vibrational energy redistribution in methane/surface scattering depends on catalytic activity

Patrick Floß[1,2†], Christopher S. Reilly[1†], Daniel J. Auerbach[1,3] and Rainer D. Beck[1,2*]

[1]Institute of Chemical Sciences and Engineering (ISIC), École Polytechnique Fédérale de Lausanne (EPFL), Lausanne, Switzerland, [2]Max Planck-EPFL Center for Molecular Nanoscience and Technology, Lausanne, Switzerland, [3]Max Planck Institute for Multidisciplinary Sciences, Göttingen, Germany

Recent state-to-state experiments of methane scattering from Ni(111) and graphene-covered Ni(111) combined with quantum mechanical simulations suggest an intriguing correlation between the surface-induced vibrational energy redistribution (SIVR) during the molecule/surface scattering event and the catalytic activity for methane dissociation of the target surface (Werdecker, Phys. Rev. Res., 2020, 2, 043251). Herein, we report new quantum state and angle-resolved measurements for methane scattering from Ni(111) and Au(111) probing the extent of $\nu_3 \rightarrow \nu_1$ antisymmetric-to-symmetric conversion of methane stretching motion for two surfaces with different catalytic activities. Consistent with the expectations, the extent of SIVR occurring on the more catalytically active Ni(111) surface, as measured by the ν_1: ν_3 scattered population ratio, is found to be several times stronger than that on the more inert Au(111) surface. We also present additional insights on the rovibrational scattering dynamics contained in the angle- and state-resolved data. The results together highlight the power of state-resolved scattering measurements as a tool for investigating methane–surface interactions.

KEYWORDS

methane dissociation, state-to-state scattering, angular distributions, surface-induced vibrational energy redistribution, optothermal spectroscopy, bolometer infrared laser tagging, heterogeneous catalysis

1 Introduction

State-to-state scattering experiments provide a powerful and well-established technique to elucidate the atomic-level details of what happens when molecules collide with other gas-phase molecules or with surfaces (Auerbach et al., 2021). Often, the connection between the measured final state distributions and the property under study is direct and obvious. For example, the degree of rotational excitation in a collision is directly related to the angular anisotropy of the potential energy surface (PES) of the system under study and can be used to test theoretical methods for calculating the PES. In other cases, the connection of the scattering data to the underlying question of what is going on is more subtle. For example, highly vibrationally excited NO or CO molecules scatter almost vibrationally elastically from insulator surfaces but undergo facile multi-quantum vibrational relaxation if they strike a metal surface. Qualitatively, these observations show that the presence of a continuum of low-lying electronically excited states in the metal is being excited by molecular vibrations-a

strong violation of the Born–Oppenheimer approximation. More detailed theoretical work established that charge transfer in the collisions is the key driving factor and that the propensity for charge transfer therefore correlates with the degree of vibrational relaxation (Wodtke et al., 2008; Shenvi et al., 2009; Wagner et al., 2019).

An intriguing example of this more subtle connection of observations to dynamical propensities emerges from the first state-to-state measurements of methane scattering from surfaces. When CH_4 ($\nu_3 = 1, J = 1$), that is, CH_4 prepared with a single vibrational quantum in the ν_3 antisymmetric C-H stretch normal mode and one quantum of vibrational angular momentum, strikes a clean Ni(111) surface, nearly 40% of the molecules scatter into a state with one quantum of the ν_1 symmetric C-H stretch normal mode (Werdecker et al., 2018). In this study, we refer to this phenomenon of surface collision-mediated conversion of vibrational energy by the term *surface-induced vibrational energy redistribution*, or SIVR for short. We note that a similar SIVR process for scattering of H_2O from Cu(111) was predicted by state-to-state quantum scattering calculations by Zhang and Jiang (2019) and Zhang and Jiang (2020).

Surprisingly, SIVR was not observed for CH_4 ($\nu_3 = 1, J = 1$) scattering from Gr/Ni(111), the graphene-covered Ni(111) surface (Werdecker et al., 2020) (for convenience we refer to reference [Werdecker et al., 2020] from now on as "*Werdecker et al.*"). Quantum dynamics calculations by Bret Jackson and coworkers propose an explanation for this remarkable difference. Their calculations show that as the incident CH_4 (ν_3) molecules approach the reactive Ni(111) surface, the C-H bond closest to the surface starts to elongate, introducing a coupling between the two C-H stretching normal modes ν_3 and ν_1 which differ only by the relative phases of the C-H stretching motions. Inelastic scattering calculations for collisions with different surface sites on Ni(111) reveal a correlation between the calculated C-H bond elongation and the catalytic activity of the surface site, resulting in an increasing probability for SIVR with increasing catalytic activity of the impact site. Based on these results, the authors hypothesized that the extent of SIVR in a molecule–surface collision is correlated with the catalytic activity of the surface.

In this paper, we present new measurements to test this hypothesis. We extend the range of surfaces studied to include the closely packed Au(111) surface which, based on density function calculations[1] of the barrier to dissociative adsorption, is expected to have a catalytic activity intermediate to that of Ni(111) (Jackson and Nave, 2013) and Gr/Ni(111) (Li et al., 2018).

In addition to providing data on a new system with catalytic activity intermediate between Ni(111) and Gr/Ni(111), we have also improved the method of determining the "branching ratio" br_{ν_1/ν_3}, which quantifies the extent of SIVR through the ratio of the total ν_1 and ν_3 scattering flux following the surface collision of an incident CH_4 (ν_3) molecule. We use a rotatable bolometer detector in this work, which allows us to measure quantum state-resolved angular distributions of scattered molecules. We base our reported values of br_{ν_1/ν_3} on the scattering angle- and rotational state-integrated scattered flux of CH_4 in the ν_1 and ν_3 states. Previous determinations of br_{ν_1/ν_3} were based on measurements at a single scattering angle due to limitations of the instrument employed in those studies. Indeed, as shown in Section 3.2, the angular distributions differ for the different scattered CH_4 rovibrational states probed. Therefore, for the measured branching ratio to reflect the total $\nu_3 \rightarrow \nu_1$ and $\nu_3 \rightarrow \nu_3$ scattering probabilities accurately, it is advantageous to measure over a wide range of scattering angles and integrate the ν_1 and ν_3 scattered intensities over the scattering angle.

Our measurements show that the value of br_{ν_1/ν_3} measured for Au(111) is intermediate to those of Ni(111) and Gr/Ni(111). The literature values of the activation barriers to dissociative chemisorption increase when proceeding from Ni(111) (Jackson and Nave, 2013) to Au(111) (Jackson) to (free-standing) graphene (Li et al., 2018). Thus, our results are in accordance with the hypothesis that SIVR correlates with the catalytic activity of the surface.

2 Materials and methods

Figure 1 shows a schematic illustration of the experimental setup. Full details can be found in Reilly et al. (2023). Briefly, a continuous supersonic expansion from a temperature-controlled nozzle into a vacuum is used to create a molecular beam of methane with the mean kinetic energy of 100 meV and a FWHM spread of 30%. Approximately 10% of the methane molecules in the molecular beam are prepared in the $J = 1$ *meta*-CH_4 (i.e., nuclear spin $I = 2$) rotational state of the ν_3 antisymmetric stretch fundamental (i.e., with one quantum of ν_3 vibration) by infrared laser excitation with a tunable, single-mode, continuous-wave (CW) infrared (IR) optical parametric oscillator (OPO) (Argos Lockheed Martin-Aculight, "Pump laser" in Figure 1) (Chadwick et al., 2014). The remaining ≈ 90% of the molecules populate rotational states in the ground vibrational state not addressed by the pump laser.

The state-prepared molecular beam collides with a single crystal surface sample in the ultrahigh vacuum surface science chamber with a base pressure of 1×10^{-10} mbar. A 4-axis manipulator permits displacement the surface in three dimensions and rotation of the incident angle θ_i made between the surface normal and the molecular beam.

Scattered molecules are detected and resolved by the quantum state and scattering angle using the bolometer infrared laser tagging (BILT) technique (Reilly et al., 2023). Here, a second, tunable, single-mode, CW IR OPO (TOPO TOPTICA Photonics, "tagging laser" in Figure 1) laser beam is chopped at 237 Hz with 50% duty cycle using an optical chopper wheel (not shown) and crosses the scattering plane perpendicularly 16 mm from the target surface. By tuning the tagging laser into resonance with different rovibrational transitions, we selectively excite the methane molecules that have scattered from the initially prepared state into the lower state of the resonant transition, transferring to those molecules one quantum of ν_3 vibrational energy. The approximately 370 meV/molecule of energy absorbed by the molecules from the tagging laser is then transferred to a cryogenic bolometer detector when the molecules adsorb on a cold 4-mm-diameter diamond absorber to which the bolometer is attached.

Using a lock-in amplifier, we record the response of the detector to the chopping of the tagging laser. To the raw lock-in output, we apply a series of corrections to obtain a "scattering intensity" $s(\theta_f)$ which is intended to provide a relative measure of the fraction of molecules scattering into the range of solid angles subtended by the

1 Jackson, B. (2023) Private communication.

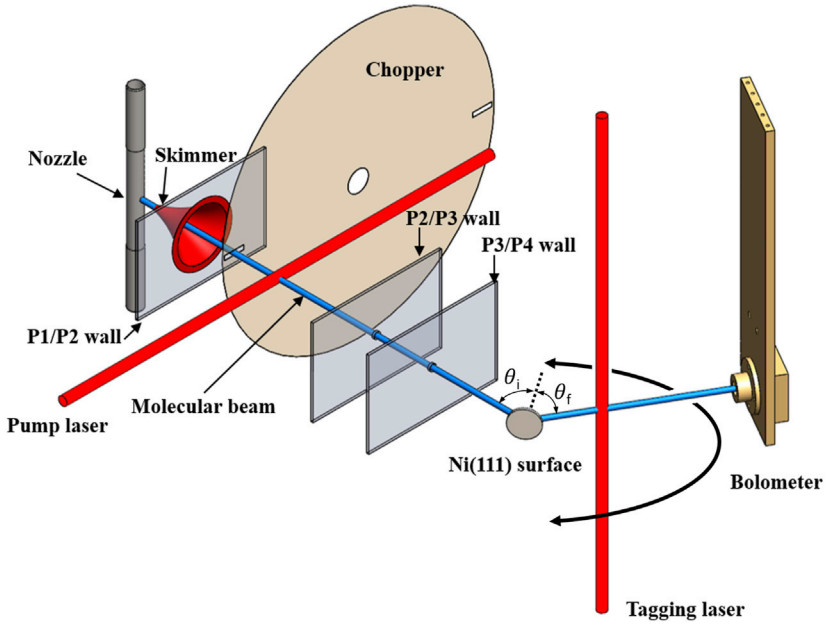

FIGURE 1
Schematic of the experimental setup used for state-to-state surface scattering of methane. A molecular beam is generated in vacuum chamber P1 and traverses the differential pumping stages P2 and P3. Quantum state-specific preparation of methane in the molecular beam occurs in P2 which also contains a chopper disk for beam modulation. The state-prepared molecular beam collides in P4 with the single crystal target surface at an incident angle θ_i with respect to the surface normal (marked by the dotted line). Molecules scattered at an angle θ_f are excited with quantum state resolution by the tagging laser and detected by the rotatable bolometer.

bolometer detector centered at an angle θ_f in the scattering plane and occupying the state being tagged. These corrections are described in detail in Section S1 of the Supplementary Material of Reilly et al. (2023).

Synchronized, computer-controlled rotation of the bolometer and the tagging laser beam enables variation of the measured final angle θ_f, enabling, in turn, measurement of the state-resolved angular distributions of scattered methane molecules, as shown in Figure 2 in the following section.

For preparation of atomically flat Ni(111) and Au(111) surfaces, we use Ar^+ sputtering followed by annealing to 973 K and 773 K, respectively. Crystallographic order of prepared surfaces is verified using low-energy electron diffraction (LEED), and the absence of surface contaminants is verified using Auger electron spectroscopy. After conducting all experiments, the contamination levels were verified to be below the detection threshold of approximately 1% ML.

3 Results and discussion

For both the Ni(111) and Au(111) surfaces, we recorded 14 state-resolved angular distributions. To identify the rovibrational level being tagged, we use the quantum numbers (ν_a, J, $F^{(b)}$, A_c, and α) which, for brevity, we sometimes condense down to a single compound index η. ν_a specifies the symmetry ($a = 1$ for symmetric and $a = 3$ for antisymmetric) of the stretch fundamental (or "stretch" for simplicity), J denotes the total angular momentum, $F^{(b)}$ denotes the Coriolis label ($b = -, 0, +$) characterizing the coupling of rotational and vibrational angular momentum (di Lauro, 2020), A_c denotes the wavefunction symmetry ($c = 1, 2$), and α denotes the polyad-level identifier (Brown et al., 1992). The rovibrational level prepared by the pump laser, for example, has quantum numbers ($\nu_3, J = 1, F^{(-)}, A_2$, and $\alpha = 3$). Note that for the subset of levels tagged in our study, the first four identifiers (i.e., ν_a, J, $F^{(b)}$, and A_c) suffice to uniquely identify a level.

Figure 2 illustrates a selected subset of the measured angular distributions. The complete set of measured distributions is available in Supplementary Section S1. The rotational states tagged include all *meta*-CH_4 states in the ν_3 and ν_1 stretch fundamentals with total angular momentum quantum number $J \leq 5$ along with one $J = 7$ rotational level for both stretches. States with nuclear spin $I \neq 2$ were not probed because interconversion among the different nuclear spin isomers in direct molecule–surface collisions is presumed to occur with negligible probability. Our own measurements using a double-resonance pump–probe technique showed no evidence of such interconversion in CH_4/Au(111) collisions.

In the following sections, we present an analysis and discussion of the measured distributions. First, in Section 3.1, we treat the central topic of SIVR before moving on to a detailed look at aspects of scattering dynamics relating to the scattering angle (Section 3.2) and rotational state (Section 3.3).

3.1 Surface-induced vibrational energy redistribution

The principle objective of the current work is to test the hypothesis advanced in *Werdecker et al.* and discussed in the Introduction of the current work. We remind the reader that this hypothesis asserts a positive correlation between the efficacy of

10.3389/fchem.2023.1238711

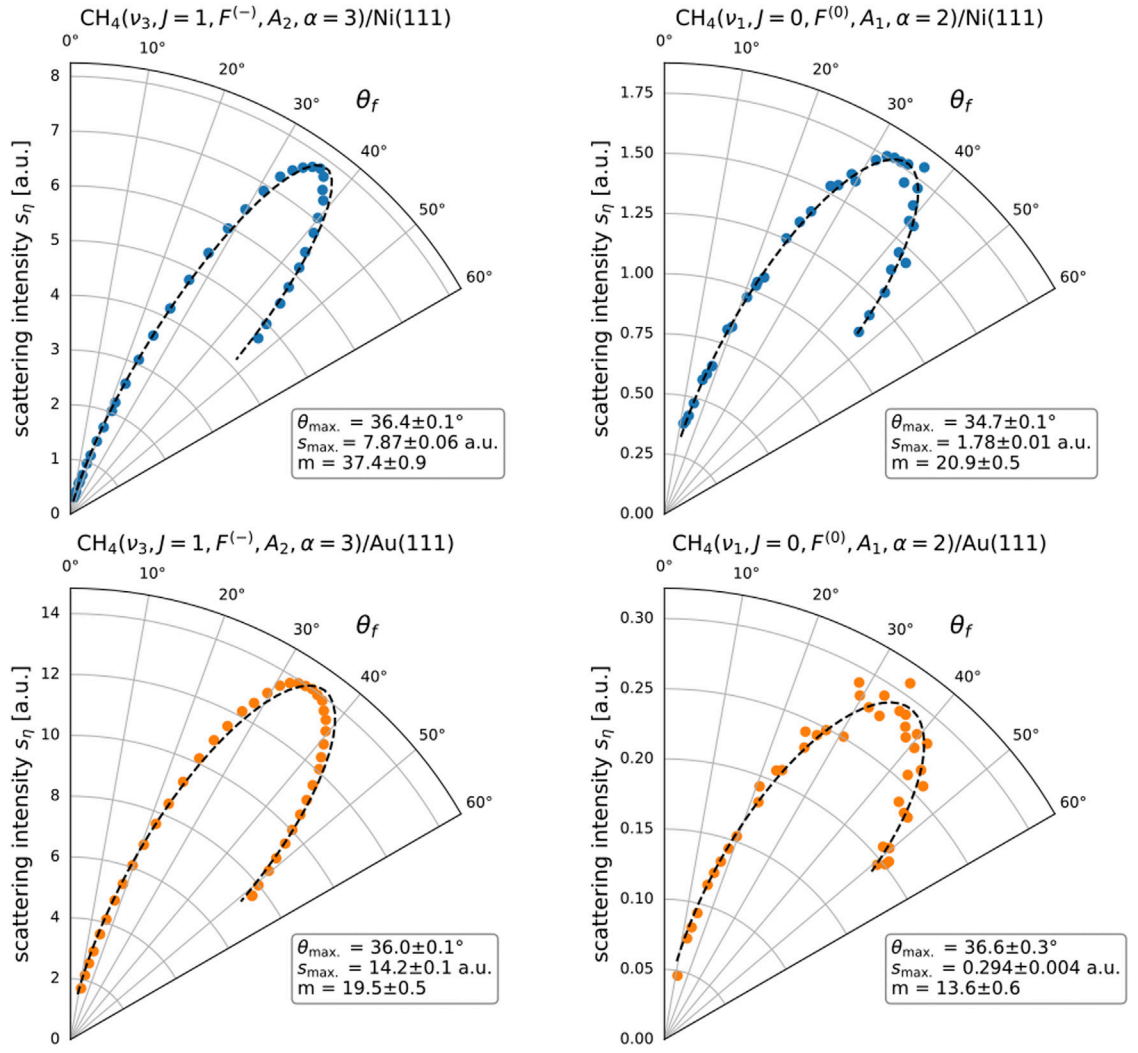

FIGURE 2
State-resolved in-plane angular distributions $s_\eta(\theta_f)$ for $CH_4(\nu_3, J = 1, F^{(-)}, A_2, \alpha = 3)$ scattering from Ni(111) (blue markers) and Au(111) (orange markers). The incoming molecules have a mean kinetic energy $E_i = 100 \pm 13$meV and strike the surface ($T_s = 473$K) at an incident angle $\theta_i = 35°$. The points correspond to measured data, and the dashed lines correspond to the associated fits (see Eq. 1). The best-fit parameter values are listed in the boxes next to their associated plots. The main text shows the explanation of quantum state identifiers (ν_a, J, $F^{(b)}$, A_c, and α). Reported scattering intensities are obtained from raw detector signals after the application of corrections for tagging efficiency and time-dependent bolometer sensitivity and represent the differential scattered flux (in molecules per steradian per second) within a multiplicative constant independent of the surface and rovibrational state. The absolute value of the angle between the surface projection of the molecule's initial velocity and the $\{\bar{1}2\bar{1}\}$ crystallographic direction of the Ni(111) and Au(111) surface samples is $10° \pm 2°$ and $1° \pm 2°$, respectively.

$\nu_3 \rightarrow \nu_1$ conversion induced in a methane–surface collision and the catalytic activity of the surface for the dissociative chemisorption of methane. To quantify the efficacy, we compute a branching ratio br_{ν_1/ν_3} using the following procedure. For each tagged rovibrational state η, we integrate the measured scattering intensity $s_\eta(\theta_f)$ over the range $11.5° = \theta_- < \theta_f < \theta_+ = 47°$ of angles probed and then sum the resulting integrated fluxes $S_\eta = \int_{\theta_-}^{\theta_+} s_\eta(\theta_f) d\theta_f$ over the different tagged rotational states of each stretch. We obtain a measure of the total scattered flux $\bar{S}_{\nu_a} = \sum_{\eta \in \nu_a} S_\eta$ of each stretch fundamental ν_a. From $\bar{S}_{\nu_1}$ and $\bar{S}_{\nu_3}$, we obtain the branching ratio $br_{\nu_1/\nu_3} = \bar{S}_{\nu_1}/\bar{S}_{\nu_3}$.

The branching ratios br_{ν_1/ν_3} obtained from the state-resolved angular distributions are shown in Table 1, along with the branching ratio of zero implied from the results of *Werdecker et al.* in their fixed scattering angle measurements for the graphene-covered nickel surface. Tabulated along with the branching ratios are the associated barrier heights for dissociative chemisorption of CH_4 as determined by density functional theory (DFT) calculations. We note that the barrier height quoted for Gr/Ni(111) was in fact computed for free-standing graphene, although the addition of a Ni(111) substrate is not expected to alter this figure significantly[1]. Taking a low barrier height as an indication of high catalytic activity, it is clear that the order of the branching ratios and barrier heights for these three surfaces agrees with the stated hypothesis.

To assess the repeatability of the branching ratio measurements the full set of measurements for the Au(111) surface was performed twice. The data from the second run showed a somewhat better signal-to-noise ratio and so we present the branching ratio of 6.6% obtained from this run in Table 1. The first run yielded a branching

TABLE 1 Scattering angle-integrated branching ratios br_{ν_1/ν_3} computed from the state-resolved angular distributions measured in this study (Figure 2) along with theoretically calculated barrier heights for methane dissociation with associated references.

Surface	br_{ν_1/ν_3} (%)	Barrier height (eV)
Ni(111)	35.1 ± 4	1.1[10]
Au(111)	6.6 ± 0.7	1.9[9]
Gr/Ni(111)	0.0†	4.1‡[11]

†From reference [Werdecker et al., 2020]. Measured under conditions E_i = 100 meV, T_s = 673K, θ_i = 65°, and fixed θ_f = 70°.
‡Calculated for free-standing graphene.

ratio of 7.9%. The percentage deviation of 100% × $\frac{7.9\%-6.6\%}{7.9\%+6.6\%}$ = 9% between runs is of the same order of magnitude as those measured for other quantities derived from the same runs (e.g., the mean rotational energies $\langle E_{\mathrm{rot.}}^{\nu_1}\rangle$ and $\langle E_{\mathrm{rot.}}^{\nu_3}\rangle$ presented in Section 3.3). As there is a lack of necessary data for a more rigorous statistical analysis, we take ± 10% as a reasonable estimate of our branching ratio uncertainty for the Ni(111) surface as well as the Au(111) surface, with the experimental procedures and data quality for the two surfaces being largely identical. From our own analysis of the signal-to-noise ratio of the measurements presented in *Werdecker et al.* on Gr/Ni(111), we arrive at a rough estimate of the upper limit of the branching ratio for this surface of 2%. We therefore consider the branching ratio order presented in Table 1 to be reliable.

3.2 Trends in state-resolved angular distributions

In computing the branching ratios, we integrate over the scattering angle and sum over rotational states and thus discard any dynamical information contained in the angular and rotational state dependence of the scattering intensities. To explore in finer detail the dynamics of the molecule–surface collision, we return in this section to the state-resolved angular distributions. In the following section (Section 3.3), we narrow our attention to the gross rotational dynamics via the scattering angle-integrated state fluxes S_η.

We have found it useful to summarize individual state-resolved angular distributions by three parameters, namely, m, $\theta_{\mathrm{max.}}$, and $s_{\mathrm{max.}}$, which characterize a distribution's width, angle of peak intensity, and peak amplitude, respectively. The parameters are determined by performing a non-linear least squares fit of the measured data using a fit function of the following form:

$$s\left(\theta_f\right) = s_{\mathrm{max.}} \cdot \cos^m\left(\theta_f - \theta_{\mathrm{max.}}\right) \quad (1)$$

That the chosen fit function gives a good description of our observations can be verified by inspection of Figure 2 which shows measured data overlaid with their associated best-fit curves (see also the Supplementary Materials for full set of angular distributions and fits).

Figure 3 shows the best-fit parameter values m, $\theta_{\mathrm{max.}}$, and $s_{\mathrm{max.}}$ for all 28 state-resolved measurements (although we include in Figure 3 the peak amplitude parameter $s_{\mathrm{max.}}$ for completeness, we omit discussion of this parameter, deferring discussion of the related scattering angle-integrated state populations S_η for Section 3.3). From the figure, one can readily deduce that for both surfaces and for all lines tagged the scattering mechanism appears to be "direct" or "impulsive" in that the measured distributions strongly deviate from the $m = 1, \theta_{\mathrm{max.}} = 0°$ behavior expected of a "trapping/desorption" scattering process characterized by an extended molecular residence time at the surface (Rettner and Auerbach, 1994). Such a lack of equilibration between the surface and the scattering methane molecule has been seen before both in experiment and calculations for Ni(111) (Milot et al., 2001; Al Taleb and Farías, 2017) and Pt (111) (Kondo et al., 2018).

In addition to our classification of the scattering as direct/impulsive, we also identify three distinct trends from the analysis of the angular distributions. First, the exponents m (Figure 3, top row) are systematically higher for scattering from Ni(111) than those from Au(111), reflecting a lower degree of angular dispersion caused by the former. Second, for both Ni(111) and Au(111), the widths of the scattering peaks increase with the rotational quantum number J, suggesting a correlation between rotational excitation and momentum transfer either between the molecule and the surface or between the parallel and perpendicular components of the molecular momentum.

Third, the peak angles $\theta_{\mathrm{max.}}$ (Figure 3, middle row) for scattering from Au(111) are shifted further away from surface normal compared to those for scattering from Ni(111). In a recent publication, we reported (Reilly et al., 2023) the same finding for CH_4/Ni(111) scattering with CH_4 prepared in the vibrational ground state and noted in addition a positive trend between $\theta_{\mathrm{max.}}$ and total angular momentum quantum number J. From Figure 3, it is clear that this correlation holds for the vibrationally excited molecules as well, the trend being somewhat more pronounced for Au(111). Note that a positive $\theta_{\mathrm{max.}}$–J correlation is what one anticipates for the scattering of a rigid body from a flat and rigid surface based on simple considerations of conservation of energy and parallel momentum (see the red curve of Figure 3). One might therefore conclude that the CH_4/Au(111) system more closely approaches this ideal than the CH_4/Ni(111) system. However, in the limit of perfect flatness and rigidity, one also expects a unique scattering angle for each final state (i.e., $m \to \infty$). On this account, the broader peaks (characterized by smaller exponents m) observed for scattering from Au(111) would then imply the opposite conclusion. Our results do not therefore admit a conclusive determination of which surface appears more "mirror-like" to a scattering methane molecule. Of course, a vibrating molecule cannot in the first place be said to be a rigid body, and certainly for the $\nu_3 \to \nu_1$ scattering channel, the situation is further complicated by the change in the vibrational mode structure and accompanying energy release.

10.3389/fchem.2023.1238711

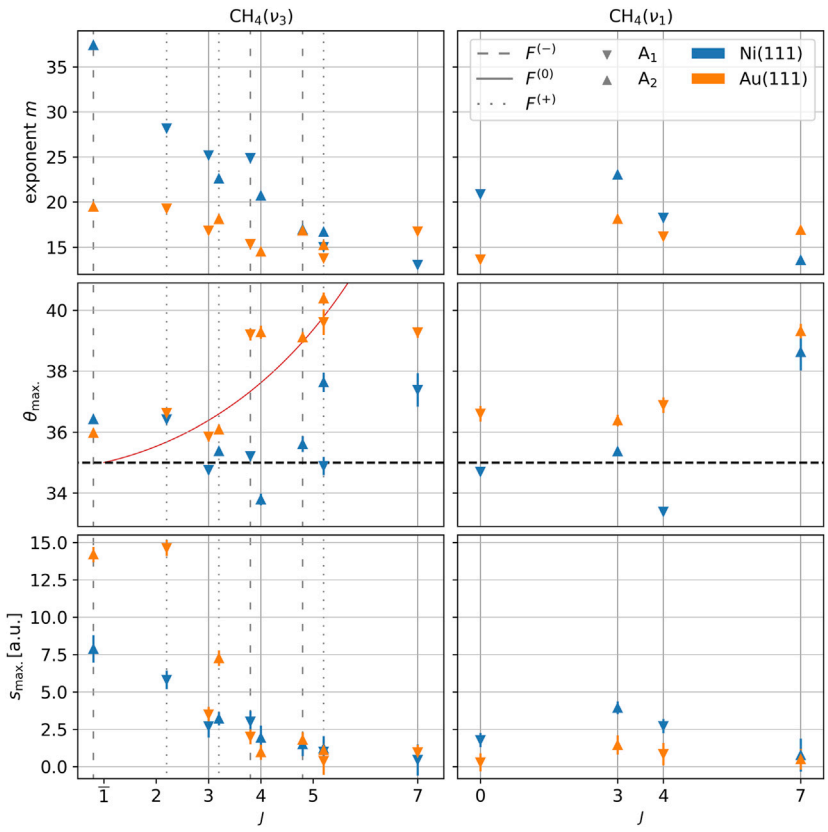

FIGURE 3
Fitting parameters obtained from fitting Eq. 1 to the measured state-resolved in-plane angular distributions $s_\eta(\theta_f)$. The rovibrational level $(\nu_3, J = 1, F^{(-)}, A_2)$ prepared by the pump laser is indicated by the overbar $\overline{1}$ on the J label. Tagged levels are grouped by the total angular momentum quantum number J and displaced slightly left, right, or not at all depending on whether their associated Coriolis stack is $F^{(-)}$, $F^{(+)}$, or $F^{(0)}$, respectively. Marker symbols denote the wavefunction symmetry. The red curve in the plot of $\theta_{max.}$ for the ν_3 levels is the predicted $\theta_{max.}$ for a rigid methane molecule with $J = 1$ scattering from a flat and rigid surface. The two black dotted horizontal lines in the $\theta_{max.}$ plots mark the angle of specular scattering.

Going beyond the trends just discussed, we can also make a few additional qualitative observations. We first point out the anomalously large exponent m for the elastic $(\nu_3, J = 1) \rightarrow (\nu_3, J = 1)$ channel on Ni(111) is 38% larger than the next-largest ν_3 channel exponent and 61% larger than the largest ν_1 exponent for the same surface. In a practical sense, this fact, combined with the fact that the elastic channel on Ni(111) is relatively intense, establishes that the angular distributions for the vibrationally elastic and inelastic channels can in fact differ and that it is, therefore, essential to measure overall scattered angles to obtain the most accurate estimate of the total $\nu_3 \rightarrow \nu_1$ scattering probability. Indeed, when we compute "fixed angle branching ratios" $\sum_{\eta \in \nu_1} s_\eta(\theta_f) / \sum_{\eta' \in \nu_3} s_{\eta'}(\theta_f)$ from our Ni(111) measurements, we find that their values vary by more than 50% over the range of scattering angles θ_f probed (Supplementary Section S2).

In another sense, that the vibrationally and rotationally elastic scattering peak is so much narrower than the others and should imply something about the molecule–surface interaction potential and associated scattering dynamics. We offer the following simple microscopic explanation for a strong and anomalously narrow elastic scattering distribution peaking near specular $(\theta_{max.} - \theta_i < 1.5^\circ)$. Of the full range of values of impact parameters characterizing the possible initial conditions of the scattering molecule (e.g., impact site, initial molecular orientation, and internal/external axis of rotation), there is a significant fraction which results in trajectories where the molecule is turned around at distances relatively far from the surface. At these distances, the interaction between the molecule and the surface manifests primarily as a mutually repulsive force directed along the surface normal. That is, for these trajectories, the molecules do not penetrate far enough for the molecule–surface interaction to either exhibit significant lateral surface corrugation or effect significant disruption of the molecule's or surface's internal structure. Thus, the various mechanisms available to induce a change in the rovibrational state or deflect the scattering molecule away from specular scattering (parallel-to-perpendicular momentum transfer, surface phonon creation/annihilation, and rovibrational inelasticity) would act only weakly, leading to a narrow elastic distribution peaking near specular scattering. On the other hand, trajectories permitting deep enough penetration for the interaction to effect change in the rovibrational state will also tend to disperse angularly due to the additional effects of lateral corrugation and phonon creation/annihilation, resulting in broader scattering distributions for the rovibrationally inelastic channels. Interestingly, the strength of these dispersive forces seems to be no

10.3389/fchem.2023.1238711

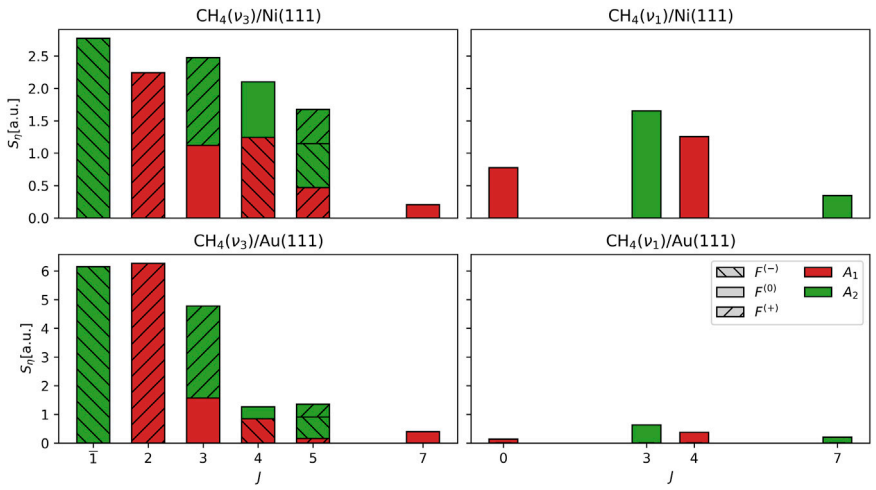

FIGURE 4
Distribution of scattering angle-integrated rovibrational state fluxes S_η, where $\eta = (\nu_3, J, F^{(b)}, A_c)$. The rovibrational level $(\nu_3, J = 1, F^{(-)}, A_2)$ prepared by the pump laser is indicated by the overbar $\bar{1}$ on the J label. The Coriolis stack ($F^{(-)}$, $F^{(0)}$, and $F^{(+)}$) of a tagged level is indicated by the hatching pattern of its associated bar and the wavefunction symmetry (A_1 and A_2) by the bar color. All ν_1 states are of the $F^{(0)}$ type. The weakly populated $(\nu_3, J = 5, A_1)$ level for the Au(111) data is of the $F^{(+)}$ type (same as for Ni(111)).

greater for the trajectories undergoing vibrational state change than those simply changing rotational state.

To qualitatively summarize the explanation just presented, our observations can be interpreted as implying a certain order in which the different aspects of the molecule–surface interaction "turn on" as the molecule approaches the surface, with a two-body repulsive force preceding the onset of dispersive forces, which in turn precedes the onset of forces acting to distort or rotate the molecule.

We close the section with a discussion regarding the differences in peak widths $\propto 1/\sqrt{m}$ and peak angles $\theta_{\max.}$, particularly for the Ni(111) data, among the levels of equal J in the ν_3 stretch. These levels have the same nominal rotational energy (within ± 2%[20]) but are distinguished by their associated Coriolis stack $F^{(b)}$ and wavefunction symmetry A_c. The Coriolis stack of a level indicates, loosely speaking, the relative orientation of its vibrational angular momentum and its total angular momentum (parallel, perpendicular, or antiparallel for $F^{(-)}$, $F^{(0)}$, and $F^{(+)}$, respectively) (di Lauro, 2020). Centrifugal coupling between rotation and vibration splits a Coriolis level (± 0.3% worst case (Hecht, 1961a)) into "sublevels" of definite symmetry with respect to the T_d point group of the CH_4 molecules (Hecht, 1961b), of which those of A_1 and A_2 symmetries belong to the *meta*-CH_4 nuclear spin isomer. The sublevels of a Coriolis stack are distinguished by the internal alignment of their total angular momentum, i.e., by the different molecule-fixed axes about which the molecule is more and less likely to be found rotating (again, loosely speaking).

Compare for example the best-fit m and $\theta_{\max.}$ values for the $(\nu_3, J = 4, F^{(-)}, A_1)$ and $(\nu_3, J = 4, F^{(0)}, A_2)$ levels scattering from Ni(111). The peak of the $F^{(0)}$ level has a 25% larger best-fit exponent m and a peak angle $\theta_{\max.}$ 1.5° closer to normal than that of the $F^{(-)}$ level. Similar differences occur between the A_1 and A_2 sublevels in the same $(\nu_3, J = 5, F^{(+)})$ Coriolis stack. These rather subtle details of the internal molecular motion have a significant impact on the scattering distributions and highlight the "dynamic" nature of the CH_4/Ni(111) interaction in that the form of the state-resolved distributions are not solely dictated by the state's energy. In a recent publication published by the authors on surface scattering of CH_4 in the vibrational ground state (Reilly et al., 2023), we found strong evidence for a more extensive molecule–surface collisional energy exchange (i.e., equilibration) after oxidation of a Ni(111) surface than before oxidation. We also found that the forms (and amplitudes) of the sublevel angular distributions (the ground vibrational state has only $F^{(0)}$ Coriolis stacks) produced upon scattering from the oxidized surface were essentially indistinguishable, while scattering from the unoxidized surface produced differences in the peak widths and peak angles for the different sublevels comparable to those observed in the ν_3 vibrationally excited state. We argued that the lack of imbalances observed in the collisions with the oxidized surface was consistent with the other reported observations in that they reflected an equilibration among the sublevels caused by a prolonged molecule–surface energetic coupling acting to scramble any delicate internal rotational motion.

Concerning the Au(111) surface data, while the form of the distributions among ν_3 levels of equal J is similar, we will see in the following section (Section 3.3) that the level populations S_η (related indirectly to the peak amplitudes $s_{\max.}$) differ dramatically depending on the internal alignment of the molecule's total and vibrational angular momentum, so that the scattering for this system is, in this sense, no less "dynamic."

3.3 Rotational dynamics

Figure 4 shows the scattering angle-integrated rovibrational state populations S_η. In addition to illustrating what is already evident from Table 1—namely, that the overall $\nu_3 \rightarrow \nu_1$ conversion is much weaker for the Au(111) surface—the plotted

10.3389/fchem.2023.1238711

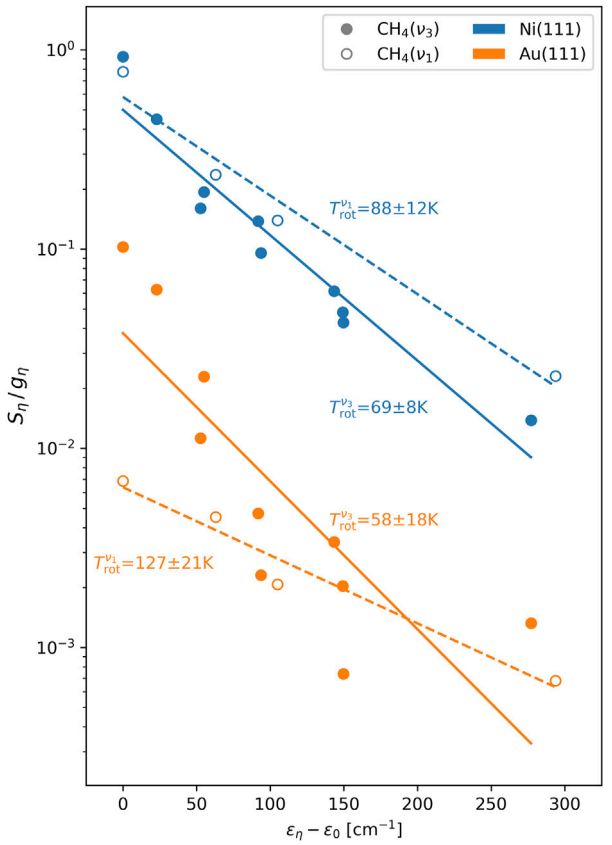

FIGURE 5
Boltzmann fits to the rotational-level population. Plotted are the scattering angle-integrated state-resolved fluxes S_η weighted by the level degeneracy $g_\eta = 2J+1$ *vs.* level energy ε_η (within a constant ν_a-dependent shift ε_0). The fluxes S_η for the Au(111) surface data have been scaled down by a factor 20 to avoid overlap with the Ni(111) data. Solid (dashed) lines indicate fits of the ν_3 (ν_1) data to the Boltzmann form $\propto \exp(-\varepsilon_\eta / kT_{\text{rot.}}^{\nu_3\,(\nu_1)})$. Best-fit effective rotational temperatures $T_{\text{rot.}}^{\nu_a}$ are printed next to the associated best-fit line. The rovibrational level $\eta = (\nu_3, J=1, F^{(-)}, A_2)$ prepared by the pump laser corresponds to the left-most solid markers. The levels of a given stretch ν_a and total angular momentum J are nominally isoenergetic ($\Delta\varepsilon_\eta < 7\text{cm}^{-1}$), with the energy ordering for the different Coriolis stacks of a given (ν_a, J) combination being $F^{(-)} < F^{(0)} < F^{(+)}$. For both surfaces, the A_2 sublevel of the $(\nu_3, J=5, F^{(+)})$ Coriolis stack is more populated than the A_1 sublevel.

distributions also reveal important additional features of the rotational dynamics of the molecular–surface collisions for the systems studied here.

One feature that is directly observable is the differences in the forms of the distributions of the vibrationally elastic ($\nu_3 \rightarrow \nu_3$) channels for the two surfaces, with the Au(111) distribution having a relatively narrow distribution concentrated at low J, suggesting a "colder" rotational population. To quantify the degree of rotational excitation in the different stretch fundamentals, we use two different measures. The first measure is the mean rotational energy $\langle E_{\text{rot.}}^{\nu_a} \rangle = \sum_{\eta \in \nu_a} S_\eta \varepsilon_\eta / \bar{S}_{\nu_a}$ obtained by taking the S_η-weighted average of the rotational energies ε_η of the different tagged levels η of the associated stretch ν_a. The rotational energy ε_η of a level $\eta = (\nu_a, J, F^{(b)}, A_c)$ is calculated by taking the energy difference

TABLE 2 Extracted mean rotational energies $\langle E_{\text{rot.}}^{\nu_a} \rangle$ and effective rotational temperatures $T_{\text{rot.}}^{\nu_a}$ from the rotational distributions presented in Figure 4. Rotational distributions were measured twice for Au(111), and we report the values of $\langle E_{\text{rot.}}^{\nu_a} \rangle$ and $T_{\text{rot.}}^{\nu_a}$ obtained from the run with the higher signal-to-noise ratio. The uncertainty of ± 5cm^{-1} reported for the Au(111) $\langle E_{\text{rot.}}^{\nu_a} \rangle$ values was obtained by taking the larger of the two deviations in $\langle E_{\text{rot.}}^{\nu_a} \rangle$ measured for the two runs. The reported uncertainties for $T_{\text{rot.}}^{\nu_a}$ are the standard errors reported by the least-squares fitting procedure implemented in the `optimize.curve_fit`function of the `SciPy`Python library (Virtanen et al., 2020).

Surface	$\langle E_{\text{rot}}^{\nu_1} \rangle$ [cm^{-1}]	$\langle E_{\text{rot}}^{\nu_3} \rangle$ [cm^{-1}]	$T_{\text{rot.}}^{\nu_1}$ [K]	$T_{\text{rot.}}^{\nu_3}$ [K]
Ni(111)	83.7	69.8	88 ± 12	69 ± 8
Au(111)	103 ± 5	51 ± 5	127 ± 21	58 ± 18

$\Delta\varepsilon_\eta^o$ between the level η and the rovibrational ground state as determined by high resolution spectroscopy (Gordon et al., 2022) and subtracting the theoretically determined energy gap $\Delta\varepsilon_{\nu_a}$ separating the ν_a vibrationally excited state from the ground vibrational state of a hypothetical non-rotating methane molecule (Boudon et al., 2006). The second measure is the effective rotational temperature $T_{\text{rot.}}^{\nu_a}$ obtained by fitting the S_η of the associated stretch ν_a to a thermal (Boltzmann) distribution of the form $S_\eta \propto g_\eta e^{-\varepsilon_\eta / kT_{\text{rot.}}^{\nu_a}}$, where k is the Boltzmann constant and $g_\eta = 2J+1$ is the level degeneracy.

The extracted mean rotational energies $\langle E_{\text{rot.}}^{\nu_a} \rangle$ and effective rotational temperatures $T_{\text{rot.}}^{\nu_a}$ (Figure 5 for fits) are presented in Table 2. The differences in the ν_3 distributions mentioned previously are reflected in the mean energies, with the $\langle E_{\text{rot.}}^{\nu_3} \rangle$ value for Ni(111) being 39% larger than that of Au(111). The difference in effective temperatures $T_{\text{rot.}}^{\nu_3}$ is less pronounced, due to the greater influence of the enhanced $J = 7$ level population scattering from the Au(111) surface (level populations contribute linearly to $\langle E_{\text{rot.}}^{\nu_a} \rangle$, while the $T_{\text{rot.}}^{\nu_a}$ fitting procedure minimizes the sum of the squared *logarithmic* population deviations). That the effective rotational temperatures for all four combinations of surfaces and stretching modes lie well below the surface temperature of 473 K and implies a lack of equilibration between molecular rotation and the surface degrees of freedom, offering further evidence against a trapping-desorption scattering mechanism.

Perhaps the most interesting result emerging from this analysis is that the ratio of the degree of rotational excitation for molecules scattered into the ν_1 and ν_3 states differs dramatically for scattering from Au(111) versus Ni(111). The ratio of the mean rotational energies $\langle E_{rot}^{\nu_1} \rangle / \langle E_{rot}^{\nu_3} \rangle$ is 71% higher for Au(111) than for Ni(111). Similarly, the ratio $\langle T_{rot}^{\nu_1} \rangle / \langle T_{rot}^{\nu_3} \rangle$ is 72% higher for Au(111) than for Ni(111).

Why do the ratios $\langle E_{rot}^{\nu_1} \rangle / \langle E_{rot}^{\nu_3} \rangle$ and $\langle T_{rot}^{\nu_1} \rangle / \langle T_{rot}^{\nu_3} \rangle$ differ so dramatically for the two surfaces? We begin by pointing out that the ν_3 fundamental lies 103 cm^{-1} in energy above the ν_1 fundamental (Boudon et al., 2006). A more general question thus poses itself: where does this extra vibrational energy go during an SIVR process? Since we cannot measure the speed of the scattered molecules or directly detect energy transfer to the surface, a complete experimental accounting of the energy balance is not possible. Nonetheless, our observations indicate that a greater portion of this excess energy is transferred to rotation in a collision with Au(111) ($\langle E_{\text{rot}}^{\nu_1} \rangle - \langle E_{\text{rot}}^{\nu_3} \rangle = 52\,\text{cm}^{-1}$)

than is transferred in a collision with Ni(111) ($\langle E_{\rm rot}^{\nu_1}\rangle - \langle E_{\rm rot}^{\nu_3}\rangle = 14\,{\rm cm}^{-1}$).

In the reduced-dimensional CH_4/Ni(111) SIVR calculations presented in *Werdecker et al.*, the surface was held frozen and the molecule was forced to assume at all times the minimum energy orientation so that energy released in the $\nu_3 \rightarrow \nu_1$ conversion was constrained to be transferred completely into translational kinetic energy of the scattering molecule. In light of our results, it would be of keen interest to learn how this energy is partitioned in a dynamical simulation that includes both molecular rotation and surface vibrations as degrees of freedom. It would be equally interesting to learn to what extent the catalytic C-H bond elongation discussed in Introduction is also operative on Au(111). Perhaps the enhanced ν_1 rotational excitation on Au(111) reflects a mechanism for SIVR on Au(111) that is fundamentally different from the catalytic effect thought to be operating on Ni(111). SIVR on Au(111) might, for example, be a purely "mechanical" effect arising from the violent recoil of the molecule experiences upon rebounding from the much more massive gold surface atoms. An influence of the surface atom mass on CH_4/metal scattering inelasticity has been observed in recent dynamical calculations (Gerrits et al., 2019; Jackson, 2022) which finds Baule-like molecule–surface energy transfer in CH_4/metal surface collisions. A measurement of CH_4/Cu (111) SIVR efficiency might shed light on the role of a mechanical mechanism. The catalytic activity of Cu(111) with a calculated barrier height of 1.32 eV (Bhati et al., 2022) falls in between that of the Ni(111) and the Au(111) surface. In light of both this and the ability of the lighter copper surface atoms to better absorb the shock of impact, a Cu(111) branching ratio weaker than that of Au(111) would stand as strong evidence for a mechanical SIVR mechanism operating on Au(111).

The last observation we wish to make about the rotational distributions concerns the ν_3 levels of equal J, a subject we began discussing at the end of the previous section (Section 3.2) in the context of angular distributions. Figures 4, 5 clearly show that scattering from the Au(111) produces a highly imbalanced distribution of populations among ν_3 sublevels of equal J. These imbalances imply a scattered molecular flux with a high degree of both internal alignment of the total angular momentum (indicated by the imbalance of the A_1 and A_2 sublevel populations within the $(\nu_3, J = 5, F^{(+)})$ Coriolis stack) and relative alignment of the total and vibrational angular momentum (indicated by imbalances among the Coriolis stacks of equal J for $J = 3, 4, 5$). From the restricted subset of levels tagged in this experiment, there appears to be a strong tendency for preservation in the CH_4/Au(111) scattering event of the parallel (i.e., $F^{(-)}$) alignment of total and vibrational angular momentum prepared by the pump laser. Although the ν_3 population imbalances within a given J are not as pronounced in the CH_4/Ni(111) scattering data, it is nonetheless interesting to note that the order of the imbalances for the two surfaces are identical for the levels probed.

At the present time, the authors have no explanation for the form and extent of this internal alignment of molecular rotation observed in the scattering. We plan to present more extensive results on these interesting alignment phenomena in CH_4 surface scattering in a future publication.

4 Summary and future directions

A number of promising avenues exist for further testing the connection between SIVR and catalytic activity. One extension of the work presented here would be a study of SIVR efficiency for a range of different incident kinetic energies E_i. In one sense, one expects SIVR to correlate positively with E_i since, with the increasing incident energy, the molecule can get closer to the surface and gain access to the catalytic forces that distort the molecule's equilibrium geometry and mediate vibrational mode coupling. Indeed, a positive E_i-SIVR correlation is observed in the CH_4/Ni (111) dynamical calculations of *Werdecker et al.* discussed in Introduction. On the other hand, depending on the form of the repulsive molecule–surface interaction, a high-incident velocity may result in the brief molecule–surface interaction time, which might tend to weaken the SIVR produced on scattering.

Another direction, one which would offer a more direct validation of the theoretical results reported in *Werdecker et al.*, would be to measure the variation in SIVR across the different microscopic impact sites of the same macroscopic surface. Although it is of course not feasible to experimentally control the impact site of a molecule, one can vary the relative concentration of different sites. In the calculations of *Werdecker et al.*, the authors find an increase in SIVR at sites where a surface Ni atom is displaced from equilibrium. Such displacements are also expected to increase a site's catalytic activity (Nave et al., 2010). By raising/lowering the surface temperature, one can increase/decrease the density of thermally generated lattice distortions and test for the expected increase/decrease in SIVR.

Another more controlled means of varying the density of different surface sites is to vary the exposed crystal plane, characterized by Miller indices (*ijk*) (Kolasinski, 2012). For *fcc* metals (e.g., Ni, Au, and Pt), the atoms of the (111) (or "close-packed") surface are highly coordinated and therefore present sites of relatively low catalytic activity. The stepped *fcc*(211) surface, however, exposes under-coordinated atoms at step sites, offering lower barrier sites for methane dissociative chemisorption, as observed in experiments and calculations for CH_4 sticking experiments on platinum (Chadwick et al., 2018). A measurement of the branching ratios for different surface planes of the same crystal could thus serve as a compelling experimental verification of the theoretically observed connection between a site's SIVR efficiency and its catalytic activity.

We conclude with a brief summary. For the Ni(111) and Au(111) surfaces, we measured rovibrational state-resolved angular distributions for 10 (4) rotational levels of the ν_3 (ν_1) stretch fundamentals produced by scattering of incident $CH_4(\nu_3, J = 1)$ molecules. From these distributions, we extracted for each surface a branching ratio br_{ν_1/ν_3} characterizing the efficiency of collision-induced $\nu_3 \rightarrow \nu_1$ conversion. The branching ratio measured for the Au(111) surface is found to be more than five times smaller than that measured for the Ni(111) surface but significantly larger than that measured by *Werdecker et al.* at a fixed scattering angle for the Gr/Ni(111) surface. The ordering of the branching ratios for the three surfaces is found to match the ordering of their catalytic activities, which is in accordance with the hypothesis advanced in *Werdecker et al.*

Analysis of the shape of angular distributions reveals for both surfaces a broadening of the scattering distributions with increasing

total angular momentum quantum number J, with the broadening stronger for scattering from the Au(111) surface. In addition, we observe a tendency for super-specular scattering, and this tendency increases with J and is more pronounced for the Au(111) surface. For the Ni(111) surface, the elastic channel is strong and anomalously narrow. The rovibrational levels of equal J in the ν_3 stretch show measurable differences in width and peak angle in scattering from the Ni(111) surface.

From the distribution of scattering angle-integrated state fluxes, the Ni(111) surface produces more highly rotationally excited molecules in the ν_3 stretch than the Au(111) surface. Molecules in the ν_1 stretch are, however, found to be dramatically more rotationally excited in scattering from Au(111) than from Ni(111), prompting a questioning into the nature of the flow of vibrational energy for the two surfaces. The rovibrational levels of equal J in the ν_3 stretch have strongly imbalanced populations upon scattering from Au(111), suggesting strong alignment of the internal angular momentum in the scattered flux and a preservation of the parallel Coriolis coupling of the total and vibrational angular momentum prepared in the incident molecules.

Data availability statement

The original contributions presented in the study are included in the article/Supplementary Material. Further inquiries can be directed to the corresponding author.

Author contributions

RB conceptualized the project, secured funding, and supervised the project. DA designed the experimental setup with support from RB. PF and CR performed the experiments, and PF analyzed the data. CR wrote the manuscript with contributions from PF, DA, and RB. All authors contributed to the article and approved the submitted version.

Acknowledgments

The authors acknowledge financial support by the Swiss National Science Foundation through Grant No. 200497 and by the Max Planck-EPFL Center for Molecular Nanoscience and Technology. The authors thank the EPFL ISIC machine shop and Bo-Jung Chen for their invaluable contributions to the construction of the apparatus used to perform the experiments presented in this manuscript. The authors would also like to thank Bret Jackson for his calculations of the CH_4/Au(111) dissociation barrier and valuable discussions. DA gratefully acknowledges support from the International Center for Advanced Energy Conversion in Göttingen, Germany.

Conflict of interest

The authors declare that the research was conducted in the absence of any commercial or financial relationships that could be construed as a potential conflict of interest.

Publisher's note

Supplementary material

The Supplementary Material for this article can be found online at: https://www.frontiersin.org/articles/10.3389/fchem.2023.1238711/full#supplementary-material

References

Al Taleb, A., and Farías, D. (2017). Coherent quantum scattering of CH_4 from Ni(111). *Phys. Chem. Chem. Phys.* 19, 21267–21271. doi:10.1039/c7cp04559j

Auerbach, D. J., Tully, J. C., and Wodtke, A. M. (2021). Chemical dynamics from the gas-phase to surfaces. *Nat. Sci.* 1, e10005. doi:10.1002/ntls.10005

Bhati, M., Dhumal, J., and Joshi, K. (2022). Lowering the C–H bond activation barrier of methane by means of SAC@Cu(111): Periodic DFT investigations. *New J. Chem.* 46, 70–74. doi:10.1039/d1nj04525c

Boudon, V., Rey, M., and Loëte, M. (2006). The vibrational levels of methane obtained from analyses of high-resolution spectra. *J. Quant. Spectrosc. Radiat. Transf.* 98, 394–404. doi:10.1016/j.jqsrt.2005.06.003

Brown, L. R., Margolis, J., Champion, J., Hilico, J., Jouvard, J., Loete, M., et al. (1992). Methane and its isotopes: Current status and prospects for improvement. *J. Quant. Spectrosc. Radiat. Transf.* 48, 617–628. doi:10.1016/0022-4073(92)90126-o

Chadwick, H., Guo, H., Gutiérrez-González, A., Menzel, J. P., Jackson, B., and Beck, R. D. (2018). Methane dissociation on the steps and terraces of Pt(211) resolved by quantum state and impact site. *J. Chem. Phys.* 148, 014701. doi:10.1063/1.5008567

Chadwick, H., Hundt, P. M., van Reijzen, M. E., Yoder, B. L., and Beck, R. D. (2014). Quantum state specific reactant preparation in a molecular beam by rapid adiabatic passage. *J. Chem. Phys.* 140, 034321. doi:10.1063/1.4861054

di Lauro, C. (2020). "Spectra of spherical top molecules," in *Rotational structure in molecular infrared spectra* (China: Elsevier), 223–242.

Gerrits, N., Chadwick, H., and Kroes, G.-J. (2019). Dynamical study of the dissociative chemisorption of CHD3 on Pd(111). *J. Phys. Chem. C* 123, 24013–24023. doi:10.1021/acs.jpcc.9b05757

Gordon, I. E., Rothman, L., Hargreaves, R., Hashemi, R., Karlovets, E., Skinner, F., et al. (2022). The HITRAN2020 molecular spectroscopic database. *J. Quant. Spectrosc. Radiat. Transf.* 277, 107949. doi:10.1016/j.jqsrt.2021.107949

Hecht, K. T. (1961b). The vibration-rotation energies of tetrahedral XY4 molecules: Part I. Theory of spherical top molecules. *J. Mol. Spectrosc.* 5, 355–389. doi:10.1016/0022-2852(61)90102-3

Hecht, K. T. (1961a). Vibration-rotation energies of tetrahedral XY4 molecules: Part II. The fundamental v3 of CH4. *J. Mol. Spectrosc.* 5, 390–404. doi:10.1016/0022-2852(61)90103-5

Jackson, B., and Nave, S. (2013). The dissociative chemisorption of methane on Ni(111): The effects of molecular vibration and lattice motion. *J. Chem. Phys.* 138, 174705. doi:10.1063/1.4802008

Jackson, B. (2022). Quantum studies of methane-metal inelastic diffraction and trapping: The variation with molecular orientation and phonon coupling. *Chem. Phys.* 559, 111516. doi:10.1016/j.chemphys.2022.111516

Kolasinski, K. (2012). "Surface and adsorbate structure," in *Surface science* (China: John Wiley and Sons, Ltd), 9–49. doi:10.1002/9781119941798.ch1

Kondo, T., Al Taleb, A., Anemone, G., and Farías, D. (2018). Low-energy methane scattering from Pt(111). *J. Chem. Phys.* 149, 084703. doi:10.1063/1.5044744

Li, K., Li, H., Yan, N., Wang, T., and Zhao, Z. (2018). Adsorption and dissociation of CH4 on graphene: A density functional theory study. *Appl. Surf. Sci.* 459, 693–699. doi:10.1016/j.apsusc.2018.08.084

Milot, R., Kleyn, A. W., and Jansen, A. P. J. (2001). Energy dissipation and scattering angle distribution analysis of the classical trajectory calculations of methane scattering from a Ni(111) surface. *J. Chem. Phys.* 115, 3888–3894. doi:10.1063/1.1388224

Nave, S., Tiwari, A. K., and Jackson, B. (2010). Methane dissociation and adsorption on Ni(111), Pt(111), Ni(100), Pt(100), and Pt(110)-(1 x 2): Energetic study. *J. Chem. Phys.* 132, 054705. doi:10.1063/1.3297885

Reilly, C. S., Floß, P., Chen, B.-J., Auerbach, D. J., and Beck, R. D. (2023). Quantum state-resolved methane scattering from Ni(111) and NiO(111) by bolometer infrared laser tagging: The effect of surface oxidation. *J. Chem. Phys.* 158, 214202. doi:10.1063/5.0150009

Rettner, C. T., and Auerbach, D. J. (1994). Distinguishing the direct and indirect products of A gas-surface reaction. *Science* 263, 365–367. doi:10.1126/science.263.5145.365

Shenvi, N., Roy, S., and Tully, J. C. (2009). Nonadiabatic dynamics at metal surfaces: Independent-electron surface hopping. *J. Chem. Phys.* 130, 174107. doi:10.1063/1.3125436

Virtanen, P., Gommers, R., Oliphant, T. E., Haberland, M., Reddy, T., Cournapeau, D., et al. (2020). SciPy 1.0: Fundamental algorithms for scientific computing in Python. *Nat. Methods* 17, 261–272. doi:10.1038/s41592-019-0686-2

Wagner, V., Park, G. B., Wallrabe, M., Wodtke, A. M., and Schäfer, T. (2019). Electron transfer mediates vibrational relaxation of CO in collisions with Ag(111). *Phys. Chem. Chem. Phys.* 21, 1650–1655. doi:10.1039/c8cp06041j

Werdecker, J., Chen, B. J., Van Reijzen, M. E., Farjamnia, A., Jackson, B., and Beck, R. D. (2020). State-to-state methane-surface scattering as a probe of catalytic activity. *Phys. Rev. Res.* 2, 043251. doi:10.1103/physrevresearch.2.043251

Werdecker, J., van Reijzen, M. E., Chen, B.-J., and Beck, R. D. (2018). Vibrational energy redistribution in a gas-surface encounter: State-to-State scattering of CH 4 from Ni(111). *Phys. Rev. Lett.* 120, 053402. doi:10.1103/physrevlett.120.053402

Wodtke, A. M., Matsiev, D., and Auerbach, D. J. (2008). Energy transfer and chemical dynamics at solid surfaces: The special role of charge transfer. *Prog. Surf. Sci.* 83, 167–214. doi:10.1016/j.progsurf.2008.02.001

Zhang, L., and Jiang, B. (2019). Efficient vibrational energy redistribution between stretching modes: State-to-State quantum scattering of H 2 O from Cu(111). *Phys. Rev. Lett.* 123, 106001. doi:10.1103/physrevlett.123.106001

Zhang, L., and Jiang, B. (2020). State-to-state quantum dynamics of H_2O/HOD scattering from Cu(111): Mode- and bond-selective vibrational energy transfer. *J. Chem. Phys.* 153, 214702. doi:10.1063/5.0030490

frontiers | Frontiers in Chemistry

TYPE Original Research
PUBLISHED 02 August 2023
DOI 10.3389/fchem.2023.1248456

OPEN ACCESS

EDITED BY
Helen Chadwick,
Swansea University, United Kingdom

REVIEWED BY
Daniel Farias,
Autonomous University of Madrid, Spain
Cristina Díaz,
Complutense University of Madrid, Spain

*CORRESPONDENCE
Tim Schäfer,
tschaef4@gwdg.de

RECEIVED 27 June 2023
ACCEPTED 20 July 2023
PUBLISHED 02 August 2023

CITATION
Dorst AC, Dissanayake REA, Schauermann D, Knies S, Wodtke AM, Killelea DR and Schäfer T (2023), Hyperthermal velocity distributions of recombinatively-desorbing oxygen from Ag(111).
Front. Chem. 11:1248456.
doi: 10.3389/fchem.2023.1248456

Hyperthermal velocity distributions of recombinatively-desorbing oxygen from Ag(111)

Arved C. Dorst[1,2], Rasika E. A. Dissanayake[1,2], Daniel Schauermann[1], Sofie Knies[3], Alec M. Wodtke[1,2], Daniel R. Killelea[4] and Tim Schäfer[1,2]*

[1]Institute of Physical Chemistry, University of Göttingen, Göttingen, Germany, [2]Max-Planck Institute for Multidisciplinary Sciences, Göttingen, Germany, [3]Faculty of Biology, Chemistry and Geosciences and Bavarian Center for Battery Technology, Bayreuth, Germany, [4]Department of Chemistry and Biochemistry, Loyola University Chicago, Chicago, IL, United States

This study presents velocity-resolved desorption experiments of recombinatively-desorbing oxygen from Ag (111). We combine molecular beam techniques, ion imaging, and temperature-programmed desorption to obtain translational energy distributions of desorbing O_2. Molecular beams of NO_2 are used to prepare a p (4 × 4)-O adlayer on the silver crystal. The translational energy distributions of O_2 are shifted towards hyperthermal energies indicating desorption from an intermediate activated molecular chemisorption state.

KEYWORDS

oxygen, silver, ion imaging, TPD, velocity-resolved, molecular beams, angular distribution, energy distribution

1 Introduction

Silver surfaces play important roles in large scale industrial heterogeneous catalytic processes such as partial oxidation of methanol to formaldehyde and ethylene to ethylene oxide (Serafin et al., 1998; Qian et al., 2003). Because of the tremendous scale of these applications, seemingly modest improvements in the reaction process may lead to big economical and ecological improvements. Therefore, this system has attracted significant attention over the years and numerous studies have focused on the microscopic details of oxidized silver surfaces. Oxygen induced reconstructions of silver surfaces have been thoroughly investigated using high-precision ultra-high vacuum (UHV) surface science techniques in combination with theoretical approaches (Bao et al., 1996; Michaelides et al., 2005; Schnadt et al., 2006; Greeley and Mavrikakis, 2007; Reichelt et al., 2007; Rocha et al., 2012; Martin et al., 2014; Jones et al., 2015a; Jones et al., 2015b). Ag (111) exhibits a variety of different reconstructed surfaces with similar stability which have been studied and discussed for many years. A detailed review about the history of considered oxygen structures on Ag (111) is given by Michaelides et al. (2005).

Experimentally, the oxidation of Ag (111) under UHV conditions with molecular oxygen is difficult due to the low sticking probability (ca. 1×10^{-6}) of O_2 (Campbell, 1985; Kleyn et al., 1996). In early UHV studies, silver surfaces were therefore oxidized under comparatively high O_2 pressures before characterization under UHV conditions (Campbell, 1985). The use of more aggressive oxidants circumvents this issue; in particular, atomic oxygen (Bukhtiyarov et al., 2003; Böcklein et al., 2013; Derouin et al.,

2015) or NO_2 (Bare et al., 1995; Huang and White, 2003) allow for silver surface oxidation under UHV compatible conditions. When using NO_2 as oxidant, the temperature range at which clean oxidized surfaces are produced is restricted between ca. 490 K and 520 K since at lower temperatures NO_2 adsorbs molecularly and at elevated temperatures, O_2 starts desorbing (Huang and White, 2003). When oxidizing at these temperatures, the reconstructed surface is indistinguishable from surfaces oxidized with molecular oxygen and consists mainly out of *p* (4 × 4)-O domains (Carlisle et al., 2000a; Carlisle et al., 2000b). In contrast, oxidizing with atomic oxygen is possible at lower temperatures. It typically results in slightly different surface phases and forms subsurface oxygen below 510 K, (Derouin et al., 2015).

The large number of reconstructed oxidized Ag (111) surfaces observed in experiments has motivated theory groups to develop models describing surface stability based on first principles theory (Michaelides et al., 2003; Li et al., 2003a,b; Michaelides et al., 2005). Using *ab initio* thermodynamics and first principles simulations, theory is able to provide (*T*, *p*) phase diagrams describing stable oxidized surface phases from UHV to high pressure conditions present at real world catalysts (Reuter, 2016). By comparison with experimental results, microscopic details of the oxidized surface structure can be elucidated.

Additional theoretical work has focused on the dynamics of the O_2 dissociation process on Ag (111). These studies do not aim for clarifying the geometry of reconstructed surfaces but provide theoretical data on the atomic scale mechanism of the oxidation process itself (Xu et al., 2005; Kunisada et al., 2011; Kunisada and Sakaguchi, 2014). Kunisada and Sakaguchi investigated quantum dynamics of O_2/Ag (111) dissociative adsorption propagating on a six-dimensional potential energy surface (PES) obtained from density-functional theory (DFT) (Kunisada and Sakaguchi, 2014). From the PES, they identify the lowest barrier near a top site with a height of 1.37 eV. Coupled-channel calculations trajectories based on this PES provide dissociation probabilities for O_2 as function of the incident translational and vibrational energy. Interestingly, dissociation occurs even with translational energies slightly below the activation barrier height, which the authors explain by O_2 tunneling effects. The computations also show a significant dissociation enhancement by increasing the incident vibrational energy caused by a late barrier in the reaction pathway. In another theoretical study based on a neural network interpolated PES, Goikoetxea et al. investigated electronically non-adiabatic effects during the dissociative adsorption of O_2 at Ag (111) (Goikoetxea et al., 2012). They also identified a large energy barrier for dissociation above 1 eV close to the surface. As non-adiabatic effects affect sticking probabilities at elevated distances to the surface and are expected to be smaller than the adiabatic energy barrier, their influence on the sticking probability is negligible.

Such theoretical work provides excellent data for comparison with surface dynamics experiments under well-controlled UHV conditions. A classical experimental approach probes the entrance channel of the reaction pathway by employing pulsed molecular beams of reactants to initiate the surface reaction (Barker and Auerbach, 1984; Kleyn et al., 1996; Sitz, 2002; Kleyn, 2003; Golibrzuch et al., 2015; Chadwick and Beck, 2016; Vattuone and Okada, 2020; Shen et al., 2022). Seeding reactants in different carrier gases allows for modification of the incident translational energy. Incident vibrational energy can be altered by thermal or laser excitation. Surface reactivity as function of varied incident parameters is probed using, for instance, Meitner-Auger electron spectroscopy (MAES) or temperature -programmed desorption (TPD) for coverage determination after exposing the surface for a selected time to a molecular beam.

Surface reaction dynamics experiments on the exit channel probe degrees of freedom of the desorbing reaction products using quantum state-resolved detection methods in combination with translational energy dependent measurements (Comsa and David, 1982; Michelsen and Auerbach, 1991; Michelsen et al., 1992; Shuai et al., 2017; Kaufmann et al., 2018; Dorst et al., 2022). From these studies, translational, rotational, and vibrational state distributions of products can be deduced. Eventually, concepts of detailed balance allow to model these distributions and to defer quantitative heights of reaction barriers.

Recently, we used this approach to investigate the recombinative desorption of oxygen from Rh (111) (Dorst et al., 2022). O_2 was detected using a velocity map imaging (VMI) setup after non-resonant ionization with a femtosecond pulse of 800 nm. The desorption process was initiated by linearly heating the sample in a TPD type approach. We identified hyperthermal velocity distributions for oxygen molecules desorbing from surface sites as well as for oxygen molecules originating from subsurface, indicating a common intermediate desorption state.

In this paper, we present angular distributions and translational energy distribution of recombinatively-desorbing O_2 from Ag (111). We prepare *p* (4 × 4)-O Ag (111) by dosing the surface with a molecular beam of NO_2 seeded in rare gases at a surface temperature of 510 K. Angular distributions are narrow and hyperthermal translational energy distributions indicate an activated desorption process.

2 Experimental

The experimental setup has been previously described in detail (Westphal et al., 2020). Briefly, experiments were conducted under ultra-high vacuum (UHV) conditions at a base pressure of $<5 \times 10^{-10}$ mbar. We dose the surface with a pulsed supersonic molecular beam of 10% NO_2 (AirLiquide, 99.5%) seeded in He (AlphaGaz, ≥99.999%) using a home-built pulsed solenoid nozzle (Park et al., 2016). During exposure, we maintain UHV conditions by differential pumping techniques.

For surface cleaning, the UHV apparatus is equipped with an ion gun (Staib Instruments IG-5-C), with which the surface is Ar^+-sputtered (2.00 kV, 2.0×10^{-7} mbar Ar) for multiple cycles. After annealing (700 K, 30 min), the surface cleanliness is checked by Meitner-Auger electron spectroscopy (OCI BDL 450) and low-energy electron diffraction (LEED) spectroscopy (OCI BDL 450). The Ag (111) crystal (MaTecK, 99.99%, ∅ 10 mm, 2 mm thickness) is mounted on a home-built sample holder and is resistively heated by Ta filaments; temperatures are monitored by a K-type thermocouple. With liquid nitrogen cooling, the accessible temperatures range from 100 K to 1,235 K. We use a home-written LabVIEW™ program for data acquisition and control of experimental parameters.

Velocity distributions of surface desorption products are obtained by combining velocity map imaging (VMI) and

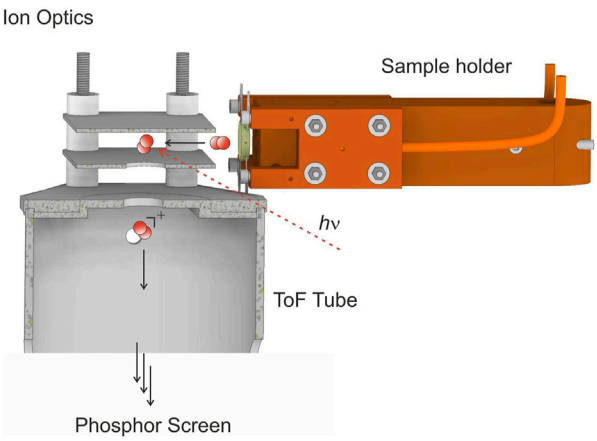

FIGURE 1
The surface temperature is linearly ramped by resistive heating. Recombinatively-desorbing molecules are ionized using non-resonant multi-photon ionization and coupled into the time-of-flight (ToF) tube by the ion optics of the velocity map imaging detector. Ions are detected on a phosphor screen at the end of the ToF tube (not shown). Velocities of desorbing molecules are deduced from the position at which the ions hit the phosphor screen.

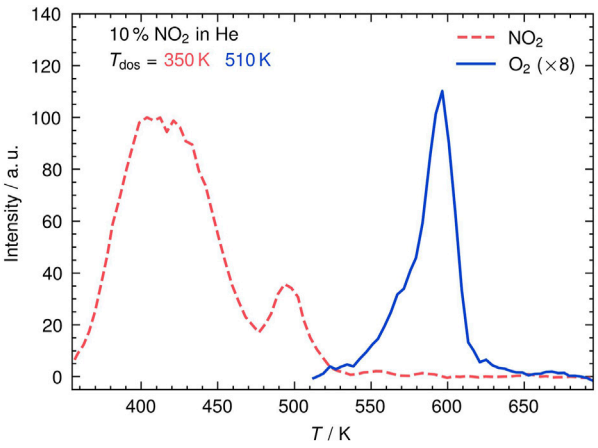

FIGURE 2
VMI-TPD spectrum of desorbing NO_2 (dashed) and recombinatively-desorbing O_2 (solid) after identical NO_2 exposure of an Ag (111) surface. The integrated flux density is plotted as a function of the temperature T; T_{dos} is the dosage temperature.

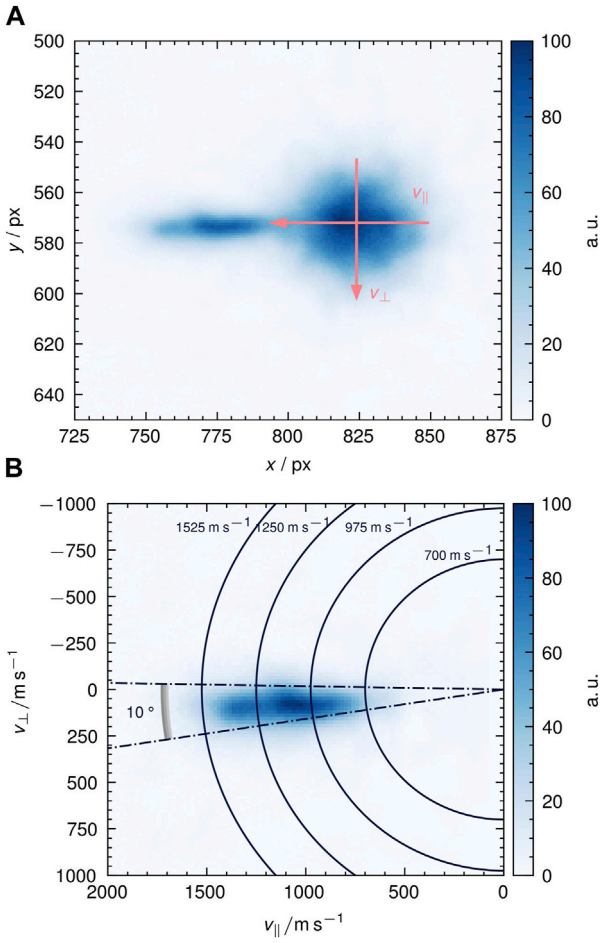

FIGURE 3
Velocity-map images of recombinatively-desorbing O_2 from Ag (111) around 600 K. $v_\perp$ and $v_\parallel$ are defined relative to the surface normal. **(A)** Raw velocity-map image with indicated thermal background. We use the thermal background for defining the point of zero velocities and to calibrate the detector. For that, we fit the room temperature thermal background with a 1-D Maxwell-Boltzmann distribution. The width of the distribution provides the calibration and the center provides zero velocity. One can clearly distinguish the hyperthermal velocities of surface desorbing oxygen and the background. **(B)** Velocity-mapped image after thermal background subtraction, v calibration, and density-to-flux conversion.

temperature-programmed desorption (TPD) experiments: we linearly heat up the surface while simultaneously detecting velocity map images of desorbing molecules. For that, the beam of a regeneratively amplified femtosecond laser (Spectra-Physics, Solstice Ace, <35 fs, 800 nm, 1 kHz) is focused by an optical lens (f = 300 mm) such that molecules are non-resonantly ionized after desorption. The ions are detected by an imaging setup which follows the design by Eppink and Parker (Eppink and Parker, 1997). Micro-channel plates (MCPs, Topag, MCP 56–15) are used for signal amplification and ions are imaged using a CMOS camera (Basler ace acA 1,920–155 µm, 1,920 px × 1,200 px) recording the images from a phosphor screen (Proxivision P43). Figure 1 shows the ionization region of the experimental setup.

Before each TPD experiment, the sample is exposed to the molecular beam at a defined dosage temperature. Afterwards, the surface is linearly heated at 4 K s^{-1} in a TPD experiment while we record images at 1 kHz laser repetition rate.

3 Results and discussion

For investigating velocity-resolved desorption of recombinatively-desorbing oxygen, we first create a complete monolayer of a p (4 × 4)-O phase on Ag (111) by dosing it with NO_2 from a molecular beam at T_{surf} = 350 K or 510 K for 2 min at a

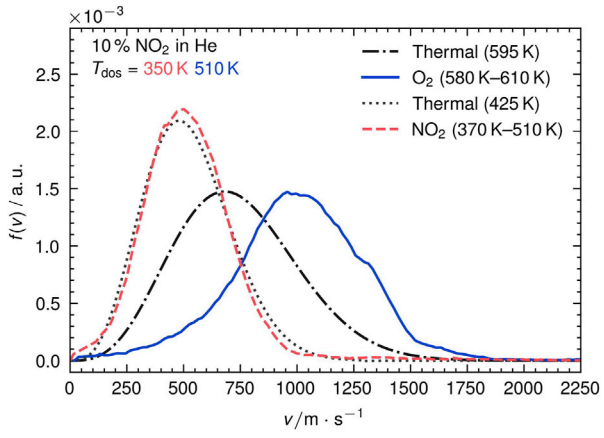

FIGURE 4
Plot of the experimental velocity distributions $f(v)$ for NO_2 and O_2 against the velocity v. For comparison, thermal distribution at the desorption peak's temperature are shown. All curves are normalized to an integral of one.

nozzle frequency of 200 Hz. We check the degree of oxidation by LEED and TPD (see Supplementary Material). Depending on the surface temperature during exposure, either nitrate (NO_3) or pure oxygen layers may form (Alemozafar and Madix, 2005). In Figure 2, we show TPD spectra of NO_2 and O_2 recorded with the VMI setup displayed in Figure 1. We record the total signal at the phosphor screen of the molecular mass of the parent ion by gating the phosphor screen to the respective time-of-flight. The VMI-TPD spectrum of NO_2 (dashed curve) shows two different desorption features after dosing at 350 K: first, a broad desorption peak ranging up to 470 K followed by a less broad, lower intensity desorption between 480 K and 510 K. These features are attributed to NO_3 decomposition into NO_2(g) and O from two different states (Alemozafar and Madix, 2005). In contrast, O_2 (solid curve) desorbs at significantly higher temperatures at T_{surf} of ≈590 K (Huang and White, 2003).

We use the VMI setup to determine velocity distributions for both, desorbing NO_2 and recombinatively-desorbing O_2. Figure 3A shows the raw image of O_2 desorption from Ag (111) around 590 K. We obtain the image by averaging all images that we record during a desorption peak in a TPD run. The raw image clearly displays the residual thermal gas background in the UHV chamber as circular spot as indicated in Figure 3A. From the background we deduce the point of zero velocity. We further calibrate the detector by fitting a one-dimensional Maxwell-Boltzmann distribution to the thermal background. Figure 3B shows the calibrated figure after subtraction of the thermal background and density-to-flux conversion (Harding et al., 2017). The velocity-mapped image shows a directed desorption feature with hyperthermal velocities between 500 m s^{-1} and 1,500 m s^{-1}. The angular tilt is due to a slightly tilted suspension of the crystal in the sample holder. From such images, we deduce velocity distributions by iterative integration over velocity increments within 10°-broad angular slices as shown in Figure 3B. In Figure 4, we show the results for the NO_2 peak at 425 K and the O_2 peak at 595 K. All curve integrals are

TABLE 1 Mean experimental velocities $\langle v \rangle$, energies $\langle E \rangle$, and the corresponding mean thermal velocities $\langle v_{th} \rangle$ for a desorption temperature $\langle T \rangle$ of desorbing NO_2 and recombinatively-desorbing O_2 from Ag (111).

Compound	$\langle T \rangle$/K	$\langle v \rangle$/m s^{-1}	$\langle v_{th} \rangle$/m s^{-1}	$\langle E \rangle$/eV
NO_2	425	530	520	0.0731
O_2	595	1,010	795	0.186

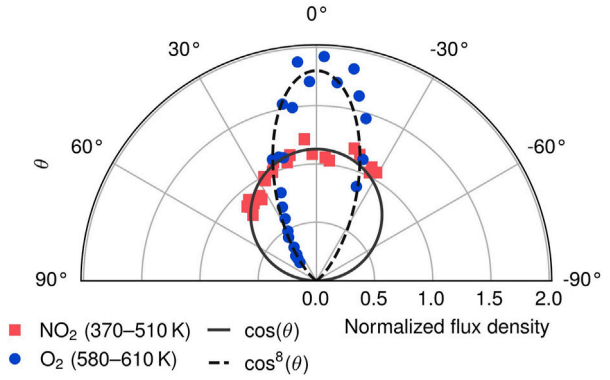

FIGURE 5
Polar plot of angular resolved flux for distinct TPD peaks for NO_2 (squares) and O_2 (circles) desorption from Ag (111) after NO_2 exposure. Thermal $\cos(\theta)$ (solid) and non-thermal $\cos^8(\theta)$ (dashed) distributions are shown for comparison. The integrals are normalized to one.

normalized to unity. For comparison, thermal flux-weighted Maxwell-Boltzmann distributions of the shape

$$f(v, T_{surf}) \propto v^3 \cdot \exp\left(-\frac{M \cdot v^2}{R \cdot T_{surf}}\right) \quad (1)$$

are plotted. M denotes the molar mass of the compounds and R is the universal gas constant. We use the signal-weighted temperature $\langle T \rangle$ of 425 K for NO_2 and 595 K for O_2 for T_{surf}.

From the figure it is obvious that O_2 desorbs with hyperthermal velocities indicated by a shift of the curve's maximum by more than 300 m s^{-1} compared to a flux-weighted thermal velocity distribution. In contrast, NO_2 desorption is clearly thermal as it can be well-reproduced by a flux-weighted Maxwell-Boltzmann distribution of the surface temperature. We did not observe any significant difference between the two desorption features of NO_3 decomposition (see Supplementary Material). Table 1 lists the characteristic properties of the shown velocity distributions.

Additionally, we record angular distributions of NO_2 and O_2 desorption from Ag (111). For that, we move the surface parellel to the detector such that only molecules from certain desorption angles are detected as described previously (Dorst et al., 2022). As VMI provides the direction of velocities in the detector plane, desorption angles are directly obtained from the ion images. Figure 5 shows a polar plot of the angular resolved flux for both, NO_2 (squares) and O_2 (circles) desorption. For comparison, a $\cos(\theta)$-distribution is shown, which would be expected for thermal desorption. We observe a narrow $\cos^8(\theta)$-angular distribution for O_2 desorption, whereas NO_2 desorption resembles the $\cos(\theta)$-distribution indicative of a thermalized (or equilibrium) desorption process.

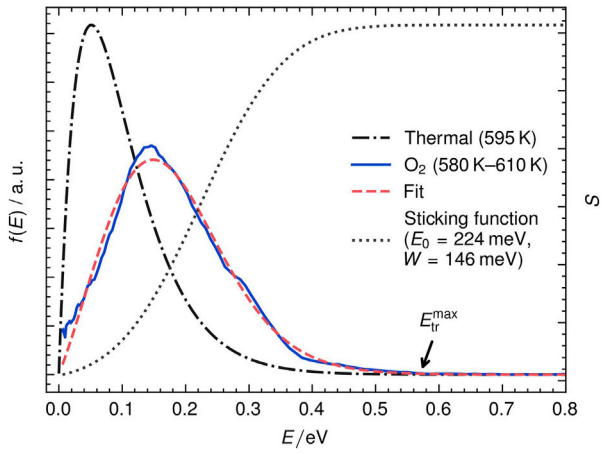

FIGURE 6
The translational energy distribution of recombinatively-desorbing O_2 (solid line) from Ag (111) can be modeled with the product (dashed) of a thermal energy distribution (dash-dotted) and a sticking function S (dotted). Highlighted is the maximum observed translational energy E_{tr}^{max}. E_0 is the energy barrier and W the width parameter in Eq. 3.

From the presented desorption dynamics, details of the underlying potential energy surface (PES) are obtained. The narrow angular distribution of O_2 desorption indicates an activated desorption process. Molecules have to overcome a barrier, on which they get accelerated into the gas phase. This is known to result in very peaked angular distributions (Comsa and David, 1985). In contrast, the release of NO_2 after surface nitrate decomposition appears with a broad angular distribution, indicating a non-activated thermalized desorption process.

Also, velocities of desorbing molecules provide valuable information about the underlying PES. Figure 6 shows the translational energy distribution of recombinatively-desorbing O_2 from Ag (111). The distributions are obtained from the velocity distributions displayed in Figure 4. The O_2 distribution is clearly shifted towards higher energies; NO_2 resembles a thermal distribution.

The shift of the hyperthermal O_2 energy distribution can be used to quantify energy-dependent sticking probabilities using the concepts of detailed balance (White and Beuhler, 2004). In an activated adsorption process, an energy barrier in the adsorption trajectory suppresses sticking at low incident translational energies. As a consequence, molecules with low translational energy are missing in translational energy distributions of desorption (Comsa and David, 1982; Michelsen and Auerbach, 1991; Shuai et al., 2017; Kaufmann et al., 2018). Following the principles of detailed balance, we can fit the hyperthermal distribution in Figure 6 using the product of a flux-weighted thermal energy distribution and a sticking function (see Eq. 2).

$$f(E_{tr}, T_{surf}) = K \cdot E_{tr} \cdot \exp\left(-\frac{E_{tr}}{k_B \cdot T_{surf}}\right) \cdot S(E_{tr}) \quad (2)$$

Here, K is a constant factor, E_{tr} is the translational energy of desorbing molecules, T_{surf} is the surface temperature and $S(E_{tr})$ is the sticking function. We apply an error function to describe sticking (see Eq. 3) as has been done in previous studies for activated adsorption processes and plot the sticking function in Figure 6 as dashed lines (Michelsen and Auerbach, 1991; Michelsen et al., 1992; Luntz, 2000).

$$S(E_{tr}) = \frac{1}{2}\left(1 + \mathrm{erf}\left(\frac{E_{tr} - E_0}{W}\right)\right) \quad (3)$$

W represents the width and E_0 represents the inflection point. We fit our data with a E_0 = 0.224 eV as shown in Figure 6. Not that the inflection point corresponds to the onset of adsorption and is related to the energy barrier height. This height is often strongly dependent on the adsorbate's rotational and vibrational state. State-resolved permeation studies on energy distributions of the H_2/Cu(111) system reveal for instance significant enhanced sticking probabilities for vibrationally excited molecules (Michelsen and Auerbach, 1991). However, in this work, we universally ionize desorption products without quantum state resolution. The translational energy distribution should therefore be considered as an averaged distribution of different states with unknown populations. We define also the maximum observable O_2 translational energy E_{tr}^{max} similar to the method developed by Fingerhut et al. (2021). In their work on formate decomposition on hydrogenated Pt (111), they identified E_{tr}^{max} as lower limit of the energy barrier in the entrance channel.

We indicate this threshold as black arrow in Figure 6 at ca. 0.57 eV (≈1850 m s^{-1}). For these fast molecules, we assume no internal energy and that the recoil against the surface from the transition state results only in minor Ag phonon excitation. This value should therefore be the lower limit to the real energy barrier height as we do not account for excitation of the solid.

Interestingly, these values are significantly lower than calculated sticking probabilities based on first principles theory (Goikoetxea et al., 2012; Kunisada and Sakaguchi, 2014). Kunisada and Sakaguchi calculate state-resolved sticking by performing quantum dynamics calculations of O_2 dissociative desorption on Ag (111) on a before computed PES (Kunisada et al., 2011). Depending on the adsorption site, they predict the onset of adsorption between 1.2 eV and 2.1 eV O_2 incident energy. They also calculate a significant influence of vibrational excitation on the dissociation probability by reducing the onset by ca. 30% when comparing O_2 ($v = 0$) to O_2 ($v = 3$). However, this reduction is still not sufficient to explain the discrepancy between the experimentally measured onset of this study of 0.57 eV and the minimum value of 0.8 eV (O_2 (v = 3) for a bridge site) of the theoretical work. We therefore suspect that we do not map a direct dissociation trajectory but desorption from another intermediate surface state under the experimental conditions applied in this study.

In a systematic molecular beam surface scattering approach, Kleyn et al. studied the interaction of O_2 molecular beams with Ag (111) at 150 K identifying several scattering pathways using ToF detection techniques (Raukema and Kleyn, 1995; Kleyn et al., 1996; Raukema et al., 1997). From the ToF of scattered O_2, translational energy distributions are obtained, which can be attributed to different surface states prior to desorption. In general, for the O_2/Ag (111) system, three adsorption states exist: a shallow physisorption well, a molecular chemisorption well, and a dissociative chemisorbed state (Campbell, 1985). At low incident translational energies, scattered oxygen exhibits low velocities, indicating desorption from the physisorbed state. At elevated incident energies, two significantly faster scattering channels are observed. The fastest channel depends on the incident energy indicating directly scattered O_2. In contrast, the other fast channel is independent on the incident energy, so that the

authors assign this pathway to transient trapping desorption from the molecular chemisorption potential energy well. Adsorption in this state is activated with a threshold mean energy of about 0.2 eV, and exhibits electron transfer from the surface to the adsorbate. The molecular chemisorption state can serve as precursor state for dissociative chemisorption (Kleyn et al., 1996). Recent calculations indicate an energy barrier of 0.8 eV between both states (Hinsch et al., 2021). The mean final energy of O_2 molecules originating from the molecular chemisorption state recorded by Kleyn et al. is 0.14 eV (Kleyn et al., 1996). It is close to 0.19 eV, which we measured in this study. The lower translational energy could be caused by the significant colder surface temperature of 150 K. This is indication that the desorption state, which we observe in TPD experiments at 590 K, is identical to the intermediate molecular chemisorption state observed in molecular beam surface scattering experiments.

4 Conclusion

We performed velocity resolved surface desorption experiments of recombinatively desorbing O_2 from Ag (111) by combining ion imaging techniques with temperature programmed desorption. Desorption occurs at 590 K, is clearly hyperthermal, and exhibits a narrow angular distribution indicating an activated desorption process. Velocity distributions are similar to previously reported distributions from molecular beam surface scattering experiments. For both studies, the energetics of desorbing molecules indicate desorption from an intermediate molecular chemisorption state. Recent theoretical papers calculate significantly higher barriers for oxygen sticking on Ag (111) than we deduce from the translational energy distribution (Kunisada and Sakaguchi, 2014). The here presented data will be a valuable experimental benchmark to refine theoretical models crucial for a better understanding of surface dynamics in metal oxidation processes.

Data availability statement

The raw data supporting the conclusion of this article will be made available by the authors, without undue reservation. It is available under GRO.data (https://data.goettingen-research-online.de/dataverse/hyperthermal_v_distr_desorbing_o2_ag111). Further inquiries can be directed to the corresponding author.

Author contributions

AD performed the experiments, data analysis and wrote a first paper draft. RD performed the experiments and analyzed the data. DS and SK contributed with experiments. AW contributed with discussion and the conception and design of the research. DK contributed with discussion and writing. TS conceptualized the experiment, analyzed the data and contributed with writing. All authors contributed to the article and approved the submitted version.

Funding

TS acknowledges support from the Deutsche Forschungsgemeinschaft (DFG) under grant SCHA 1946/5-1 and INST 186/1302-1 and support from the Deutscher Akademische Austauschdienst (DAAD) (Grant 57651434). RD acknowledges funding under a Georg Forster research fellowship from the Humboldt foundation. DK acknowledges support from the National Science Foundation through award CHE-2155068 and ICASEC at University of Göttingen.

Acknowledgments

The authors acknowledge support by Max Planck society for open access publishing.

Conflict of interest

The authors declare that the research was conducted in the absence of any commercial or financial relationships that could be construed as a potential conflict of interest.

Publisher's note

Supplementary material

The Supplementary Material for this article can be found online at: https://www.frontiersin.org/articles/10.3389/fchem.2023.1248456/full#supplementary-material

References

Alemozafar, A. R., and Madix, R. J. (2005). The adsorption of and reaction of NO_2 on Ag(111)-*p*(4×4)-O and formation of surface nitrate. *Surf. Sci.* 587, 193–204. doi:10.1016/j.susc.2005.05.019

Bao, X., Muhler, M., Schedel-Niedrig, T., and Schlögl, R. (1996). Interaction of oxygen with silver at high temperature and atmospheric pressure: A spectroscopic and structural analysis of a strongly bound surface species. *Phys. Rev. B* 54, 2249–2262. doi:10.1103/physrevb.54.2249

Bare, S. R., Griffiths, K., Lennard, W. N., and Tang, H. T. (1995). Generation of atomic oxygen on Ag(111) and Ag(110) using NO_2: A TPD, LEED, HREELS, XPS and NRA study. *Surf. Sci.* 342, 185–198. doi:10.1016/0039-6028(95)00670-2

Barker, J. A., and Auerbach, D. J. (1984). Gas-surface interactions and dynamics; thermal energy atomic and molecular beam studies. *Surf. Sci. Rep.* 4, 1–99. doi:10.1016/0167-5729(84)90005-0

Böcklein, S., Günther, S., and Wintterlin, J. (2013). High-pressure scanning tunneling microscopy of a silver surface during catalytic formation of ethylene oxide. *Angew. Chem. Int. Ed.* 52, 5518–5521. doi:10.1002/anie.201210209

Bukhtiyarov, V. I., Hävecker, M., Kaichev, V. V., Knop-Gericke, A., Mayer, R. W., and Schlögl, R. (2003). Atomic oxygen species on silver: Photoelectron spectroscopy and X-ray absorption studies. *Phys. Rev. B* 67, 235422. doi:10.1103/physrevb.67.235422

Campbell, C. T. (1985). Atomic and molecular oxygen adsorption on Ag(111). *Surf. Sci.* 157, 43–60. doi:10.1016/0039-6028(85)90634-x

Carlisle, C. I., Fujimoto, T., Sim, W. S., and King, D. A. (2000a). Atomic imaging of the transition between oxygen chemisorption and oxide film growth on Ag(111). *Surf. Sci.* 470, 15–31. doi:10.1016/s0039-6028(00)00831-1

Carlisle, C. I., King, D. A., Bocquet, M. L., Cerdá, J., and Sautet, P. (2000b). Imaging the surface and the interface atoms of an oxide film on Ag(111) by scanning tunneling microscopy: Experiment and theory. *Phys. Rev. Lett.* 84, 3899–3902. doi:10.1103/physrevlett.84.3899

Chadwick, H., and Beck, R. D. (2016). Quantum state resolved gas–surface reaction dynamics experiments: A tutorial review. *Chem. Soc. Rev.* 45, 3576–3594. doi:10.1039/c5cs00476d

Comsa, G., and David, R. (1985). Dynamical parameters of desorbing molecules. *Surf. Sci. Rep.* 5, 145–198. doi:10.1016/0167-5729(85)90009-3

Comsa, G., and David, R. (1982). The purely fast distribution of H_2 and D_2 molecules desorbing from Cu(100) and Cu(111) surfaces. *Surf. Sci.* 117, 77–84. doi:10.1016/0039-6028(82)90487-3

Derouin, J., Farber, R. G., Heslop, S. L., and Killelea, D. R. (2015). Formation of surface oxides and Ag_2O thin films with atomic oxygen on Ag(111). *Surf. Sci.* 641, L1–L4. doi:10.1016/j.susc.2015.07.003

Dorst, A. C., Güthoff, F., Schauermann, D., Wodtke, A. M., Killelea, D. R., and Schäfer, T. (2022). Velocity map images of desorbing oxygen from sub-surface states of Rh(111). *Phys. Chem. Chem. Phys.* 24, 26421–26427. doi:10.1039/d2cp03369k

Eppink, A. T. J. B., and Parker, D. H. (1997). Velocity map imaging of ions and electrons using electrostatic lenses: Application in photoelectron and photofragment ion imaging of molecular oxygen. *Rev. Sci. Instrum.* 68, 3477–3484. doi:10.1063/1.1148310

Fingerhut, J., Borodin, D., Schwarzer, M., Skoulatakis, G., Auerbach, D. J., Wodtke, A. M., et al. (2021). The barrier for CO_2 functionalization to formate on hydrogenated Pt. *J. Phys. Chem. A* 125, 7396–7405. doi:10.1021/acs.jpca.1c04833

Goikoetxea, I., Beltràn, J., Meyer, J., Juaristi, J. I., Alducin, M., and Reuter, K. (2012). Non-adiabatic effects during the dissociative adsorption of o2 at Ag(111)? A first-principles divide and conquer study. *New J. Phys.* 14, 013050. doi:10.1088/1367-2630/14/1/013050

Golibrzuch, K., Bartels, N., Auerbach, D. J., and Wodtke, A. M. (2015). The dynamics of molecular interactions and chemical reactions at metal surfaces: Testing the foundations of theory. *Annu. Rev. Phys. Chem.* 66, 399–425. doi:10.1146/annurev-physchem-040214-121958

Greeley, J., and Mavrikakis, M. (2007). On the role of subsurface oxygen and ethylenedioxy in ethylene epoxidation on silver. *J. Phys. Chem. C* 111, 7992–7999. doi:10.1021/jp070490i

Harding, D. J., Neugebohren, J., Hahn, H., Auerbach, D. J., Kitsopoulos, T. N., and Wodtke, A. M. (2017). Ion and velocity map imaging for surface dynamics and kinetics. *J. Chem. Phys.* 147, 013939. doi:10.1063/1.4983307

Hinsch, J. J., Liu, J., and Wang, Y. (2021). Reinvestigating oxygen adsorption on Ag(111) by using strongly constrained and appropriately normed semi-local density functional with the revised vydrov van voorhis van der waals force correction. *J. Chem. Phys.* 155, 234704. doi:10.1063/5.0073407

Huang, W. X., and White, J. M. (2003). Revisiting NO_2 on Ag(111): A detailed TPD and rairs study. *Surf. Sci.* 529, 455–470. doi:10.1016/s0039-6028(03)00332-7

Jones, T. E., Rocha, T. C. R., Knop-Gericke, A., Stampfl, C., Schlögl, R., and Piccinin, S. (2015a). Insights into the electronic structure of the oxygen species active in alkene epoxidation on silver. *ACS Catal.* 5, 5846–5850. doi:10.1021/acscatal.5b01543

Jones, T. E., Rocha, T. C. R., Knop-Gericke, A., Stampfl, C., Schlögl, R., and Piccinin, S. (2015b). Thermodynamic and spectroscopic properties of oxygen on silver under an oxygen atmosphere. *Phys. Chem. Chem. Phys.* 17, 9288–9312. doi:10.1039/c5cp00342c

Kaufmann, S., Shuai, Q., Auerbach, D. J., Schwarzer, D., and Wodtke, A. M. (2018). Associative desorption of hydrogen isotopologues from copper surfaces: Characterization of two reaction mechanisms. *J. Chem. Phys.* 148, 194703. doi:10.1063/1.5025666

Kleyn, A. W., Butler, D. A., and Raukema, A. (1996). Dynamics of the interaction of O_2 with silver surfaces. *Surf. Sci.* 363, 29–41. doi:10.1016/0039-6028(96)00089-1

Kleyn, A. W. (2003). Molecular beams and chemical dynamics at surfaces. *Chem. Soc. Rev.* 32, 87–95. doi:10.1039/b105760j

Kunisada, Y., Nakanishi, H., and Kasai, H. (2011). A first principles study of O_2/Ag(111) adsorption and magnetic properties. *J. Phys. Soc. Jpn.* 80, 084605. doi:10.1143/jpsj.80.084605

Kunisada, Y., and Sakaguchi, N. (2014). Two-dimensional quantum dynamics of O_2 dissociative adsorption on Ag(111). *RSC Adv.* 4, 63508–63512. doi:10.1039/c4ra12448k

Li, W. X., Stampfl, C., and Scheffler, M. (2003a). Subsurface oxygen and surface oxide formation at Ag(111): A density-functional theory investigation. *Phys. Rev. B* 67, 045408. doi:10.1103/physrevb.67.045408

Li, W. X., Stampfl, C., and Scheffler, M. (2003b). Why is a noble metal catalytically active? The role of the O-Ag interaction in the function of silver as an oxidation catalyst. *Phys. Rev. Lett.* 90, 256102. doi:10.1103/physrevlett.90.256102

Luntz, A. C. (2000). A simple model for associative desorption and dissociative chemisorption. *J. Chem. Phys.* 113, 6901–6905. doi:10.1063/1.1311280

Martin, N. M., Klacar, S., Grönbeck, H., Knudsen, J., Schnadt, J., Blomberg, S., et al. (2014). High-coverage oxygen-induced surface structures on Ag(111). *J. Phys. Chem. C* 118, 15324–15331. doi:10.1021/jp504387p

Michaelides, A., Bocquet, M. L., Sautet, P., Alavi, A., and King, D. A. (2003). Structures and thermodynamic phase transitions for oxygen and silver oxide phases on Ag(111). *Chem. Phys. Lett.* 367, 344–350. doi:10.1016/s0009-2614(02)01699-8

Michaelides, A., Reuter, K., and Scheffler, M. (2005). When seeing is not believing: Oxygen on Ag(111), a simple adsorption system? *J. Vac. Sci. Technol. A Vac. Surf. Films* 23, 1487–1497. doi:10.1116/1.2049302

Michelsen, H. A., and Auerbach, D. J. (1991). A critical examination of data on the dissociative adsorption and associative desorption of hydrogen at copper surfaces. *J. Chem. Phys.* 94, 7502–7520. doi:10.1063/1.460182

Michelsen, H. A., Rettner, C. T., and Auerbach, D. J. (1992). On the influence of surface temperature on adsorption and desorption in the D_2/Cu(111) system. *Surf. Sci.* 272, 65–72. doi:10.1016/0039-6028(92)91422-8

Park, G. B., Krüger, B. C., Meyer, S., Schwarzer, D., and Schäfer, T. (2016). The ν_6 fundamental frequency of the ã state of formaldehyde and coriolis perturbations in the $3\nu_4$ level. *J. Chem. Phys.* 144, 194308. doi:10.1063/1.4948635

Qian, M., Liauw, M. A., and Emig, G. (2003). Formaldehyde synthesis from methanol over silver catalysts. *Appl. Catal. A* 238, 211–222. doi:10.1016/s0926-860x(02)00340-x

Raukema, A., Butler, D. A., and Kleyn, A. W. (1997). O_2 transient trapping-desorption at the Ag(111) surface. *J. Chem. Phys.* 106, 2477–2491. doi:10.1063/1.473155

Raukema, A., and Kleyn, A. W. (1995). Transient trapping desorption of molecules at surfaces. *Phys. Rev. Lett.* 74, 4333–4336. doi:10.1103/physrevlett.74.4333

Reichelt, R., Günther, S., Wintterlin, J., Moritz, W., Aballe, L., and Mentes, T. O. (2007). Low energy electron diffraction and low energy electron microscopy microspot I/V analysis of the (4×4)O structure on Ag(111): Surface oxide or reconstruction? *J. Chem. Phys.* 127, 134706. doi:10.1063/1.2779028

Reuter, K. (2016). *Ab initio* thermodynamics and first-principles microkinetics for surface catalysis. *Catal. Lett.* 146, 541–563. doi:10.1007/s10562-015-1684-3

Rocha, T. C. R., Oestereich, A., Demidov, D. V., Hävecker, M., Zafeiratos, S., Weinberg, G., et al. (2012). The silver-Oxygen system in catalysis: New insights by near ambient pressure x-ray photoelectron spectroscopy. *Phys. Chem. Chem. Phys.* 14, 4554. doi:10.1039/c2cp22472k

Schnadt, J., Michaelides, A., Knudsen, J., Vang, R. T., Reuter, K., Lægsgaard, E., et al. (2006). Revisiting the structure of the $p(4\times 4)$ surface oxide on Ag(111). *Phys. Rev. Lett.* 96, 146101. doi:10.1103/physrevlett.96.146101

Serafin, J. G., Liu, A. C., and Seyedmonir, S. R. (1998). Surface science and the silver-catalyzed epoxidation of ethylene: An industrial perspective. *J. Mol. Catal. A Chem.* 131, 157–168. doi:10.1016/s1381-1169(97)00263-x

Shen, Q., Wu, J., Zhou, F., Song, Y., Dong, W., Wang, X., et al. (2022). A molecular beam-surface apparatus for quantum state-resolved adsorption studies. *Rev. Sci. Instrum.* 93, 013201. doi:10.1063/5.0049178

Shuai, Q., Kaufmann, S., Auerbach, D. J., Schwarzer, D., and Wodtke, A. M. (2017). Evidence for electron-hole pair excitation in the associative desorption of H_2 and D_2 from Au(111). *J. Phys. Chem. Lett.* 8, 1657–1663. doi:10.1021/acs.jpclett.7b00265

Sitz, G. O. (2002). Gas surface interactions studied with state-prepared molecules. *Rep. Prog. Phys.* 65, 1165–1193. doi:10.1088/0034-4885/65/8/202

Vattuone, L., and Okada, M. (2020). "State resolved sticking probability in gas-surface interaction," in *Springer handbook of surface science*. Editors M. Rocca, T. S. Rahman, and L. Vattuone (Cham: Springer), 1053–1084.

Westphal, G., Wallrabe, M., and Schäfer, T. (2020). Unravelling reaction products of styrene oxide adsorbed on ag(111) using rempi-assisted temperature-programmed desorption. *J. Phys. Chem. C* 124, 799–804. doi:10.1021/acs.jpcc.9b10358

White, M. G., and Beuhler, R. J. (2004). State-resolved dynamics of oxygen atom recombination on polycrystalline Ag. *J. Chem. Phys.* 120, 2445–2455. doi:10.1063/1.1637333

Xu, Y., Greeley, J., and Mavrikakis, M. (2005). Effect of subsurface oxygen on the reactivity of the Ag(111) surface. *J. Am. Chem. Soc.* 127, 12823–12827. doi:10.1021/ja043727m

frontiers | Frontiers in Chemistry

TYPE Original Research
PUBLISHED 24 August 2023
DOI 10.3389/fchem.2023.1250711

OPEN ACCESS

EDITED BY
Helen Chadwick,
Swansea University, United Kingdom

REVIEWED BY
Li Chen,
Chinese Academy of Sciences (CAS), China
Arthur Utz,
Tufts University, United States

*CORRESPONDENCE
Ludo B. F. Juurlink,
l.juurlink@chem.leidenuniv.nl

RECEIVED 30 June 2023
ACCEPTED 10 August 2023
PUBLISHED 24 August 2023

CITATION
Jansen C and Juurlink LBF (2023), State-resolved studies of CO_2 sticking to CO_2 ice.
Front. Chem. 11:1250711.
doi: 10.3389/fchem.2023.1250711

State-resolved studies of CO_2 sticking to CO_2 ice

Charlotte Jansen and Ludo B. F. Juurlink*

Leiden Institute of Chemistry, Leiden University, Leiden, Netherlands

Internal vibrations may affect the adsorption, scattering, and reactions of molecules impinging onto a surface. The energy of the ν_3 antisymmetric stretch vibration of CO_2 slightly exceeds the desorption energy of CO_2 bound to CO_2 ice. We use supersonic molecular beam techniques and rovibrationally state-resolved excitation to determine whether this vibration affects condensation of gas phase CO_2 to its ice. We detect sticking and CO_2 ice formation using RAIRS and quantify the sticking probability using the King and Wells method with modulation of the vibrational excitation and Fourier transform based detection. We find that the influence of this vibration on the structure of the formed ice and on the sticking probability is negligible under our conditions. Based on our detection limit, we quantify the weighted average sticking probability at approximately 0.9 and the difference between the state-resolved and weighted average sticking probability as below 0.5%.

KEYWORDS

CO_2, nu3, state resolved, molecular beam, condensation

1 Introduction

Collisions of CO_2 with surfaces are of interest to a broad range of scientific fields. In astronomy and astrochemistry, CO_2 occurs, a. o., in the interstellar medium (ISM) (d'Hendecourt and Jourdain de Muizon, 1989), both in gaseous and ice phases (Van Dishoeck, 2004), and in comets (Despois et al., 2005). In the chemical industry, CO_2 is a major reactant in the Cu/ZnO-based catalytic production of methanol (Rostrup-Nielsen, 1984). Collisions of CO_2 with surfaces are generally not reactive in a direct sense (Burghaus, 2014). Molecular sticking to a surface likely precedes subsequent chemical processes, especially at low-temperature conditions, such as those prevalent in interstellar space.

Molecular vibrations may affect the adsorption, desorption, and reactions of molecules to surfaces. Sibener and Lee (Sibener and Lee, 1994) found that internal vibrations of SF_6 and CCl_4 had a significant impact on the adsorption and reflection of these gas-phase molecules onto their bulk solids at low collision energies. In precursor-mediated reaction of CH_4 on Ir (111) (Dombrowski et al., 2015) and SiH_4 on Si(100) (Bisson et al., 2008), internal vibrations were found to enhance dissociative adsorption. A study of NO's trapping probability on Au (111) found, on the contrary, no effect of vibrational excitation (Wodtke et al., 2005).

For CO_2, a study by Weida et al. (Weida et al., 1996) investigated CO_2 desorption from crystalline CO_2 ice at varying temperatures, hence varying desorption rates, using state-selected detection. They found no evidence of an effect on the desorption by the molecules' vibrations, rotations and even orientations. From detailed balance, they argued that if there is no preference for a certain quantum state for desorption, neither will there be for the process of adsorption. However, due to the limitations of their methods, only the ν_2 bend vibration in CO_2 was studied. Its vibrational energy (667 cm^{-1} or 8.0 kJ/mol) is well below the desorption barrier, the sublimation energy being approximately 26 kJ/mol. The ν_3 fundamental

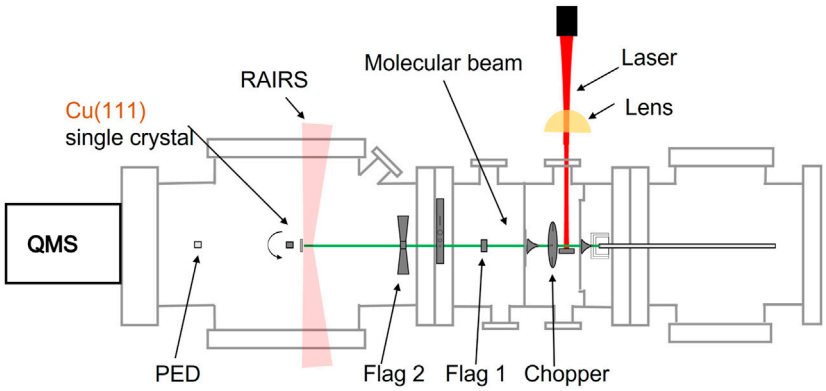

FIGURE 1
Schematic representation of the apparatus, consisting of 4 connected and differentially pumped vacuum chambers through which a molecular beam travel from right to left, the light from an excitation laser (red) and lens (yellow), a fast chopper wheel, a Cu(111) single crystal held on an x, y, z, θ manipulator in the UHV chamber of the system, a room temperature bolometer (PED), two quadrupole mass spectrometers (QMS), and RAIRS capability.

vibrational mode (2,349 cm^{-1} or 28.1 kJ/mol) slightly exceeds the latter. A more recent study by Ioppolo et al. (Ioppolo et al., 2022) found restructuring and minor desorption of amorphous CO_2 ice after irradiation with resonant IR light (ν_2 and ν_3). For crystalline ice, they found no restructuring, but possible desorption. Their results were inconclusive on vibrational effects to desorption.

Here, we study the effect of vibrational excitation (ν_3) on the adsorption of CO_2 onto CO_2 ice grown on a Cu(111) surface at 80 K. We excite the ν_3 asymmetric stretch of CO_2 molecules in a molecular beam with light from a tunable continuous wave (cw)-infrared (IR) laser. We look for any changes in the sticking probability of the CO_2 by modulating the excitation and using a Fourier transform based detection scheme. An effect of vibrational excitation on either the adsorption or the desorption rate will change the effective sticking probability. We also monitor the surface with Reflection Absorption IR Spectroscopy (RAIRS) and look for any structural differences in the spectra of the resulting CO_2 ice layer with and without the additional vibrational excitation. At 80 K, the ice will be crystalline. Ioppolo et al. found no restructuring after IR irradiation of crystalline CO_2 ice. However, our situation may be different, as they irradiated the CO_2 ice after deposition, while we resonantly excite vibrations in the gaseous CO_2 molecules prior to adsorption.

2 Experimental

Our experiments are performed using a home-built ultra-high vacuum (UHV) system, that has been used for non-state-resolved reaction dynamics measurements before (Cao et al., 2018; van Lent et al., 2019; Jansen and Juurlink, 2021). It consists of an analysis chamber with a base pressure of 2×10^{-10} mbar and a series of differentially pumped chambers for creation of a molecular beam. Figure 1 schematically illustrates the apparatus. The molecular beam is shaped by various skimmers that separate differential pumping stages and doses CO_2 onto a Cu (111) single crystal in the UHV chamber.

The molecular beam is created by expanding high-purity CO_2 (Linde Gas, purity 5.3) at 300 K. A flow controller feeds the gas at 4 bar into a vacuum chamber ($< 1 \times 10^{-3}$ mbar) through a 28 μm circular orifice in a tungsten nozzle. Two skimmers and a third orifice select only the center part of the expansion, resulting in a molecular beam with an angular spread of less than 1°. During the expansion, kinetic and rotational energies are converted to translational energy along the beam axis, resulting in an average beam velocity of approximately 587 m/s as determined by time-of-flight (TOF) spectrometry (see Supplementary Material S1). The rotational temperature within the beam is cooled to approximately 26 K [see ref (Jansen et al., 2023)].

The molecular beam travels from the source chamber through two differentially pumped vacuum chambers and finally enters the UHV analysis chamber. In the first of these two chambers, a high-speed chopper wheel allows us to create short gas pulses from the continuous gas expansion for TOF spectrometry. The wheel can be stopped in the 'open' position. In the second of these chambers, a beam stopper can block the beam from hitting a sliding beam valve that separates this chamber from the UHV analysis chamber. The sliding beam valve contains various openings and controls the size and shape of the beam impinging onto the sample, a room temperature bolometer (pyro-electric detector, PED)) and the ionizer of the QMS used for TOF measurements.

On the beam axis in the analysis chamber, the edge of a disc can be rotated by an UHV-compatible stepper motor. The disc's edge is manufactured to have two identical 'open' and two 'closed' sections, each of 90°. The closed sections have a slanted edge as not to reflect the molecular beam back into the last of the differentially pumped chambers. Combined with the beam stopper in the differential stage, this disc allows us to accurately perform King and Wells-type sticking probability measurements (King and Wells, 1972), but using a modulation technique as described below. We will refer to the beam blocker and the disc as the two beam flags from here onward.

The Cu single crystal is suspended from a copper block at the end of a vertical 'cold finger', i.e., a hollow tube protruding through an x, y, z, θ manipulator. The crystal is cooled by pouring liquid nitrogen (LN2) into the tube. It is kept at a constant temperature of 80 ± 1 K during experiments, as measured by a K-type thermocouple

laser welded to the crystal's edge. Adsorption of CO_2 onto the sample is monitored using an FTIR (Bruker Vertex 70) with an external LN2-cooled MCT detector to perform RAIRS during the experiments. The IR beam paths outside of the UHV chamber, including internal parts of the FTIR, are purged continuously with gaseous dry N_2 from an in-house system fueled by the exhaust from the local NMR facility.

The CO_2 ν_3 antisymmetric stretch vibration is excited in the molecular beam with laser light from an OPO (Argos model 2,400, module D), which we will from now on simply refer to as the laser. Its output can be tuned and is stabilized on a CO_2 absorption frequency using the lamb dip measured in a reference cell. The laser light crosses the molecular beam a few cm after the initial expansion in the apparatus and 37 cm before molecules hit the Cu crystal. For this experiment, we tune the laser to the R (4) transition at 4,249.99 nm, where CO_2 molecules are excited from the $v = 0$, $J = 4$ state to the $v = 1$, $J = 5$ state. This transition was chosen because $J = 4$ has the highest population at the rotational temperature of the molecular beam [see (Jansen et al., 2023)]. A cylindrical lens in the path of the laser is used to achieve rapid adiabatic passage (Jansen et al., 2023; Chadwick et al., 2014), resulting in nearly full (80%) population inversion. Considering the fractional population of the ground rotational state and the level of saturation, we excite approximately 15% of the CO_2 molecules in the molecular beam. Herein, we neglect the fraction of vibrationally excited states nascent to the molecular beam. A moveable room-temperature bolometer (pyro-electric detector, Eltec model 406) in the UHV chamber is used to quantify IR power absorption by CO_2 molecules on the molecular beam axis. All laser beam paths outside of the UHV chamber, including the entire OPO and optical components required for frequency detection and stabilization, are enclosed and purged continuously by dry gaseous N_2. The > 400 ppm concentration of CO_2 in air otherwise destabilizes the OPO and results in large power losses through absorption in the 1–2 m beam path between the laser and the UHV chamber.

At the start of an experiment, the Cu crystal is flashed to 300 K to remove any buildup of CO_2, CO and H_2O. As we do not regularly perform extensive sputtering and annealing cycles for these experiments, the surface should not be considered an atomically clean Cu(111) surface. It is most likely partially oxidized, as studied previously (Zhang et al., 2023). When the crystal has cooled to 80 K, a RAIRS background spectrum is taken. Subsequently, the surface is continuously monitored with RAIRS while CO_2 is dosed from the molecular beam. The CO_2 flux is estimated to be 0.15 ML/s as referenced to the Cu atom surface density for Cu(111). The experiment is repeated multiple times with the laser tuned to the CO_2 excitation frequency and several times tuned to a non-resonant frequency as a control experiment. Between each experiment, the crystal is flashed to 300 K.

As described below, attempts to obtain information on the effective state-resolved sticking probability of CO_2 by analyzing IR peak integrals was unsuccessful. The integrals increase with the CO_2 dose time but did not allow us to detect variations in 'laser on' and' laser off' experiments. Hence, we measure the sticking probability of CO_2 onto CO_2 ice at 80 K with a modulated version of the King and Wells method (King and Wells, 1972) and a quadrupole mass spectrometer (QMS, Pfeiffer QMA 200) tuned to m/z 44.

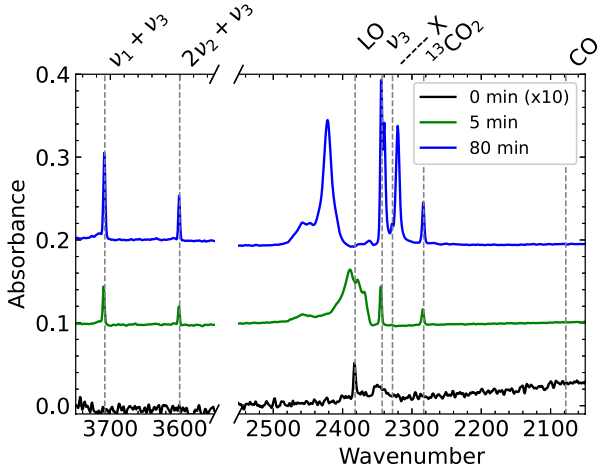

FIGURE 2
RAIR spectra after dosing CO_2 from a pure CO_2 molecular beam for 0–3 mintues (black), 5 min (green) and 80 min (blue). The 0 min spectrum is scaled by a factor of 10. At the start of dosing, only the Longitudinal Optical mode and one absorbance at 2,350 cm^{-1} appear. We assign the peak at 2,350 cm^{-1} to CO_2 directly physisorbed on the Cu(111) surface. The known peaks for CO_2 ice from literature are clearly visible in the 5 and 80 min spectra. Note that the apparent absorbance at 2,320 cm^{-1} in the blue spectrum is an artifact discussed in more detail in the Supplementary Information.

A sticking probability experiment starts with a CO_2 ice being prepared by continuously dosing CO_2 onto the Cu crystal while being monitored with RAIRS. When the RAIRS spectrum shows sufficient intensity of the CO_2 absorption line, the King & Wells experiment is started by closing both molecular beam flags. The first flag is reopened and the beam enters the UHV chamber, but is blocked by the second flag. This causes a rise in the CO_2 partial pressure in the vacuum chamber, which is continuously monitored with the QMS. When the second flag is reopened, the beam impinges again onto the CO_2 ice. The fraction of CO_2 molecules that is adsorbed on the surface is removed from the background pressure in the chamber, resulting in a drop in the total pressure. The effective sticking probability is the ratio of the pressure drop after the beam impinges onto the ice and the pressure rise when the beam enters the chamber.

Note that the rate of desorption of CO_2 at 80 K from the CO_2 ice film is not affected by the molecular beam impinging onto the sample as the ice is many layers thick. The contribution of CO_2 evaporation from the film to the background pressure is unaltered when the beam hits the sample. Hence, our measurement solely detects if the effective sticking coefficient, i.e., the net condensation of CO_2 molecules onto the ice from the impinging beam, depends on the vibrational state population of that beam. It is only the latter that we alter by turning the laser 'on' and 'off'. In the laser 'on' case, the heavily populated vibrationally excited state may adsorb or scatter more effectively in a direct sense than the vibrational ground state does. In case a vibrationally excited molecule adsorbs, it may also desorb again on a time scale much shorter than the experiment by V → T energy transfer. As adsorption is not activated, but desorption is, it is very unlikely that vibrational effects to both processes would be identical and cancel in an experiment that probes the effective sticking coefficient.

TABLE 1 Several peaks in the RAIRS spectrum associated with CO_2 ice, as found in literature.

Wavenumber	Explanation and references
2,078	CO on Cu(111) (not present) Hollins and Pritchard, (1979); Zhang et al. (2022)
2,283	ν_3 for $^{13}CO_2$ Sandford and Allamandola, (1990)
2,328	X, Amorphous CO_2 ice Escribano et al. (2013); Falk, (1987)
2,343	ν_3 Escribano et al. (2013); Sandford and Allamandola, (1990); Falk, (1987)
2,382	Longitudinal Optical mode Escribano et al. (2013); Baratta and Palumbo, (1998)
2,360–2,385	Multilayers, ν_3 coupled to lattice vibrations Ioppolo et al.(2022); Pachecka et al. (2017)
2,385–2,420	Fano line shape Koitaya et al. (2016)
3,601	$2\nu_2 + \nu_3$ Sandford and Allamandola, (1990)
3,708	$\nu_1 + \nu_3$ Sandford and Allamandola, (1990)

During the experiment, the laser is continuously modulated at 3 Hz. The measured partial pressure is directly related to the fraction of the molecular beam that is adsorbed. Therefore, we expect any effect of the vibrational excitation on the sticking probability to be visible in the measured partial pressure at the same modulation frequency. Inspection of the Fourier transform of the measured partial pressure allows us to quantify any effect of the vibrational excitation.

3 Results and discussion

3.1 RAIR spectra of CO_2 ice

We first study the RAIR spectra of the first few layers of physisorbed CO_2 on the Cu(111) surface. Figure 2 shows three spectra zoomed in on the regions of interest. Outside of these regions, the spectrum shows no features, except for a large set of water absorbances due to the formation of ice on the detector. After dosing for 0–3 min (the time it takes to complete the RAIRS measurement), only two very small peaks are visible, one around 2,350 cm^{-1} and the Longitudinal Optical mode. We assign this peak at 2,350 cm^{-1} to the CO_2 physisorbed directly on the (uncleaned) Cu(111) surface, as it is the first peak to appear and it becomes masked after dosing many layers of CO_2. A much narrower and redshifted peak appears in the spectrum taken after dosing for 5 min. This ν_3 CO_2 ice absorbance and the other absorbances are listed and assigned in Table 1). These peaks continue growing and changing throughout the exposure to the molecular beam. The absorbance of surface-bound CO at 2078 cm^{-1} for (oxidized) Cu(111) (Zhang et al., 2022), that could indicate dissociative CO_2 adsorption or CO contamination from the background, is absent. Due to the water condensation on the detector, we cannot quantify water contamination in the ice with RAIRS. However, in previous Temperature Programmed Desorption (TPD) experiments, we studied CO and H_2O desorption and found that water contamination was even less than CO contamination on the sample's surface. The absorbance suddenly appearing in the final spectrum (blue) at 2,320 cm^{-1} is an artifact. See the Supplementary Information for more detail.

We hypothesize that vibrational excitation of CO_2 prior to impinging onto the surface may have two effects. Firstly, as discussed before, it may affect the effective sticking probability of CO_2. Secondly, it may affect the structure of the resulting CO_2 ice. The ice is known to grow both in amorphous and crystalline phases (Falk, 1987). Dissipation of vibrational energy during the collision or after trapping may locally affect the ice's growth mode. The introduction of defects would lower the crystallinity of the ice. We investigate our results for clues to either effect.

We examine the integrals of two peaks in the spectra as a function of time to address a possible influence on the effective sticking probability. We use the peaks at 2,383 cm^{-1} ($^{13}CO_2$) and 3,708 cm^{-1} ($\nu_1 + \nu_3$). These are sharp, isolated peaks that can be integrated accurately and identify two different subsets of molecules. The former is an isotopologue and cannot have been affected by laser excitation. The latter does results from $^{12}CO_2$ and may have been affected. Figure 3A shows the integrals for four different experiments performed consecutively. Two of the experiments had the laser tuned to the resonance frequency (red circles), and two experiments had it tuned to a non-resonant frequency (blue squares). The legend (and the lightness of the colors) shows the order in which the measurements were performed. The data show, in general, very similar growth rates. For both absorbances, the earliest experiment lags slightly in comparison to the subsequent measurements. As it happens for both absorbances (one potentially affected by laser excitation and the other surely not), it is most likely the result of small changes in the crystal surface, e.g., cleanliness affecting binding, hence the relative adsorption and desorption rates (see Supplementary Material S1). We do not expect the background pressure of CO_2 in the vacuum chamber to contribute to the ice growth significantly, as the flux of the molecular beam is approximately two orders of magnitude larger than the background flux. Regardless of the (dominant) origin, the variation in time-dependent absorbance is, apparently, significant in comparison to any potential effect of vibrational excitation on the net sticking.

To address a potential effect of vibrational excitation on the grown CO_2 ice structure, we study the shape and position of the peaks in the RAIR spectra. Figure 3B shows the spectrum between 2,320 and 2,440 cm^{-1} for the four measurements at three points in time. The visible features here are the peak of CO_2 on Cu(111) at 2,350 cm^{-1}, the ν_3 ice peak at 2,343 cm^{-1}, the broad peaks at 2,360–2,385 cm^{-1} and the fano line shape at 2,385–2,420 cm^{-1}. As expected from the previous discussion, we find minor variations in peak height between the different measurements. When looking for any spectral change, such

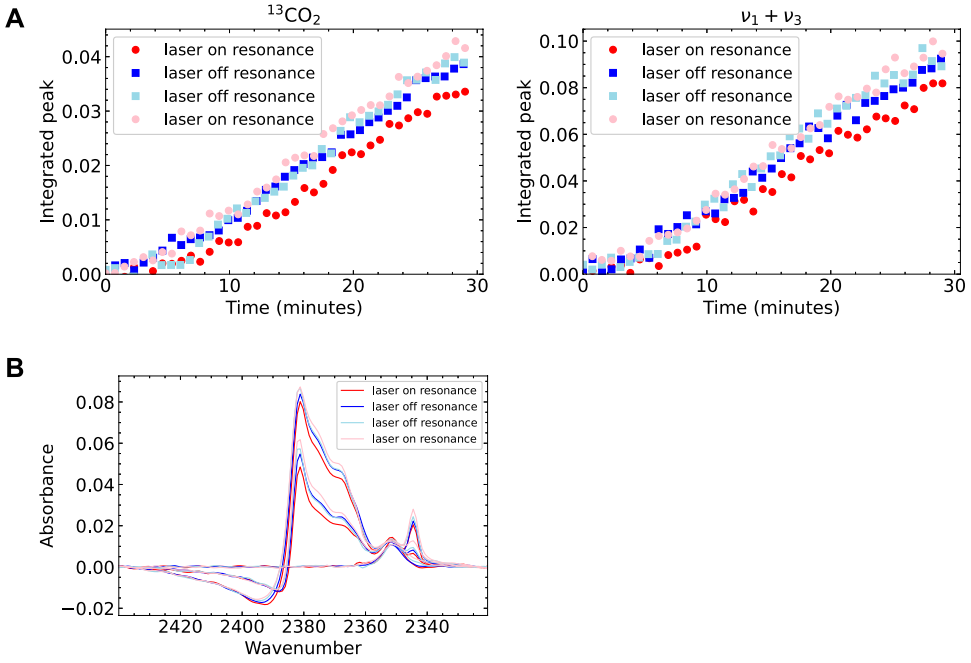

FIGURE 3
Analyzed RAIRS data for four experiments, of which two had the laser tuned to the CO_2 resonance frequency. On resonance shown in red (circles), off resonance shown in blue (squares). The experiments were performed in the order as shown in the legend **(A)** Integrals of two peaks in the CO_2 RAIR spectrum as a function of dosing time **(B)** The large peak in the RAIR spectrum for 3 different points in time during dosing. Note that there is some variation between the measurements which can be seen in both the integral plots and the spectrum plot. The peak growth is slower for the experiments performed later. However, there is no obvious difference between laser on or off resonance. In the bottom figure several features can be seen in the peak. These also seem to be the same for laser on and off resonance, suggesting there is no difference in CO_2 structure.

as a peak or shoulder that is only present in the data sets where the laser was on resonance, or a shifted peak position, we do not find any such differences. We also looked at changes in the other absorbances outside of the displayed wavenumber range also show no differences between laser 'on' and 'off' experiments. We conclude that vibrational excitation of the incident molecule does not measurably affect the ice's IR absorbances, hence the crystallinity of growth at 80 K, nor does the ν_3 vibrational excitation affect the rate of CO_2 ice growth on the Cu(111) surface significantly.

3.2 Sticking probability of CO_2 on CO_2 ice

Figure 4A shows an example of a King & Wells experiment for CO_2 adsorption on CO_2 ice at 80 K after the beam has been on for more than 1 hour. The results are normalized to the partial pressure of the incoming molecular beam, as this pressure change corresponds to a sticking probability of 1. If all molecules from the beam are adsorbed, the partial pressure would be the same as when the beam does not enter the vacuum chamber at all. CO_2 sticking occurs when the second flag is opened, which is approximately between 35 and 110 s. We use the ratios of the first pressure drop and the initial pressure rise and the second pressure rise and final pressure drop to calculate the overall sticking probability, shown in Figure 4A as the light blue areas. We find values over 0.9. Obtaining absolute values is complicated by the varying effective pumping speed for CO_2 as evident from the curvature in the time-dependence after opening and closing flags. The effective pumping speed varies as a consequence of the changing CO_2 partial pressure in the UHV chamber and the cold finger acting as a cyrogenic pump, similar to earlier studies performed on NO sticking (Berenbak et al., 1998). However, in this work we are mainly interested in changes in sticking due to vibrational excitation, which happens fast (at 3 Hz), so we expect no interference of the slowly changing background. Additionally, the effective pumping speed changes slightly when flag 2 is opened or closed, as the molecular beam is scattered from a different location in the vacuum chamber. This may also affect the effective pumping speeds of the turbomolecular pumps and the cryostat, and, hence cause a change in background pressure. During the laser on/off experiment, however, flag 2 is not opened or closed and the data cannot be affected by this potential influence. Figure 4B zooms in on a single second of a King & Wells measurement and the laser modulatation signal at 3 Hz, which is measured simultaneously to verify the modulation frequency. On this time scale, there is no clear switching between two different sticking probabilities.

We calculate the Fast Fourier Transform (FFT) of both the measured partial pressure and the laser modulation signal. The data is not always measured at regular intervals. Since the FFT calculation requires a regular sampling rate, we first interpolate the data to a sampling rate of 100 Hz. The absolute values of the FFT are normalized such that they reflect the quantity of interest: for the laser modulation data, this is the amplitude of the measured square

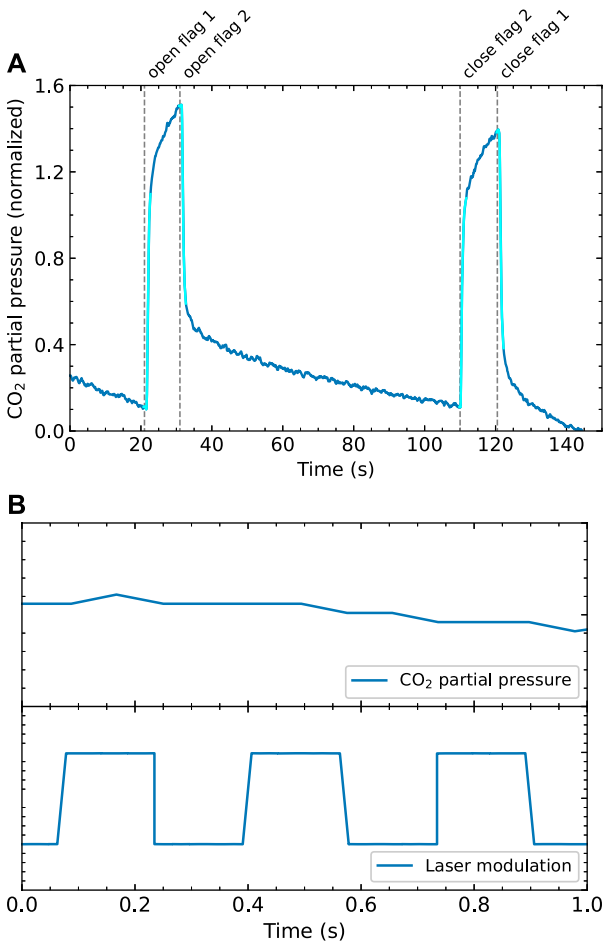

FIGURE 4
(A) An example of a King&Wells experiment of CO_2 on CO_2 ice. The signal is normalized to the pressure difference caused by the molecular beam (corresponding to a sticking probability of 1). CO_2 sticking occurs approximately between 35 and 110 s **(B)** Zoomed in plot of a K&W experiment with the laser modulated at 3 Hz, which shows the measured partial pressure (top) and measured laser modulation (bottom) during 1 s.

wave (which is normalized to 1). For the partial pressure data, it is the amplitude of the square wave normalized to reflect the change in sticking probability. This means that a peak in the sticking probability FFT spectrum with an integral of 1 would correspond to a change in sticking probability of 1 due to laser excitation, or an integral of 0.05 of the peak would correspond to a change in sticking probability of 0.05, *etc.* The results are shown in Figure 5. In the laser modulation FFT spectrum, the peak at 3 Hz is clearly visible, as expected. However, in the FFT spectrum of the sticking probability, it is unclear if there is a peak at 3 Hz. If it is there, it is not clearly distinguishable from the surrounding noise. This implies that if there is any effect of the vibrational excitation on the effective sticking probability, it is below our detection limit.

We can quantify this detection limit to calculate an upper limit for the effect of vibrational excitation of the sticking probability. Due to the finite (and slightly irregular) sampling rate of the measurement, the peak in the FFT spectrum is broadened. Therefore we take the integral of the peak between 2.998 and 3.002 Hz, which is shown as a filled gray area in Figure 5B. For the sticking probability FFT, the peak (if there is any) is not visible, so we have to make some assumptions to calculate its integral. We assume the peak shape is the same as for the laser modulation FFT, because we expect the modulation in the sticking probability to have the same square wave shape as the laser modulation data. We also assume that the value of the FFT at 3.00 Hz is the maximum of this peak. The resulting peak is shown as a gray area in Figure 5A. The integral of the peak, which corresponds to our detection limit for the sticking probability, is calculated to be 6×10^{-4} whereas the sticking probability itself is near unity.

The detection limit is the minimum change in sticking probability that we can detect. This does not correspond directly to the minimum effect of vibrational excitation as not all CO_2 in the beam is vibrationally excited by our laser. Its linewidth allows only excitation of molecules from a particular initial rotational state, and only a fraction of all CO_2 in the molecular beam is in that initial rotational state. Furthermore, due to limited laser power, less than 100% of the CO_2 in a particular initial state is excited, even when using rapid adiabatic passage. Finally, spontaneous emission during the 37 cm flight path to the sample after excitation region, also lowers the vibrationally excited fraction of the molecular beam. We have determined the rotational state distribution of the molecular beam and the excited population of the R (4) transition. The methods and results are described elsewhere (Jansen et al., 2023). There, we find that approximately 20% of the CO_2 molecules are initially in the $J = 4$ state and approximately 80% of these are excited during the experiment. Based on the natural life time 2.4 ms (Gordon et al., 2022) and average velocity of 587 m/s, as determined by TOF, approximately 30% of the excited population is lost via spontaneous emission. Applying these corrections to our detection limit, we find that the upper limit for the change in the CO_2 sticking probability on CO_2 ice due to the asymmetric stretch vibration is approximately 5×10^{-3}.

In comparison to the earlier study on the condensation of CCl_4 and SF_6 onto their ices by Sibener & Lee (Sibener and Lee, 1994) our results are somewhat surprising. Although their study was not state-resolved, using different oven temperatures to create a molecular beam in combination with a velocity selector, they convincingly showed that, at low translational energy, molecular sticking is inhibited by the excitation of internal modes. This inhibiting effect was argued to result from (V, R) → T energy transfer. The velocity dependence of this effect, however, also showed that the inhibition decreased with increasing kinetic energy. This was argued to result from a loss of relevance when kinetic energy is too high to be accommodated in the collision for trapping and thermalization to occur. At similar speeds for our experiments and theirs (exceeding 500 m/s), the influence of internal energy on condensation was lost. Hence, although our experiments clearly show that under current conditions potential V (ν_3) → T energy transfer is not affecting the effective sticking probability through enhanced direct scattering or more efficient desorption, it may be of relevance at considerably lower collision energies. In that case, a difference may be more readily detected by monitoring the scattered fraction as it constitutes the minority, as done by Sibener and Lee.

4 Summary

Using a combination of molecular beam techniques, state-resolved excitation, and RAIRS detection, we have investigated the possible

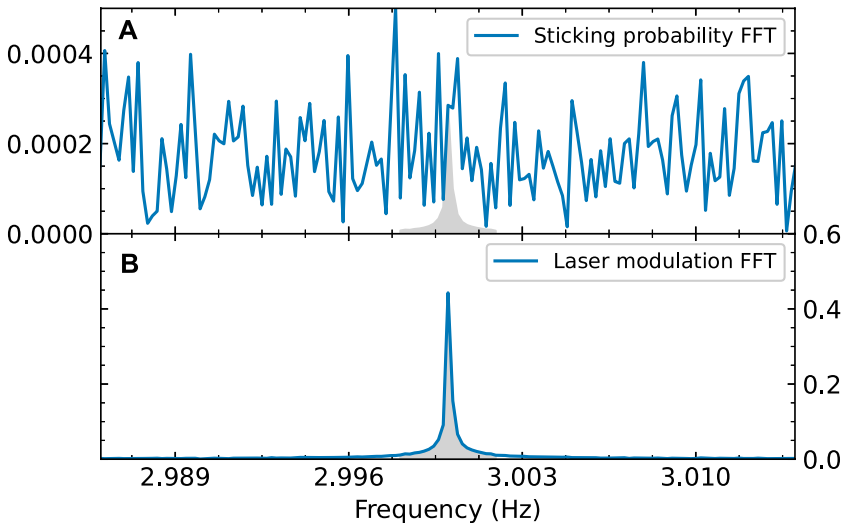

FIGURE 5
FFT of the measured sticking probability of CO_2 **(A)** and of the modulation signal of the laser **(B)**. Both are normalized; **(A)** is normalized so the amplitude of the FFT reflects the sticking probability, **(B)** is normalized so an FFT amplitude of 1 corresponds to a square wave with an amplitude of 1. The gray area in **(B)** shows an integral of 1. The modulation frequency of the laser is clearly visible in the FFT spectrum, but in the data it is absent or indistinguishable from the noise. To calculate the integral of the "peak" (shown as the gray area in **(A)**), we assume the same peak shape as in the modulation FFT.

influences of vibrational excitation on both the sticking of CO_2 on CO_2 ice and the structure of the resulting ice on a cryogenically cooled Cu sample. We find no evidence of an influence of the ν_3 mode on either possible effect within our detection limits at an incident velocity of 587 m/s. With regards to the ice structure are our results consistent with the results of Ioppolo et al. (Ioppolo et al., 2022) for crystalline CO_2 ice. Neither vibrational excitation of molecules prior to impact nor when already in the ice seems to affect the ice structure significantly. With regards to the sticking probability we find that our detection limit supports that, in comparison to the measured average sticking probability for all states present in the beam, it is safe to assume that a single quantum in the ν_3 mode is of no relevant influence to the effective sticking probability. This may result from a fortuitous cancellation of effects on the adsorption vs. direct scattering and desorption rates for the excited state, but this seems unlikely. The result, therefore, expands upon the conclusion from an earlier study that used state-resolved detection of CO_2 molecules desorbing from its ice: even vibrational energies exceeding the desorption energy seem not relevant to the growth or evaporation of CO_2 ice.

Data availability statement

The raw data supporting the conclusion of this article will be made available by the authors, without undue reservation.

Author contributions

CJ and JL contributed to conception and design of the study. CJ performed the experiments, analyzed the data, and wrote the first draft of the manuscript. All authors contributed to the article and approved the submitted version.

Funding

This work is part of the research programme Materials for Sustainability with project number 739.017.008, which is (partly) financed by the Dutch Research Council (NWO).

Conflict of interest

The authors declare that the research was conducted in the absence of any commercial or financial relationships that could be construed as a potential conflict of interest.

Publisher's note

Supplementary material

The Supplementary Material for this article can be found online at: https://www.frontiersin.org/articles/10.3389/fchem.2023.1250711/full#supplementary-material

References

Baratta, G. A., and Palumbo, M. E. (1998). Infrared optical constants of CO and CO_2 thin icy films. *JOSA A* 15 (12), 3076–3085. doi:10.1364/josaa.15.003076

Berenbak, B., Butler, D. A., Riedmüller, B., Papageorgopoulos, D. C., Stolte, S., and Kleyn, A. W. (1998). Sticking probability measurement in a reactive system. *Surf. Sci.* 414 (1-2), 271–278. doi:10.1016/s0039-6028(98)00525-1

Bisson, R., Dang, T. T., Sacchi, M., and Beck, R. D. (2008). Vibrational activation in direct and precursor-mediated chemisorption of SiH4 on Si(100). *J. Chem. Phys.* 129 (8), 081103. doi:10.1063/1.2976563

Burghaus, U. (2014). Surface chemistry of co2–adsorption of carbon dioxide on clean surfaces at ultrahigh vacuum. *Prog. Surf. Sci.* 89 (2), 161–217. doi:10.1016/j.progsurf.2014.03.002

Cao, K., van Lent, R., Kleyn, A. W., Kurahashi, M., and Juurlink, L. B. F. (2019). Steps on pt stereodynamically filter sticking of o2. *Proc. Natl. Acad. Sci.* 116 (28), 13862–13866. doi:10.1073/pnas.1902846116

Cao, K., van Lent, R., Kleyn, A. W., and Juurlink, L. B. F. (2018). A molecular beam study of D_2 dissociation on Pt(111): testing SRP-DFT calculations. *Chem. Phys. Lett.* 706, 680–683. doi:10.1016/j.cplett.2018.07.024

Chadwick, H., Hundt, P. M., Maartenvan Reijzen, E., Yoder, B. L., and Beck, R. D. (2014). Quantum state specific reactant preparation in a molecular beam by rapid adiabatic passage. *J. Chem. Phys.* 140 (3), 034321. doi:10.1063/1.4861054

Despois, D., Biver, N., Bockelée-Morvan, D., and Crovisier, J. (2005). Observations of molecules in comets. *Proc. Int. Astronomical Union* 1 (S231), 469–478. doi:10.1017/s1743921306007484

d'Hendecourt, L. B., and Jourdain de Muizon, M. (1989). The discovery of interstellar carbon dioxide. *Astronomy Astrophysics* 223, L5–L8.

Dombrowski, E., Peterson, E., Del Sesto, D., and Utz, A. L. (2015). Precursor-mediated reactivity of vibrationally hot molecules: methane activation on Ir(111). *Catal. Today* 244, 10–18. doi:10.1016/j.cattod.2014.10.025

Escribano, R. M., Munoz Caro, G. M., Cruz-Diaz, G. A., Rodriguez-Lazcano, Y., and Mate, B. (2013). Crystallization of CO2 ice and the absence of amorphous CO2 ice in space. *Proc. Natl. Acad. Sci.* 110 (32), 12899–12904. doi:10.1073/pnas.1222228110

Falk, M. (1987). Amorphous solid carbon dioxide. *J. Chem. Phys.* 86 (2), 560–564. doi:10.1063/1.452307

Gordon, I. E., Rothman, L. S., Hargreaves, R. J., Hashemi, R., Karlovets, E. V., Skinner, F. M., et al. (2022). The HITRAN2020 molecular spectroscopic database. *J. Quantitative Spectrosc. Radiat. Transf.* 277, 107949. doi:10.1016/j.jqsrt.2021.107949

Hollins, P., and Pritchard, J. (1979). Interactions of CO molecules adsorbed on Cu(111). *Surf. Sci.* 89 (1), 486–495. doi:10.1016/0039-6028(79)90633-2

Ioppolo, S., Noble, J. A., Traspas Muiña, A., Cuppen, H. M., Coussan, S., and Redlich, B. (2022). Infrared free-electron laser irradiation of carbon dioxide ice. *J. Mol. Spectrosc.* 385, 111601. doi:10.1016/j.jms.2022.111601

Jansen, C., and Juurlink, L. (2021). Absolute dissociation cross sections for D2 dissociation on Pt steps. *Chem. Phys. Lett.* 776, 138679. doi:10.1016/j.cplett.2021.138679

Jansen, C., van Lent, R., Chadwick, H., and Juurlink, L. B. F. (2023) *A state-selected cw laser excitation method for determining co2's rotational state distribution in a supersonic molecular beam*. Submitted.

King, D. A., and Wells, G. (1972). Molecular beam investigation of adsorption kinetics on bulk metal targets: nitrogen on tungsten. *Nitrogen tungsten* 29 (2), 454–482. doi:10.1016/0039-6028(72)90232-4

Koitaya, T., Shiozawa, Y., Mukai, K., Yoshimoto, S., and Yoshinobu, J. (2016). Observation of Fano line shapes in infrared vibrational spectra of CO_2 adsorbed on Cu(997) and Cu(111). *J. Chem. Phys.* 144 (5), 054703. doi:10.1063/1.4941060

Kurahashi, M. (2016). Oxygen adsorption on surfaces studied by a spin-and alignment-controlled o2 beam. *Prog. Surf. Sci.* 91 (1), 29–55. doi:10.1016/j.progsurf.2016.03.001

Pachecka, M., Sturm, J. M., Lee, C. J., and Bijkerk, F. (2017). Adsorption and dissociation of CO_2 on Ru(0001). *J. Phys. Chem. C* 121 (12), 6729–6735. doi:10.1021/acs.jpcc.7b00021

Rostrup-Nielsen, J. R. (1984). "Catalytic steam reforming," in *Catalysis* (Springer), 1–117.

Sandford, S. A., and Allamandola, L. J. (1990). The physical and infrared spectral properties of CO2 in astrophysical ice analogs. *Astrophysical J.* 355 (1), 357–372. doi:10.1086/168770

Sibener, S. J., and Lee, Y. T. (1994). The internal and translational energy dependence of molecular condensation coefficients: sf6 and ccl4. *J. Chem. Phys.* 101 (2), 1693–1703. doi:10.1063/1.467791

Van Dishoeck, E. F. (2004). Iso spectroscopy of gas and dust: from molecular clouds to protoplanetary disks. *Annu. Rev. Astron. Astrophys.* 42, 119–167. doi:10.1146/annurev.astro.42.053102.134010

van Lent, R., Auras, S. V., Cao, K., Walsh, A. J., Gleeson, M. A., and Juurlink, L. B. F. (2019). Site-specific reactivity of molecules with surface defects—The case of H_2 dissociation on Pt. *Science* 363 (6423), 155–157. doi:10.1126/science.aau6716

Weida, J. M., Sperhac, J. M., and Nesbitt, D. J. (1996). Sublimation dynamics of CO2 thin films: a high resolution diode laser study of quantum state resolved sticking coefficients. *J. Chem. Phys.* 105 (2), 749–766. doi:10.1063/1.472814

Wodtke, A. M., Huang, Y., and Auerbach, D. J. (2005). Insensitivity of trapping at surfaces to molecular vibration. *Chem. Phys. Lett.* 413 (4-6), 326–330. doi:10.1016/j.cplett.2005.06.031

Zhang, D., Jansen, C., Berg, O. T., Bakker, J. M., Meyer, J., Kleyn, A. W., et al. (2022). RAIRS characterization of CO and O coadsorption on Cu(111). *J. Phys. Chem. C* 126 (31), 13114–13121. doi:10.1021/acs.jpcc.2c02541

Zhang, D., Jansen, C., Kleyn, A. W., and Juurlink, L. B. F. (2023). Adsorption dynamics of O_2 on Cu(111): a supersonic molecular beam study. *Phys. Chem. Chem. Phys.* 25 (21), 14862–14868. doi:10.1039/d3cp01215h

frontiers | Frontiers in Chemistry

TYPE Correction
PUBLISHED 17 January 2024
DOI 10.3389/fchem.2024.1361255

OPEN ACCESS

EDITED AND REVIEWED BY
Helen Chadwick,
Swansea University, United Kingdom

*CORRESPONDENCE
Ludo B. F. Juurlink,
l.juurlink@chem.leidenuniv.nl

RECEIVED 25 December 2023
ACCEPTED 08 January 2024
PUBLISHED 17 January 2024

CITATION
Jansen C and Juurlink LBF (2024), Corrigendum: State-resolved studies of CO_2 sticking to CO_2 ice.
Front. Chem. 12:1361255.
doi: 10.3389/fchem.2024.1361255

Corrigendum: State-resolved studies of CO_2 sticking to CO_2 ice

Charlotte Jansen and Ludo B. F. Juurlink*

Leiden Institute of Chemistry, Leiden University, Leiden, Netherlands

KEYWORDS

CO_2, nu3, state resolved, molecular beam, condensation

A Corrigendum on
State-resolved studies of CO_2 sticking to CO_2 ice

by Jansen C and Juurlink LBF (2023). Front. Chem. 11:1250711. doi: 10.3389/fchem.2023.1250711

In the published article, there was an error in Figure 5 as published. The wrong dataset was used, see text correction. The corrected Figure 5 and its caption appear below.

In the published article, there was an error. The King and Wells measurements were done with a cold cathode pressure gauge (Pfeiffer IKR 270). This pressure gauge was found to have a relatively slow response time. A test measurement showed that the sensitivity at 3 Hz is approximately 300 times lower than the maximum sensitivity at 0 Hz. As our measurements were done with a modulating input (laser excitation) at 3 Hz, the upper limit for the effect of laser excitation on sticking probability was overestimated by a factor of 300. However, we have another dataset of the same measurement, but measured with a quadrupole mass spectrometer (QMS, Pfeiffer QMA 200). The change in sensitivity of the QMS between 0 Hz and 3 Hz is negligible. While the overall noise level of the QMS is higher than that of the pressure gauge, it is still much more sensitive at 3 Hz and it is therefore better to use the QMS data.

A correction has been made to **Abstract**. This sentence previously stated:

"Based on our detection limit, we quantify the weighted average sticking probability at approximately 0.9 and the difference between the state-resolved and weighted average sticking probability as below 0.03%."

The corrected sentence appears below:

"Based on our detection limit, we quantify the weighted average sticking probability at approximately 0.9 and the difference between the state-resolved and weighted average sticking probability as below 0.5%."

A correction has been made to **Experimental**, 8. This sentence previously stated:

"Hence, we measure the sticking probability of CO_2 onto CO_2 ice at 80 K with a modulated version of the King and Wells method (**King and Wells, 1972**) and a cold cathode pressure gauge (Pfeiffer IKR 270). The absolute pressure changes in the UHV chamber are dominated by the molecular beam, which consists (nearly) only of CO_2. As the ion gauge signal yields considerably better signal-to-noise than our QMS tuned to m/z 44, and it allows for higher detection frequency, it is easier to detect small differences in the sticking probability. The use of an ion gauge instead of a QMS was inspired by prior O_2 state-resolved measurements (**Kurahashi, 2016**; **Cao et al., 2019**)."

The corrected sentence appears below:

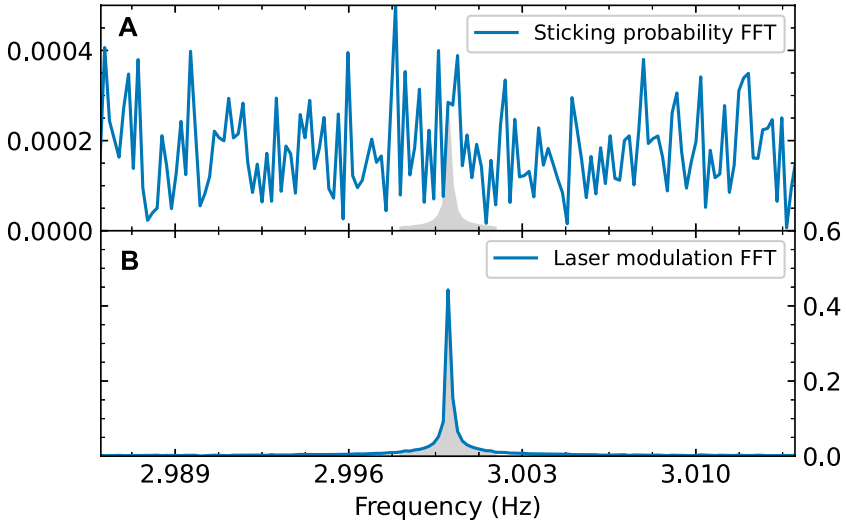

FIGURE 5
FFT of the measured sticking probability of CO_2 **(A)** and of the modulation signal of the laser **(B)**. Both are normalized; **(A)** is normalized so the amplitude of the FFT reflects the sticking probability, **(B)** is normalized so an FFT amplitude of 1 corresponds to a square wave with an amplitude of 1. The gray area in **(B)** shows an integral of 1. The modulation frequency of the laser is clearly visible in the FFT spectrum, but in the data it is absent or indistinguishable from the noise. To calculate the integral of the "peak" (shown as the gray area in **(A)**), we assume the same peak shape as in the modulation FFT.

"Hence, we measure the sticking probability of CO_2 onto CO_2 ice at 80 K with a modulated version of the King and Wells method (**King and Wells, 1972**) and a quadrupole mass spectrometer (QMS, Pfeiffer QMA 200) tuned to m/z 44."

A correction has been made to **Experimental**, 9. This sentence previously stated:

"This causes a rise in the CO_2 partial pressure in the vacuum chamber, which is continuously monitored with the pressure gauge."

The corrected sentence appears below:

"This causes a rise in the CO_2 partial pressure in the vacuum chamber, which is continuously monitored with the QMS."

A correction has been made to **Results and discussion**, *Sticking probability of CO_2 on CO_2 ice*, 3. This sentence previously stated:

"The integral of the peak, which corresponds to our detection limit for the sticking probability, is calculated to be 3×10^{-5} whereas the sticking probability itself is near unity."

The corrected sentence appears below:

"The integral of the peak, which corresponds to our detection limit for the sticking probability, is calculated to be 6×10^{-4} whereas the sticking probability itself is near unity."

A correction has been made to **Results and discussion**, *Sticking probability of CO_2 on CO_2 ice*, 4. This sentence previously stated:

"Applying these corrections to our detection limit, we find that the upper limit for the change in the CO_2 sticking probability on CO_2 ice due to the asymmetric stretch vibration is approximately 3×10^{-4}."

The corrected sentence appears below:

"Applying these corrections to our detection limit, we find that the upper limit for the change in the CO_2 sticking probability on CO_2 ice due to the asymmetric stretch vibration is approximately 5×10^{-3}."

The authors apologize for these errors and state that this does not change the scientific conclusions of the article in any way. The original article has been updated.

Publisher's note

frontiers | Frontiers in Chemistry

TYPE Mini Review
PUBLISHED 29 August 2023
DOI 10.3389/fchem.2023.1258035

OPEN ACCESS

EDITED BY
Marco Sacchi,
University of Surrey, United Kingdom

REVIEWED BY
Tomás González-Lezana,
Spanish National Research Council (CSIC), Spain
Masashi Tsuge,
Hokkaido University, Japan

*CORRESPONDENCE
Koichiro Yamakawa,
yamakawa.koichiro@jaea.go.jp
Hirokazu Ueta,
ueta.hirokazu@jaea.go.jp

RECEIVED 13 July 2023
ACCEPTED 27 July 2023
PUBLISHED 29 August 2023

CITATION
Ueta H, Fukutani K and Yamakawa K (2023), Fast ortho-to-para conversion of molecular hydrogen in chemisorption and matrix-isolation systems.
Front. Chem. 11:1258035.
doi: 10.3389/fchem.2023.1258035

Fast ortho-to-para conversion of molecular hydrogen in chemisorption and matrix-isolation systems

Hirokazu Ueta[1]*, Katsuyuki Fukutani[1,2] and Koichiro Yamakawa[1]*

[1]Advanced Science Research Center, Japan Atomic Energy Agency, Ibaraki, Japan, [2]Institute of Industrial Science, The University of Tokyo, Tokyo, Japan

Molecular hydrogen has two nuclear-spin modifications called *ortho* and *para*. Because of the symmetry restriction with respect to permutation of the two protons, the *ortho* and *para* isomers take only odd and even values of the rotational quantum number, respectively. The *ortho*-to-*para* conversion is promoted in condensed systems, to which the excess rotational energy and spin angular momentum are transferred. We review recent studies on fast *ortho*-to-*para* conversion of hydrogen in molecular chemisorption and matrix isolation systems, discussing the conversion mechanism as well as rotational-relaxation pathways.

KEYWORDS

hydrogen, nuclear spin, rotational energy, adsorption, surface, matrix isolation

1 Introduction

Molecular hydrogen has a remarkable feature of nuclear-spin isomers. According to the quantum number I of the total nuclear spin, a hydrogen molecule has two modifications called *ortho* ($I = 1$) and *para* ($I = 0$) species. Because of the symmetry restriction, *ortho* (*para*) H_2 takes only odd (even) values of the rotational quantum number J. Whereas the transition between *ortho* and *para* species is strictly forbidden in the isolated state, it is significantly promoted upon interaction with other substances. Because the nuclear-spin isomers are identified by I and J, the *ortho*-to-*para* (*o*-*p*) conversion of H_2 involves two aspects of the nuclear-spin flip and the rotational-energy transfer to a surface or a surrounding material.

The gas-surface energy transfer has been one of the main topics in surface physics and chemistry; a typical example is the adsorption event, where the translational and adsorption energy of a molecule is transferred to a surface. In addition to the translational energy, internal degrees of freedom such as molecular vibration and rotation are also of considerable importance. Owing to the advance in laser techniques, the relaxation processes of vibrationally-excited molecules have been well studied to date (Beckerle et al., 1990; Chang and Ewing, 1990; Morin et al., 1992; Laß et al., 2005; Chen et al., 2019; Kumar et al., 2019). Compared to the vibration, on the other hand, the energy transfer from the molecular rotation to surface degrees of freedom has been poorly understood. One promising approach for the elucidation of the rotational-energy transfer is to investigate the *o*-*p* conversion of H_2 on surfaces and in matrices. After adsorption on a cold surface or trapping in a matrix, *ortho* (*para*) H_2 predominantly occupies its lowest rotational level with $J = 1$ ($J = 0$). Upon *o*-*p* conversion of H_2, the rotational-energy needs to be dissipated into surface or matrix degrees of freedom.

The *o-p* conversion of H_2 has been observed on various systems (Fukutani and Sugimoto, 2013). The *o-p* conversion is closely related to the quest for efficient ways of the H_2 storage (Ilisca, 2021), and therefore is being investigated not only on surfaces but also inside solids (Lavrov and Weber, 2002; Hiller et al., 2007; Peng et al., 2009) and nano-cages (Carravetta et al., 2004; Carravetta et al., 2006; Carravetta et al., 2007). Stimulated by the development of the experimental investigations, several conversion mechanisms have been also proposed depending on the interacting materials (Yamakawa and Fukutani, 2020): the Wigner model (Wigner, 1933), where the proton spin interacts with the inhomogeneous magnetic field generated by localized paramagnetic ions; the electron-spin-induced conversion models categorized into the second- (Ilisca, 1991) and third-order (Ilisca and Ghiglieno, 2016) perturbation theories, where the virtual electron exchange or transfer between H_2 and a surface is involved along with the Fermi contact interaction between an electron and a proton in H_2; the electric-field-induced conversion model (Sugimoto and Fukutani, 2011), where the Stark, spin-orbit, and Fermi-contact couplings mix the *ortho* and *para* states.

In spite of the extensive studies on the H_2 *o-p* conversion in the last decades, there still remain controversial issues; one is fast conversion and the other is the rotational-energy dissipation. In contrast to the *o-p* conversion time of ~10^3 s or longer observed on various surfaces and in solids, H_2 *o-p* conversion with a time constant shorter than ~10^2 s was recently observed on Pd(210) and inside a molecular solid of CO_2. On the Pd(210) surface, furthermore, rotational-energy transfer was investigated in detail taking account of electrons and phonons of surfaces. In this review paper, we expound the studies of the fast *o-p* conversion in a CO_2 matrix (Section 2) and on Pd(210) (Section 3), discussing the spin and rotational-energy transfer.

2 Matrix isolation system

The techniques of nuclear magnetic resonance (NMR), neutron scattering, Raman spectroscopy, and infrared absorption spectroscopy have been applied to *in situ* observation of the H_2 conversion in fullerene (C_{60}) (Carravetta et al., 2004; 2006; 2007), metal-organic frameworks (MOFs) (FitzGerald et al., 2010), porous coordination polymers (Kosone et al., 2015), semiconductors (Lavrov and Weber, 2002; Hiller et al., 2007; Peng et al., 2009), and viscous organic solutions (Aroulanda et al., 2007), as was reviewed recently (Ilisca, 2021). Whereas NMR directly probes the nuclear spin, the other methods enable one to resolve the rotational states of *ortho-* and *para*-H_2. In the nuclear-spin conversion study of polyatomic molecules such as H_2O (Fajardo et al., 2004; Abouaf-Marguin et al., 2007; Fillion et al., 2012), NH_3 (Boissel et al., 1993; Gauthier-Roy et al., 1993; Ruzi and Anderson, 2013), and CH_4 (Miyamoto et al., 2008; Sugimoto et al., 2015; Sugimoto and Yamakawa, 2021), the most popular technique has been rovibrational spectroscopy combined with the matrix-isolation method, where target molecules are isolated in molecular solids, e.g., rare-gas ones. Indeed, the temperature dependence of the conversion rate has been intensively studied in this way to reveal the pathways for the rotational relaxation (Sugimoto et al., 2015; Turgeon et al., 2017; Yamakawa et al., 2017).

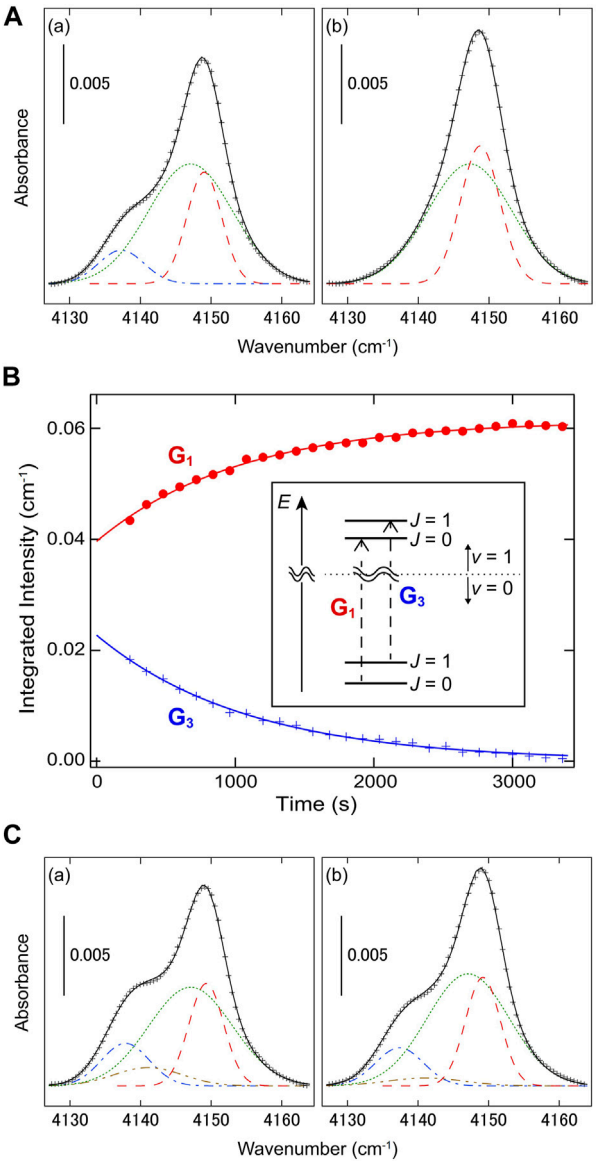

FIGURE 1
Nuclear spin conversion of H_2 trapped in solid CO_2 at 5.4 K (Yamakawa et al., 2020) (Copyright 2020; American Physical Society). **(A)** Induced infrared-absorption bands of H_2 (a) 240 s and (b) 3,360 s after the sample deposition. The result of multi-gaussian fitting is also shown; the gaussian curves of G_1, G_2, and G_3, are represented by dashed, dotted, and dashed-dotted lines, respectively. **(B)** The integrated intensities of G_1 and G_3 are plotted against time. The solid lines denote the result of monoexponential fitting. The vibrational transitions of H_2 corresponding to G_1 and G_3 are schematically shown in the inset. **(C)** Induced infrared-absorption bands of H_2 (a) 0 s and (b) 120 s after the sample deposition. The result of tetra-gaussian fitting is also shown; G_1, G_2, G_3, and G_4, are denoted by dashed, dotted, dashed-dotted, and dashed double-dotted lines, respectively.

Since H_2 is the lightest molecule and has a relatively small interaction with matrix molecules, rather low temperatures (typically T < 15 K) are required to suppress its diffusion and formation of aggregates. In previous studies, the *ortho* and *para* isomers of H_2 have been separately detected in various matrices of Ar, Kr, Xe, N_2, and CO by using Raman spectroscopy (Prochaska and Andrews, 1977; Alikhani et al., 1989; Kornath et al., 1999). In

particular, Alikhani *et al.* kept Ar-isolated H_2 at 9 K for 24 h and observed no change of the intensity ratio of the *ortho* and *para* signals, which means the *o-p* conversion was suppressed significantly in solid Ar. In contrast, comparing the ratio with a calculated value, the *o-p* conversion was found to partially proceed just during the sample deposition; they pointed out the possibility that this conversion was catalyzed by O_2 impurities. Although H_2 has no permanent electric dipole moment, one is able to detect matrix-isolated H_2 also by infrared absorption spectroscopy because of its weak polarization. Warren et al. measured infrared spectra of H_2 trapped inside Ar, Kr, N_2, and CO matrices in the wavenumber regions of pure rotational and vibrational transitions; except for the rotational spectrum of Kr-isolated H_2, the *ortho* and *para* signals were resolved (Warren et al., 1980). They also found the *ortho*-to-*para* ratio of H_2 trapped in solid Ar to be decreased by ~25% after 2–3 days and attributed this *o-p* conversion to the accidental contamination of magnetic impurities, though the accurate conversion rate was not determined. In a recent study (Yamakawa et al., 2020), H_2 was trapped and polarized in solid CO_2, so that the conversion rate of H_2 was derived from the time evolution of its infrared absorption band, as is expounded below.

The room-temperature gaseous mixture of CO_2 and H_2 at a molar ratio of $CO_2/H_2 = 100$ was condensed onto a gold substrate at 5.4 K for 10 min, and infrared spectra were measured in the reflection configuration. From the film interference pattern appearing in the baseline of the spectrum, the thickness of the CO_2 matrix was determined to be 4.5 μm. Just after the condensation, the spectrum showed not only intense absorption bands of CO_2 but also a weak band of H_2. At a trapping site of H_2, the electric fields generated by surrounding CO_2 molecules did not cancel each other out, resulting in slight electric-polarization of H_2. The time evolution of the H_2 band after the sample deposition is displayed in Figure 1A. The absorption band was well-reproduced by the combination of three gaussian curves: G_1 at 4,149 cm^{-1}, G_2 at 4,147 cm^{-1}, and G_3 at 4,138 cm^{-1}. Whereas G_1 grew with increasing time, G_3 decayed and finally disappeared. This time development was attributed to the conversion of H_2 from *ortho* to *para*; in other words, G_1 and G_3 were assigned to the Q_1 (0) and Q_1 (1) transitions of *para*- and *ortho*-H_2, respectively. In the gas phase, the transition energy of Q_1 (0), 4,161.1 cm^{-1}, is also higher than that of Q_1 (1), 4,155.3 cm^{-1} (Dabrowski, 1984), owing to the rovibrational coupling in H_2. As shown in Figure 1B, the integrated intensities of G_m (m = 1, 3) were analyzed as a function of time, and were found to follow the monoexponential function:

$$I_m(t) = [I_m(0) - I_m(\infty)] \exp(-k_m t) + I_m(\infty),$$

where $I_m(0)$ and $I_m(\infty)$ denotes the initial and equilibrium intensities, respectively. The conversion rate derived from G_1, $k_1 = (9.6 \pm 0.4) \times 10^{-4}$ s^{-1}, coincided within error with that from G_3, $k_3 = (9.2 \pm 0.4) \times 10^{-4}$ s^{-1}.

To reveal the origin of G_2, Yamakawa *et al.* also investigated the time evolution of the infrared spectrum just after the sample deposition, as shown in Figure 1C; in the time range of $t = 0 - 120$ s, an additional component, G_4, was detected at 4,141 cm^{-1}, and the decay of G_4 was observed simultaneously with the growth of G_2. Thus, it was likely that there were two kinds of trapping sites for H_2 inside solid CO_2; while G_1 and G_3 were attributed to H_2 at site A, G_2 (G_4) was to *para* (*ortho*) H_2 at site B. The frequency difference between the *para* and *ortho* species at site B was about a half of that at site A. This suggests the approach of the lowest rotational levels of *ortho*- and *para*-H_2 and relatively high anisotropy of the confining potential at site B. Note that the estimated *o-p* conversion rate at site B was as high as 6×10^{-3} s^{-1}. In a previous study with use of electron-energy-loss spectroscopy, the conversion rate of H_2 adsorbed on the stepped surface of Cu(510), where the adsorption potential is strongly anisotropic, was evaluated to be on the order of 1 s (Svensson and Andersson, 2007). These results suggest fast conversion of rotationally hindered H_2, which is also shown in Section 3.

In most of the condensed systems, the vibrational-frequency shift of H_2 with respect to the gas phase, ΔQ_1 (0), was negative: −12 (−14) cm^{-1} at site A (B) of solid CO_2 (Yamakawa et al., 2020), −17 cm^{-1} in solid N_2 and CO (Warren et al., 1980), −20 cm^{-1} on amorphous D_2O ice (Hixson et al., 1992). Despite the relatively small red-shift, the conversion rate of H_2 in solid CO_2 at 5.4 K was even higher than that on amorphous H_2O ice at 9.2 K, 2.4×10^{-4} s^{-1}, measured by Ueta et al., 2016, who also reported the monotonical increase of the rate with temperature below 14 K. This result is not explained by the electric-field-induced conversion mechanism (Sugimoto and Fukutani, 2011); instead, probable is the three-step conversion model (Ilisca and Ghiglieno, 2016; Ilisca, 2018), which consists of electron exchange between H_2 and a solvent, hyperfine contact interaction in H_2, and spin-orbit interaction inside the solvent.

Interestingly enough, the conversion time-constants (the inverse of the conversion rate) of H_2 in non-magnetic systems accompanied by energy gaps are distributed quite widely: a few or tens of minutes in MOFs (FitzGerald et al., 2010) and solid CO_2 (Yamakawa et al., 2020), and tens or hundreds of hours in crystalline Si (Lavrov and Weber, 2002; Hiller et al., 2007; Peng et al., 2009) and the cage of C_{60} (Chen et al., 2013). Note that the CO_2 film deposited below ~9 K has a porous structure with the enhanced surface area and exhibits a unique feature of "thermal spikes", which are abrupt temperature rises due to the structural rearrangement during the film deposition (Arakawa et al., 1979). The enhanced *o-p* conversion of H_2 is possibly related to the characteristically unstable and porous structure of the CO_2 film. In order to further investigate the origin of the large difference in the conversion time, the electronic structure of the H_2-solvent system, including the anisotropy of a confining potential, should be also studied. The temperature dependence of the conversion rate of H_2 trapped in matrices is under investigation and will bring about information on the channels of the rotational relaxation, just like the surface system described in the following section.

3 Molecular chemisorption system

As typical adsorption schemes of H_2, dissociative chemisorption and molecular physisorption are recognized. In most of past studies on *o-p* conversion at surfaces, H_2 in the physisorption state via the van der Waals interaction was focused, in which the molecule is in a nearly-free rotational state (Stulen, 1988; Sugimoto and Fukutani, 2014). On the other hand, some stepped surfaces exhibit a peculiar adsorption of molecular chemisorption (Mårtensson et al., 1986; Svensson et al., 1999; Schmidt et al., 2001; Sun et al., 2004; Svensson and Andersson, 2007; Christmann, 2009; Shan et al., 2009), in which the adsorption potential is anisotropic with respect to the molecular-axis angle and the rotational motion is strongly hindered. Although the rotational state is modified under the anisotropic potential, the rotational state of H_2 chemisorbed

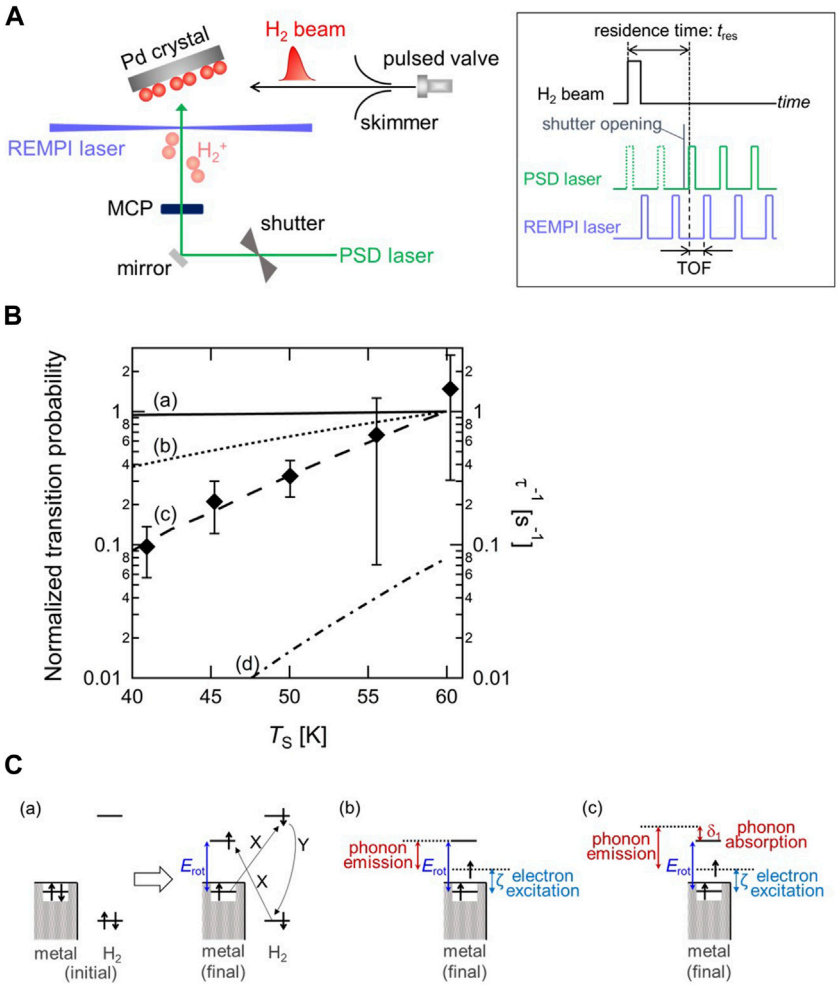

FIGURE 2
(A) Schematic diagram of the experimental setup and pulse sequence driving the molecular beam and two lasers for the *o-p* conversion measurement (Ueta et al., 2020) (Copyright 2020; American Physical Society). **(B)** Surface temperature dependence of the *o-p* conversion rate (τ^{-1}) with calculated *o-p* transition probability through (a) the *XY* model (solid line), (b) a combination model of electron transition and one-phonon process (dotted line), and (c) a combination model of electron transition and two-phonon process (dashed line). The value of transition probability at T_S = 60 K is normalized to 1 for three models. On the other hand, (d) the *p-o* transition probability through a combination model of electron transition and two-phonon process at T_S = 60 K is normalized to the value of the *o-p* transition probability through the same model at the same T_S (dashed-dotted line). Note that the experimentally determined conversion rates correspond to right axis, and the results of model calculation correspond to left axis (Ueta and Fukutani, 2023) (Copyright 2023 American Chemical Society). **(C)** Schematic illustration of the rotational-energy transfer in *o-p* conversion through (a) the *XY* model, (b) the electronic excitation and one-phonon process, and (c) the electronic excitation and two-phonon process. *X* and *Y* denotes the Coulomb interaction and the Fermi contact hyperfine interaction, respectively (Ueta and Fukutani, 2023) (Copyright 2023 American Chemical Society).

on surfaces is correlated with the nuclear-spin state, either *ortho* or *para*. In the past, while the occurrence of fast *o-p* conversion under an anisotropic potential was indicated for the systems of Cu(510) and Pd(210), direct evidence was lacking due to the limited time resolution of the experimental technique used in previous studies (Svensson and Andersson, 2007; Ohno et al., 2018). In this section, fast *o-p* conversion and associated rotational-energy transfer are discussed for H_2 molecularly chemisorbed on Pd(210).

The Pd(210) surface has (100) terraces with steps running along the [001] direction forming open (110)-like microfacets. H_2 chemisorbs on the step-edge of Pd atoms, so that H_2 binds strongly to the surface compared with the physisorption systems (Schmidt et al., 2001). The adsorption state of H_2 has been studied experimentally and theoretically (Lischka and Groß, 2002; Arguelles and Kasai, 2018a; Arguelles and Kasai, 2018b). The H_2 adsorption potential is highly anisotropic, which induces lifting of the rotational state degeneracy of the triply degenerate J = 1 state in gas-phase into doubly degenerate state (m = ±1, m: z component of J) and a non-degenerate state (m = 0) in the adsorption state. Hence the lowest *o*-H_2 (m = ±1) behaves like a two-dimensional rotor (Svensson et al., 1999).

To track the fast *o-p* conversion directly, a new experimental method was developed by combining a pulsed molecular beam (MB), photo-stimulated desorption (PSD), and resonance-enhanced multiphoton ionization (REMPI). Figure 2A shows a schematic diagram of the experimental setup and a timing chart of the MB-PSD–REMPI measurement for probing the time evolution of the rotational states of H_2 on surfaces (Ueta et al., 2020). Probing the change in the rotational state distribution allows us to track *o-p* conversion owing to the fact that the rotational states of H_2 couple with nuclear spins. With *n*-H_2 molecular beam deposition, the *o-p* ratio

at a surface temporarily becomes out-of-thermal-equilibrium, and then relaxes to the thermal equilibrium. From the change in the two nuclear-spin-state populations as a function of the adsorption time, the conversion rate can be determined, similar to that shown in Figure 1B. The conversion rate has been successfully determined on Pd(210) as a function of the surface temperature (T_S) in the range of 41–60 K as shown in Figure 2B. It is found the conversion rate increases with increasing temperature. Note that the values of the conversion time (inverse of conversion rate) are on the order of 1–10 s, demonstrating the occurrence of fast conversion on Pd(210).

Since the *o-p* conversion is accompanied by the rotational transition as well as the nuclear spin flip, the surface temperature dependence of *o-p* conversion allows us to investigate the rotational-energy (E_{rot}) transfer process in *o-p* conversion. The rotational-energy dissipation process has been discussed in previous studies on the *o-p* conversion of physisorbed H_2 on amorphous solid water, silicate and carbon materials (Ueta et al., 2016; Tsuge et al., 2021; Tsuge et al., 2021). These studies suggested that substrate phonons play an important role in the rotational-energy transfer in the conversion. Depending on the substrate, two kinds of phonon dissipation process have been considered in those studies; one-phonon and two-phonon processes. Whereas in the former process the rotational energy is dissipated into the surface by excitation of a phonon, the latter process proceeds via the simultaneous absorption of a phonon from the initial up to an intermediate state, and the emission of another from the intermediate to the final states (Scott and Jeffries, 1962). Since those materials are all non-metallic, the influence of surface electrons in the rotational-energy transfer process can be neglected.

On the other hand, Pd is a non-magnetic metal, where substrate electrons are expected to play an important role in analogy with the vibrational-energy relaxation. A widely accepted conversion model on a non-magnetic metal surface is the electron-exchange-hyperfine-contact (*XY*) model proposed by Ilisca (Ilisca, 1991) (Figure 2C-(a)). In this model, an electron in the σ_g orbital of H_2 is excited to the surface and an electron in the surface is excited to the σ_u orbital of H_2 with the Coulomb interaction, followed by nuclear-spin flip with the Fermi contact hyperfine interaction between the electron in the σ_u orbital and the hydrogen nuclei leading to the *o-p* conversion. Consequently, a surface electron is excited to the level above the Fermi level (E_F) by the amount of E_{rot}, and thus E_{rot} is dissipated into metal *electron-hole* pairs. Assuming that the electron transfer probability is independent of its energy, the *o-p* transition probability in this model is proportional to the numbers of electron and hole states available. The calculated transition probabilities are plotted in Figure 2B, showing that the transition probability does not change significantly with T_S, which is inconsistent with the experimental data. Therefore, two combination models based on the *XY* model, namely, E_{rot} transfer is shared by both electronic transition and phonon excitation through either one-phonon or two-phonon processes, are proposed (Figure 2C-(b)(c)). It should be mentioned that the electron transition process is essential for nuclear-spin flip via the Fermi contact hyperfine interaction. The results of both combination models in Figure 2B show that the transition probability varies substantially with T_S in contrast with the result based on the *XY* model. Particularly, the tendency of the combination model of electronic transition and two-phonon process is in good agreement with that of the experimentally determined *o-p* conversion rate. This indicates that the rotational energy of H_2 transfers into not only electrons but also phonons of surfaces (Ueta and Fukutani, 2023).

Recalling the fact that the vibrational energy is transferred to electrons at metal surfaces, this rotational-energy transfer process might be counterintuitive, because E_{rot} is transferred into phonons as well as electrons of surfaces despite a metallic surface. The difference between vibrational- and rotational-energy transfer paths could be ascribed to the energy scale of both degrees of freedom. While the magnitude of the rotational energy of H_2 (~10 meV) is much smaller than the vibrational energy such as the CO stretch mode (~0.26 eV), that is comparable with the magnitude of the substrate phonon energy. The energy transfer path might be determined by the energy-scale matching between the molecular degree of freedom and surfaces as a receiver.

4 Concluding remarks

We have expounded a recent advance in the *o-p* conversion study of H_2, dealing with the fast conversion in the two novel systems characterized by the matrix isolation and molecular chemisorption. It is notable that the conversion time-scale was ~10^2 s or shorter in spite of the non-magnetic properties of these systems. While a variety of metal oxides have been investigated as the magnetic catalysts of the H_2 *o-p* conversion for many decades, expanding needs for the efficient H_2 storage and high-performance electrodes for the water electrolysis promotes the studies of H_2 interacting with non-magnetic substances such as MOFs and carbon nanomaterials. Since the *o-p* conversion involving both the spin- and energy-transfers influences the storage and chemical reaction of H_2, further studies of the conversion mechanism in the non-magnetic systems are required to reveal the determinant of the conversion time-scale. The anisotropy of a confining potential should be one of the key factors, and the temperature dependence of the conversion rate will provide essential information on the rotational-relaxation pathways also in other systems.

Author contributions

HU: Writing–original draft, Writing–review and editing. KF: Writing–review and editing. KY: Writing–original draft, Writing–review and editing.

Funding

The authors declare financial support was received for the research, authorship, and/or publication of this article. This work was supported by the Japan Society for the Promotion of Science (KAKENHI; Grant JP18H05518, JP20K05424, JP20K05337, JP21H04650, JP23H01856, and JP23K04593) and Grant for Basic Science Research Projects from the Sumitomo Foundation. HU was partially supported by MEXT Japan, Leading Initiative for Excellent Young Researchers.

Conflict of interest

The authors declare that the research was conducted in the absence of any commercial or financial relationships that could be construed as a potential conflict of interest.

Publisher's note

References

Abouaf-Marguin, L., Vasserot, A. M., Pardanaud, C., and Michaut, X. (2007). Nuclear spin conversion of water diluted in solid argon at 4.2K: Environment and atmospheric impurities effects. *Chem. Phys. Lett.* 447 (4–6), 232–235. doi:10.1016/j.cplett.2007.09.014

Alikhani, M. E., Silvi, B., Perchard, J. P., and Chandrasekharan, V. (1989). Reinvestigation of the Raman spectra of dihydrogen trapped in rare gas solids. I. H_2, HD, and D_2 monomeric species. *J. Chem. Phys.* 90 (10), 5221–5231. doi:10.1063/1.456475

Arakawa, I., Kobayashi, M., and Tuzi, Y. (1979). Effects of thermal spikes on the characteristics of cryosorption pumps with condensed carbon dioxide layers. *J. Vac. Sci. Technol.* 16 (2), 738–740. doi:10.1116/1.570072

Arguelles, E. F., and Kasai, H. (2018a). Bound nuclear spin states of H_2 in an anisotropic potential induced by a stepped metal surface. *J. Vac. Sci. Technol. A Vac. Surfaces, Films* 36 (3), 030601. doi:10.1116/1.5023158

Arguelles, E. F., and Kasai, H. (2018b). Hindered rotation and nuclear spin isomers separation of molecularly chemisorbed H_2 on Pd(210). *J. Appl. Phys.* 123 (11), 115301. doi:10.1063/1.5021994

Aroulanda, C., Starovoytova, L., and Canet, D. (2007). Longitudinal nuclear spin relaxation of ortho- and para-hydrogen dissolved in organic solvents. *J. Phys. Chem. A* 111 (42), 10615–10624. doi:10.1021/jp073162r

Beckerle, J. D., Casassa, M. P., Cavanagh, R. R., Heilweil, E. J., and Stephenson, J. C. (1990). Ultrafast infrared response of adsorbates on metal surfaces: Vibrational lifetime of CO/Pt(111). *Phys. Rev. Lett.* 64 (17), 2090–2093. doi:10.1103/PhysRevLett.64.2090

Boissel, P., Gauthier-Roy, B., and Abouaf-Marguin, L. (1993). Dipolar interactions between NH_3 molecules trapped in solid argon. II. Line narrowing during nuclear spin species conversion. *J. Chem. Phys.* 98 (9), 6835–6842. doi:10.1063/1.464775

Carravetta, M., Danquigny, A., Mamone, S., Cuda, F., Johannessen, O. G., Heinmaa, I., et al. (2007). Solid-state NMR of endohedral hydrogen–fullerene complexes. *Phys. Chem. Chem. Phys.* 9 (35), 4879–4894. doi:10.1039/B707075F

Carravetta, M., Johannessen, O. G., Levitt, M. H., Heinmaa, I., Stern, R., Samoson, A., et al. (2006). Cryogenic NMR spectroscopy of endohedral hydrogen-fullerene complexes. *J. Chem. Phys.* 124 (10), 104507. doi:10.1063/1.2174012

Carravetta, M., Murata, Y., Murata, M., Heinmaa, I., Stern, R., Tontcheva, A., et al. (2004). Solid-state NMR spectroscopy of molecular hydrogen trapped inside an open-cage fullerene. *J. Am. Chem. Soc.* 126 (13), 4092–4093. doi:10.1021/ja031536y

Chang, H.-C., and Ewing, G. E. (1990). Infrared fluorescence from a monolayer of CO on NaCl(100). *Phys. Rev. Lett.* 65 (17), 2125–2128. doi:10.1103/PhysRevLett.65.2125

Chen, J. Y.-C., Li, Y., Frunzi, M., Lei, X., Murata, Y., Lawler, R. G., et al. (2013). 'Nuclear spin isomers of guest molecules in $H_2@C_{60}$, $H_2O@C_{60}$ and other endofullerenes', *Philosophical Trans. R. Soc. A Math. Phys. Eng. Sci.*, 371, p. 20110628. doi:10.1098/rsta.2011.0628

Chen, L., Lau, J. A., Schwarzer, D., Meyer, J., Verma, V. B., and Wodtke, A. M. (2019). The Sommerfeld ground-wave limit for a molecule adsorbed at a surface. *Science* 363 (6423), 158–161. doi:10.1126/science.aav4278

Christmann, K. (2009). Interaction of hydrogen with (210)-oriented metal surfaces: Molecular precursors, chemisorbed atoms and subsurface states. *Surf. Sci.* 603 (10–12), 1405–1414. doi:10.1016/J.SUSC.2008.09.066

Dabrowski, I. (1984). The lyman and werner bands of H_2. *Can. J. Phys.* 62 (12), 1639–1664. doi:10.1139/p84-210

Fajardo, M. E., Tam, S., and DeRose, M. E. (2004) 'Matrix isolation spectroscopy of H_2O, D_2O, and HDO in solid parahydrogen', *J. Mol. Struct.*, 695–696, pp. 111–127. doi:10.1016/j.molstruc.2003.11.043

Fillion, J.-H., et al. (2012). Understanding the relationship between gas and ice: Experimental investigations on ortho-para ratios. *EAS Publ. Ser.* 58, 307–314. doi:10.1051/eas/1258051

FitzGerald, S. A., Hopkins, J., Burkholder, B., Friedman, M., and Rowsell, J. L. C. (2010). Quantum dynamics of adsorbed normal- and para-H_2, HD, and D_2 in the microporous framework MOF-74 analyzed using infrared spectroscopy. *Phys. Rev. B* 81 (10), 104305. doi:10.1103/PhysRevB.81.104305

Fukutani, K., and Sugimoto, T. (2013). Physisorption and ortho–para conversion of molecular hydrogen on solid surfaces. *Prog. Surf. Sci.* 88 (4), 279–348. doi:10.1016/j.progsurf.2013.09.001

Gauthier-Roy, B., Abouaf-Marguin, L., and Boissel, P. (1993). Dipolar interactions between NH_3 molecules trapped in solid argon. I. Kinetics of the nuclear spin species conversion. *J. Chem. Phys.* 98 (9), 6827–6834. doi:10.1063/1.464774

Hiller, M., Lavrov, E. V., and Weber, J. (2007). Ortho-para conversion of interstitial H_2 in Si. *Phys. Rev. Lett.* 98 (5), 055504. doi:10.1103/PhysRevLett.98.055504

Hixson, H. G., Wojcik, M. J., Devlin, M. S., Devlin, J. P., and Buch, V. (1992). Experimental and simulated vibrational spectra of H_2 absorbed in amorphous ice: Surface structures, energetics, and relaxations. *J. Chem. Phys.* 97 (2), 753–767. doi:10.1063/1.463240

Ilisca, E. (1991). Ortho-para H_2 conversion on a cold Ag(111) metal surface. *Phys. Rev. Lett.* 66 (5), 667–670. doi:10.1103/PhysRevLett.66.667

Ilisca, E., and Ghiglieno, F. (2016). Nuclear conversion theory: Molecular hydrogen in non-magnetic insulators. *R. Soc. Open Sci.* 3 (9), 160042. doi:10.1098/rsos.160042

Ilisca, E. (2018) 'Electromagnetic nuclear spin conversion: Hydrogen on amorphous solid water', *Chem. Phys. Lett.*, 713, pp. 289–292. doi:10.1016/j.cplett.2018.10.053

Ilisca, E. (2021). Hydrogen conversion in nanocages. *Hydrogen* 2 (2), 160–206. doi:10.3390/hydrogen2020010

Kornath, A., Zoermer, A., and Köper, I. (1999) 'Raman spectroscopic studies on matrix-isolated hydrogen and deuterium. 3. Molecular dynamics in matrices', *Spectrochimica Acta Part A Mol. Biomol. Spectrosc.*, 55(13), pp. 2593–2599. doi:10.1016/S1386-1425(99)00054-2

Kosone, T., Hori, A., Nishibori, E., Kubota, Y., Mishima, A., Ohba, M., et al. (2015). Coordination nano-space as stage of hydrogen ortho–para conversion. *R. Soc. Open Sci.* 2 (7), 150006. doi:10.1098/rsos.150006

Kumar, S., Jiang, H., Schwarzer, M., Kandratsenka, A., Schwarzer, D., and Wodtke, A. (2019). Vibrational relaxation lifetime of a physisorbed molecule at a metal surface. *Phys. Rev. Lett.* 123 (15), 156101. doi:10.1103/PhysRevLett.123.156101

Lavrov, E. V., and Weber, J. (2002). Ortho and para interstitial H_2 in silicon. *Phys. Rev. Lett.* 89 (21), 215501. doi:10.1103/PhysRevLett.89.215501

Laß, K., Han, X., and Hasselbrink, E. (2005). The surprisingly short vibrational lifetime of the internal stretch of CO adsorbed on Si(100). *J. Chem. Phys.* 123 (5), 051102. doi:10.1063/1.1993550

Lischka, M., and Groß, A. (2002). Hydrogen adsorption on an open metal surface: H_2/Pd(210). *Phys. Rev. B* 65 (7), 75420. doi:10.1103/PhysRevB.65.075420

Mårtensson, A.-S., Nyberg, C., and Andersson, S. (1986). Observation of molecular H_2 chemisorption on a nickel surface. *Phys. Rev. Lett.* 57 (16), 2045–2048. doi:10.1103/PhysRevLett.57.2045

Miyamoto, Y., Fushitani, M., Ando, D., and Momose, T. (2008) 'Nuclear spin conversion of methane in solid parahydrogen', *J. Chem. Phys.*, 128(11), p. 114502. doi:10.1063/1.2889002

Morin, M., Levinos, N. J., and Harris, A. L. (1992). Vibrational energy transfer of CO/Cu(100): Nonadiabatic vibration/electron coupling. *J. Chem. Phys.* 96 (5), 3950–3956. doi:10.1063/1.461897

Ohno, S., Ivanov, D., Ogura, S., Wilde, M., Arguelles, E. F., Diño, W. A., et al. (2018). Rotational state modification and fast ortho-para conversion of H_2 trapped within the highly anisotropic potential of Pd(210). *Phys. Rev. B* 97 (8), 085436. doi:10.1103/PhysRevB.97.085436

Peng, C., Stavola, M., Fowler, W. B., and Lockwood, M. (2009). Ortho-para transition of interstitial H_2 and D_2 in Si. *Phys. Rev. B* 80 (12), 125207. doi:10.1103/PhysRevB.80.125207

Prochaska, F. T., and Andrews, L. (1977). Vibration–rotational and pure rotational laser–Raman spectra of H_2, D_2, and HD in matrices at 12 K. *J. Chem. Phys.* 67 (3), 1139–1143. doi:10.1063/1.434965

Ruzi, M., and Anderson, T. D. (2013). Matrix isolation spectroscopy and nuclear spin conversion of NH_3 and ND_3 in solid parahydrogen. *J. Phys. Chem. A* 117 (39), 9712–9724. doi:10.1021/jp3123727

Schmidt, P. K., Christmann, K., Kresse, G., Hafner, J., Lischka, M., and Groß, A. (2001). Coexistence of atomic and molecular chemisorption states: H_2/Pd(210). *Phys. Rev. Lett.* 87 (9), 096103. doi:10.1103/PhysRevLett.87.096103

Scott, P. L., and Jeffries, C. D. (1962). Spin-lattice relaxation in some rare-earth salts at helium temperatures; observation of the phonon bottleneck. *Phys. Rev.* 127 (1), 32–51. doi:10.1103/PhysRev.127.32

Shan, J., Kleyn, A. W., and Juurlink, L. B. F. (2009). Adsorption of molecular hydrogen on an ultrathin layer of Ni(111) hydride. *Chem. Phys. Lett.* 474 (1–3), 107–111. doi:10.1016/J.CPLETT.2009.04.051

Stulen, R. H. (1988). Summary Abstract: Observation of molecular H_2 and D_2 on Pd and Ag using thermal desorption between 5 and 20 K. *J. Vac. Sci. Technol. A* 6 (3), 776–778. doi:10.1116/1.575111

Sugimoto, T., and Fukutani, K. (2014). Effects of rotational-symmetry breaking on physisorption of ortho- and para-H_2 on Ag(111). *Phys. Rev. Lett.* 112 (14), 146101. doi:10.1103/PhysRevLett.112.146101

Sugimoto, T., and Fukutani, K. (2011). Electric-field-induced nuclear-spin flips mediated by enhanced spin-orbit coupling. *Nat. Phys.* 7 (4), 307–310. doi:10.1038/nphys1883

Sugimoto, T., Yamakawa, K., and Arakawa, I. (2015). Infrared spectroscopic investigation of nuclear spin conversion in solid CH_4. *J. Chem. Phys.* 143 (22), 224305. doi:10.1063/1.4936655

Sugimoto, T., and Yamakawa, K. (2021). Nuclear-spin conversion analysis of $\nu_2 + \nu_4$ combination band of crystalline methane in phase II. *J. Chem. Phys.* 154 (2), 026101. doi:10.1063/5.0031272

Sun, Q., Reuter, K., and Scheffler, M. (2004). Hydrogen adsorption on RuO_2(110): Density-functional calculations. *Phys. Rev. B* 70 (23), 235402. doi:10.1103/PhysRevB.70.235402

Svensson, K., and Andersson, S. (2007). Fast ortho-para conversion of H_2 adsorbed at copper surface step atoms. *Phys. Rev. Lett.* 98 (9), 096105. doi:10.1103/PhysRevLett.98.096105

Svensson, K., Bengtsson, L., Bellman, J., Hassel, M., Persson, M., and Andersson, S. (1999). Two-dimensional quantum rotation of adsorbed H_2. *Phys. Rev. Lett.* 83 (1), 124–127. doi:10.1103/PhysRevLett.83.124

Tsuge, M., Kouchi, A., and Watanabe, N. (2021). Measurements of ortho-to-para nuclear spin conversion of H_2 on low-temperature carbonaceous grain analogs: Diamond-like carbon and graphite. *Astrophysical J.* 923 (1), 71. doi:10.3847/1538-4357/ac2a33

Tsuge, M., Namiyoshi, T., Furuya, K., Yamazaki, T., Kouchi, A., and Watanabe, N. (2021). Rapid ortho-to-para nuclear spin conversion of H_2 on a silicate dust surface. *Astrophysical J.* 908 (2), 234. doi:10.3847/1538-4357/abd9c0

Turgeon, P.-A., Vermette, J., Alexandrowicz, G., Peperstraete, Y., Philippe, L., Bertin, M., et al. (2017). Confinement effects on the nuclear spin isomer conversion of H_2O. *J. Phys. Chem. A* 121 (8), 1571–1576. doi:10.1021/acs.jpca.7b00893

Ueta, H., and Fukutani, K. (2023). Rotational-energy transfer in H_2 ortho-paraconversion on a metal surface: Interplay between electron and phonon systems. *J. Phys. Chem. Lett.* 14, 7591–7596. doi:10.1021/acs.jpclett.3c01209

Ueta, H., Sasakawa, Y., Ivanov, D., Ohno, S., Ogura, S., and Fukutani, K. (2020). Direct measurement of fast ortho-para conversion of molecularly chemisorbed H_2 on Pd(210). *Phys. Rev. B* 102 (12), 121407. doi:10.1103/PhysRevB.102.121407

Ueta, H., Watanabe, N., Hama, T., and Kouchi, A. (2016). Surface temperature dependence of hydrogen ortho-para conversion on amorphous solid water. *Phys. Rev. Lett.* 116 (25), 253201. doi:10.1103/PhysRevLett.116.253201

Warren, J. A., Smith, G. R., and Guillory, W. A. (1980). The infrared spectrum of matrix isolated hydrogen and deuterium. *J. Chem. Phys.* 72 (9), 4901–4908. doi:10.1063/1.439774

Wigner, E. P. (1933). Uber die paramagnetische U mwandlung on Para-Orthowasserstoff. III. *Z. Phys. Chem. B* 23, 28.

Yamakawa, K., Azami, S., and Arakawa, I. (2017). Phonon-mediated nuclear spin relaxation in H_2O. *Eur. Phys. J. D* 71 (3), 70. doi:10.1140/epjd/e2017-70642-8

Yamakawa, K., and Fukutani, K. (2020). Nuclear spin conversion of H_2, H_2O, and CH_4 interacting with diamagnetic insulators. *J. Phys. Soc. Jpn.* 89 (5), 051016. doi:10.7566/JPSJ.89.051016

Yamakawa, K., Ishibashi, A., Namiyoshi, T., Azuma, Y., and Arakawa, I. (2020). Fast nuclear-spin conversion of H_2 trapped and polarized in a CO_2 matrix. *Phys. Rev. B* 102 (4), 041401. doi:10.1103/PhysRevB.102.041401

frontiers | Frontiers in Physics

TYPE Original Research
PUBLISHED 14 September 2023
DOI 10.3389/fphy.2023.1240731

OPEN ACCESS

EDITED BY
Marco Sacchi,
University of Surrey, United Kingdom

REVIEWED BY
Yukun Lu,
China University of Petroleum, China
Jatis Kumar Dash,
SRM University, India

*CORRESPONDENCE
I. M. N. Groot,
✉ i.m.n.groot@lic.leidenuniv.nl

RECEIVED 15 June 2023
ACCEPTED 04 September 2023
PUBLISHED 14 September 2023

CITATION
Prabhu MK and Groot IMN (2023), From a Co-Mo precursor to 1H and 1T Co-promoted MoS_2: exploring the effects of gas pressure.
Front. Phys. 11:1240731.
doi: 10.3389/fphy.2023.1240731

From a Co-Mo precursor to 1H and 1T Co-promoted MoS_2: exploring the effects of gas pressure

M. K. Prabhu and I. M. N. Groot*

Leiden Institute of Chemistry, Leiden University, Leiden, Netherlands

The work presented in this paper makes use of the high-pressure *in situ* imaging capabilities of the ReactorSTM to demonstrate that single layer 1T Co-promoted MoS_2 can be directly synthesized without the use of any intercalating agents by applying highly reducing conditions during the growth. In this work, we have sulfided a CoMo nanoparticle precursor supported on Au(111) using a H_2:CH_3SH gas mixture at 1 bar and imaged the crystallization process *in situ* using the ReactorSTM. We have observed that at low temperatures (~500 K), an intermediate disordered $CoMoS_x$ phase is formed which crystallizes into metallic single-layer 1T Co-promoted MoS_2 slabs at temperatures close to 600 K. We also show that semiconducting 1H Co-promoted MoS_2 slabs synthesized under sulfur-rich conditions using a vacuum physical vapor deposition process, do not transform into their metallic 1T counterparts when exposed to the same reducing gas pressures and temperatures, thus, demonstrating the importance of the highly reducing conditions during the crystallization process for inducing the formation of the metastable 1T phase. XPS spectra of the 1T Co-promoted MoS_2 slabs indicate a sulfur deficiency of up to 11% in the top layer S, suggesting the likely role of sulfur vacancies in the formation of the 1T phase.

KEYWORDS

1T Co-promoted MoS_2, scanning tunneling microscopy, atmospheric-pressure studies, *in situ*, X-ray photoelectron spectroscopy

1 Introduction

Single-layer transition metal dichalcogenides (TMDCs) based on MoS_2 have garnered a lot of attention in both fundamental and applied research over the last several decades. A classic example of such an MoS_2-based TMDC is Co-promoted MoS_2 which is very important for many globally-relevant applications involving optoelectronics, heterogeneous catalysis, and electrocatalysis. For instance, catalysts based on Co-promoted MoS_2, a transition metal dichalcogenide formed by sulfiding mixed Co-Mo nanoparticles, are used for reducing global SO_x emissions via hydroprocessing in petroleum refineries [1], mixed alcohol synthesis [2], selective olefin hydrogenation [3], and selective mercaptan synthesis [4, 5]. Co-promoted MoS_2 is also widely used as a noble-metal-free electrocatalyst for the hydrogen evolution reaction (HER) [6] and Li-ion battery electrodes [7]. Particularly, its 1T metastable counterpart, has been of great relevance to van der Waals heterostructure-based optoelectronic devices due to its room temperature ferromagnetism [8–11].

In the laboratory, the 1T and 1T' analogues of pristine and promoted MoS_2 can be synthesized by various strategies. One of the techniques involves using alkali metals like Li, Na, or K during the MoS_2 synthesis. The alkali metals intercalate in the MoS_2 van der Waals gap and stabilize the 1T and 1T' phases, thus lowering the bandgap for the metastable phase formation with Mo in an octahedral coordination environment [12–17]. This technique has been used to synthesize and explore applications of Na- and K-doped single-layer MoS_2 and Co-promoted MoS_2 for gas-phase and HER catalysis [5, 18]. Intercalation with electron-donating aromatic amines has also proven to be successful in inducing the phase transformation from 1H to 1T [19]. An alternative synthesis strategy for the 1T or 1T' MoS_2 phase involves using a sulfur-deficient environment during the synthesis by lowering the chemical potential of sulfur [15, 20]. Additionally, using argon ion bombardment of 2H MoS_2 has been shown to generate local 1T mosaic structures [21]. The sulfur vacancy may also be generated by doping with a foreign metal atom of a different formal charge, for instance, Ru or substitutionally co-doping Ni and Co, to generate the 1T phase from the 2H phase [22, 23]. Similarly, oxygen doping has also been used as a technique to generate sulfur vacancies, and thereby, induce the formation of the 1T phase [24]. Electrochemical incorporation of S vacancies to induce a 2H–1T phase transition has also been reported [25]. Chalcogen vacancies in other Mo TMDCs have also been shown to induce a phase transition to the 1T and 1T' counterpart [26]. These experiments have generated a lot of excitement in the scientific community, because 1T polymorphs of MoS_2 have been shown to have high hydrogen evolution activity due to its metallic nature, unlike the 1H counterpart, and have been explored for applications in energy production and storage devices, in addition to applications in spintronics due to room temperature ferromagnetism [27–30]. Especially, many metastable 1T and 1T' phases of Co-doped MoS_2 have been demonstrated to be very competitive noble metal-free alternatives for green hydrogen production via water splitting, which has generated a lot of interest in the synthesis of 1T and 1T' counterparts of Co-promoted MoS_2 [6, 31, 32].

Based on these experimental findings, we hypothesize that it should be possible to directly synthesize 1T Co-promoted MoS_2 slabs from metallic Co and Mo nanoparticles by maintaining highly reducing environments during the synthesis, e.g., through a combination of hydrogen gas and the sulfiding agent. Use of hydrogen during the crystallization is expected to generate S-vacanies on the edges and the basal plane. According to the recent work of Jin et. al. [20], formation of edge S defects and edge sulfur saturations of less than 50% can kinetically favor the formation of the 1T phase by layer sliding. Additionally, the ease of hydrogen dissociation on under-coordinated and metallic Mo [33, 34] during the synthesis may even allow for some stabilization of the Co-promoted MoS_2 slabs through hydride intercalation. Based on the works of Mom et. al. and Grønborg et. al. [33, 34], such reducing conditions can be achieved by using background pressures of hydrogen approaching several bars, typically not possible in an ultra-high vacuum (UHV) setup. Furthermore, using a lower temperature for sulfidation may arrest the transition to the 2H phase. For instance, heating K-promoted MoS_2 to 650 K and above, under high gas pressures has been observed to induce irreversible transition to the 1H phase [5]. Burkhanov et. al. have shown that hydrogen intercalation achieved using H plasma under vacuum environments leads to lattice expansion of MoS_2 similar to that from the 1H to 1T phase transition [35].

In order to test our hypothesis, we have sulfided a precursor containing mixed Co-Mo nanoparticles supported on Au(111) under high-pressure sulfo-reductive conditions and observed *in situ* the crystallization process using the ReactorSTM setup. At temperatures of up to ~500 K, a disordered $CoMoS_x$ phase is observed to form which then crystallizes into single-layer 1T Co-promoted MoS_2 when the temperature is raised to 600 K. Sulfiding an identical CoMo precursor using H_2S under vacuum results in the formation of 1H Co-promoted MoS_2 slabs which do not transform into the 1T counterpart when exposed to the same sulfo-reductive conditions, suggesting that reducing conditions are necessary during the crystallization step to form the 1T phase. XPS spectra acquired post synthesis show that the 1T Co-promoted MoS_2 slabs are largely sulfur-deficient, suggesting the role of sulfur vacancies in metastable phase formation. Thus, we demonstrate that the 1T Co-promoted MoS_2 can be readily synthesized and stabilized by using a lower sulfidation temperature and sufficiently sulfo-reductive conditions, without the need for any additional intercalating agents. Furthermore, the ability to observe the formation of a metastable 1T Co-MoS_2 phase *in situ* (i.e., *while it happens*) with atomic resolution under 1 bar of gas pressure, elevated temperature, and aggressive chemical conditions, is the main novelty of this work, as it has remained an experimental challenge to do so for several decades. Additionally, the experimental observation that elevating the gas pressure to attain sufficiently reducing conditions to favor the formation of 1T Co-MoS_2 without the need of an intercalating agent is a very important finding that provides us a fundamental understanding of the 1T phase formation process and is also an additional novelty. To the best of our knowledge, the experimental work presented in this paper has not been carried out elsewhere in the past.

2 Materials and Methods

2.1 Sample cleaning

All the experiments were carried out in the ReactorSTM setup [36]. The sample cleaning procedure reported in our previous works has been used [37]. Briefly, a polished Au(111) crystal was cleaned by a cyclic sputtering and annealing procedure until XPS could no longer detect any impurities (<0.001 monolayers (ML)). 1.5 keV Ar^+ ions were used for the sputtering and annealing at 873 K was performed using radiative heating from a thoriated-tungsten filament at the back of the sample.

2.2 Physical vapor deposition (PVD)

To grow Mo and Co nanoparticles, Mo and Co rods of 99.99% purity purchased from Goodfellow were used. The evaporation of the respective metals was carried out using an EGCO4 e-beam evaporator. During the evaporation, the clean Au(111) sample was held at room temperature until the coverage of the respective metal was measured to be ~0.2 monolayers (ML). The coverage was

measured by analyzing the XPS spectra of Co and Mo with respect to Au(111) surface layers. Identical samples were prepared for the low-pressure and high-pressure sulfidation.

2.3 Low-pressure sulfidation

The mixed Co-Mo nanoparticles supported on Au(111) were sulfided at 650 K in a 2×10^{-6} mbar H_2S atmosphere. The heating from room temperature to 650 K was carried out in the same H_2S background at a rate of 4 K/s and held at 650 K for 20 min. The sample was then cooled in the H_2S background to 450 K over 15 min and thereafter, to room temperature in UHV over 150 min.

2.4 High-pressure sulfidation

The high-pressure sulfidation of the mixed Co-Mo precursor was carried out in the ReactorSTM. For this purpose, a sulfo-reductive gas mixture containing 9 H_2: 1 CH_3SH at a total pressure of 1 bar was chosen as the sulfiding agent. A temperature of 603 K was used for sulfidation as this is the highest temperature attainable in the ReactorSTM [38, 39]. A temperature of 520 K was also selected as an intermediate temperature to observe the effect of temperature.

After loading the sample for sulfidation into the reactor, the STM was first pressurized to 0.1 bar with the sulfo-reductive mixture and thereafter, the temperature was raised to 520 K with a heating rate of 2 K/min. A slow heating rate was chosen because rapid heating would cause rupturing of the fluor-elastomer seals used for isolating the ReactorSTM from the rest of the UHV. After this step, the total pressure was raised to 1 bar at a rate of 0.1 bar/min. The system was allowed to reach thermal steady-state for 90 min in order to minimize the thermal drift. The STM tip was brought into tunneling contact thereafter and the scanning was commenced. After scanning for ~70 min, the tip was retracted, the sample temperature was raised to 603 K at 3 K/min, and the system was allowed to thermally stabilize for 30 min before continuing the STM scanning.

2.5 Scanning tunneling microscopy

STM scanning was performed with the ReactorSTM using both the UHV mode and the high-pressure mode. STM tips were prepared by cutting polycrystalline Pt-Ir 90–10 wires purchased from Goodfellow without further processing. Constant-current scans were performed using LPM video-rate scanning electronics described in detail elsewhere [40, 41]. Home-developed Camera software and WSxM were used for STM image processing [42, 42]. Line-by-line background subtraction was used for the ease of viewing of the STM images. All UHV scans were carried out at room temperature.

For the high-pressure STM imaging, the sample was loaded into the STM assembly and a Kalrez seal was placed between the sample and the reactor. Thereafter, the bellows of the reactor were actuated to close the reactor and establish the closed volume for introducing the reaction gases. Gas bottles of Ar (N5.0), H_2 (N5.0), and CH_3SH (N2.8) {dimethylsulfide and dimethyldisulfide are the primary impurities} procured from Westfalen AG were used for all the experiments. The gas purity was confirmed using a mass spectrometer before use. The gas lines were flushed with Ar and baked out at 423 K for 12 h to remove any residual water and volatiles before commencing all experiments presented in this work.

For the post-sulfidation characterization, depressurizing the ReactorSTM to UHV conditions is necessary. For this purpose, the total pressure in the ReactorSTM was reduced to 0.1 bar and the model catalyst was allowed to cool down to 373 K under the flow of gases over 15 min. Thereafter, the gases were pumped away, the ReactorSTM was brought under UHV conditions, and the sample allowed to cool to room temperature over 60 min.

2.6 X-ray photoelectron spectroscopy

A commercial SPECS Phoibos system equipped with an XRM50 X-ray source set to the Al K-alpha line and coupled to a monochromator was used to excite the sample with a 54.6° incidence angle and with the X-rays generated using an acceleration voltage of 10 kV, 250 W. A HSA3500 hemispherical analyzer with a pass energy of 30 eV was used to acquire all the XPS spectra reported in this paper. All spectra were calibrated using the peak position of the Au 4f signal (84.0 eV) of the Au(111) substrate. For all the acquired data, 30 integrations were performed to have a sufficiently high signal-to-noise ratio. XPSPEAK41 software was used for the peak deconvolution. Relative sensitivity factors for surfaces were obtained from literature [43]. Shirley background subtraction was performed for all the spectra and a non-linear least squares fit method was used for convergence. The XPS spectra were fit using mixed Gaussian (65%) –Lorentzian (35%) (GL) curves. Asymmetric GL curves were used to fit the spectra of Co $2p_{3/2}$. For the Mo 3d and S 2p, paired GL peaks with a constrained area ratio of 3:2 and 1:2, respectively, were used to account for the spin-orbit splitting. For Co 2p, the fitting is performed for the Co $2p_{3/2}$ component. All the signature peak positions are based on previously reported literature work and are tabulated in Table 1 along with the references.

3 Results and discussion

We first prepare identical precursors containing Co-Mo mixed nanoparticles supported on a clean Au(111) substrate by sequential physical vapor deposition (PVD) of 0.2 monolayers (ML) Mo metal, followed by 0.2 ML Co metal at room temperature. The exact synthesis procedure is detailed in the Materials and Methods section and in the Supplementary Materials.

First, as a control experiment, one of the identical Co-Mo precursors was sulfided at 650 K under 2×10^{-6} mbar of H_2S and cooled to room temperature according to the recipe detailed in the Materials and Methods section, in order to replicate the vacuum synthesis recipe of single layer 1H Co-promoted MoS_2 slabs on Au(111) [48]. After this step, the sample was loaded into the ReactorSTM operated in the UHV mode. Figure 1 shows a large-scale STM image thus obtained. In Figure 1, we observe the formation of atomically-flat hexagonal slabs which are identified as single-layer 1H Co-promoted MoS_2 slabs. Under the sulfur-rich

TABLE 1 XPS binding energies for various components used for peak fitting.

Components	Binding energy (BE) (eV)	ΔBE[a] (eV)	References
1H MoS_2 Mo $3d_{5/2}$	229.2	3.15	[5, 27, 44, 45]
1T MoS_2 Mo $3d_{5/2}$	228.3	3.15	[5, 27, 44, 45]
S $2p_{3/2}$ (1T MoS_2)	161.8	1.16	[5, 27, 44, 45]
S $2p_{3/2}$ (2D CoS_2, 1H MoS_2)	162.7	1.16	[5, 27, 37, 44–46]
S 2s	226.9		[5, 27, 37, 44–46]
CoS_2 main Co $2p_{3/2}$	778.1		[27, 44, 47]
CoS_2 satellites Co $2p_{3/2}$	781.1, 783.1		[27, 44, 47]
Co-MoS_2 main Co $2p_{3/2}$	778.6		[27, 44, 47]
Co-MoS_2 satellite Co $2p_{3/2}$	781.6, 783.6		[27, 44, 47]

[a]ΔBE, is the energy difference between the spin-orbit splitting components. For example, ΔBE(3d) = BE, $3d_{5/2}$–BE, $3d_{3/2}$.

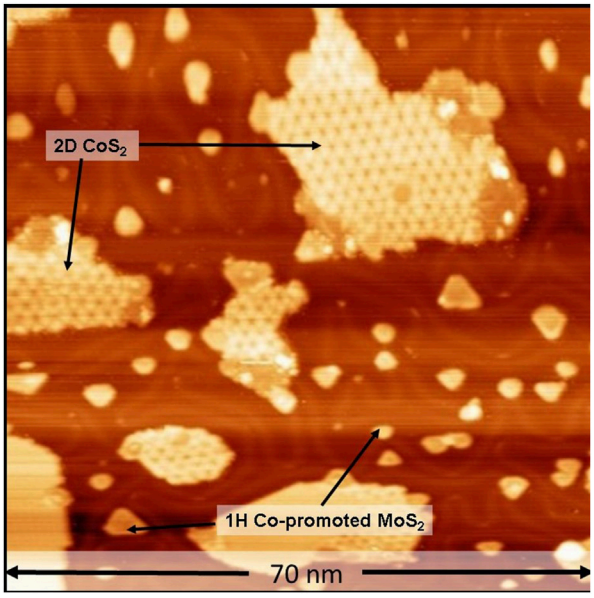

FIGURE 1
STM image of single-layer 1H Co-promoted MoS_2 slabs prepared by sulfidation of the Co-Mo precursor with H_2S (2×10^{-6} mbar). The STM image was acquired in UHV with a sample voltage of −1 V and tunneling current of 100 pA.

conditions used in this experiment, pristine MoS_2 slabs are known to display only the Mo-terminated edges due to the thermodynamic stability of the Mo-termination and hence, adopt a triangular shape [49]. The substitution of Mo atoms by Co along the S-terminated edges leads to the thermodynamic stability of the S-termination as well, thus, driving the formation of hexagon-shaped slabs such as those in Figure 1 [33]. The Co-promoted MoS_2 slabs have a bright outline along their periphery while their basal planes are imaged relatively darker. The darker basal plane is attributed to the semiconducting nature of 1H Co-promoted MoS_2 while the bright edge features are attributed to the 1D metallic edge states called BRIM sites [33]. Additionally, we also observe the formation of the single-layer 2D CoS_2 phase as a byproduct, with the characteristic hexagonal moiré structure which is 7 × 7 Au atoms (1.95 nm × 1.95 nm) wide. The 2D CoS_2 phase is also observed to form between the Co-promoted MoS_2 slabs on the Au(111) steps. These observations are in excellent agreement with our recent work on 2D CoS_2 slabs supported on Au(111) [46]. Furthermore, the observation of the complete conversion of the Co and Mo nanoparticles into the respective TMDC phases after the sulfidation process is in agreement with the prior experimental works on the sulfidation of Co and Mo nanoparticles under controlled vacuum conditions [33, 49, 50].

In order to test our hypothesis on the formation of 1T Co-promoted MoS_2 slabs under highly reducing conditions, a freshly prepared identical Co-Mo precursor was sulfided using high-pressure sulfo-reductive conditions within the ReactorSTM. For this purpose, a sulfo-reductive gas mixture (9:1 H_2:CH_3SH) was used to pressurize the ReactorSTM to 1 bar. Thereafter, the temperature was raised from room temperature to 520 K at a rate of 2 K/min. Figure 2A shows a large-scale STM image obtained *in situ* during the sulfidation under the sulfo-reductive gas mixture. We observed the formation of two phases: islands with a somewhat hexagonal shape and disordered arrangement of bright protrusions and large atomically-flat islands with an ordered hexagonal pattern, both of which are seen in Figures 2A, B.

The somewhat hexagon-shaped islands are identified as those of poorly crystalline molybdenum sulfide (MoS_x). Due to the presence of a sufficient number of diffusing cobalt atoms, we expect that any MoS_x phase formed will likely be doped with Co atoms, and hence, we denote this phase as $CoMoS_x$. The $CoMoS_x$ islands are measured to be 2.8 Å high (see heightline, Figure 2B), matching closely with the measured height of single-layer Co-promoted MoS_2 from previous experimental reports [33]. The $CoMoS_x$ islands are likely an intermediate phase towards the formation of crystalline Co-promoted MoS_2. No further changes are observed in this disordered $CoMoS_x$ phase up to 67 min into the scanning in the sulfo-reductive gas environment at 520 K (see Figures 2C, D), suggesting that the temperature is insufficient for any crystallization to occur.

The atomically-flat slabs with a hexagonal moiré pattern on their basal plane are identified as 2D CoS_2 islands. These slabs were also observed to form in our control experiment (see Figure 1).

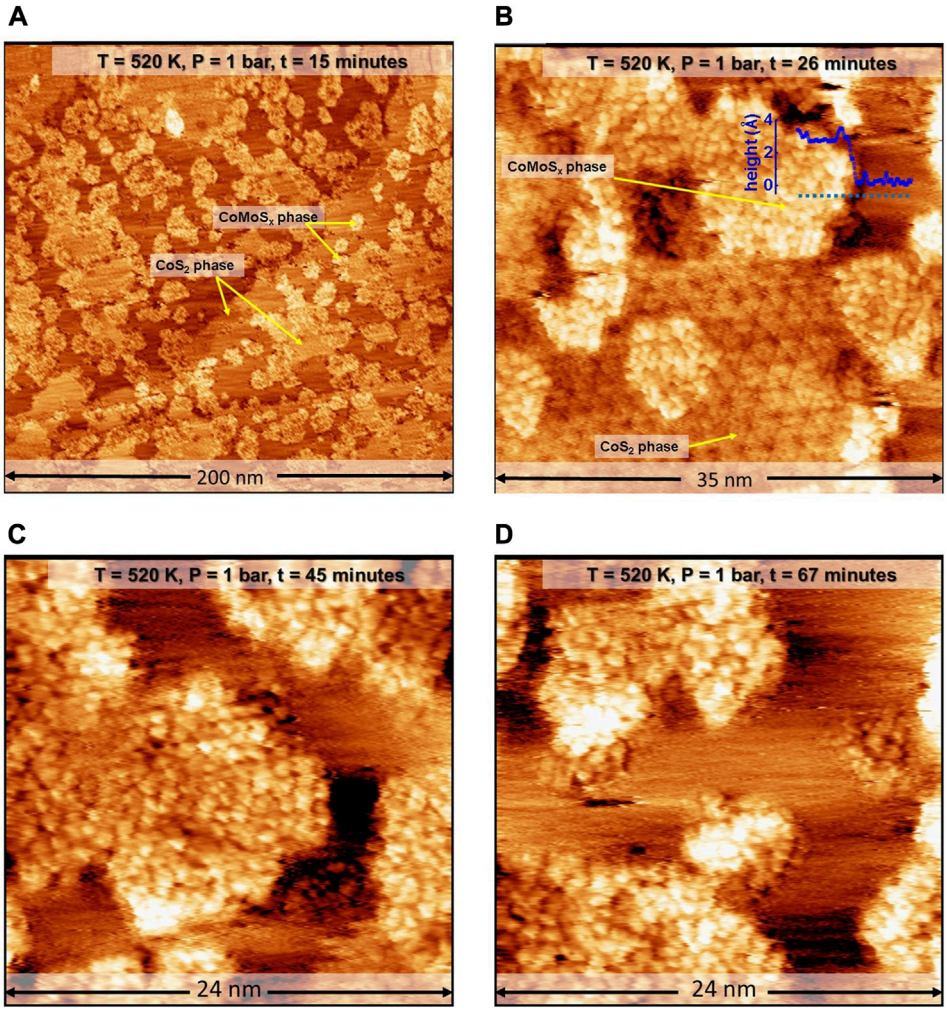

FIGURE 2
(A–D) STM images of the Co-Mo precursor acquired *in situ* during the sulfidation by a sulfo-reductive gas mixture (1 bar, $9H_2$: $1CH_3SH$) at 520 K. The MoS_x and 2D CoS_2 phases are identified. The STM images were aquired at −0.3 V sample voltage and 500 pA tunneling current. The "t" indicated in the label bars at the top of each STM image indicates the time stamp of acquisition from the commencing of the scanning.

The 2D CoS_2 also retains the characteristic hexagonal moiré structure indicating that the basal plane of 2D CoS_2 does not undergo significant structural changes under the sulfo-reductive gas mixture used. Additionally, the formation of this moiré structure shows that the 2D CoS_2 islands are crystalline in nature and that the sulfidation of Co nanoparticles is already complete during the process of bringing the ReactorSTM to the operating conditions. This rapid spread and reaction of Co is attributed to the cluster diffusion behavior of Co nanoparticles in the presence of S adatoms which leads to rapid growth of 2D CoS_2 [50].

To speed up the process of $CoMoS_x$ crystallization, we further increased the temperature to 603 K at the rate of 2 K/min while maintaining the sulfo-reductive reaction gases and thermally stabilize the STM before commencing the scanning *in situ*. Figure 3A shows a large-scale STM image obtained *in situ* at 603 K at t = 121 min. Ten minutesafter attaining 603K, the edges of the $CoMoS_x$ islands are observed to appear slightly brighter in the STM images, as can be seen in Figure 3B. Over the next 35 min, the $CoMoS_x$ slabs are observed to crystallize from the step edges towards the interior (see Figures 3B–F). The crystallization is evident from the formation of an ordered hexagonal lattice. The new crystalline phase has a hexagonal arrangement of bright protrusions which are 0.33 ± 0.01 nm apart (see Figure 3F; height profile in Figure 3G). This matches closely with the basal plane S-S distance of single-layer MoS_2 and Co-promoted MoS_2 [49]. Furthermore, the basal plane protrusions are imaged bright with respect to gold, unlike the 1H Co-promoted MoS_2 in Figure 1, suggesting that this phase has a metallic nature. The crystalline Co-promoted MoS_2 formed under sulfo-reductive conditions (see Figures 3B–D), however, does not have a bright BRIM along the edges, unlike the 1H Co-promoted MoS_2 slabs in the control experiment (see Figure 1). All characteristics of this new crystalline phase formed in the sulfo-reductive environment agree very well with those reported for a metastable 1T-MoS_2 phase in which Mo is in an octahedral coordination environment [15, 28]. Therefore, we identify this new phase as that of single-layer 1T Co-promoted MoS_2. Figures 3B–D also show that the crystalline phase is not resolved well along

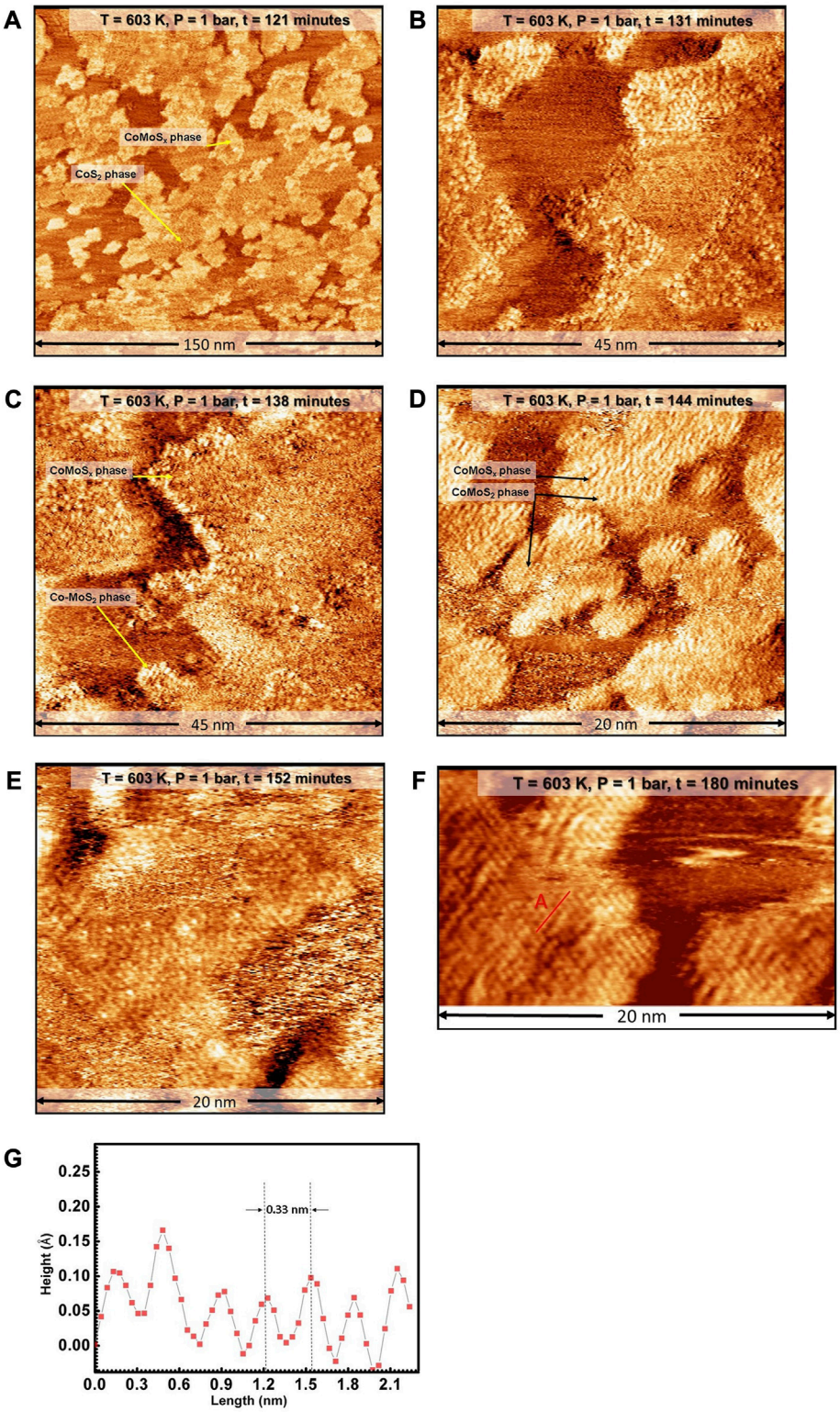

FIGURE 3
(A–F) STM images of the Co-Mo precursor acquired *in situ* during the sulfidation by a sulfo-reductive gas mixture (1 bar, $9H_2$: $1CH_3SH$) at 603 K. The MoS_x and 2D CoS_2 phases are identified. The STM images were aquired at −0.3 V sample voltage and 500 pA tunneling current. The "t" indicated in the label bars at the top of each STM image indicates the time stamp of acquisition from the commencing of the scanning. **(G)** Height profile along the red line marked A in F. E anf F have additional derivative enhancing in order to bring forward the detail for the ease of viewing.

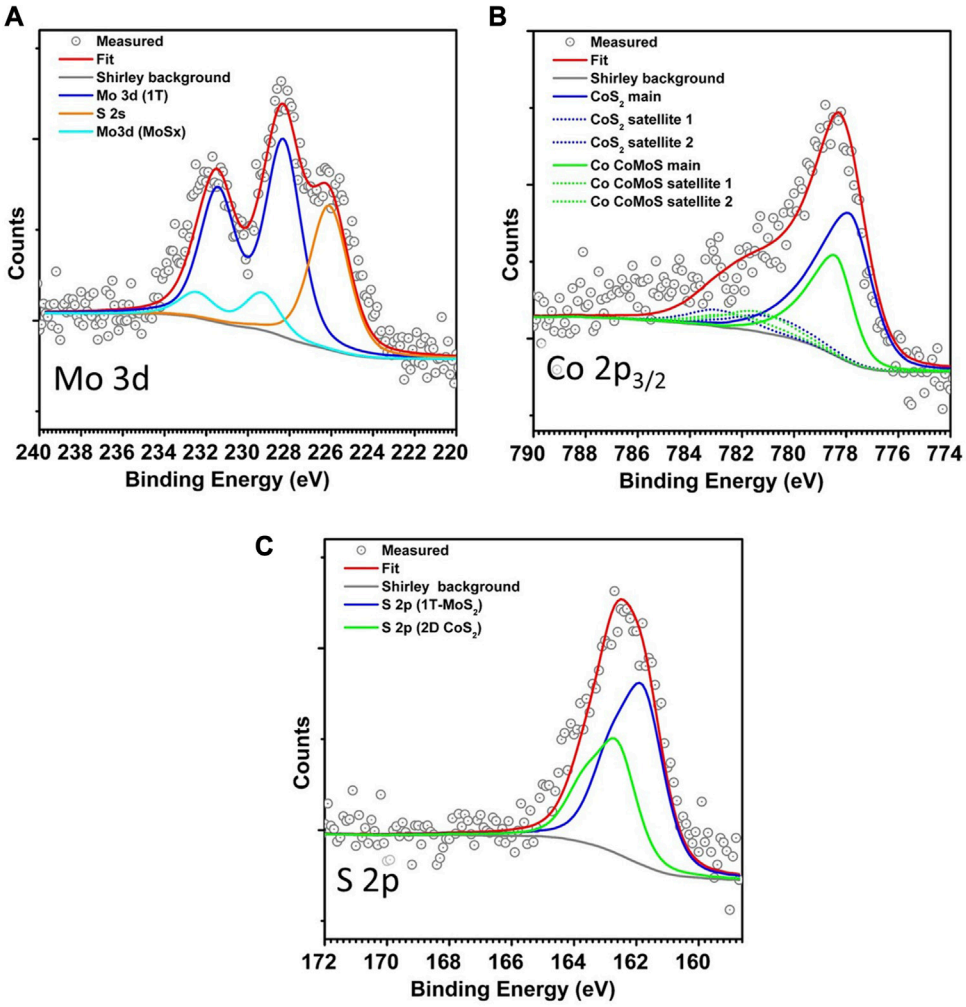

FIGURE 4
(A–C) Mo 3d, Co $2p_{3/2}$, and S 2p XPS spectra of the Co-Mo precursor supported on Au(111) after sulfidation in the high-pressure sulfo-reductive gases at 603 K.

one of the crystallographic directions especially along the slow scan direction (top to down), giving the appearance of lines. We attribute this to tip assymetry arising from interaction with the gases, especially CH_3SH at the elevated temperature and pressure used. Such effects were also observed by Mom et. al. under similar gas conditions when using similar as-cut Pt-Ir tips [34].

One may expect that employing a high partial pressure of hydrogen during the cyrstallization favors the formation of a large number of sulfur vacancies along the Co-MoS_2 edges and the basal plane. Recent theoretical work [20] has shown that increasing the number of sulfur vacancies can make translational layer sliding to form the 1T configuration more kinetically favorable in pristine MoS_2 slabs. While it may also be argued that the electron donation from Co also aids in the formation of 1T Co-promoted MoS_2, merely having the Co alone does not yield the formation of the 1T phase under the vacuum sulfidation-based control experiment. We also consider the possibility that using a different sulfiding agent may also aid in the formation of the 1T phase as we have used H_2S for our control experiment and CH_3SH for the high-pressure sulfidation as the sulfiding agents. Research carried out in the past has shown that the effect of sulfiding agents on the chemical potential of sulfur is minor for small thiol-containing molecules like H_2S and CH_3SH, as they all readily disssociate on the gold surface and form adsorbed–SH while aromatic (such as thiophenes) and doubly substituted thiols (like dimethyl sulfide) lead to a lower chemical potential of sulfur [33], [51–53]. Additionally, previous experiments using a variety of H_2:H_2S mixtures under vacuum pressures for MoS_2 synthesis did not lead to the formation of the 1T phase [49]. Therefore, the elevated H_2 gas pressure used in our experiment to form a sufficient number of sulfur vacancies remains as a major factor that assists in the formation of 1T Co-promoted MoS_2.

We make use of XPS analysis to determine the number of sulfur vacancies and the amount of Co incorporation into the edges of 1T Co-promoted MoS_2. As the 1T phase is metallic, BRIM sites are not present on the edges, making the identification of the Co-substituted S edges from the STM images alone difficult. XPS, on the other hand, can detect and resolve Co present in 1T MoS_2 and CoS_2 phases, albeit in a statistically averaged manner [9, 54]. Typically, the Co

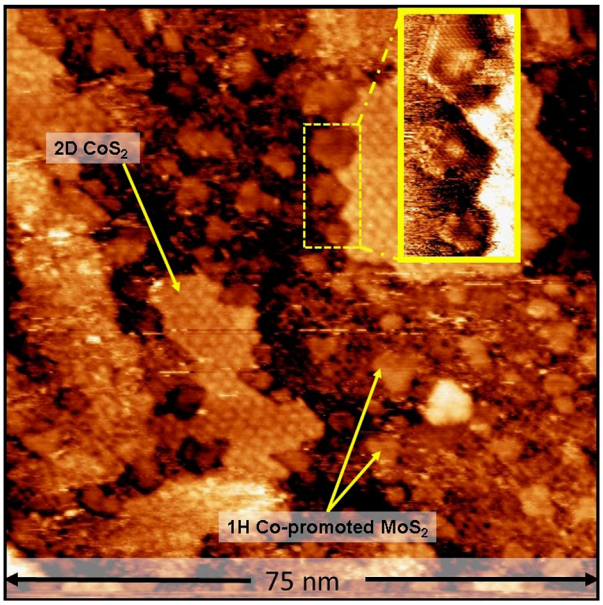

FIGURE 5
In situ STM image of vacuum-synthesized Co-promoted MoS_2 slabs after 6 h under the sulfo-reductive gas environment (1 bar, 9:1 H_2:CH_3SH, 603 K). The inset shows atom-resolved 1H Co-promoted MoS_2 slabs with BRIM sites. STM image acquired with a sample voltage of −0.3 V and tunneling current of 500 pA.

present on the S edges of 1H and 1T MoS_2 has a signal resembling metallic Co sulfide but shifted by 0.6–0.8 eV to higher binding energy depending on the metallicity of the support [9, 54, 55]. Additionally, the structural relaxation upon the transformation of the 1T phase into the 2H phase results in a downshift in binding energy of the Mo 3days and S 2p spectra of the 1T phase by ~0.9 eV with respect to the 1H phase, thus allowing for the identification of the 1T phase [56, 57]. Before measuring the XPS spectra, the sample exposed to high pressure was cooled to room temperature in the sulfo-reductive gas environment and then pumped down to UHV. Thereafter, XPS spectra of Mo 3d, S 2p and Co 2p were acquired and analyzed. The Mo 3d spectrum (see Figure 4A) shows the main Mo $3d_{5/2}$ peak at 282.3 eV which matches well with the reported XPS spectra of 1T-MoS_2 and 1T-Co-promoted MoS_2 [54, 57]. The component at 290.2 eV is attributed to the unconverted MoS_x phase as we did not observe any 1H Co-promoted MoS_2 in the STM images. The Co $2p_{3/2}$ spectrum (see Figure 4B) shows the presence of 2 types of cobalt species, namely, the Co in metallic 2D CoS_2 at 778.1 eV (55%) and the Co present on the edges of MoS_2 at 778.7 eV (45%). The corresponding S 2p spectrum (see Figure 4C) shows an asymmetric peak that consists of contributions from S in 2D CoS_2 and the 1T phase. Furthermore, comparing the overall signals of Co, Mo, and S, the molecuar formula of 1T Co-MoS_2 is determined to be $Mo_{0.67}Co_{0.32}S_{1.89}$, with 11% sulfur vacancies in the top layer (see Supplementary Material S1.2, Supplementary Table S2). The high number of sulfur vacancies is expected due to the highly reducing environment used during the synthesis in the ReactorSTM. In comparison, the molecular formula of the 1H Co-promoted MoS_2 from the control experiment is determined to be $Mo_{0.65}Co_{0.35}S_{2.05}$.

As an additional control experiment, the control sample containing 1H Co-promoted MoS_2 slabs grown using 2×10^{-6} mbar H_2S was loaded into the ReactorSTM and exposed to the high-pressure sulfo-reductive gas mixture (9:1 H_2:CH_3SH, 1 bar) at 603 K for up to 6 h. Figure 5 shows a large-scale STM image obtained *in situ* after 6 h. Comparing Figures 1, 5, we observe that the morphology of the Co-promoted MoS_2 slabs is largely preserved. Under these gas conditions, we expect that the edges of the Co-promoted MoS_2 slabs are reduced to the same degree as in our high-pressure sullfidation experiment since the gas conditions are identical. In Figure 5, we clearly observe that all the Co-promoted MoS_2 slabs remain in the 1H state and do not transform into the 1T state, as can also be seen in the atom-resolved inset where 1H Co-promoted MoS_2 slabs with BRIM sites

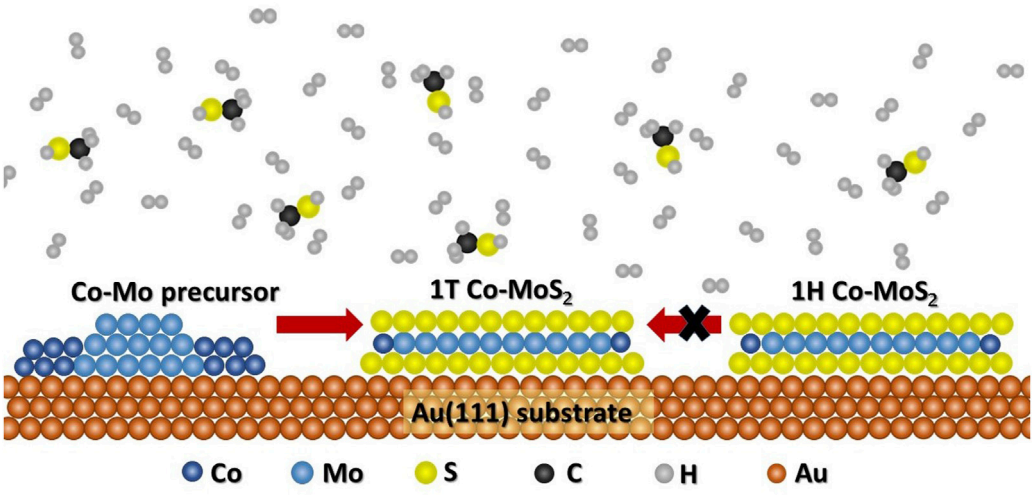

FIGURE 6
Schematic diagram describing the kinetically favorable and unfavorable routes for the 1T Co-promoted MoS_2 formation.

are clearly imaged. This shows that the 1T state is accessible at the gas conditions and temperatures used, if and only if, the thermodynamically stable 1H state has not already been formed. A schematic summarizing all our findings is shown in Figure 6.

4 Conclusion

We have demonstrated using the *in situ* STM imaging capabilities of the ReactorSTM, that using sufficiently reducing environments during the crystallization phase can favor the formation of metallic 1T Co-promoted MoS_2. On the other hand, if 1H Co-promoted MoS_2 is already formed, then there are large kinetic barriers that hinder the formation of a sufficient number of S vacancies to drive the transformation to the 1T phase through atomic S-layer sliding. These observations with the STM are confirmed and supported very well by the corresponding XPS spectra which show that the 1T Co-MoS_2 slabs have a large number of sulfur vacancies in comparison to the 1H Co-MoS_2 slabs. The formation of pure 1T Co-promoted MoS_2 under sulfo-reductive conditions without an alkali metal intercalator is remarkable as it demonstrates the feasibility for directly synthesizing monolayers of pure 1T or 1H Co-promoted MoS_2. This is of great relevance for fundamental research in optoelectronics, green hydrogen production, and heterogeneous and electro-catalysis.

Data availability statement

The original contributions presented in the study are included in the article/Supplementary Material, further inquiries can be directed to the corresponding author.

Author contributions

MP performed all experiments and analyzed all data. IG conceived and supervised the project. All authors contributed to the article and approved the submitted version.

Funding

This project received funding from the Leiden Institute of Chemistry, Leiden University.

Conflict of interest

The authors declare that the research was conducted in the absence of any commercial or financial relationships that could be construed as a potential conflict of interest.

Publisher's note

Supplementary material

The Supplementary Material for this article can be found online at: https://www.frontiersin.org/articles/10.3389/fphy.2023.1240731/full#supplementary-material

References

1. Sanders AFH, De Jong AM, De Beer VHJ, Van Veen JAR, Niemantsverdriet JW. Formation of cobalt-molybdenum sulfides in hydrotreating catalysts: A surface science approach. *Appl Surf Sci* (1999) 144–145:380–4. doi:10.1016/S0169-4332(98)00831-9

2. Taborga Claure M, Chai SH, Dai S, Unocic KA, Alamgir FM, Agrawal PK, et al. Tuning of higher alcohol selectivity and productivity in CO hydrogenation reactions over K/MoS_2 domains supported on mesoporous activated carbon and mixed MgAl oxide. *J Catal* (2015) 324:88–97. doi:10.1016/j.jcat.2015.01.015

3. Liu B, Liu L, Chai YM, Zhao JC, Liu CG. Essential role of promoter Co on the MoS_2 catalyst in selective hydrodesulfurization of FCC gasoline. *Ranliao Huaxue Xuebao/journal Fuel Chem Technol* (2018) 46(4):441–50. doi:10.1016/s1872-5813(18)30019-7

4. Gutiérrez OY, Kaufmann C, Hrabar A, Zhu Y, Lercher JA. Synthesis of methyl mercaptan from carbonyl sulfide over sulfide K $_2MoO_4/SiO_2$. *J Catal* (2011) 280(2): 264–73. doi:10.1016/j.jcat.2011.03.027

5. Yu M, Kosinov N, Van Haandel L, Kooyman PJ, Hensen EJM. Investigation of the active phase in K-promoted MoS_2 catalysts for methanethiol synthesis. *ACS Catal* (2020) 10(3):1838–46. doi:10.1021/acscatal.9b03178

6. Dai X, Du K, Li Z, Liu M, Ma Y, Sun H, et al. Co-doped MoS_2 nanosheets with the dominant CoMoS phase coated on carbon as an excellent electrocatalyst for hydrogen evolution. *ACS Appl Mater Inter* (2015) 7(49):27242–53. doi:10.1021/acsami.5b08420

7. Chen B, Liu E, He F, Shi C, He C, Li J, et al. 2D sandwich-like carbon-coated ultrathin TiO_2@defect-rich MoS_2 hybrid nanosheets: Synergistic-Effect-Promoted electrochemical performance for lithium ion batteries. *Nano Energy* (2016) 26: 541–9. doi:10.1016/j.nanoen.2016.06.003

8. Wang Y, Li S, Yi J. Electronic and magnetic properties of Co doped MoS_2 monolayer. *Sci Rep* (2016) 6:24153. doi:10.1038/srep24153

9. Nethravathi C, Prabhu J, Lakshmipriya S, Rajamathi M. Magnetic Co-doped MoS_2 nanosheets for efficient catalysis of nitroarene reduction. *ACS Omega* (2017) 2:5891–7. doi:10.1021/acsomega.7b00848

10. Sanikop R, Gautam S, Chae KH, Sudakar C. Robust ferromagnetism in Mn and Co doped 2D-MoS_2 nanosheets: Dopant and phase segregation effects. *J Magn Magn Mater* (2021) 2021:168226. doi:10.1016/j.jmmm.2021.168226

11. Lin X, Ni J. Charge and magnetic states of Mn-Fe-and Co-doped monolayer MoS 2. *J Appl Phys* (2014) 116(4). doi:10.1063/1.4891495

12. Silambarasan K, Archana J, Harish S, Navaneethan M, Sankar Ganesh R, Ponnusamy S, et al. One-step fabrication of ultrathin layered 1T@2H phase MoS_2 with high catalytic activity based counter electrode for photovoltaic devices. *J Mater Sci Technol* (2020) 51:94–101. doi:10.1016/j.jmst.2020.01.024

13. Liu L, Wu J, Wu L, Ye M, Liu X, Wang Q, et al. Phase-selective synthesis of 1T′ MoS $_2$ monolayers and heterophase bilayers. *Nat Mater* (2018) 17(12):1108–14. doi:10.1038/s41563-018-0187-1

14. Sharma CH, Surendran AP, Varma SS, Thalakulam M. 2D superconductivity and vortex dynamics in 1T-MoS_2. *Commun Phys* (2018) 1(1):90. doi:10.1038/s42005-018-0091-7

15. Xu H, Han D, Bao Y, Cheng F, Ding Z, Tan SJR, et al. Observation of gap opening in 1T′ phase MoS_2 nanocrystals. *Nano Lett* (2018) 18(8):5085–90. doi:10.1021/acs.nanolett.8b01953

16. Friedman AL, Hanbicki AT, Perkins FK, Jernigan GG, Culbertson JC, Campbell PM. Evidence for chemical vapor induced 2H to 1T phase transition in MoX_2 (X = Se, S) transition metal dichalcogenide films. *Sci Rep* (2017) 7(1):3836. doi:10.1038/s41598-017-04224-4

17. Rajapakse M, Karki B, Abu UO, Pishgar S, Musa MRK, Riyadh SMS, et al. Intercalation as a versatile tool for fabrication, property tuning, and phase transitions in 2D materials. *npj 2D Mater Appl* (2021) 5:30. doi:10.1038/s41699-021-00211-6

18. Palencia-Ruiz S, Uzio D, Legens C, Laurenti D, Afanasiev P. Stability and catalytic properties of 1T-MoS_2 obtained via solvothermal synthesis. *Appl Catal A Gen* (2021) 2021:118355. doi:10.1016/j.apcata.2021.118355

19. Kwon IS, Kwak IH, Abbas HG, Jung G, Lee Y, Park J, et al. Intercalation of aromatic amine for the 2H-1T′ phase transition of MoS_2 by experiments and calculations. *Nanoscale* (2018) 10(24):11349–56. doi:10.1039/c8nr02365d

20. Jin Q, Liu N, Chen B, Mei D. Mechanisms of semiconducting 2H to metallic 1T phase transition in two-dimensional MoS_2 nanosheets. *J Phys Chem C* (2018) 122(49): 28215–24. doi:10.1021/acs.jpcc.8b10256

21. Zhu J, Wang Z, Yu H, Li N, Zhang J, Meng J, et al. Argon plasma induced phase transition in monolayer MoS2. *J Am Chem Soc* (2017) 139(30):10216–9. doi:10.1021/jacs.7b05765

22. Zhang J, Xu X, Yang L, Cheng D, Cao D. Single-atom Ru doping induced phase transition of MoS_2 and S vacancy for hydrogen evolution reaction. *Small Methods* (2019) 3(12). doi:10.1002/smtd.201900653

23. Gao B, Zhao Y, Du X, Li D, Ding S, Li Y, et al. Electron injection induced phase transition of 2H to 1T MoS_2 by cobalt and nickel substitutional doping. *Chem Eng J* (2021) 2021:128567. doi:10.1016/j.cej.2021.128567

24. Ge J, Zhang D, Jin J, Han X, Wang Y, Zhang F, et al. Oxygen atoms substituting sulfur atoms of MoS_2 to activate the basal plane and induce the phase transition for boosting hydrogen evolution. *Mater Today Energ* (2021) 2021:100854. doi:10.1016/j.mtener.2021.100854

25. Gan X, Lee LYS, Wong KY, Lo TW, Ho KH, Lei DY, et al. 2H/1T phase transition of multilayer MoS_2 by electrochemical incorporation of S vacancies. *ACS Appl Energ Mater.* (2018) 1(9):4754–65. doi:10.1021/acsaem.8b00875

26. Hwang DY, Choi KH, Suh DH. A vacancy-driven phase transition in MoX_2 (X: S, Se and Te) nanoscrolls. *Nanoscale* (2018) 10(17):7918–26. doi:10.1039/c7nr08634b

27. Bremmer GM, Van Haandel L, Hensen EJM, Frenken JWM, Kooyman PJ. Instability of $NiMoS_2$ and $CoMoS_2$ hydrodesulfurization catalysts at ambient conditions: A quasi *in situ* high-resolution transmission electron microscopy and X-ray photoelectron spectroscopy study. *J Phys Chem C* (2016) 120(34):19204–11. doi:10.1021/acs.jpcc.6b06030

28. Shi S, Sun Z, Hu YH. Stabilization and applications of 2-dimensional 1T metallic MoS_2. *J Mater Chem A* (2018) 6:23932–77. doi:10.1039/c8ta08152b

29. Han SW, Park Y, Hwang YH, Jekal S, Kang M, Lee WG, et al. Electron beam-formed ferromagnetic defects on MoS_2 surface along 1 T phase transition. *Sci Rep* (2016) 6:38730. doi:10.1038/srep38730

30. Sanikop R, Budumuru AK, Gautam S, Chae KH, Sudakar C. Robust ferromagnetism in Li-intercalated and -deintercalated MoS_2 nanosheets: Implications for 2D spintronics. *ACS Appl Nano Mater* (2020) 3(12):11825–37. doi:10.1021/acsanm.0c02349

31. Ma F, Liang Y, Zhou P, Tong F, Wang Z, Wang P, et al. One-step synthesis of Co-doped 1T-MoS_2 nanosheets with efficient and stable HER activity in alkaline solutions. *Mater Chem Phys* (2020) 244:122642. doi:10.1016/j.matchemphys.2020.122642

32. Li P, Yang Y, Gong S, Lv F, Wang W, Li Y, et al. Co-doped 1T-MoS_2 nanosheets embedded in N, S-doped carbon nanobowls for high-rate and ultra-stable sodium-ion batteries. *Nano Res* (2019) 12(9):2218–23. doi:10.1007/s12274-018-2250-2

33. Grønborg SS, Salazar N, Bruix A, Rodríguez-Fernández J, Thomsen SD, Hammer B, et al. Visualizing hydrogen-induced reshaping and edge activation in MoS_2 and Co-promoted MoS2 catalyst clusters. *Nat Commun* (2018) 9(1):2211–11. doi:10.1038/s41467-018-04615-9

34. Mom RV, Louwen JN, Frenken JWM, Groot IMN. *In situ* observations of an active MoS_2 model hydrodesulfurization catalyst. *Nat Commun* (2019) 10(1):2546. doi:10.1038/s41467-019-10526-0

35. Burkhanov GS, Lachenkov SA, Kononov MA, Vlasenko VA, Mikhaylova AB, Korenovsky NL. Hydrogen intercalation of compounds with FeSe and MoS_2 layered crystal structures. *Inorg Mater Appl Res* (2017) 8:759–62. doi:10.1134/S2075113317050082

36. Herbschleb CT, Van Der Tuijn PC, Roobol SB, Navarro V, Bakker JW, Liu Q, et al. The ReactorSTM: Atomically resolved scanning tunneling microscopy under high-pressure, high-temperature catalytic reaction conditions. *Rev Sci Instrum* (2014) 85(8): 083703. doi:10.1063/1.4891811

37. Prabhu MK, Groot IMN. Simultaneous sulfidation of Mo and Co oxides supported on Au(111). *Phys Chem Chem Phys* (2021) 23(14):8403–12. doi:10.1039/d0cp03481a

38. Shafiq I, Shafique S, Akhter P, Yang W, Hussain M. Recent developments in alumina supported hydrodesulfurization catalysts for the production of sulfur-free refinery products: A technical review. *Catal Rev - Sci Eng* (2022) 64(1):1–86. doi:10.1080/01614940.2020.1780824

39. Brunet S, Mey D, Pérot G, Bouchy C, Diehl F. On the hydrodesulfurization of FCC gasoline: A review. *Appl Catal A: Gen* (2005) 278:143–72. doi:10.1016/j.apcata.2004.10.012

40. Rost MJ, Crama L, Schakel P, Van Tol E, Van Velzen-Williams GBEM, Overgauw CF, et al. Scanning probe microscopes go video rate and beyond. *Rev Sci Instrum* (2005) 76(5):053710. doi:10.1063/1.1915288

41. Rost MJ, van Baarle GJC, Katan AJ, van Spengen WM, Schakel P, van Loo WA, et al. Video-rate scanning probe control challenges: Setting the stage for a microscopy revolution. *Asian J Control* (2009) 11(2):110–29. doi:10.1002/asjc.88

42. Horcas I, Fernández R, Gómez-Rodríguez JM, Colchero J, Gómez-Herrero J, Baro AMWSXM. Wsxm: A software for scanning probe microscopy and a tool for nanotechnology. *Rev Sci Instrum* (2007) 78(1):013705. doi:10.1063/1.2432410

43. Wagner CD. Sensitivity factors for XPS analysis of surface atoms. *J Electron Spectros Relat Phenomena* (1983) 32(2):99–102. doi:10.1016/0368-2048(83)85087-7

44. Bremmer GM, van Haandel L, Hensen EJM, Frenken JWM, Kooyman PJ. The effect of oxidation and resulfidation on (Ni/Co)MoS_2 hydrodesulfurisation catalysts. *Appl Catal B Environ* (2019) 243:145–50. doi:10.1016/j.apcatb.2018.10.014

45. Cordova A, Blanchard P, Lancelot C, Frémy G, Lamonier C. Probing the nature of the active phase of molybdenum-supported catalysts for the direct synthesis of methylmercaptan from syngas and H_2S. *ACS Catal* (2015) 5(5):2966–81. doi:10.1021/cs502031f

46. Prabhu MK, Boden D, Rost MJ, Meyer J, Groot IMN. Structural characterization of a novel two-dimensional material: Cobalt sulfide sheets on Au(111). *J Phys Chem Lett* (2020) 11(21):9038–44. doi:10.1021/acs.jpclett.0c02268

47. Gandubert AD, Krebs E, Legens C, Costa D, Guillaume D, Raybaud P. Optimal promoter edge decoration of CoMoS catalysts: A combined theoretical and experimental study. *Catal Today* (2008) 130(1):149–59. doi:10.1016/j.cattod.2007.06.041

48. Lauritsen JV, Kibsgaard J, Olesen GH, Moses PG, Hinnemann B, Helveg S, et al. Location and coordination of promoter atoms in Co- and Ni-promoted MoS_2-based hydrotreating catalysts. *J Catal* (2007) 249(2):220–33. doi:10.1016/j.jcat.2007.04.013

49. Lauritsen JV, Bollinger MV, Lægsgaard E, Jacobsen KW, Nørskov JK, Clausen BS, et al. Atomic-scale insight into structure and morphology changes of MoS_2 nanoclusters in hydrotreating catalysts. *J Catal* (2004) 221(2):510–22. doi:10.1016/j.jcat.2003.09.015

50. Kibsgaard J, Morgenstern K, Lægsgaard E, Lauritsen JV, Besenbacher F. Restructuring of cobalt nanoparticles induced by formation and diffusion of monodisperse metal-sulfur complexes. *Phys Rev Lett* (2008) 100(11):116104. doi:10.1103/PhysRevLett.100.116104

51. Kibsgaard J, Lauritsen JV, Lægsgaard E, Clausen BS, Topsøe H, Besenbacher F. Cluster-support interactions and morphology of MoS_2 nanoclusters in a graphite-supported hydrotreating model catalyst. *J Am Chem Soc* (2006) 128(42):13950–8. doi:10.1021/ja0651106

52. Füchtbauer HG, Tuxen AK, Li Z, Topsøe H, Lauritsen JV, Besenbacher F. Morphology and atomic-scale structure of MoS_2 nanoclusters synthesized with different sulfiding agents. *Top Catal* (2014) 57(1–4):207–14. doi:10.1007/s11244-013-0176-1

53. van Haandel L, Smolentsev G, van Bokhoven JA, Hensen EJM, Weber T. Evidence of octahedral Co–Mo–S sites in hydrodesulfurization catalysts as determined by resonant inelastic X-ray scattering and X-ray absorption spectroscopy. *ACS Catal* (2020) 10(19):10978–88. doi:10.1021/acscatal.0c03062

54. Yue C, Zhou Y, Liu Y, Feng C, Bao W, Sun F, et al. Achieving ultra-dispersed 1T-Co-MoS_2@HMCS via space-confined engineering for highly efficient hydrogen evolution in the universal PH range. *Inorg Chem Front* (2022) 9:2617–27. doi:10.1039/d2qi00269h

55. Bravo-Sanchez M, Romero-Galarza A, Ramírez J, Gutiérrez-Alejandre A, Solís-Casados DA. Quantification of the sulfidation extent of Mo in CoMo HDS catalyst through XPS. *Appl Surf Sci* (2019) 493:587–92. doi:10.1016/j.apsusc.2019.07.012

56. Kappera R, Voiry D, Yalcin SE, Branch B, Gupta G, Mohite AD, et al. Phase-engineered low-resistance contacts for ultrathin MoS_2 transistors. *Nat Mater* (2014) 13(12):1128–34. doi:10.1038/nmat4080

57. Yao Y, Ao K, Lv P, Wei Q. MoS2 coexisting in 1T and 2H phases synthesized by common hydrothermal method for hydrogen evolution reaction. *Nanomaterials* (2019) 9(6):844. doi:10.3390/nano9060844

frontiers | Frontiers in Chemistry

TYPE Original Research
PUBLISHED 06 October 2023
DOI 10.3389/fchem.2023.1229546

OPEN ACCESS

EDITED BY
Marco Sacchi,
University of Surrey, United Kingdom

REVIEWED BY
Luca Bellucci,
National Research Council (CNR), Italy
Anton Tamtögl,
Graz University of Technology, Austria
Philipp Maier,
Graz University of Technology, Austria, in collaboration with reviewer AT

*CORRESPONDENCE
Andrew Cassidy,
amc@phys.au.dk

RECEIVED 26 May 2023
ACCEPTED 18 September 2023
PUBLISHED 06 October 2023

CITATION
Kyrkjebø S, Cassidy A, Lambrick S, Jardine A, Holst B and Hornekær L (2023), ^{3}He spin-echo scattering indicates hindered diffusion of isolated water molecules on graphene-covered Ir(111). *Front. Chem.* 11:1229546. doi: 10.3389/fchem.2023.1229546

^{3}He spin-echo scattering indicates hindered diffusion of isolated water molecules on graphene-covered Ir(111)

Signe Kyrkjebø[1,2], Andrew Cassidy[1]*, Sam Lambrick[3], Andrew Jardine[3], Bodil Holst[4] and Liv Hornekær[1,2]

[1]Center for Interstellar Catalysis, Department of Physics and Astronomy, Aarhus University, Aarhus, Denmark, [2]Interdisciplinary Nanoscience Center, Aarhus University, Aarhus, Denmark, [3]Cavendish Laboratory, University of Cambridge, Cambridge, United Kingdom, [4]Institute of Physics and Technology, University of Bergen, Bergen, Norway

The dynamics of water diffusion on carbon surfaces are of interest in fields as diverse as furthering the use of graphene as an industrial-coating technology and understanding the catalytic role of carbon-based dust grains in the interstellar medium. The early stages of water–ice growth and the mobility of water adsorbates are inherently dependent on the microscopic mechanisms that facilitate water diffusion. Here, we use ^{3}He spin-echo quasi-inelastic scattering to probe the microscopic mechanisms responsible for the diffusion of isolated water molecules on graphene-covered and bare Ir(111). The scattering of He atoms provides a non-invasive and highly surface-sensitive means to measure the rate at which absorbates move around on a substrate at very low coverage. Our results provide an approximate upper limit on the diffusion coefficient for water molecules on GrIr(111) of $<10^{-12}$ m^2/s, an order of magnitude lower than the coefficient that describes the diffusion of water molecules on the bare Ir(111) surface. We attribute the hindered diffusion of water molecules on the GrIr(111) surface to water trapping at specific areas of the corrugated moiré superstructure. Lower mobility of water molecules on a surface is expected to lead to a lower ice nucleation rate and may enhance the macroscopic anti-icing properties of a surface.

KEYWORDS

surface dynamics, surface diffusion, wettability, helium-3 spin-echo scattering, graphene, iridium

1 Introduction

The microscopic mechanisms that facilitate water transport on carbon surfaces are not well understood (Bartels-Rausch, 2013; Bui et al., 2023) despite water diffusion on carbon playing a role in a wide range of fields, including material science and astrochemistry (Shavlov et al., 2007; Hama and Watanabe, 2013; Schertzer and Iglesias, 2018). Graphene, a 2D array of sp^2-hybridized carbon atoms, has attracted interest as a potential anti-corrosion (Kyhl et al., 2015; Yu et al., 2018; Camilli et al., 2019) or anti-icing coating (Akhtar et al., 2019; Kyrkjebø et al., 2021). Water molecules on a surface may react with surface atoms, contributing to corrosion, or cause friction and wear. By understanding the principles of molecular diffusion in more detail, it may be possible to develop more effective strategies to control these processes. In the interstellar medium, the freeze-out of water molecules onto

the surfaces of dust grains, some of which are made from carbonaceous materials, provides chemical repositories for increasing molecular complexity. Water–ice-covered dust grains act as seeds for the formation of complex organic molecules, boosting interstellar chemical complexity (Hama and Watanabe, 2013; Van Dishoeck et al., 2013; Fulvio et al., 2021). To understand the role of the carbon surface in these processes, it is crucial to consider the initial stages of ice nucleation and crystalline growth, and the diffusion of water molecules on carbon surfaces is key to both.

Macroscopically, the ability of a surface to maintain contact with water, commonly referred to as wetting, can be measured as the contact angle of an equilibrated liquid water droplet placed on the surface. The ability of water to wet a layer of graphene has been intensively studied over the last decade, with a large variation in the reported water contact angles, ranging from $(42 \pm 3)^{\circ}$ (Prydatko et al., 2018) to $(127 \pm 4)^{\circ}$ (Wang et al., 2009). While external parameters like contamination, environmental effects, and graphene synthesis differences contribute to the discrepancies reported in the literature, the measured contact angle is highly dependent on the substrate used (Rafiee et al., 2012; Li et al., 2013; Raj et al., 2013; Taherian et al., 2013; Parobek and Liu, 2015; Belyaeva and Schneider, 2020). Theoretical studies predict that the contact angle of graphene is controlled by the balance of polarization at the graphene–water interface and polarization at the graphene–substrate interface (Shih et al., 2013; Kong et al., 2018).

Microscopic measurements of the water–surface interaction focus on the adsorption and desorption kinetics of water molecules, utilizing experimental techniques such as low-temperature scanning tunneling microscopy (LT-STM) (Standop et al., 2015), temperature-programmed desorption (TPD) (Souda, 2012; Smith et al., 2014), and helium atom scattering (HAS). HAS is a technique particularly suitable for studying the microscopic morphology, structure, and dynamics of water (Daschbach et al., 2004; Andersson et al., 2007). As a surface probe, helium atoms are chemically inert and uncharged, and scatter from the outermost electron density distribution of the surface atoms. This makes HAS a non-destructive and highly surface-sensitive technique that can be used to study the properties of water on a surface without altering its structure or behavior. The cross-section for helium atoms to scatter from a single adsorbate is large, typically approaching 120 $Å^2$ (Farias and Rieder, 1998), making helium atoms particularly suitable for studying adsorbate behavior at low coverages in the single molecule diffusion regime.

Helium atoms may scatter elastically from static surface atoms or quasi-elastically from moving adsorbates. In the energy transfer spectrum, quasi-elastic scattering from moving adsorbates will contribute to a broadening around the elastic peak, which gives information on the dynamics of the moving adsorbates on the surface. Helium-3 spin-echo scattering (^{3}HeSE) significantly increases the energy resolution of He scattering techniques by avoiding the use of time-of-flight measurements to detect quasi-elastic scattering losses (Jardine et al., 2009). In ^{3}HeSE, incoming helium atoms are spin-polarized and split into two spin components using a magnetic field. One of the spin components is accelerated, while the other is deaccelerated, separating the atoms in the so-called "spin-echo time," τ_{SE}. The spin-encoded components scatter from the surface and are subsequently recombined. The polarized spin of the scattered beam is then measured as a function of τ_{SE}, providing a measure of the loss in the correlation of the spin-encoded beam as it scatters from the surface. Aperiodic motion on the surface, such as a diffusing adsorbate, will give rise to quasi-elastic scattering, leading to a loss in correlation, which is measured as an exponential decay in the polarized signal of scattered ^{3}HeSE atoms.

^{3}HeSE has recently been used to measure the diffusion properties of molecular water on a range of surfaces (Tamtögl et al., 2020; Tamtögl et al., 2021). Tamtögl et al. (2021) studied the diffusion of single water molecules on graphene prepared on Ni(111). They demonstrated that single water molecules jump from the center of one hexagon in graphene to the center of another, with a tracer diffusion coefficient of $(4.1 \pm 0.2) \times 10^{-10}$ m^2/s and an activation barrier of (60 ± 4) meV. Graphene prepared on Ni(111) is a strongly coupled system that, due to almost identical lattice constants, results in a relatively flat surface energy landscape (Batzill, 2012). Whether these results correlate with water diffusion on other graphene-supported systems is the focus of the current study.

In this study, we use ^{3}HeSE measurements to investigate the diffusion properties of water molecules on Ir(111) and graphene prepared on Ir(111). The Ir(111) substrate is used because, in contrast to GrNi(111), GrIr(111) is a weakly bound system in which graphene can be considered to be quasi-free-standing (Busse et al., 2011; Batzill, 2012). The slight mismatch in lattice constant between the graphene unit cell and the Ir(111) unit cell gives rise to a moiré superstructure. The results are compared to the previous measurements performed on graphene on Ni(111).

2 Materials and methods

The ^{3}HeSE instrument at the Cavendish Laboratory, University of Cambridge, was used for He scattering measurements (Jardine et al., 2009). The instrument consists of an ultra-high-vacuum chamber with a base pressure below 5×10^{-11} mbar. The sample sits at the end of a cryo-finger cooled with liquid nitrogen, where a filament allows for sample heating. The sample is interrogated by a 2 mm-focused beam of ^{3}He atoms, which arrives at the sample via supersonic expansion through a nozzle cooled via a closed-cycle He compressor, giving the ^{3}He atoms a nominal kinetic energy of 8 meV corresponding to a wavevector of 3.4 $Å^{-1}$ (Jardine et al., 2009). The focused ^{3}He beam is scattered from the sample, and scattered atoms are detected. The source-detector angle is fixed at 44.4°, and the scattering angle is changed by rotating the sample with 3 rotational degrees of freedom. For the ^{3}HeSE experiments, the incoming ^{3}He atoms are nuclear spin-polarized in a magnetic field; the polarized atom beam then enters a solenoid, where the magnetic field encodes nuclear spin. This beam of spin-polarized, spin-encoded ^{3}He atoms scatters from the sample before passing through an identical but sign-reversed magnetic field at a second solenoid, where spins are decoded and spin-analyzed before reaching the detector. The temporal window of the instrument is between sub-picoseconds and 2 nanoseconds (Jardine et al., 2009). Further details about the instrument are provided elsewhere (Alexandrowicz and Jardine, 2007; Jardine et al., 2009). Scanning tunneling microscopy (STM) images were recorded in separate ultra-high-vacuum chambers at

10.3389/fchem.2023.1229546

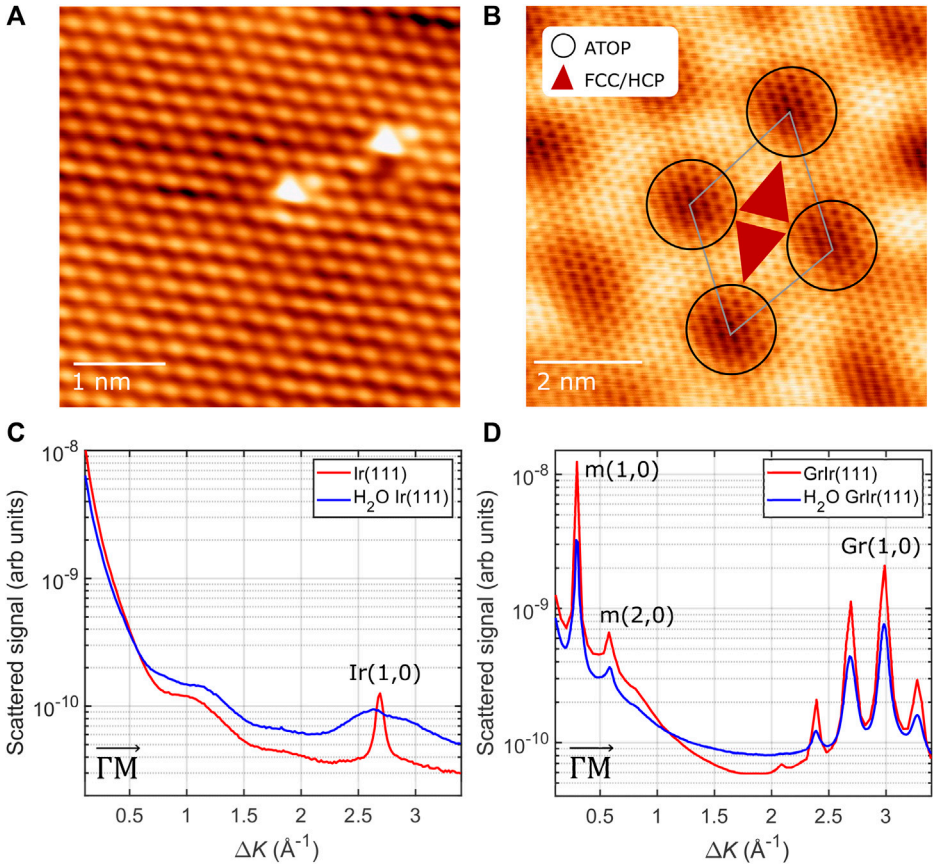

FIGURE 1
Top: STM images of **(A)** clean Ir(111) (Vt: 5.8 mV, It: 56.0 nA) and **(B)** graphene on Ir(111) (Vt: 7.6 mV, It: 0.94 nA); the schematic indicates the moiré unit cell with the repeating length scale of (25.02 ± 0.03) Å. The three high-symmetry regions of the moiré are as described in the main text. Bottom: diffraction scans from **(C)** a clean Ir(111) surface and **(D)** the GrIr(111) surface before (red) and after (blue) exposure to 0.1 L [Ir(111)] and 0.25 L [GrIr(111)] of water at 120 K. The diffraction peaks with the diffraction order are marked and labeled in the figure. The peaks arising from the moiré superstructure, labeled "m," appear at low ΔK values and appear again around the first-order graphene peak, the latter labeled "Gr."

the Center for Interstellar Catalysis, Aarhus University. The pristine Ir(111) surface was characterized using a CreaTec STM at LN_2 temperatures, and the GrIr(111) was characterized using an Aarhus-type STM at room temperature. STM images were analyzed using WSxM software (Horcas et al., 2007).

The sample is a 3 mm-thick Ir single crystal with a diameter of 7 mm, polished at the (111) surface (±0.1°). This Ir(111) surface was cleaned, *in situ*, at the characterization chamber, with several cycles of Ar^+ sputtering and annealing, followed by annealing in an oxygen atmosphere. Graphene sheets were prepared on the clean Ir(111) via a combination of temperature-programmed growth and chemical vapor deposition (Coraux et al., 2009). The substrate was exposed to ethylene gas at room temperature and a partial pressure of 2×10^{-7} mbar for 15 min. The gas was pumped away, and the sample was flashed to 1,180°C and then cooled to 900°C in an ethylene partial pressure of 8×10^{-7} mbar for 15 min.

For water adsorption experiments, deionized water was purified via several freeze–pump–thaw cycles. Water was deposited onto LN_2-cooled Ir(111) and GrIr(111) samples via chamber backfilling using a needle valve to achieve the required partial pressure in the sample chamber. To measure water diffusion via ^{3}HeSE measurements, water was adsorbed on the substrate at 120 K while the elastically scattered helium reflectivity signal was monitored. 0.1 and 0.25 L water was deposited on Ir(111) and GrIr(111), respectively, which, in both cases, resulted in a 60% attenuation of the helium reflectivity signal. An attenuation of 75% of the helium signal was recently estimated to correspond to a coverage of 0.07 ML on GrNi(111) (Tamtögl et al., 2021), and we use this as a rough estimation for the coverage obtained on Ir(111) and GrIr(111). It should be noted that we do not expect our analysis and conclusions to be sensitive to the actual coverage achieved. This sample was then interrogated by the spin-polarized, spin-encoded beam of ^{3}He atoms, and the scattering signal was recorded.

3 Results and analysis

Figures 1A, B show atomic-resolution STM images of Ir(111) and GrIr(111), respectively. The lattice constant of the Ir(111) surface was measured as (2.7 ± 0.1) Å, slightly larger than the lattice constant of graphene, which was measured as (2.5 ± 0.1) Å, in agreement with literature values (N'Diaye et al., 2008). This

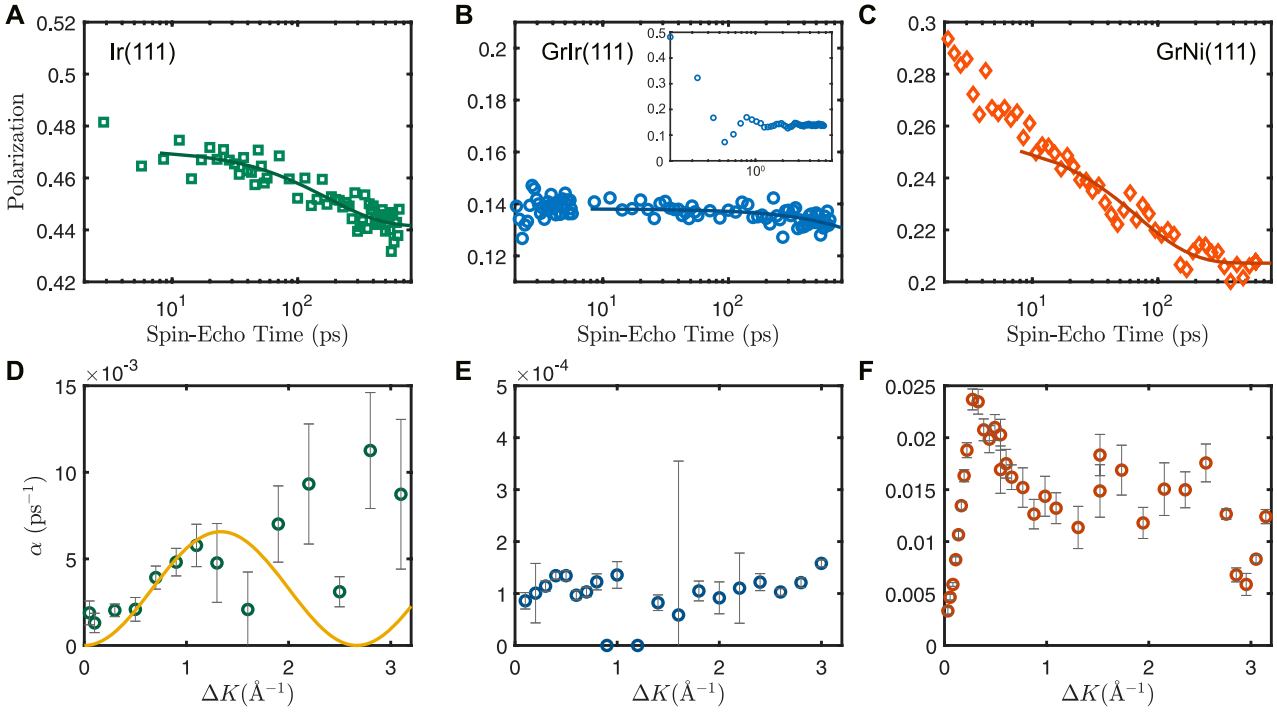

FIGURE 2
Top: Reduction in surface correlation as a function of spin-echo time following ^{3}He scattering from approximately 0.07 ML water adsorbed at 125 K on **(A)** Ir(111), **(B)** GrIr(111), and **(C)** GrNi(111) at ΔK = 1 Å^{-1}, measured in the $\overline{\Gamma M}$ direction. The data (unfilled symbols) were fitted with the ISF function (Eq. 1), resulting in the solid lines. Bottom: Dephasing rate, α, obtained from the ISF fit at each ΔK measurement in the $\overline{\Gamma M}$ direction is plotted for **(D)** Ir(111), **(E)** GrIr(111), and **(F)** GrNi(111). Uncertainty in α is given as the corresponding confidence bounds (1σ) of each exponential fit. Data shown in **(D)** can be fitted to the Chudley–Elliot model (Eq. 2), and the fit is shown with a solid line, allowing for jumps to the nearest neighbor only. Data presented in **(C,F)** for GrNi(111) were measured elsewhere and are adapted from the study by Tamtögl et al. (2021).

slight lattice mismatch gives rise to a moiré superstructure, visible as the large-scale repeating depressions in the STM image of GrIr(111) (Figure 1B). The moiré unit cell is schematically illustrated in Figure 1B. There are three high-symmetry regions: ATOP regions, where the center of a carbon hexagon sits directly on top of an Ir atom and are seen as dark depressions in the STM image (N'Diaye et al., 2008), and HCP and FCC regions, where every second carbon atom is positioned directly above an Ir atom with every other carbon atom in a bridge site. In the HCP regions, the carbon atoms in bridge sites lie above an Ir atom in the third surface layer, while in the FCC regions, the carbon atoms in bridge sites lie above an Ir atom located in the second layer. The bright protrusions in the STM image of the bare Ir(111) surface in Figure 1A indicate adsorbates, most likely oxygen atoms that remain chemisorbed following cleaning.

Diffraction patterns were recorded from both the Ir(111) and GrIr(111) substrates using HAS before and after exposure to the water dose that roughly corresponds to 0.07 ML of water at 120 K. The intensity of elastically scattered helium atoms versus the scattering momentum transfer, ΔK, along the $\overline{\Gamma M}$ direction is shown in Figures 1C, D. The Ir(111) surface gives rise to a single diffraction peak at ΔK = 2.69 Å^{-1} corresponding to a lattice spacing of (2.70 ± 0.03) Å equivalent to the Ir atom lattice. The diffraction pattern for the GrIr(111) sample shows peaks at ΔK = 0.30 Å^{-1} and ΔK = 3.00 Å^{-1}, corresponding to lattice spacings of (25.02 ± 0.03) Å and (2.43 ± 0.03) Å, respectively. These values agree with the periodicities of the moiré lattice and graphene lattice measured with the STM (N'Diaye et al., 2008). All peak intensities are slightly reduced after water is adsorbed on the surface, indicating low water coverage. Water exposure on either surface did not result in any new peaks, indicating that no new lattice emerges following water adsorption.

The diffusion of H_2O monomers adsorbed on Ir(111) and GrIr(111) was studied experimentally via the ^{3}HeSE method by measuring the polarization of scattered ^{3}He atoms after scattering from the substrate as a function of spin-echo time. The polarization gives the intermediate scattering function (ISF), $I(\Delta K, t)$, described by Eq. 1. Since ^{3}He scattering is a surface-only effect, the ISF provides a measure of surface correlation on the length scale and direction given by the scattering momentum transfer, ΔK, after the spin-echo time $t = t_{SE}$. Both parameters were varied in the experiment: t_{SE} was varied by adjusting the solenoid fields that spin-encode the ^{3}He atoms; the ΔK direction was varied by adjusting the angle of the incident beam. For scattering from mobile species, the ISF can usually be written as

$$I(\Delta\mathbf{K}, t) = I_0(\Delta\mathbf{K}, 0)e^{-\alpha(\Delta\mathbf{K})\cdot t} + C(\Delta\mathbf{K}), \quad (1)$$

where I_0 is the polarization measured at t = 0 and C is an offset reflecting persistent polarization caused by elastic scattering of ^{3}He atoms from static defects on the substrate, i.e., vacancies or adsorbates. The change in the degree of correlation with spin-echo times is described by the dephasing rate, $\alpha(\Delta K)$. The loss in

TABLE 1 Experimentally determined diffusion parameters for water monomers on Ir(111), GrIr(111), and GrNi(111).

Diffusion parameters					
	α at ΔK = 1 Å^{-1} (ps^{-1})	τ (ps)	D (m^2/s)	E_a (meV)	α_0 (ps^{-1})
Ir(111)	~ 10^{-3}	1,200 ± 300	(1.5 ± 0.4) × 10^{-11}	90 ± 40	-
GrIr(111)	~ 10^{-4}	-	< 10^{-12}	-	-
GrNi(111)	~ 10^{-2}	65 ± 3	(4.1 ± 0.2) × 10^{-10}	60 ± 4	5 ± 1

The columns provide the following: the dephasing rate α, resident time τ, diffusion coefficient D, activation energy E_a, and the Arrhenius prefactor α_0. Values for GrIr(111) are provided as approximate upper limits. Standard deviation is found through error propagation. Values for GrNi(111) are taken from the study by Tamtögl et al. (2021).

correlation arises from ^{3}He atoms that scatter quasi-inelastically from diffusing adsorbates and, when analyzed as a function of ΔK, provides information on the diffusing species in k-space.

The results of typical H_2O diffusion measurements on Ir(111) and GrIr(111) are presented in Figures 2A, B, respectively. Water was adsorbed to approximately 0.07 ML coverage at 125 K, and the polarization was measured along the $\overline{\Gamma M}$ direction as a function of spin-echo times from 0 to 642 ps at ΔK values from 0 to 3.1 Å^{-1}. Figure 2C includes measurements for H_2O dynamics on GrNi(111) collected by Tamtögl et al. (2021) using the same HeSE setup, and these data are included for comparison. In Figures 2A–C, the degree of polarization is plotted as a function of spin-echo times at ΔK = 1 Å^{-1}. For GrIr(111), we ascribe the oscillating signal at spin-echo times below 8 ps to scattering from phonons. These data are shown as the inset in Figure 2B. The oscillating signals at short spin-echo times lack any characteristic dependence on ΔK and, while this initial decay could relate to vibrational or rotational motions within a unit cell, such effects would not alter the subsequent analysis or conclusions. The data for Ir(111) in Figure 2A extend to low spin-echo times, but as for data for GrIr(111), only the loss in correlation after 8 ps was fitted to Eq. 1 to obtain the dephasing rate, α. Dephasing rates were analyzed for ΔK in the range 0–3.1 Å^{-1}, and the results are plotted in Figures 2D–F. Again, data for H_2O dynamics on GrNi(111) were taken from the study by Tamtögl et al. (2021) and are included for comparison.

The data recorded from water adsorbed on Ir(111) show a tendency to decay at longer spin-echo times (Figure 2A), demonstrating quasi-elastic scattering from diffusing water molecules on the Ir(111) surface. The values for α obtained by fitting the ISF function in Eq. 1 at ΔK from 0 to 3.1 Å^{-1} are plotted in Figure 2D. In contrast, the data recorded from water adsorbed on GrIr(111) (Figure 2B) indicate no evidence of H_2O translational diffusion on GrIr(111) across the spin-echo times accessible with this experiment. There was little loss of correlation for H_2O on GrIr(111), on a timescale of hundreds of ps, at any ΔK value between 0 and 3.1 Å^{-1} across the temperatures investigated, from 120 to 160 K. Thus, we conclude that water should diffuse at a lower rate than can be assessed via our ^{3}HeSE experiment. To set an upper limit for a loss of correlation, we assume that there is decay to some arbitrary point beyond the timescale accessible with the ^{3}HeSE measurement. By setting this offset to half of the value of the last data point, we obtain α values on the order of 10^{-4} ps^{-1}, plotted in Figure 2E. Changing the offset to 25% or 75% of the last data point does not change the order of magnitude of the α values. The values of α at ΔK = 1 Å^{-1} for each substrate are summarized in Table 1. The dephasing rates, α, for GrNi(111), 10^{-2} ps^{-1}, are an order of magnitude larger than values for water diffusing on Ir(111), 10^{-3} ps^{-1}, which, in turn, are an order of magnitude larger than the upper limit values for water diffusing on GrIr(111), 10^{-4} ps^{-1}. This trend is already evident from visual inspection of the loss in correlation as a function of spin-echo times in Figures 2A–C.

The dephasing data obtained from H_2O adsorbed on Ir(111) can be compared to the analytical Chudley–Elliot (CE) model, which is the simplest approach to describe molecular single-jump diffusion (Chudley and Elliott, 1961; Barth, 2000; Jardine et al., 2009). This model assumes that an adsorbate rests at time τ between jumps from one adsorption site to another. The model describes α as

$$\alpha(\Delta\mathbf{K}) = \frac{2}{\tau}\sum_n p_n \sin^2\left(\frac{\Delta\mathbf{K}\cdot\mathbf{j}_n}{2}\right), \tag{2}$$

where each n represents a unique jump, represented by $\mathbf{j}_n$, the jump vector for that particular jump, and p_n, the probability that an adsorbate will make that particular jump.

The CE model, described by Eq. 2, was applied to the α values plotted in Figure 2D for n = 1, i.e., for a jump to the nearest neighbor with p_1 = 1. Increasing n > 1 did not improve the goodness of fit. The resulting fit, weighted towards lower ΔK values by the uncertainties of the data points, is shown as the solid line in Figure 2D. We estimate a residence time, τ = (1200 ± 300 ps), with a jump length $\langle l\rangle$ = (2.72 ± 0.03) Å, where the uncertainty was measured from the diffraction scan in Figure 1C. We assume that the water molecule sits on top of a surface Ir(111) atom as water molecules sit in atop positions on other close-packed transition metal surfaces (Carrasco et al., 2013). Water dissociation has been reported to be thermally activated on Ir(111) (Pan et al., 2011), and this may explain the absence of any decay in polarization in our experiments when the sample temperature was increased above 135 K. It may be that at these elevated surface temperatures, water molecules fragment to form smaller radical species, which may chemisorb to the Ir(111) surface.

Using the values of τ and $\langle l\rangle$ from Eq. 2, we can then calculate a value for the diffusion coefficient, D, using

$$D = \frac{1}{4\tau}\langle l^2\rangle, \tag{3}$$

giving a diffusion coefficient of (1.5 ± 0.4) × 10^{-11} m^2/s for water on Ir(111) at 125 K in the $\overline{\Gamma M}$ direction. It should be noted that in arriving at this value for the diffusion coefficient, we have used the simplest possible hopping model in the CE model, and we assumed that water molecules are non-interacting, which may not be the case at a coverage we can, at best, estimate to be roughly 0.07 ML. We can also approximate an upper limit for the diffusion coefficient for

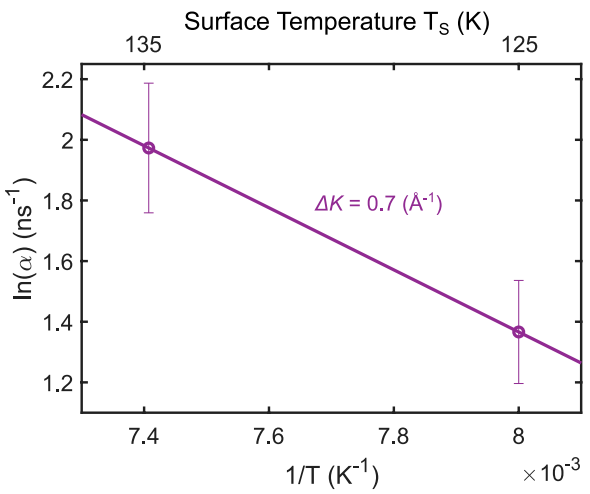

FIGURE 3
Arrhenius plot showing the temperature dependence of α at ΔK = 0.7 Å^{-1} for water on Ir(111). The error bars arise following error propagation.

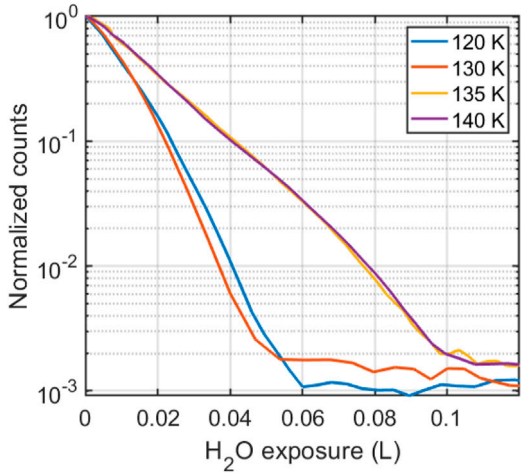

FIGURE 4
Helium scattering intensity at the specular angle, as a function of water fluence on GrIr(111), for sample temperatures in the range 120–140 K. The helium reflectivity signal decreases with an increase in water exposure, with a change in the rate of decrease between 130 and 135 K.

water on GrIr(111). For GrIr(111), the upper limits of the dephasing rates are one order of magnitude lower than what we report for water on Ir(111) and two orders of magnitude lower than the values reported for water on GrNi(111). We assume that this translates to a water residence time of at least one order of magnitude longer than for water on Ir(111), i.e., $\tau > 12$ ns. With a residence time of this order and assuming that the jumping length stays in the Å length scale (similar to that for water hopping on GrNi(111)), we can approximate that the diffusion coefficient for water on GrIr(111) is $< 10^{-12}$ m^2/s.

If we assume that diffusion is an activated process, with an activation energy barrier E_a, then the relationship between α values at the same ΔK measured as a function of temperature is modeled by the Arrhenius relation as follows:

$$\alpha = \alpha_0 \exp\left(\frac{-E_a}{k_B T_s}\right), \quad (4)$$

where α_0 is the pre-exponential factor describing the jump frequency, k_B is the Boltzmann constant, and T_s is the temperature of the surface.

Figure 3 shows an Arrhenius plot for α measured at 125 K and 135 K at $\Delta K = 0.7$ Å^{-1}. The data at 125 K were measured immediately after water deposition at this temperature, and data at 135 K were measured by annealing this sample to 135 K. Only data at these two temperatures were available in our experiments. The ΔK value of 0.7 Å^{-1} was chosen for the Arrhenius analysis because it provided the best signal-to-noise ratio in the experiment, with a low value of ΔK representing the jump to the nearest neighbor on the Ir(111) surface. The activation energy E_a can be extracted from the slope between these data points and is estimated to be (90 ± 40) meV. The large uncertainty of the measurement does not allow for an estimation of the exponential prefactor α_0. Our value of E_a is similar to the barrier of (80 ± 8) meV, which is measured for water monomer diffusion on Cu(100) at temperatures below 30 K (Bertram et al., 2019). This is despite our ^{3}HeSE measurements arising from water adsorbed at considerably higher temperatures, 125–135 K, demonstrating the veracity of the conclusion drawn by Bertram et al. that their value should be accurate across a large temperature range. An alternative approach to calculate the activation energy is to arbitrarily assume that the value of α_0 is identical for water on Ir(111) and water on GrNi(111), i.e., 5 ps^{-1} (Tamtögl et al., 2021). This gives an activation energy of (77 ± 3) meV for $\Delta K = 0.7$ Å^{-1} at 125 K, agreeing with the value found in Figure 3.

4 Discussion

Our results demonstrate that if water is diffusing on GrIr(111), it must happen with a rate that is an order of magnitude lower than that of water diffusing on Ir(111) and two orders of magnitude lower than that of water diffusing on GrNi(111) (Tamtögl et al., 2021). Before discussing what might hinder water diffusion on GrIr(111), we first ask if we expect diffusion to occur in the temperature window studied, i.e., between 120 and 160 K. To this end, water was adsorbed onto the GrIr(111) substrate, and the helium reflectivity at the specular angle was recorded as a function of water exposure, at temperatures of adsorption between 120 and 160 K. The results, plotted in Figure 4, show a decrease in the intensity of elastically scattered helium atoms as a function of water exposure. The decrease results from the diffuse scattering of He atoms from water adsorbates on the GrIr(111) substrate as water molecules adsorb on the substrate. In all cases, the decrease is exponential, suggesting that adsorbates are isolated as they stick on the substrate (Farias and Rieder, 1998). There is minimal difference between the rate of decrease in the reflectivity between 120 and 130 K, indicating similar adsorption kinetics at these temperatures. The rate of decrease with an increase in exposure corresponds to the overlap of scattering cross-sections of the adsorbates on the surface. If the

adsorbates "sit and stick", the cross-sections will overlap, giving a simple relationship for the rate of reduction in the reflectivity signal. However, if the adsorbates repel or attract each other, that will increase or decrease the rate of loss in reflectivity, respectively (Farias and Rieder, 1998). There is a clear change in the rate at which reflectivity decreases when the substrate temperature increases from 130 to 135 K, with the reflectivity decreasing much slower at the higher adsorption temperatures. This low rate indicates an abrupt change in the adsorption kinetics at 135 K, which we attribute to either a sudden change in the sticking coefficient at 135 K or to the growth of a more ordered ice layer. Infrared reflection absorption spectroscopy experiments indicate that at low coverage, water adsorbates tend to aggregate into clusters at HCP regions on the GrIr(111) moiré, providing a confined environment for these water molecules and a distinctive IR spectrum (Gleißner et al., 2019). This interpretation concurs with results from low-temperature STM experiments (Standop et al., 2015). Infrared spectroscopy shows an annealing-induced structural change for water confined to HCP regions on GrIr(111) when the temperature is increased above 140 K (Gleißner et al., 2019). Increasing the surface temperature to 150 K led to water desorption (Supplementary Figure S1 in Supplementary Material), which agrees well with TPD measurements (Standop et al., 2015). The data in Figure 4 indicate that water gains some mobility across the temperature range in which ^{3}HeSE measurements were recorded, specifically between 130 and 135 K, and one might expect the change in sticking coefficient and/or the structural rearrangement to coincide with a higher rate of water diffusion. Such diffusion was not observed in the ^{3}HeSE data, indicating that if isolated water molecules do diffuse, they do so at a low rate, a rate much lower than the rate at which water diffuses on GrNi(111) (Tamtögl et al., 2021).

We note that the He reflectivity signal remained low at all temperatures below 150 K, even after extended waiting times, following water adsorption on the GrIr(111) substrate. This is in contrast to He scattering from water adsorbed on GrNi(111), where it was reported that the helium reflectivity signal recovered after water adsorption at 110 K and a diffraction pattern emerged (Tamtögl et al., 2021). Those authors attributed this increase in reflectivity to mobile water that migrated to form large ice clusters at 110 K. The moiré superstructure of GrIr(111) has been reported to lead to patterned adsorption of hydrogen atoms (Jørgensen et al., 2016), oxygen atoms (Cassidy et al., 2018; Kyrkjebø et al., 2021), metal clusters (N'Diaye et al., 2009; Feibelman, 2008), and water ice (Standop et al., 2015), with a slight preference for absorbates to be confined to the HCP regions of the moiré. Carbon atoms in the graphene basal plane have a registry with every second carbon atom above an Ir atom and lie closest to the Ir(111) substrate in the HCP regions, making the carbon atoms in those areas most readily available to form covalent bonds with the underlying Ir surface (Jørgensen et al., 2016). Standop et al. (2015) showed, with the LT-STM, that solid amorphous water became trapped in the HCP regions when adsorbed at temperatures below 80 K. Due to the patterned adsorption of water on GrIr(111), the surface was described as a pattern of hydrophilic regions in a hydrophobic matrix. In our experiments, we observed no measurable diffusion of water species, even at temperatures close to the water desorption temperature. We speculate, then, that water species on the GrIr surface are trapped in clusters at the HCP regions of the GrIr moiré. The high binding energies for adsorbates in these clusters at the HCP regions of the moiré might increase the activation energy for water monomer/dimer/trimer diffusion to a value comparable to that of desorption so that desorption competes with the diffusion of isolated water species.

Recently, it was shown, by measuring the freezing onset temperature of a water droplet on a cooled surface, that pristine and functionalized graphene grown on Ir(111) and Ru(0001) exhibit anti-icing properties (Akhtar et al., 2019; Kyrkjebø et al., 2021). Interestingly, graphene prepared on both of these surfaces gives rise to moiré superstructures, which are preserved after the adsorption of functional groups (Cassidy et al., 2018; Novotny et al., 2018). The freezing onset of a water droplet on GrIr(111) was reported as (−15 ± 3)°C and reduced to (−21 ± 1)°C after the introduction of chemisorbed oxygen on the GrIr(111) surface (Kyrkjebø et al., 2021). Kyrkjebø et al. (2021) proposed that a lower rate of ice nucleation occurred on the O-Gr/Ir(111) systems because interfacial water became more viscous in the presence of the chemisorbed oxygen (Zokaie and Foroutan, 2015). This increased viscosity provides a barrier to ice nucleation (Li et al., 2014). According to the crystal nucleation theory, ice growth becomes exothermic when a nucleus reaches a critical size, meaning that the initial nucleation step is rate-determining for ice growth. We speculate that the macroscopic anti-icing properties of the modulated graphene-based surfaces can be explained by the slow molecular diffusion of water reported here for water adsorbed on the GrIr(111) surface.

Our results demonstrate that the microscopic mechanism for water molecule diffusion on graphene is strongly substrate dependent, with the rate of water diffusion on GrIr(111) being at least two orders of magnitude lower than water diffusion on GrNi(111). Since water diffusion is faster on the bare Ir(111) surface than on the Gr/Ir(111) surface, we conclude that the graphene-Ir interaction determines the microscopic diffusion properties of single water molecules. Hence, tuning of the graphene-substrate interaction may provide a pathway to improve the de-icing properties of graphene films on metallic substrates.

5 Summary

Isolated water molecules on GrIr(111) are reported to diffuse at a rate with an approximate upper limit of 10^{-12} m^2/s. This rate is at least one order of magnitude lower than that of isolated water molecule diffusion on Ir(111) and two orders of magnitude lower than that of water diffusion on GrNi(111). We propose that it is the graphene–metal interaction that determines the microscopic diffusion properties of single water molecules on the water–Gr/Ir(111) system. Specifically, the corrugated moiré superstructure of the loosely coupled GrIr(111) system can be viewed as a landscape of different binding energies, with water molecules binding more strongly at the so-called HCP regions, which may then hinder the diffusion of isolated species. Future research will aim to understand the nature of the interaction between water molecules and the graphene basal plane in these confined spaces at the HCP regions. Understanding the nature of this bond, i.e., chemisorption versus physisorption, may be important for hindering water diffusion on other potential graphene-based, anti-icing coatings.

Data availability statement

The datasets presented in this study can be found in online repositories. The data are archived on Zenodo with DOI: https://doi.org/10.5281/zenodo.8124927.

Author contributions

BH and LH conceived the project; SK and AC performed the experiments with the assistance of SL and AJ; STM images were collected in the laboratory of LH; all authors contributed to data analysis; and SK and AC drafted the manuscript with support from all authors. All authors contributed to the article and approved the submitted version.

Funding

This work was supported by the Danish National Research Foundation through the Center of Excellence "InterCat" (Grant Agreement No. DNRF150) and the EPSRC award EP/T00634X/1.

Acknowledgments

The authors acknowledge the use of and support by the Cambridge Atom Scattering Facility (https://atomscattering.phy.cam.ac.uk) and thank Tamtögl et al. for providing data associated with ^{3}HeSE measurements for water adsorbed on GrNi(111) and Richard Balog for supplying STM data describing the bare Ir(111) surface.

Conflict of interest

The authors declare that the research was conducted in the absence of any commercial or financial relationships that could be construed as a potential conflict of interest.

The handling editor MS declares a past collaboration with the authors BH and AJ.

Publisher's note

Supplementary material

The Supplementary Material for this article can be found online at: https://www.frontiersin.org/articles/10.3389/fchem.2023.1229546/full#supplementary-material

References

Akhtar, N., Anemone, G., Farias, D., and Holst, B. (2019). Fluorinated graphene provides long lasting ice inhibition in high humidity. *Carbon* 141, 451–456. doi:10.1016/j.carbon.2018.09.008

Alexandrowicz, G., and Jardine, A. P. (2007). Helium spin-echo spectroscopy: Studying surface dynamics with ultra-high-energy resolution. *J. Phys. Condens. Matter* 19, 305001. doi:10.1088/0953-8984/19/30/305001

Andersson, P. U., Suter, M. T., Marković, N., and Pettersson, J. B. C. (2007). Water condensation on graphite studied by elastic helium scattering and molecular dynamics simulations. *J. Phys. Chem. C* 111, 15258–15266. doi:10.1021/jp068984n

Bartels-Rausch, T. (2013). Ten things we need to know about ice and snow. *Nature* 494, 27–29. doi:10.1038/494027a

Barth, J. V. (2000). Transport of adsorbates at metal surfaces: From thermal migration to hot precursors. *Surf. Sci. Rep.* 40, 75–149. doi:10.1016/s0167-5729(00)00002-9

Batzill, M. (2012). The surface science of graphene: Metal interfaces, cvd synthesis, nanoribbons, chemical modifications, and defects. *Surf. Sci. Rep.* 67, 83–115. doi:10.1016/j.surfrep.2011.12.001

Belyaeva, L. A., and Schneider, G. F. (2020). Wettability of graphene. *Surf. Sci. Rep.* 75, 100482. doi:10.1016/j.surfrep.2020.100482

Bertram, C., Fang, W., Pedevilla, P., Michaelides, A., and Morgenstern, K. (2019). Anomalously low barrier for water dimer diffusion on Cu(111). *Nano. Lett.* 19, 3049–3056. doi:10.1021/acs.nanolett.9b00392

Bui, A. T., Thiemann, F. L., Michaelides, A., and Cox, S. J. (2023). Classical quantum friction at water–carbon interfaces. *Nano. Lett.* 23, 580–587. doi:10.1021/acs.nanolett.2c04187

Busse, C., Lazić, P., Djemour, R., Coraux, J., Gerber, T., Atodiresei, N., et al. (2011). Graphene on Ir (111): Physisorption with chemical modulation. *Phys. Rev. Lett.* 107, 036101. doi:10.1103/physrevlett.107.036101

Camilli, L., Yu, F., Cassidy, A., Hornekær, L., and Bøggild, P. (2019). Challenges for continuous graphene as a corrosion barrier. *2D Mater.* 6, 022002. doi:10.1088/2053-1583/ab04d4

Carrasco, J., Klimeš, J., and Michaelides, A. (2013). The role of van der waals forces in water adsorption on metals. *J. Chem. Phys.* 138, 024708. doi:10.1063/1.4773901

Cassidy, A., Pedersen, S., Bluhm, H., Calisti, V., Angot, T., Salomon, E., et al. (2018). Patterned formation of enolate functional groups on the graphene basal plane. *Phys. Chem. Chem. Phys.* 20, 28370–28374. doi:10.1039/c8cp05730c

Chudley, C., and Elliott, R. (1961). Neutron scattering from a liquid on a jump diffusion model. *Proc. Phys. Soc.* 77, 353–361. doi:10.1088/0370-1328/77/2/319

Coraux, J., Engler, M., Busse, C., Wall, D., Buckanie, N., Zu Heringdorf, F. J. M., et al. (2009). Growth of graphene on Ir (111). *New J. Phys.* 11, 023006. doi:10.1088/1367-2630/11/2/023006

Daschbach, J. L., Peden, B. M., Smith, R. S., and Kay, B. D. (2004). Adsorption, desorption, and clustering of H_2O on Pt(111). *J. Chem. Phys.* 120, 1516–1523. doi:10.1063/1.1633752

Farias, D., and Rieder, K. H. (1998). Atomic beam diffraction from solid surfaces. *Rep. Prog. Phys.* 61, 1575–1664. doi:10.1088/0034-4885/61/12/001

Feibelman, P. J. (2008). Pinning of graphene to Ir(111) by flat Ir dots. *Phys. Rev. B* 77, 165419. doi:10.1103/PhysRevB.77.165419

Fulvio, D., Potapov, A., He, J., and Henning, T. (2021). Astrochemical pathways to complex organic and prebiotic molecules: Experimental perspectives for *in situ* solid-state studies. *Life* 11, 568. doi:10.3390/life11060568

Gleißner, R., Creutzburg, M., Noei, H., and Stierle, A. (2019). Interaction of water with graphene/Ir (111) studied by vibrational spectroscopy. *Langmuir* 35, 11285–11290. doi:10.1021/acs.langmuir.9b01205

Hama, T., and Watanabe, N. (2013). Surface processes on interstellar amorphous solid water: Adsorption, diffusion, tunneling reactions, and nuclear-spin conversion. *Chem. Rev.* 113, 8783–8839. doi:10.1021/cr4000978

Horcas, I., Fernández, R., Gomez-Rodriguez, J., Colchero, J., Gómez-Herrero, J., and Baro, A. (2007). Wsxm: A software for scanning probe microscopy and a tool for nanotechnology. *Rev. Sci. Instrum.* 78, 013705. doi:10.1063/1.2432410

Jardine, A., Hedgeland, H., Alexandrowicz, G., Allison, W., and Ellis, J. (2009). Helium-3 spin-echo: Principles and application to dynamics at surfaces. *Prog. Surf. Sci.* 84, 323–379. doi:10.1016/j.progsurf.2009.07.001

Jørgensen, J. H., Čabo, A. G., Balog, R., Kyhl, L., Groves, M. N., Cassidy, A. M., et al. (2016). Symmetry-driven band gap engineering in hydrogen functionalized graphene. *ACS Nano* 10, 10798–10807. doi:10.1021/acsnano.6b04671

Kong, W., Li, H., Qiao, K., Kim, Y., Lee, K., Nie, Y., et al. (2018). Polarity governs atomic interaction through two-dimensional materials. *Nat. Mater.* 17, 999–1004. doi:10.1038/s41563-018-0176-4

Kyhl, L., Nielsen, S. F., Čabo, A. G., Cassidy, A., Miwa, J. A., and Hornekær, L. (2015). Graphene as an anti-corrosion coating layer. *Faraday Discuss.* 180, 495–509. doi:10.1039/c4fd00259h

Kyrkjebø, S., Cassidy, A., Akhtar, N., Balog, R., Scheffler, M., Hornekær, L., et al. (2021). Graphene and graphene oxide on Ir(111) are transparent to wetting but not to icing. *Carbon* 174, 396–403. doi:10.1016/j.carbon.2020.12.030

Li, K., Xu, S., Chen, J., Zhang, Q., Zhang, Y., Cui, D., et al. (2014). Viscosity of interfacial water regulates ice nucleation. *Appl. Phys. Lett.* 104, 101605. doi:10.1063/1.4868255

Li, Z., Wang, Y., Kozbial, A., Shenoy, G., Zhou, F., McGinley, R., et al. (2013). Effect of airborne contaminants on the wettability of supported graphene and graphite. *Nat. Mater.* 12, 925–931. doi:10.1038/nmat3709

N'Diaye, A. T., Coraux, J., Plasa, T. N., Busse, C., and Michely, T. (2008). Structure of epitaxial graphene on Ir(111). *New J. Phys.* 10, 043033. doi:10.1088/1367-2630/10/4/043033

N'Diaye, A. T., Gerber, T., Busse, C., Mysliveček, J., Coraux, J., and Michely, T. (2009). A versatile fabrication method for cluster superlattices. *New J. Phys.* 11, 103045. doi:10.1088/1367-2630/11/10/103045

Novotny, Z., Nguyen, M. T., Netzer, F. P., Glezakou, V. A., Rousseau, R., and Dohnalek, Z. (2018). Formation of supported graphene oxide: Evidence for enolate species. *J. Am. Chem. Soc.* 140, 5102–5109. doi:10.1021/jacs.7b12791

Pan, M., Hoang, S., and Mullins, C. B. (2011). Interaction of water with the clean and oxygen pre-covered ir (1 1 1) surface. *Catal. today* 160, 198–203. doi:10.1016/j.cattod.2010.05.008

Parobek, D., and Liu, H. (2015). Wettability of graphene. *2D Mater.* 2, 032001. doi:10.1088/2053-1583/2/3/032001

Prydatko, A. V., Belyaeva, L. A., Jiang, L., Lima, L., and Schneider, G. F. (2018). Contact angle measurement of free-standing square-millimeter single-layer graphene. *Nat. Commun.* 9, 4185–4187. doi:10.1038/s41467-018-06608-0

Rafiee, J., Mi, X., Gullapalli, H., Thomas, A. V., Yavari, F., Shi, Y., et al. (2012). Wetting transparency of graphene. *Nat. Mater.* 11, 217–222. doi:10.1038/nmat3228

Raj, R., Maroo, S. C., and Wang, E. N. (2013). Wettability of graphene. *Nano. Lett.* 13, 1509–1515. doi:10.1021/nl304647t

Schertzer, M. J., and Iglesias, P. (2018). Meta-analysis comparing wettability parameters and the effect of wettability on friction coefficient in lubrication. *Lubricants* 6, 70. doi:10.3390/lubricants6030070

Shavlov, A., Pisarev, A., and Ryabtseva, A. (2007). Corrosion of metal films in ice: The dynamics of the conductivity of films. *Russ. J. Phys. Chem. A* 81, 1030–1034. doi:10.1134/s0036024407070047

Shih, C. J., Strano, M. S., and Blankschtein, D. (2013). Wetting translucency of graphene. *Nat. Mater.* 12, 866–869. doi:10.1038/nmat3760

Smith, R. S., Matthiesen, J., and Kay, B. D. (2014). Desorption kinetics of methanol, ethanol, and water from graphene. *J. Phys. Chem. A* 118, 8242–8250. doi:10.1021/jp501038z

Souda, R. (2012). Nanoconfinement effects of water on hydrophilic and hydrophobic substrates at cryogenic temperatures. *J. Phys. Chem. C* 116, 20895–20901. doi:10.1021/jp3061587

Standop, S., Michely, T., and Busse, C. (2015). H_2O on graphene/Ir (111): A periodic array of frozen droplets. *J. Phys. Chem. C* 119, 1418–1423. doi:10.1021/jp510140a

Taherian, F., Marcon, V., van der Vegt, N. F., and Leroy, F. (2013). What is the contact angle of water on graphene? *Langmuir* 29, 1457–1465. doi:10.1021/la304645w

Tamtögl, A., Bahn, E., Sacchi, M., Zhu, J., Ward, D. J., Jardine, A. P., et al. (2021). Motion of water monomers reveals a kinetic barrier to ice nucleation on graphene. *Nat. Commun.* 12, 3120–3128. doi:10.1038/s41467-021-23226-5

Tamtögl, A., Sacchi, M., Avidor, N., Calvo-Almazán, I., Townsend, P. S., Bremholm, M., et al. (2020). Nanoscopic diffusion of water on a topological insulator. *Nat. Commun.* 11, 278. doi:10.1038/s41467-019-14064-7

Van Dishoeck, E. F., Herbst, E., and Neufeld, D. A. (2013). Interstellar water chemistry: From laboratory to observations. *Chem. Rev.* 113, 9043–9085. doi:10.1021/cr4003177

Wang, S., Zhang, Y., Abidi, N., and Cabrales, L. (2009). Wettability and surface free energy of graphene films. *Langmuir* 25, 11078–11081. doi:10.1021/la901402f

Yu, F., Camilli, L., Wang, T., Mackenzie, D. M., Curioni, M., Akid, R., et al. (2018). Complete long-term corrosion protection with chemical vapor deposited graphene. *Carbon* 132, 78–84. doi:10.1016/j.carbon.2018.02.035

Zokaie, M., and Foroutan, M. (2015). Confinement effects of graphene oxide nanosheets on liquid–solid phase transition of water. *RSC Adv.* 5, 97446–97457. doi:10.1039/c5ra21480g

frontiers | Frontiers in Chemistry

TYPE Original Research
PUBLISHED 16 November 2023
DOI 10.3389/fchem.2023.1291065

OPEN ACCESS

EDITED BY
Marco Sacchi,
University of Surrey, United Kingdom

REVIEWED BY
Thomas Reisinger,
Karlsruhe Institute of Technology (KIT), Germany
Anton Tamtögl,
Graz University of Technology, Austria

*CORRESPONDENCE
Christian Brand,
christian.brand@dlr.de

RECEIVED 08 September 2023
ACCEPTED 06 November 2023
PUBLISHED 16 November 2023

CITATION
Bühler J, Roncin P and Brand C (2023), Describing the scattering of keV protons through graphene.
Front. Chem. 11:1291065.
doi: 10.3389/fchem.2023.1291065

Describing the scattering of keV protons through graphene

Jakob Bühler[1], Philippe Roncin[2] and Christian Brand[1]*

[1]Department of Quantum Nanophysics, German Aerospace Center (DLR), Institute of Quantum Technologies, Ulm, Germany, [2]Institut des Sciences Moléculaires d'Orsay (ISMO), Centre national de la recherche scientifique (CNRS), University Paris-Sud, Université Paris-Saclay, Orsay, France

Implementing two-dimensional materials in technological solutions requires fast, economic, and non-destructive tools to ensure efficient characterization. In this context, scattering of keV protons through free-standing graphene was proposed as an analytical tool. Here, we critically evaluate the predicted effects using classical simulations including a description of the lattice's thermal motion and the membrane corrugation via statistical averaging. Our study shows that the zero-point motion of the lattice atoms alone leads to considerable broadening of the signal that is not properly described by thermal averaging of the interaction potential. In combination with the non-negligible probability for introducing defects, it limits the prospect of proton scattering at 5 keV as an analytic tool.

KEYWORDS

graphene, scattering, protons, statistical averaging, 2D-materials, analytic method

1 Introduction

There are numerous experimental techniques available to study and analyze two-dimensional (2D) materials. Most commonly Raman spectroscopy [Ferrari et al. (2006); Tan (2019); Saito et al. (2016)], electron microscopy [Meyer et al. (2007); Li et al. (2018); Chen et al. (2020)], and scanning probe microscopy [Novoselov et al. (2004); Zhang et al. (2018); Marchini et al. (2007)] are employed. These are complemented by other methods, such as diffraction and scattering of massive particles at the membranes [Woznica et al. (2015); Brand et al. (2015); Brand et al. (2019); Al Taleb et al. (2015); Debiossac et al. (2016); Borca et al. (2010); Maccariello et al. (2015); Tamtögl et al. (2015); Anemone et al. (2016); Benedek et al. (2021); Tømterud et al. (2022); Al Taleb and Farías (2016); Tamtögl et al. (2021); Sacchi and Tamtögl (2023); Bahn et al. (2017); Jiang et al. (2019); Jiang et al. (2021)]. They yield valuable insights into the large-scale structure of the membrane, interaction potentials, and low-energy excitations. In such measurements, often atomic beams are used. As the interaction energy is typically in the meV-regime, this approach is completely non-destructive [Al Taleb et al. (2015)]. It sheds light on the particle-membrane interaction in the low-energy regime [Zugarramurdi et al. (2015); Debiossac et al. (2016)] and is used to assess the interaction of graphene with various materials [Borca et al. (2010); Maccariello et al. (2015); Tamtögl et al. (2015); Anemone et al. (2016)]. If the membrane is weakly bound to the substrate, intrinsic properties of materials can be assessed, such as electron-phonon couplings [Benedek et al. (2021)] and the membrane's bending rigidity [Tømterud et al. (2022); Al Taleb and Farías (2016)]. Moreover, it is also possible to study the dynamics of adsorbates on membranes [Tamtögl et al. (2021); Sacchi and Tamtögl (2023); Bahn et al. (2017)], including the creation of transient molecular bonds [Jiang et al. (2019); Jiang et al. (2021)].

In this context transmission of protons at 5 keV through graphene has been proposed as an analytic tool [Ćosić et al. (2018); Ćosić et al. (2019); Hadžijojić et al.

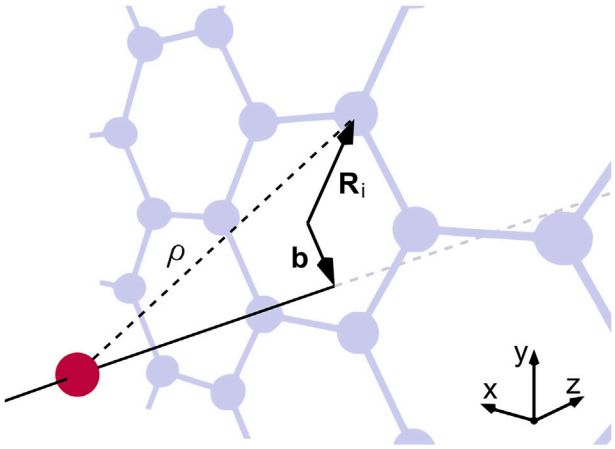

FIGURE 1
Schematic of a proton (red) impinging on a graphene lattice (grey) at right angles. The interaction with an individual carbon atom depends on ρ and the in-plane distance r, which is the difference between the impact parameter **b** and the position vector $\mathbf{R}_i$ of the atom.

(2021); Ćosić et al. (2021)]. Describing the interaction of protons with the membrane via a thermally averaged potential, two rainbow features are predicted: an "inner" and an "outer" one. The inner rainbow is present at a few mrad and arises from trajectories close to center of the hexagon. The outer one stems from a maximum in the deflection function close to a carbon atom, leading to a signal at around 170 mrad [Ćosić et al. (2018)]. The authors argue that in combination these give very detailed insights into the internal temperature [Ćosić et al. (2019)] and the interaction potential [Ćosić et al. (2021)], the defect concentration [Hadžijojić et al. (2021)] as well as the membrane's orientation and inclination [Ćosić et al. (2018); Ćosić et al. (2021)]. However, there are several conceptual issues with the underlying theoretical description. For instance, even when the protons hit a nucleus head-on they are always transmitted.

In this publication, we provide a description of the scattering process based on classical trajectories. We incorporate thermal effects by statistical averaging over displaced carbon atoms for each individual scattering event. Additionally, we account for the membrane's corrugation as well as the experimental resolution and quantify their impact on the pattern at the detector. Based on this, we evaluate the predictions from the literature [Ćosić et al. (2018); Ćosić et al. (2019); Hadžijojić et al. (2021); Ćosić et al. (2021)] and test whether classical scattering through membranes can be used as an analytic tool. In our analysis we find that the predicted outer rainbow is an artifact from an improper description of the scattering process. For the inner rainbow already the zero-point motion of the membrane atoms leads to a significant broadening of the signal, obscuring part of the details. Together with the fact that protons at 5 keV have a non-negligible cross-section for displacing atoms in graphene [Shi et al. (2019)], this limits their use as an analytic tool for the study of 2D materials.

2 Theory and methods

To capture the behavior described previously in the literature [Ćosić et al. (2018); Ćosić et al. (2019); Hadžijojić et al. (2021)], we consider the transmission of protons with a kinetic energy of 5 keV through single-layer graphene. These particles propagate along the z-direction with velocity v_z until they interact with the 2D membrane where they are scattered, as shown in Figure 1. To describe the interaction of the collision partners, we use the ZBL potential [Ziegler and Biersack (1985); Ziegler et al. (1983)]

$$V^{\mathrm{ZBL}}(\rho) = \frac{Z_{\mathrm{H}}\, Z_{\mathrm{C}}\, e^2}{4\pi\varepsilon_0} \cdot \frac{1}{\rho} \sum_n \alpha_n \exp\left[-\beta_n \frac{\rho}{a}\right]. \tag{1}$$

Here, ρ is the proton-carbon distance, Z_{H} and Z_{C} are the atomic numbers of hydrogen and carbon, e is the elementary charge, and ε_0 is the vacuum permittivity. The screening radius a and the fitting parameters α_n and β_n account for the distance-dependent shielding of the nuclear Coulomb interaction by the electrons [Ziegler et al. (1983)].

For small scattering angles ($\theta \ll 1$ rad) the magnitude of the transferred transverse momentum $p_\perp$ for the binary interaction between a proton and a lattice atom is

$$p_\perp(r) = -\frac{r}{v_z} \int_{-\infty}^{\infty} \frac{\mathrm{d}V(\rho)}{\mathrm{d}\rho} \frac{1}{\sqrt{z^2 + r^2}}\, \mathrm{d}z, \tag{2}$$

where r is the proton-carbon distance in the scattering plane and $\rho = \sqrt{z^2 + r^2}$. The total transverse momentum vector $\mathbf{p}_{\perp,\mathrm{tot}}$ depends on the impact parameter **b** and is obtained by summing over all considered binary interactions [Lehtinen et al. (2010)]

$$\mathbf{p}_{\perp,\mathrm{tot}}(\mathbf{b}) = \sum_i p_\perp(\|\mathbf{b} - \mathbf{R}_i\|) \frac{\mathbf{b} - \mathbf{R}_i}{\|\mathbf{b} - \mathbf{R}_i\|}. \tag{3}$$

The deflection angle $\boldsymbol{\theta} = (\theta_x, \theta_y)$ is obtained within the small-angle approximation

$$\boldsymbol{\theta} = \frac{\mathbf{p}_{\perp,\mathrm{tot.}}}{p_z}. \tag{4}$$

While here the protons are always scattered through a single, central carbon ring, we added six additional hexagons around the central one to form a coronene-like structure. Furthermore, we restrict the integration in Eq. 2 to ±1 nm around the scattering plane (see Supplementary Material). In this description we treat the protons as classical particles and neglect the wave-nature of the protons. This is justified by the significant experimental challenges that ions pose to matter-wave diffraction, which have not yet been overcome.

To account for the finite angular resolution, we assume a 2D-Gaussian distribution of incoming angles with a variable standard deviation. For each scattering event, a random angle was chosen from the distribution and added to the calculated scattering angle. Also, the natural corrugation of free-standing single-layer graphene, that is, its three-dimensional waviness was included [Meyer et al. (2007)]. When protons scatter at a corrugated membrane, the effective scattering geometry corresponds to the projection of the graphene sheet onto the xy-plane. Here, we consider a root-mean-squared inclination of 75.7 mrad, corresponding to the experimental value reported for exfoliated graphene [Singh et al. (2022)].

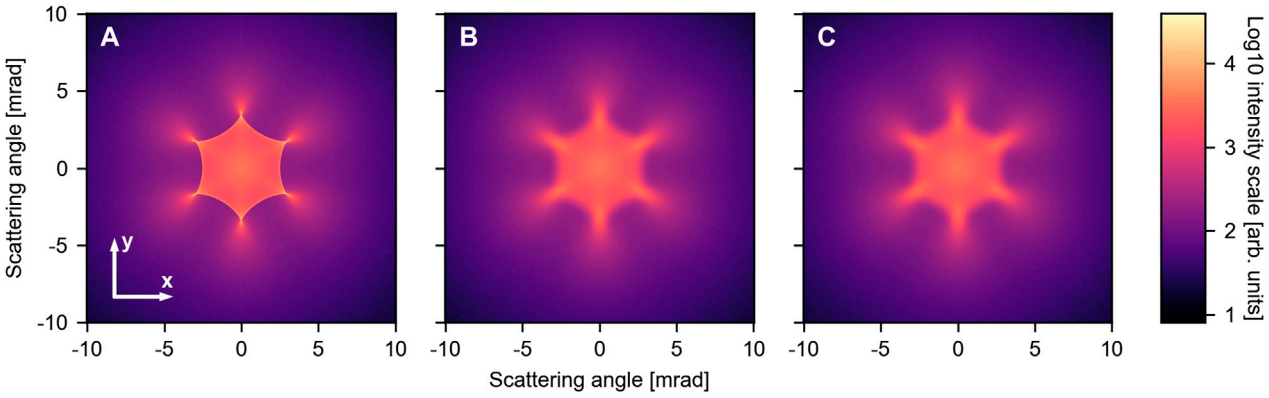

FIGURE 2
Scattering simulations including different effects: **(A)** Flat membrane with atoms fixed at their equilibrium position, **(B)** flat membrane exhibiting zero-point motion, and **(C)** corrugated membrane with a root mean square (rms) inclination angle of 75.7 mrad at T =300 K. In **(C)** we further included an angular resolution of 100 µrad. All intensities are plotted on a logarithmic scale.

2.1 Modelling thermal motion

A proton with an energy of 5 keV moves at 979 km/s, traversing the interaction zone of 2 nm within 2 fs. This has to be compared to the frequency range of phonons in graphene, which reaches up to 50 THz [Yang et al. (2021)]. So, even at the highest phonon mode, atoms undergo only 0.1 vibrations while a proton is within the interaction zone. Hence, the movement of the atoms can be approximated as quasi-static [Pfandzelter et al. (2001)]. However, each proton encounters a different scattering geometry and one has to average over many different scattering geometries to obtain a realistic picture. Using the Debye model for the density of states [Kittel (2018)] and describing each atom as a harmonic oscillator around its lattice site [Cohen-Tannoudji et al. (1991)], the mean squared displacement σ^2 can be expressed as a function of membrane temperature T [Chen and Yang (2007)]

$$\sigma^2 = \frac{3\hbar^2}{m_C k_B \Theta_D}\left[\frac{T}{\Theta_D} D_1\left(\frac{\Theta_D}{T}\right) + \frac{1}{4}\right]. \tag{5}$$

Here m_C is the mass of a carbon atom, k_B is the Boltzmann constant, Θ_D = 2100 K the in-plane Debye temperature of graphene [Tohei et al. (2006); Pop et al. (2012)], and D_1 the first Debye function. We use the same model to describe the zero-point motion of the lattice atoms. For T close to 0 K, Eq. 5 simplifies to

$$\sigma_0^2 = \frac{3}{4}\frac{\hbar^2}{m_C k_B \Theta_D} \tag{6}$$

resulting in an in-plane displacement for single-layer graphene of $\sigma_0^2 = 1.4 \times 10^{-5}$ nm^2. In this study, we assume an uncorrelated 2D normal distribution for the in-plane displacement of each atom. Out-of-plane displacements have not been included, as they have no effect on the signal within this description.

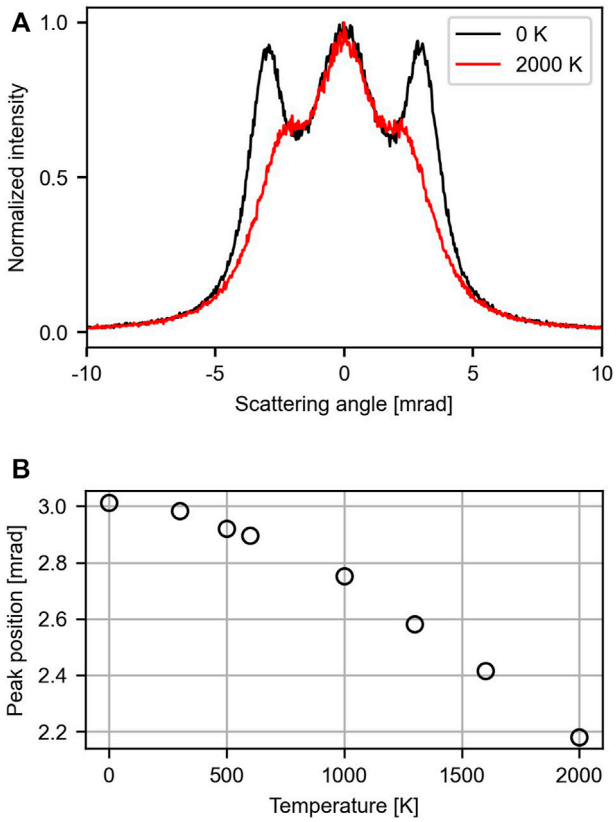

FIGURE 3
Influence of the membrane temperature on the scattering pattern. Here the effect of the membrane's corrugation and the angular resolution was neglected. **(A)** Line traces through the y-axis shown for 0 K (black) and 2000 K (red). **(B)** Dependence of the side lobe's position on temperature between 0 and 2000 K.

3 Results

We first consider a perfectly collimated beam impinging on a flat membrane where the position of all carbon atoms is fixed at their equilibrium position. While such a situation cannot be realized experimentally, the respective pattern shown in Figure 2A may act as a point of reference for the latter simulations. It exhibits a six-fold symmetry, mirroring the honeycomb structure of graphene. Most

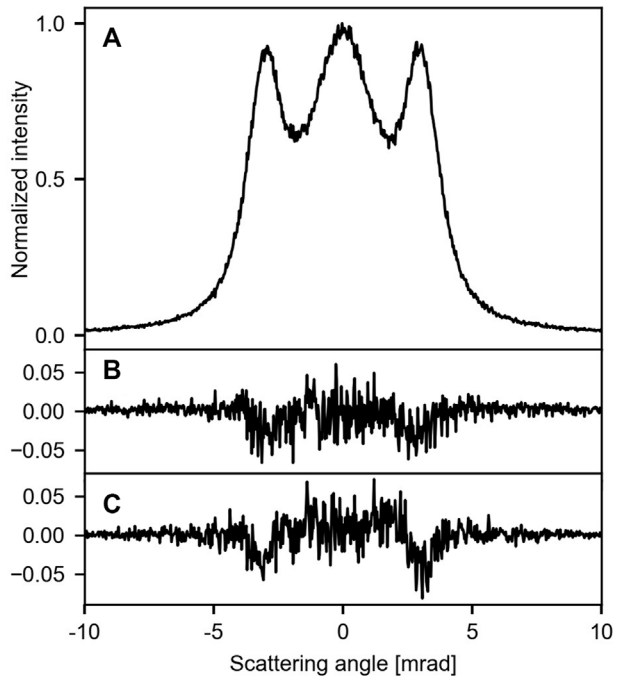

FIGURE 4
Influence of the corrugation and the angular resolution on the signal at 0 K (traces along the *y*-axis through the center): **(A)** flat membrane and infinite angular resolution, **(B)** corrugated membrane with a rms inclination of 75.5 mrad, **(C)** flat membrane and an angular resolution of 100 μrad. For **(B, C)** the difference to trace **(A)** is shown.

intensity is scattered at angles below 7.5 mrad and we observe rather sharp features. These can be traced back to rainbow scattering originating from a maximum in the deflection angle close to the center of the hexagon. For larger scattering angles, the signal continuously decreases in intensity with no discernible features, as shown in the Supplementary Material. Thus, we do not observe the outer rainbow feature reported previously in the literature [Ćosić et al. (2018); Ćosić et al. (2019); Hadžijojić et al. (2021)]. We can, however, artificially reproduce these features by thermally averaging the interaction potential (Supplementary Material).

Including the lattice atoms zero-point motion already leads to a significant broadening of the rainbow lines, as shown in Figure 2B. While the general shape remains unaffected, the fine features are washed out. To study the temperature-dependence, we extended the simulations to a range between 0 and 2000 K. The line plots through the center of the pattern along the *y*-axis for 0 and 2000 K are shown in Figure 3A. The data for the other temperatures and the traces through the *x*-axis can be found in the Supplementary Material. In general, the plots exhibit just a few features: a central lobe and the rainbow peaks located at ≈ 3.0 mrad. With increasing temperature these peaks become less prominent and shift to smaller angles. At 2000 K they are reduced to shoulders located at $\theta \approx 2.2$ mrad. The dependence of the peak position on the temperature is shown in Figure 3B.

Both the membrane's corrugation and the angular resolution may lead to further broadening of the signal at the detector. This is shown in Figure 4. In comparison to a flat membrane (Figure 4A), the effect of the corrugation [Singh et al. (2022)] on the pattern is on the percentage level and thus challenging to resolve (Figure 4B). The same is true for an angular resolution of $\phi = 100$ μrad (Figure 4C). Combining these two effects thus yields a pattern, which is virtually identical to the flat membrane. This is illustrated in Figures 2B, C for $T = 300$ K. Degrading the angular resolution leads to a decrease in the relative intensity of the side lobes. Furthermore, their position is shifted to smaller angles (Supplementary Material), resembling the effect of increasing temperature.

4 Discussion

Classically, rainbow scattering occurs at the extrema of the scattering function, which maps the impact parameter to a scattering angle θ. Usually, this is the case at inflection points of the scattering potential and results in a sharp intensity maximum at the corresponding scattering angle. Thus, the shape and the position of the rainbow pattern contain information about the interaction potential between the membrane and the protons.

Previous calculations of proton transmission through graphene used thermal averaging of the potential to describe the interaction [Ćosić et al. (2018)]. In that model, the charge of the C nucleus is spread over a volume $\propto \sigma_0^3$, replacing the Coulombic singularity at $r = 0$ by a Gaussian. Its inflection point produces a second outer rainbow, which was predicted to be sensitive to temperature and the orientation of the membrane [Ćosić et al. (2018); Ćosić et al. (2019); Ćosić et al. (2021); Hadžijojić et al. (2021)]. However, it also entails that protons are transmitted during head-on collisions.

Thermal averaging of the interaction potential was introduced in channeling of high-energy ions through crystals [Krause et al. (1986)] and is still used to investigate possible bias in the detection of dark matter [Bozorgnia et al. (2010)]. During channeling the ion trajectory oscillates within the potential originating from the atomic strings. Thermal averaging of the potential along the channel is the simplest model to describe these complex oscillations and preserve the axial symmetry. However, this approach is limited and the effect of crystal atoms protruding into the channel requires a statistical evaluation [Andersen and Feldman (1970)]. In the case of 2D materials the thickness is orders of magnitude smaller than the typical distance between oscillations in the axial potential. This suggests that there are not enough interactions along the trajectory to justify an averaged potential.

We start the evaluation of the predicted effects by addressing the impact of temperature on the scattering pattern. As illustrated in Figure 3B, the peak position of the side lobes changes by only 0.12 mrad when going from 0 to 600 K. To realize a temperature resolution of 100 K (500–600 K), a shift in peak position relative to the peak width of only 4% has to be resolved, which we consider to be challenging. This has to be compared to Raman spectroscopy and surface diffraction where a temperature difference of about 60 K can be resolved [Calizo et al. (2009); Pan et al. (2022)]. Above 1000 K the impact of temperature becomes more pronounced, but the intensity of the side lobes deteriorates, making it harder to determine their position accurately. In general, such issues can be mended by a thorough characterization of the setup and long integration times. However, in the current situation we face two fundamental limitations. First, protons at 5 keV create a single vacancy in graphene with a probability 2×10^{-3} [Shi et al. (2019)]. Thus, the membrane is destroyed continuously during the measurement process. Second, the constant

stream of protons colliding with the membrane leads to artificial heating. This suggests that scattering of protons at 5 keV provides only limited insights into the membrane's temperature.

The large-scale corrugation of the membrane has only a minor effect on the scattering pattern. Thus, stretching the membrane as discussed in Nicholl et al. (2017); Nicholl et al. (2015) does not seem necessary. Regarding angular resolution, we observe that increasing the value of ϕ resembles the effect of increasing temperature (see Supplementary Material): at 400 µrad the intensity of the rainbow peaks is comparable to that at T = 2000 K, cf. Figure 3. The optimal resolution to study scattering of protons at 5 keV is around ϕ = 100 µrad. It can be easily realized experimentally and the resulting pattern (Figure 2C) is virtually indistinguishable from the one with a perfectly collimated beam (Figure 2B). This allows to capture all essential details of the pattern.

So far, we have considered a perfect crystal in a single orientation. This is motivated by advances in the synthesis of graphene [Chen et al. (2013); Gao et al. (2012); Wu et al. (2013); Yan et al. (2014)]. However, irradiating such a sample with protons at 5 keV leads to substantial damage. If we multiply the probability to introduce defects with the 1.6×10^8 scattered protons required to create an image in Figure 2, we end up with 3.2×10^5 additional generated vacancies. Thus, using this method to study defects and assess their concentration is at least questionable. Extracting information from a poly-crystalline sample with grain boundaries is even more challenging. Here, several lattices with different orientations will contribute, further obscuring the image. In the extreme case of small grain size one would expect a circularly symmetrical image. However, if the experiment is restricted to low doses, it should be possible to extract some information on the interaction potential from the position of the rainbow peaks before the membrane is damaged too much. The same applies to orientation of the membrane, which is encoded in the scattering pattern at least for samples with one predominant crystal orientation.

5 Summary and outlook

In summary, we have investigated classical scattering of protons through graphene. Including the temperature of the lattice by displacing the lattice atoms for each scattering event, we could show that the outer rainbow previously described in the literature is an artifact. In contrast to that, statistical averaging performed here quantitatively indicates the maximum level of detail that can be observed in an experiment. Regarding thermometry, we observe only a weak dependence of the peak positions on temperature, which might additionally be obscured by the angular resolution and the artificial heating due to the colliding protons. Based on this, we cannot confirm the predicted high sensitivity regarding temperature based on the contribution of in-plane and out-of-plane motion.

If the dose is restricted, it should be possible to extract some information on the interaction potential and the orientation of the membrane. The possibility to study defects seems unrealistic as the method has a non-negligible probability for inducing defects itself. This limits the applicability of the proposed method as an analytical tool as the membrane is always changed during the analysis.

To avoid beam damage and turn proton scattering into a useful technique, the interaction energy has to be reduced below the damage threshold, which is predicted around 80 eV [Brand et al. (2019)]. In turn, this opens new vistas to study the interaction of protons with the membrane. On the one hand, neutralization will be more prominent at these energies [Kononov and Schleife (2021)], bringing energy- and angle-resolved neutralization studies within reach. On the other hand, exchanging protons by neutral hydrogen atoms facilitates matter-wave diffraction [Brand et al. (2019)]. In this case the level of detail is expected to be much higher, allowing to study elastic and inelastic interactions in detail.

Data availability statement

The raw data supporting the conclusion of this article will be made available by the authors, without undue reservation.

Author contributions

JB: Formal Analysis, Investigation, Software, Writing–original draft, Writing–review and editing. PR: Conceptualization, Methodology, Writing–original draft, Formal Analysis, Supervision, Writing–review and editing. CB: Conceptualization, Supervision, Writing–original draft, Formal Analysis, Writing–review and editing.

Funding

The author(s) declare that no financial support was received for the research, authorship, and/or publication of this article.

Acknowledgments

We thank Maxime Debiossac, Maxim Efremov, and François Aguillon for fruitful discussions.

Conflict of interest

The authors declare that the research was conducted in the absence of any commercial or financial relationships that could be construed as a potential conflict of interest.

Publisher's note

All claims expressed in this article are solely those of the authors and do not necessarily represent those of their affiliated organizations, or those of the publisher, the editors and the reviewers. Any product that may be evaluated in this article, or claim that may be made by its manufacturer, is not guaranteed or endorsed by the publisher.

Supplementary material

The Supplementary Material for this article can be found online at: https://www.frontiersin.org/articles/10.3389/fchem.2023.1291065/full#supplementary-material

References

Al Taleb, A., and Farías, D. (2016). Phonon dynamics of graphene on metals. *J. Phys. Condens. Matter* 28, 103005. doi:10.1088/0953-8984/28/10/103005

Al Taleb, A., Yu, H. K., Anemone, G., Farías, D., and Wodtke, A. M. (2015). Helium diffraction and acoustic phonons of graphene grown on copper foil. *Carbon* 95, 731–737. doi:10.1016/j.carbon.2015.08.110

Andersen, J., and Feldman, L. (1970). Comparison of average-potential models and binary-collision models of axial channeling and blocking. *Phys. Rev. B* 1, 2063–2069. doi:10.1103/physrevb.1.2063

Anemone, G., Climent-Pascual, E., Yu, H. K., Al Taleb, A., Jiménez-Villacorta, F., Prieto, C., et al. (2016). Quality of graphene on sapphire: long-range order from helium diffraction versus lattice defects from Raman spectroscopy. *RSC Adv.* 6, 21235–21245. doi:10.1039/C5RA27452D

Bahn, E., Tamtögl, A., Ellis, J., Allison, W., and Fouquet, P. (2017). Structure and dynamics investigations of a partially hydrogenated graphene/Ni(111) surface. *Carbon* 114, 504–510. doi:10.1016/j.carbon.2016.12.055

Benedek, G., Manson, J. R., and Miret-Artés, S. (2021). The electron–phonon coupling constant for single-layer graphene on metal substrates determined from He atom scattering. *Phys. Chem. Chem. Phys.* 23, 7575–7585. doi:10.1039/D0CP04729E

Borca, B., Barja, S., Garnica, M., Minniti, M., Politano, A., Rodriguez-García, J. M., et al. (2010). Electronic and geometric corrugation of periodically rippled, self-nanostructured graphene epitaxially grown on Ru(0001). *New J. Phys.* 12, 093018. doi:10.1088/1367-2630/12/9/093018

Bozorgnia, N., Gelmini, G. B., and Gondolo, P. (2010). Channeling in direct dark matter detection I: channeling fraction in NaI (Tl) crystals. *J. Cosmol. Astropart. Phys.* 019. doi:10.1088/1475-7516/2010/11/019

Brand, C., Debiossac, M., Susi, T., Aguillon, F., Kotakoski, J., Roncin, P., et al. (2019). Coherent diffraction of hydrogen through the 246 pm lattice of graphene. *New J. Phys.* 21, 033004. doi:10.1088/1367-2630/ab05ed

Brand, C., Sclafani, M., Knobloch, C., Lilach, Y., Juffmann, T., Kotakoski, J., et al. (2015). An atomically thin matter-wave beamsplitter. *Nat. Nanotechnol.* 10, 845–848. doi:10.1038/nnano.2015.179

Calizo, I., Ghosh, S., Bao, W., Miao, F., Ning Lau, C., and Balandin, A. A. (2009). Raman nanometrology of graphene: temperature and substrate effects. *Solid State Commun.* 149, 1132–1135. doi:10.1016/j.ssc.2009.01.036

Chen, Q., Dwyer, C., Sheng, G., Zhu, C., Li, X., Zheng, C., et al. (2020). Imaging beam-sensitive materials by electron microscopy. *Adv. Mater.* 32, 1907619. doi:10.1002/adma.201907619

Chen, S., Ji, H., Chou, H., Li, Q., Li, H., Suk, J. W., et al. (2013). Millimeter-size single-crystal graphene by suppressing evaporative loss of Cu during low pressure chemical vapor deposition. *Adv. Mater.* 25, 2062–2065. doi:10.1002/adma.201204000

Chen, Y.-L., and Yang, D.-P. (2007). *Mössbauer effect in lattice dynamics: experimental techniques and applications*. United States: John Wiley and Sons.

Cohen-Tannoudji, C., Diu, B., and Laloë, F. (1991). *Quantum mechanics*, vol. 1 (United States: Wiley), 1. edn.

Ćosić, M., Hadžijojić, M., Petrović, S., and Rymzhanov, R. (2021). Morphological study of the rainbow scattering of protons by graphene. *Chaos Interdiscip. J. Nonlinear Sci.* 31, 093115. doi:10.1063/5.0059093

Ćosić, M., Hadžijojić, M., Rymzhanov, R., Petrović, S., and Bellucci, S. (2019). Investigation of the graphene thermal motion by rainbow scattering. *Carbon* 145, 161–174. doi:10.1016/j.carbon.2019.01.020

Ćosić, M., Petrović, S., and Nešković, N. (2018). The forward rainbow scattering of low energy protons by a graphene sheet. *Nucl. Instrum. Methods Phys. Res. Sect. B* 422, 54–62. doi:10.1016/j.nimb.2018.02.028

Debiossac, M., Zugarramurdi, A., Mu, Z., Lunca-Popa, P., Mayne, A. J., and Roncin, P. (2016). Helium diffraction on SiC grown graphene: qualitative and quantitative descriptions with the hard-corrugated-wall model. *Phys. Rev. B* 94, 205403. doi:10.1103/PhysRevB.94.205403

Ferrari, A. C., Meyer, J. C., Scardaci, V., Casiraghi, C., Lazzeri, M., Mauri, F., et al. (2006). Raman spectrum of graphene and graphene layers. *Phys. Rev. Lett.* 97, 187401. doi:10.1103/physrevlett.97.187401

Gao, L., Ren, W., Xu, H., Jin, L., Wang, Z., Ma, T., et al. (2012). Repeated growth and bubbling transfer of graphene with millimetre-size single-crystal grains using platinum. *Nat. Commun.* 3, 699. doi:10.1038/ncomms1702

Hadžijojić, M., Ćosić, M., and Rymzhanov, R. (2021). Morphological analysis of the rainbow patterns created by point defects of graphene. *J. Phys. Chem. C* 125, 21030–21043. doi:10.1021/acs.jpcc.1c05971

Jiang, H., Kammler, M., Ding, F., Dorenkamp, Y., Manby, F. R., Wodtke, A. M., et al. (2019). Imaging covalent bond formation by h atom scattering from graphene. *Science* 364, 379–382. doi:10.1126/science.aaw6378

Jiang, H., Tao, X., Kammler, M., Ding, F., Wodtke, A. M., Kandratsenka, A., et al. (2021). Small nuclear quantum effects in scattering of H and D from graphene. *J. Phys. Chem. Lett.* 12, 1991–1996. doi:10.1021/acs.jpclett.0c02933

Kittel, C. (2018). *Kittel's introduction to solid state Physics* (United States: Wiley), 9. edn.

Kononov, A., and Schleife, A. (2021). Anomalous stopping and charge transfer in proton-irradiated graphene. *Nano Lett.* 21, 4816–4822. doi:10.1021/acs.nanolett.1c01416

Krause, H., Datz, S., Dittner, P., del Campo, J. G., Miller, P., Moak, C., et al. (1986). Rainbow effect in axial ion channeling. *Phys. Rev. B* 33, 6036–6044. doi:10.1103/physrevb.33.6036

Lehtinen, O., Kotakoski, J., Krasheninnikov, A., Tolvanen, A., Nordlund, K., and Keinonen, J. (2010). Effects of ion bombardment on a two-dimensional target: atomistic simulations of graphene irradiation. *Phys. Rev. B* 81, 153401. doi:10.1103/physrevb.81.153401

Li, X., Sun, M., Shan, C., Chen, Q., and Wei, X. (2018). Mechanical properties of 2D materials studied by *in situ* microscopy techniques. *Adv. Mater. Interfaces* 5, 1701246. doi:10.1002/admi.201701246

Maccariello, D., Campi, D., Al Taleb, A., Benedek, G., Farías, D., Bernasconi, M., et al. (2015). Low-energy excitations of graphene on Ru(0001). *Carbon* 93, 1–10. doi:10.1016/j.carbon.2015.05.028

Marchini, S., Günther, S., and Wintterlin, J. (2007). Scanning tunneling microscopy of graphene on Ru(0001). *Phys. Rev. B* 76, 075429. doi:10.1103/PhysRevB.76.075429

Meyer, J. C., Geim, A. K., Katsnelson, M. I., Novoselov, K. S., Booth, T. J., and Roth, S. (2007). The structure of suspended graphene sheets. *Nature* 446, 60–63. doi:10.1038/nature05545

Nicholl, R. J. T., Conley, H. J., Lavrik, N. V., Vlassiouk, I., Puzyrev, Y. S., Sreenivas, V. P., et al. (2015). The effect of intrinsic crumpling on the mechanics of free-standing graphene. *Nat. Commun.* 6, 8789. doi:10.1038/ncomms9789

Nicholl, R. J. T., Lavrik, N. V., Vlassiouk, I., Srijanto, B. R., and Bolotin, K. I. (2017). Hidden area and mechanical nonlinearities in freestanding graphene. *Phys. Rev. Lett.* 118, 266101. doi:10.1103/physrevlett.118.266101

Novoselov, K. S., Geim, A. K., Morozov, S. V., Jiang, D., Zhang, Y., Dubonos, S. V., et al. (2004). Electric field effect in atomically thin carbon films. *Science* 306, 666–669. doi:10.1126/science.1102896

Pan, P., Debiossac, M., and Roncin, P. (2022). Temperature dependence in fast-atom diffraction at surfaces. *Phys. Chem. Chem. Phys.* 24, 12319–12328. doi:10.1039/D2CP00829G

Pfandzelter, R., Mertens, A., and Winter, H. (2001). Computer simulations on energy transfer of fast atoms to a crystal lattice under surface channeling. *Phys. Lett. A* 290, 145–150. doi:10.1016/s0375-9601(01)00605-3

Pop, E., Varshney, V., and Roy, A. K. (2012). Thermal properties of graphene: fundamentals and applications. *MRS Bull.* 37, 1273–1281. doi:10.1557/mrs.2012.203

Sacchi, M., and Tamtögl, A. (2023). Water adsorption and dynamics on graphene and other 2D materials: computational and experimental advances. *Adv. Phys. X* 8, 2134051. doi:10.1080/23746149.2022.2134051

Saito, R., Tatsumi, Y., Huang, S., Ling, X., and Dresselhaus, M. S. (2016). Raman spectroscopy of transition metal dichalcogenides. *J. Phys. Condens. Matter* 28, 353002. doi:10.1088/0953-8984/28/35/353002

Shi, T., Peng, Q., Bai, Z., Gao, F., and Jovanovic, I. (2019). Proton irradiation of graphene: insights from atomistic modeling. *Nanoscale* 11, 20754–20765. doi:10.1039/C9NR06502D

Singh, R., Scheinecker, D., Ludacka, U., and Kotakoski, J. (2022). Corrugations in free-standing graphene. *Nanomaterials* 12, 3562. doi:10.3390/nano12203562

Tamtögl, A., Bahn, E., Sacchi, M., Zhu, J., Ward, D. J., Jardine, A. P., et al. (2021). Motion of water monomers reveals a kinetic barrier to ice nucleation on graphene. *Nat. Commun.* 12, 3120. doi:10.1038/s41467-021-23226-5

Tamtögl, A., Bahn, E., Zhu, J., Fouquet, P., Ellis, J., and Allison, W. (2015). Graphene on Ni(111): electronic corrugation and dynamics from helium atom scattering. *J. Phys. Chem. C* 119, 25983–25990. doi:10.1021/acs.jpcc.5b08284

Tan, P.-H. (2019). "Raman spectroscopy of two-dimensional materials," in *Springer series in materials science*. edn (Singapore: Springer Singapore), 1. doi:10.1007/978-981-13-1828-3

Tohei, T., Kuwabara, A., Oba, F., and Tanaka, I. (2006). Debye temperature and stiffness of carbon and boron nitride polymorphs from first principles calculations. *Phys. Rev. B* 73, 064304. doi:10.1103/PhysRevB.73.064304

Tømterud, M., Hellner, S. K., Eder, S. D., Forti, S., Manson, J. R., Colletti, C., et al. (2022). *Temperature dependent bending rigidity of graphene*. ArXiv:2210.17250.

Woznica, N., Hawelek, L., Fischer, H. E., Bobrinetskiy, I., and Burian, A. (2015). The atomic scale structure of graphene powder studied by neutron and X-ray diffraction. *J. Appl. Crystallogr.* 48, 1429–1436. doi:10.1107/S1600576715014053

Wu, T., Ding, G., Shen, H., Wang, H., Sun, L., Jiang, D., et al. (2013). Triggering the continuous growth of graphene toward millimeter-sized grains. *Adv. Funct. Mater.* 23, 198–203. doi:10.1002/adfm.201201577

Yan, Z., Peng, Z., and Tour, J. M. (2014). Chemical vapor deposition of graphene single crystals. *Accounts Chem. Res.* 47, 1327–1337. doi:10.1021/ar4003043x

Yang, X., Han, D., Fan, H., Wang, M., Du, M., and Wang, X. (2021). First-principles calculations of phonon behaviors in graphether: a comparative study with graphene. *Phys. Chem. Chem. Phys.* 23, 123–130. doi:10.1039/D0CP03191G

Zhang, H., Huang, J., Wang, Y., Liu, R., Huai, X., Jiang, J., et al. (2018). Atomic force microscopy for two-dimensional materials: a tutorial review. *Opt. Commun.* 406, 3–17. doi:10.1016/j.optcom.2017.05.015

Ziegler, J., Biersack, J., and Littmark, U. (1983). Empirical stopping powers for ions in solids. *Charge states Dyn. Screen. swift ions solids*, 88–100.

Ziegler, J. F., and Biersack, J. P. (1985). *The stopping and range of ions in matter*. Boston, MA: Springer US, 93–129. doi:10.1007/978-1-4615-8103-1_3

Zugarramurdi, A., Debiossac, M., Lunca-Popa, P., Mayne, A. J., Momeni, A., Borisov, A. G., et al. (2015). Determination of the geometric corrugation of graphene on SiC(0001) by grazing incidence fast atom diffraction. *Appl. Phys. Lett.* 106, 101902. doi:10.1063/1.4914178

frontiers | Frontiers in Chemistry

TYPE Original Research
PUBLISHED 16 November 2023
DOI 10.3389/fchem.2023.1249290

OPEN ACCESS

EDITED BY
Malgorzata Biczysko,
Shanghai University, China

REVIEWED BY
Tie Yang,
Southwest University, China
Sergey Eremeev,
Institute of Strength Physics and Materials Science (ISPMS SB RAS), Russia

*CORRESPONDENCE
Philipp Maier,
philipp.maier@tugraz.at

RECEIVED 28 June 2023
ACCEPTED 19 October 2023
PUBLISHED 16 November 2023

CITATION
Maier P, Hourigan NJ, Ruckhofer A, Bremholm M and Tamtögl A (2023), Surface properties of 1T-TaS_2 and contrasting its electron-phonon coupling with $TlBiTe_2$ from helium atom scattering. *Front. Chem.* 11:1249290. doi: 10.3389/fchem.2023.1249290

Surface properties of 1T-TaS_2 and contrasting its electron-phonon coupling with $TlBiTe_2$ from helium atom scattering

Philipp Maier[1]*, Noah. J. Hourigan[1], Adrian Ruckhofer[1], Martin Bremholm[2] and Anton Tamtögl[1]

[1]Institute of Experimental Physics, Graz University of Technology, Graz, Austria, [2]Department of Chemistry and iNANO, Aarhus University, Aarhus, Denmark

We present a detailed helium atom scattering study of the charge-density wave (CDW) system and transition metal dichalcogenide 1T-TaS_2. In terms of energy dissipation, we determine the electron-phonon (e-ph) coupling, a quantity that is at the heart of conventional superconductivity and may even "drive" phase transitions such as CDWs. The e-ph coupling of TaS_2 in the commensurate CDW phase ($\lambda = 0.59 \pm 0.12$) is compared with measurements of the topological insulator $TlBiTe_2$ ($\lambda = 0.09 \pm 0.01$). Furthermore, by means of elastic He diffraction and resonance/interference effects in He scattering, the thermal expansion of the surface lattice, the surface step height, and the three-dimensional atom-surface interaction potential are determined including the electronic corrugation of 1T-TaS_2. The linear thermal expansion coefficient is similar to that of other transition-metal dichalcogenides. The He–TaS_2 interaction is best described by a corrugated Morse potential with a relatively large well depth and supports a large number of bound states, comparable to the surface of Bi_2Se_3, and the surface electronic corrugation of 1T-TaS_2 is similar to the ones found for semimetal surfaces.

KEYWORDS

transition metal dichalcogenide, topological insulator, charge density wave, helium atom scattering, electron-phonon coupling, thermal expansion

1 Introduction

While it has long been known that the weak short-range van der Waals (vdW) interaction holds together layered materials like graphite and MoS_2 (Fiedler et al., 2023), with the availability of graphene by the so-called scotch tape technique, a vast class of two-dimensional (2D) materials has been investigated (Duong et al., 2017). Mechanical cleavage can be used to prepare monolayers of vdW layered materials, a preparation technique that also works for the layered class of 3D topological insulators (TIs), and first attempts to use these materials in vdW heterostructures and devices are described in Liu et al. (2016). The well-known physics and chemistry of three-dimensional bulk matter often become irrelevant for 2D materials, revealing exotic phenomena in vdW-layered crystals (Duong et al., 2017). Among the most prominent 2D materials are the semimetal graphene, and the transition metal dichalcogenides (TMdCs), which tend to be semiconductors. Here, we provide a detailed helium atom scattering (HAS) study of the TMdC and archetypal charge-density wave (CDW) system 1T-TaS_2 (Rossnagel, 2011). The electron-phonon coupling of the latter

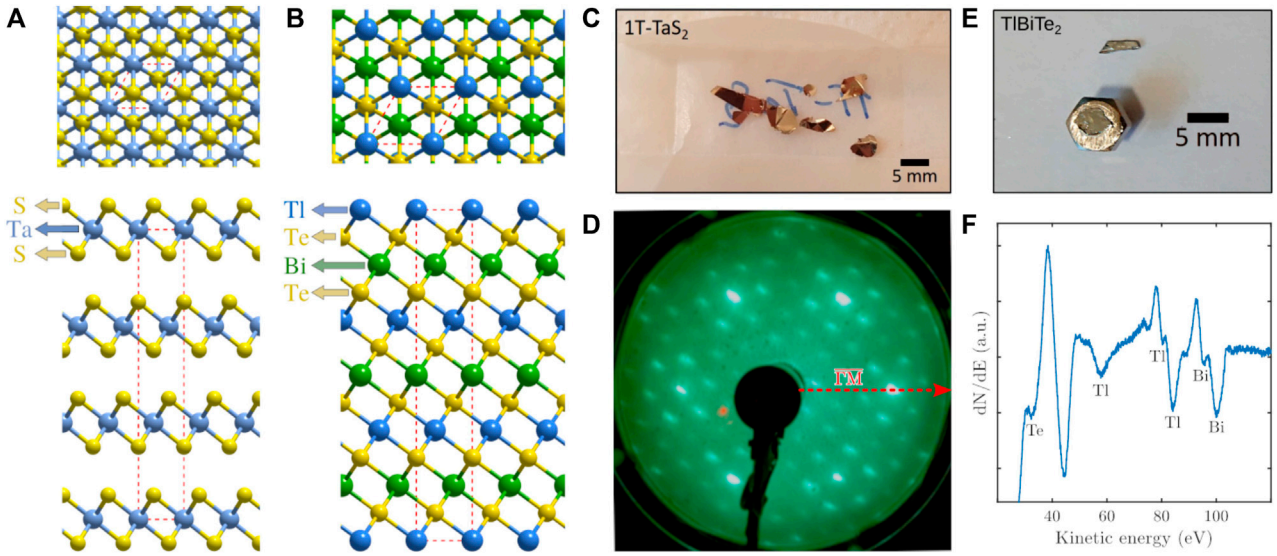

FIGURE 1
Top and side view of **(A)** 1T-TaS_2(0001) and $TlBiTe_2$(111) **(B)**. **(C)** Image of the as-grown 1T-TaS_2 crystals. **(D)** shows the low energy electron diffraction (LEED) pattern of 1T-TaS_2 with the sample aligned along the high symmetry $\overline{\Gamma M}$ orientation at room temperature. The six main (bright) spots according to the hexagonal crystal structure are surrounded by the so-called "star of David" pattern from corresponding clusters in the nearly commensurate charge-density wave phase. **(E)** Image of a $TlBiTe_2$ crystal together with the cleavage post and the attached remaining crystal. **(F)** shows an Auger electron spectrum of the same crystal with signatures of mostly Tl and Bi.

is further compared with measurements of the topological insulator $TlBiTe_2$, which in contrast exhibits a stronger bonding between the layers. Scattering and diffraction from both surfaces are compared in terms of interlayer bonding and surface quality, and completed with measurements of the thermal expansion and a determination of the three-dimensional atom-surface interaction potential of 1T-TaS_2.

TMdCs are atomically thin semiconductors of the type MCh_2, with M being a transition metal atom and Ch a chalcogen atom, where one layer of M atoms is sandwiched between two layers of Ch atoms [see Figure 1A (Duong et al., 2017)]. A TMdC with a particular rich phase diagram is TaS_2. The phase diagram of the 1T polytype of TaS_2 (Figure 1A) involves several CDW transitions driven by strong electronic correlations and electron-phonon (e-ph) coupling upon changes of the surface temperature (Tsen et al., 2015; Vaskivskyi et al., 2015). No final agreement on the electronic ground state of the material or the role of correlations has been reached, and it has even been suggested that the existing experimental evidence for 1T-TaS_2 is consistent with the ground state being a quantum spin liquid (Klanjšek et al., 2017; Law and Lee, 2017).

$TlBiTe_2$ on the other hand is a trigonal crystal with 4 layers as shown in Figure 1B forming a repeated elemental sequence (Tl-Te-Bi-Te-Tl) and $TlBiTe_2$ as well $TlBiSe_2$ are thallium-based ternary narrow-band semiconductors (Singh et al., 2016). It was predicted theoretically that this class of materials are 3D TIs (Eremeev et al., 2010; Eremeev et al., 2011; Lin et al., 2010; Yan et al., 2010), later followed by experimental evidence of its topological properties (Chen et al., 2010; Kuroda et al., 2010; Kuroda et al., 2013). Chen et al. measured the 3D band structure of $TlBiTe_2$ using angle-resolved photoemission spectroscopy (ARPES) and found a single Dirac cone in the center of the surface Brillouin zone (Chen et al., 2010; Singh et al., 2012). Due to the observation of the negative bulk band gap of −10 meV they concluded that $TlBiTe_2$ may be classified as a semimetal rather than a narrow-gap semiconductor as suggested by theory and that this semimetallic nature explains its small thermoelectric power (Spitzer and Sykes, 1966; Kurosaki et al., 2003; Chen et al., 2010). Furthermore, according to Singh et al., Weyl semimetals can be realized at the topological critical point in alloys $TlBi(S_{1-x}Te_x)_2$ by breaking the inversion symmetry in layer-by-layer growth in the order Tl-Te-Bi-S (Singh et al., 2012). However, such kind of structures have not been realized so far.

Similar to 1T-TaS_2 and the 3D TI family Bi_2Te_3/Bi_2Se_3, where the quintuple layers are weakly bound by vdW interactions (Zhang et al., 2009), $TlBiTe_2$ is also a layered material but its atomic layers are bonded covalently (Yan et al., 2010). While the e-ph coupling has been measured for a variety of TIs in particular the class of binary TIs (Ruckhofer et al., 2020), much less experimental information about the $TlBiTe_2$ system is available not least in terms of the e-ph coupling.

2 Methods

HAS is ideally suited to study CDW phases since the neutral He beam is directly scattered by the surface electrons and HAS permits determination of the e-ph coupling λ (Manson et al., 2022) which specifies also conventional superconductivity (Benedek et al., 2020b). Previous HAS diffraction and phase transition data from HAS are described in Benedek et al. (2020b), including CDW systems with HAS (Tamtögl et al., 2019; Ruckhofer et al., 2023).

Our experiments were performed at the HAS apparatus in Graz. A detailed description of the experimental setup has been given elsewhere (Tamtögl et al., 2010). A nearly monochromatic beam ($\Delta E/E \approx 2\%$) of ^{4}He which is generated by a supersonic expansion through a cooled 10 µm nozzle, passes through a skimmer and is scattered off the sample

surface. By varying the nozzle temperature, the beam energy of the incident helium beam can be tuned between 9 and 20 meV. In our setup, the angle between the source arm and the detector arm is fixed at 91.5°. After hitting the sample in the main chamber under ultra-high vacuum (UHV) conditions ($p < 2 \cdot 10^{-10}$ mbar) the beam is detected using a quadrupole mass spectrometer. By rotating the sample, the angle of incidence ϑ_i can be varied.

TaS_2 crystals were grown by chemical vapor transport using I_2 as transport agent and the 1T-TaS_2 phase was obtained by quenching the crystals from ≈ 1000 °C. 1T-TaS_2 was further characterized by X-ray diffraction, resistivity measurements, and ARPES (Ngankeu et al., 2017). From single crystal X-ray diffraction, some stacking disorder is observed in the bulk, which does, however, not affect HAS or any other surface sensitive method. The crystals, as shown in Figure 1C, are thin and can only be cleaved a limited number of times *in situ* by the scotch tape method. Prior to the measurements a clean surface was prepared by applying scotch tape to the TaS_2 sample surface and peeling it off in a UHV transfer chamber (Tamtögl et al., 2016).

The $TlBiTe_2$ sample was grown in the group of C. Felser (Li et al., 2017; Pei et al., 2022). Due to the stronger bonding between the layers as illustrated in Figure 1B, cleaving requires knocking off an attached post *in situ* in the mentioned transfer chamber. The latter had been attached with epoxy prior to transferring the sample into the transfer chamber. Figure 1E shows an image of the post with the remaining attached crystal after it had been removed from the chamber.

Following cleavage, both samples can be inserted into the scattering chamber. For temperature-dependent measurements, the sample can be cooled down to 115 K via a thermal connection to a liquid nitrogen reservoir and heated using a button heater.

3 Results and discussion

Figures 1A, B illustrate the structures of both 1T-TaS_2 and $TlBiTe_2$. As mentioned in the introduction, it is evident from the side view of $TlBiTe_2$ that the coupling between the atomic layers is much stronger and less of a vdW type compared to the TMdCs but also compared to bonding between the quintuple layers of the binary TIs. The latter is actually confirmed in our experiments as $TlBiTe_2$ is much more difficult to cleave as mentioned above. In the Auger electron spectroscopy (AES) spectrum shown in Figure 1F mostly the main peaks from Tl and Bi are present, the peak at about 45 eV stems most likely from elements in the sample holder. As said above, $TlBiTe_2$ is a trigonal crystal but similar to the binary TIs it is more convenient to consider them in the conventional hexagonal notation (red dashed line in Figure 1B) with $c = 3c_0$, i.e. three repeated elemental sequences. These repeatable sequences, consisting of four layers each, are however compared to the quintuple layers in the binary TIs not separated by a vdW gap.

The surface termination of $TlBiSe_2$ has been studied experimentally by Kuroda et al. using scanning tunneling microscopy (STM) and core-level photoelectron spectroscopy (CL-PES) (Kuroda et al., 2013) and by Pielmeier et al. using ARPES, X-ray photoelectron spectroscopy (XPS), STM and atomic force microscopy (AFM) (Pielmeier et al., 2015). Both studies agree that cleaving happens between Tl and Se layers since the bonding strength between these layers is weaker compared to other layers according to *ab initio* calculations (Eremeev et al., 2011). Their STM and CL-PES results showed that after cleavage the surface is terminated by a Se layer with islands of Tl atoms on top of the Se layer covering roughly half of the surface which is further supported by *ab initio* calculations for $TlBiSe_2$ and $TlBiTe_2$ (Singh et al., 2016). Following the reports which suggest a rough, nonpolar surface model (Kuroda et al., 2013; Singh et al., 2016) it appears likely that the same scenario holds for $TlBiTe_2$, i.e., a Te layer covered by Tl islands forms the termination after cleavage. In fact the inset of Figure 2B which shows the first order diffraction and the specular along $\overline{\Gamma M}$ also suggests a rough surface with diffuse scattering due to the small specular which is a measure for the surface order (Farías and Rieder, 1998) and described in more detail in Section 3.2.

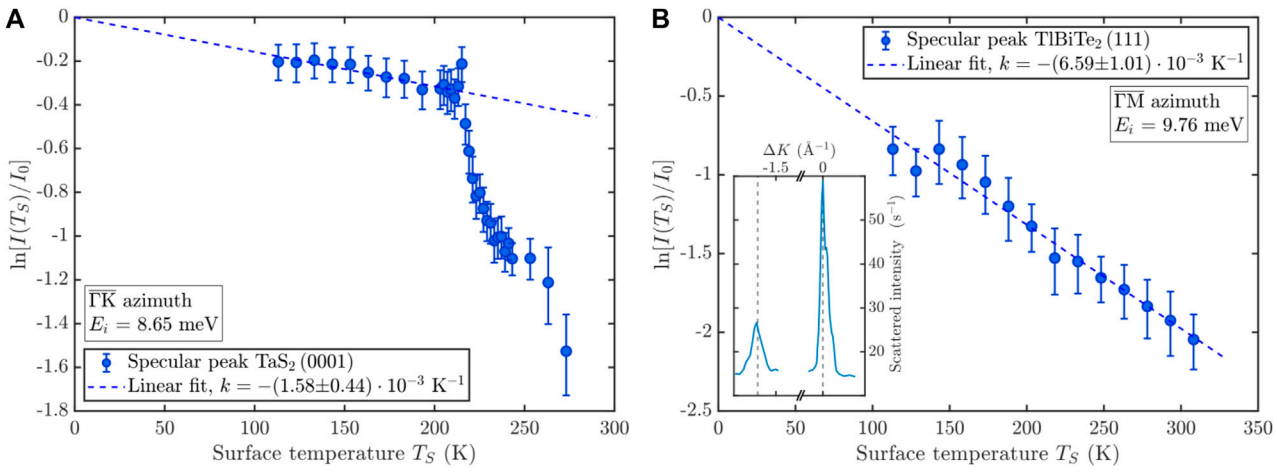

FIGURE 2
The temperature dependencies of the Debye-Waller exponents of **(A)** 1T-TaS_2 for the specular peak with the sample aligned along $\overline{\Gamma K}$ and of **(B)** $TlBiTe_2$(111) aligned along $\overline{\Gamma M}$. $TlBiTe_2$ exhibits the typical linear behavior over the entire temperature range, whereas, after heating 1T-TaS_2, the intensity follows a linear decrease within the commensurate CDW phase, followed by a small increase when entering the triclinic CDW phase at around 210 K and an abrupt decrease with a further transition to the incommensurate CDW phase at around 270 K. The inset of **(B)** shows an angular scan of $TlBiTe_2$ along $\overline{\Gamma M}$ indicating a rough surface with diffuse scattering.

After cleavage of 1T-TaS_2 on the other hand we can clearly resolve the first order diffraction peaks as illustrated in Figure 3, both at room temperature as well as for the cooled sample. The complex CDW structure of 1T-TaS_2, as described by Wilson et al. (Wilson et al., 1975; Wilson et al., 2001; Coleman et al., 1992), and more recently by (Yu et al., 2015) has previously been studied with HAS by (Cantini et al., 1980) and Brusdeylins et al. (Brusdeylins et al., 1989; Benedek et al., 2020b). Here we concentrate on a more detailed study and analysis of the nearly commensurate and commensurate CDW phase of 1T-TaS_2. As described in recent transport measurements, upon cooling 1T-TaS_2 sequentially enters an incommensurate CDW (I-CDW) phase below 550 K, a nearly commensurate CDW (NC-CDW) phase below 350 K, and finally a commensurate CDW (C-CDW) phase below 180 K (Wang et al., 2020). When comparing the cooling and heating data a hysteretic behavior is typically observed both in resistivity (Wang et al., 2020) as well as in HAS measurements (Benedek et al., 2020b). Moreover, upon heating, 1T-TaS_2 enters a triclinic CDW (T-CDW) phase at 220 K, followed by the NC-CDW phase at 280 K (Wang et al., 2020). The space modulations of different CDWs form so-called star-of-David clusters which can be clearly seen in the low energy electron diffraction (LEED) pattern in Figure 1D. In the C-CDW phase, the star of David clusters cover the entire lattice, forming a commensurate $(\sqrt{13} \times \sqrt{13})$R13.54°, with the high symmetry $\overline{\Gamma M}$ azimuth of 1T-TaS_2 highlighted as red dashed arrow in Figure 1D.

In general, weakly coupled layered structures such as TaS_2 have many polymorphs with different stackings and the contrasting behavior between both investigated samples becomes evident from the Debye-Waller plot in Figure 2. $TlBiTe_2$ exhibits only one phase within the covered temperature region and shows the typical linear decrease of the specular intensity. For 1T-TaS_2 on the other hand, upon heating, the typical linear decrease of the specular intensity within the commensurate CDW phase is followed by a small increase upon entering the triclinic CDW phase at around 210 K and an abrupt decrease with a further transition to the incommensurate CDW phase around 270 K. In the following, we describe how HAS permits to determine the e-ph coupling and compare the obtained values for both systems.

3.1 Electron-phonon coupling from temperature dependent atom-scattering measurements

A convenient parameter to characterize the e-ph coupling strength is the mass-enhancement λ (Grimvall, 1981). Since the e-ph coupling describes the interaction between the electronic system and the lattice dynamics (phonons), experimental studies at finite temperatures can either concentrate on the electronic or the phononic system. The former is mostly available via ARPES by examining the renormalization of the electron energy dispersion in the vicinity of the Fermi surface as a result of e-ph interactions. The latter can be carried out using HAS, which on the contrary studies the renormalisation of the surface phonon dispersion due to e-ph interactions. As shown in recent works (Tamtögl et al., 2017; Benedek et al., 2018; Benedek et al., 2020c; Manson et al., 2022), the temperature dependence of the Debye-Waller (DW) exponent plotted in Figure 2 permits to extract, for a conducting surface, the mass-enhancement parameter λ. The Debye-Waller factor takes into account the thermal attenuation of the elastic helium intensity due to atomic motion. The attenuated intensity $I(T_S)$ with respect to I_0, the intensity at rest (T_S = 0 K) in the absence of zero-point motion is given as

$$I(T_S) = I_0 e^{-2W(\mathbf{k}_i, \mathbf{k}_f, T_S)}, \tag{1}$$

with $\mathbf{k}_i$ and $\mathbf{k}_f$ being the wave vectors before and after scattering, respectively. Since a He beam with energies in the meV region is scattered on a conducting surface by the surface free electron density, the exchange of energy with the phonon gas occurs via the phonon-induced modulation of the surface electron gas, that is, via the e-ph interaction (Benedek et al., 2020c; Tamtögl et al., 2021a; Manson et al., 2022). Therefore, the DW-factor, originating from the integrated action of all phonons weighted by their respective Bose factors, turns out to be directly proportional, under reasonable approximations, to the mass-enhancement factor λ (Manson et al., 2022).

The relation between λ and the DW-exponent is given by the equations:

$$\lambda = \frac{\pi}{2n_s}\alpha, \quad \alpha \equiv \frac{\phi}{A_c k_{iz}^2}\frac{\partial \ln I(T_S)}{k_B \partial T_S}, \tag{2}$$

where ϕ is the work function, A_c the unit cell area, $I(T_S)$ the He-beam specular intensity, T_S the surface temperature, k_{iz} the normal component of the incident wavevector and n_s the number of conducting layers which contribute to the phonon-induced modulation of the surface charge density. The latter is estimated to be $n_s = 2\lambda_{TF}/c_0$, where λ_{TF} is the Thomas–Fermi screening length characterizing the surface band-bending region, c_0 the thickness of the cleaved layer, and the factor two considers two metallic sheets per layer.

The advantage of HAS is that it directly provides a surface sensitive measure of the mode-averaged λ. On the contrary, with ARPES a dependence of λ on the initial-state electron energy has been reported (Kumar et al., 2022) and it remains difficult to distinguish between surface and bulk states which is why often time-resolved methods are used (Sobota et al., 2023). Similarly, Raman measurements provide access to the e-ph interaction of optical modes, but again, the method is rather bulk sensitive (Shojaei et al., 2021).

3.1.1 Electron-phonon coupling of 1T-TaS_2

As described above, from the slopes of the HAS specular intensity as a function of surface temperature the corresponding e-ph coupling can be determined using Eq. 2. We follow here the transition from the C-CDW phase to the NC-CDW phase more closely via individual small diffraction scans over the specular peak. According to Benedek et al. (2020b) the observed specular intensity slopes in the corresponding phases give λ(C-CDW) = (0.61 ± 0.06), λ(NC-CDW) = (0.91 ± 0.09), and λ(I-CDW) = (0.61 ± 0.10) for the three phases, which neglects however the triclinic phase (T-CDW) upon heating.

Using the slope in Figure 2A obtained in the C-CDW phase for the calculation of λ together with k_{iz} = 2.85 Å^{-1}, ϕ = 5.2 eV (Shimada et al., 1994), A_c = 9.48 Å^2 and n_s = 3.28 from c_0 = 6.1 Å and a Thomas–Fermi screening length not exceeding 1 nm (Yu et al., 2015) we obtain:

$$\lambda(\text{C-CDW}) = 0.59 \pm 0.12.$$

The e-ph coupling λ in the C-CDW phase is thus consistent with the value obtained by Benedek et al. (2020b), although for $n_s = 2$ as in the mentioned work we would obtain an even larger value with $\lambda = 0.97 \pm 0.19$.

On the other hand, as the attractive part of the surface potential with $D = 8.4$ meV (see Section 3.4 for an exact determination) is comparable to the kinetic energy of the He atoms (8.65 meV) one needs to correct k_{iz}^2 to account for the acceleration by the attractive part of the potential on the He atom when approaching the surface turning point [Beeby correction (Farías and Rieder, 1998)]. Therefore, k_{iz}^2 is replaced by $k_{iz}^{'2} = k_{iz}^2 + 2\,mD/\hbar^2$, where m is the He mass and D the He-surface potential well depth and considering the Beeby correction, we obtain λ(C-CDW) = 0.32 ± 0.06.

In general, low-dimensional materials typically exhibit strong Peierls instabilities and e-ph interactions, and vdW materials such as 1T-TaS_2 provide an ideal platform to study CDWs and the associated superconductivity (Johannes and Mazin, 2008; Rossnagel, 2011). However, while optical methods provide an effective tool to identify the transition temperature of the CDW phase (Lai et al., 2021), quantitative experimental reports about the mode-averaged λ are again quite scarce (Clerc et al., 2006). Compared to the e-ph coupling of $TlBiTe_2$ as described below, it is evident that on the 1T-TaS_2 surface and, in particular in the C-CDW phase a much stronger e-ph coupling λ is present. Further HAS studies that follow the temperature dependence of the DW-exponent in other TMdDCs obtain similar values for λ with an overview being given in Benedek et al. (2020a).

3.1.2 Electron-phonon coupling of $TlBiTe_2$

For $TlBiTe_2$ we use Eq. 2 together with $\phi = 4.2$ eV (National Institute of Standards and Technology, 2018), $A_c = 18.2$ Å^2 and $k_{iz} = 3.02$ Å^{-1}. The Thomas–Fermi screening length λ_{TF} could be estimated according to the formula used for TMdCs such as 2H-MoS_2 with $\lambda_{TF} = (\frac{\hbar^2 \epsilon_r}{4m^* e^2})^{1/2} (\frac{\pi c}{3n_c})^{1/6}$, yielding with Refs (Lubell and Mazelsky, 1965; Paraskevopoulos, 1985)[1] $\lambda_{TF} \approx 30$ Å. However, since $TlBiTe_2$ is a 3D TI, $\lambda_{TF} \approx 60$ Å similar to the values found for other TIs such as Bi_2Se_3 and Bi_2Te_2Se seems to be more appropriate (Benedek et al., 2020c). We further note that such a large λ_{TF} compared to the TMdCs is supported by *ab initio* calculations by Eremeev et al. (2011) which found that the conducting Dirac state penetrates deep into the bulk and even for slabs of 23-layer thickness (≈ 55 Å) an almost unsplit Dirac cone was obtained. Thus, with $c_0 = 7.89$ Å the quadruple layer thickness (Eremeev et al., 2011) and the experimental DW derivative with respect to T_S in Figure 2B, we obtain

$$\lambda = 0.21 \pm 0.03.$$

The factor 2 for n_s in Eq. 2 is here again needed since c_0 encompasses two distinct metal layers, i.e., Tl and Bi. It should be noted that, unlike in the case of low-index metal surfaces, characterized by a soft-wall repulsive potential and negligible corrugation, here the large electronic corrugation (Ruckhofer et al., 2019) implies again a hard-wall potential with an attractive part comparable to the kinetic energy of the He atoms. With the Beeby correction and $D = 6.22$ meV for the He-surface potential well depth (Tamtögl et al., 2021b) it is found:

$$\lambda = 0.09 \pm 0.01.$$

While no values for $TlBiTe_2$ have been reported, it is interesting to compare the value to the ones found for other TIs. It appears that λ found for $TlBiTe_2$ is smaller compared to the binary TIs such as Bi_2Se_3 while at the same time, considering the Beeby correction, equal to the value found for Bi_2Te_2Se (Benedek et al., 2020c) with $\lambda = 0.09$. As the latter exhibits in analogy to $TlBiTe_2$ only a single Dirac cone, it confirms previous reports that an appreciable part of the e–ph interaction is provided by quantum well states as present on the binary TIs. Finally, λ seems to be certainly much smaller compared to the e-ph coupling of the archetypal CDW system in 1T-TaS_2 as described above. In general, a rather small λ is also in line with the fact that $TlBiTe_2$ does not enter a superconducting phase or if so only at very low temperatures (Benedek et al., 2020b). For example, for early reports about a superconducting phase of bulk $TlBiTe_2$ well below 1 K by Hein and Swiggard (1970) it was later argued that it may rather be due to a phase separation of TlTe from BiTe (Popovich et al., 1984). Finally, compared to other topological materials, i.e., in Weyl semimetal systems, recent theoretical reports of the bulk e-ph coupling λ vary between values of 0.13 for NbAs and 0.43 for TaAs (Han et al., 2023), where in both cases the major contribution comes from acoustic phonon modes. These results suggest an equal or even more significant λ compared to TIs such as $TlBiTe_2$. However, experimental approaches in connection with Weyl materials are mainly based on temperature-dependent Raman studies, thus focusing on optical phonon modes and being rather bulk sensitive (Xu et al., 2017; Choe et al., 2021; Osterhoudt et al., 2021; Al-Makeen et al., 2022). In light of these results, surface-sensitive experimental reports about the average e-ph coupling λ of Weyl semimetals are not available to the best of our knowledge, preventing us from providing a decent comparison with these.

3.2 Helium scattering and diffraction from 1T-TaS_2 and $TlBiTe_2$

Since thermal helium atoms have a wavelength comparable to inter-atomic distances the elastic scattering of a helium beam from a periodic surface gives rise to a diffraction pattern. The distances between the diffraction peaks can then be used to calculate the surface lattice constant and in a second step the in-plane linear thermal expansion coefficient. Figure 3 shows several recorded angular diffraction scans (ϑ-scans) obtained by rotating the sample in the scattering plane. Conversion to parallel momentum transfer ΔK follows from

$$\Delta K = |\Delta \mathbf{K}| = |\mathbf{K}_f - \mathbf{K}_i| = |\mathbf{k}_i|\left(\sin\vartheta_f - \sin\vartheta_i\right), \tag{3}$$

with $\mathbf{k}_i$ being the incident wave vector and ϑ_i and ϑ_f the incident and final angles with respect to the surface normal, respectively. The scans in Figure 3 were taken along the high symmetry $\overline{\Gamma M}$ orientation keeping the surface at temperatures of $T_S = 113$ K (left panel) and 296 K (right panel), respectively. The intensity of each specular peak was used for normalization. All scans show clearly a very pronounced specular peak ($\vartheta_i = \vartheta_f$) and two first order diffraction peaks.

The small side peak next to the specular peak for the scan with $E_i = 10.4$ meV occurs due to the presence of the atom-surface potential, which will be further described in Section 3.4. In

1 $m^* = 0.086\,m_e$, $\epsilon_r = 56.15$ and $n_c = 2{\cdot}10^{19}$ cm^{-3}

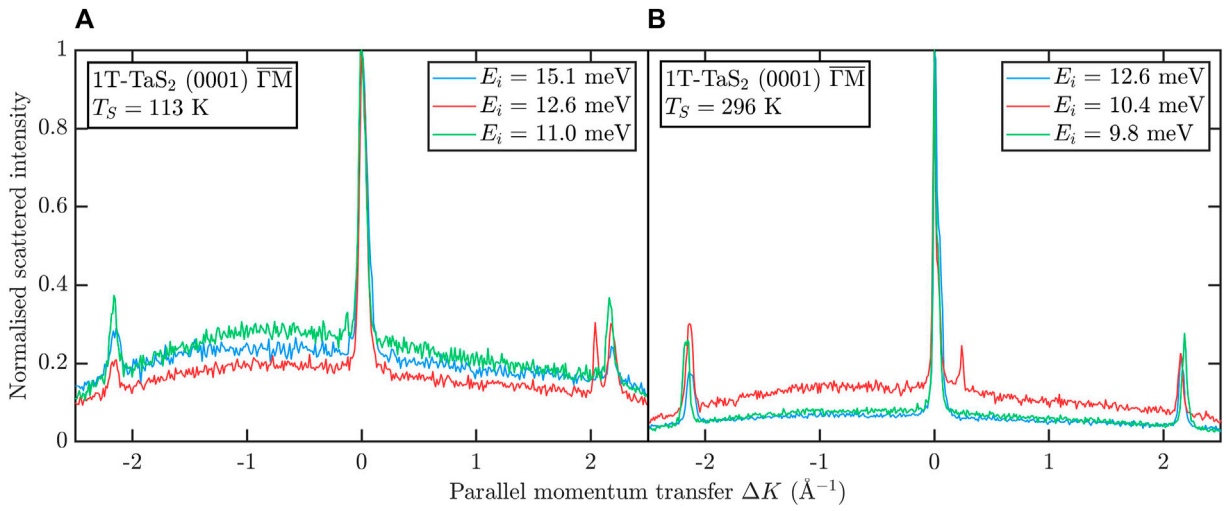

FIGURE 3
Diffraction scans of TaS_2 at surface temperatures of **(A)** T_S = 113 K and **(B)** T_S = 296 K both in $\overline{\Gamma M}$ direction and at various incident beam energies show the corresponding first order diffraction. Even though it is not directly in the scanning direction, a superlattice peak appears in **(A)** only for E_i = 12.6 meV (red curve). The additional peak next to the specular peak in **(B)** for E_i = 10.4 meV is a feature of resonant processes at the surface.

addition to diffraction peaks, the angular scan at E_i = 12.6 meV and T_S = 113 K (red curve in the left panel of Figure 3) shows a very sharp satellite peak next to the (1,0)-diffraction peak at ΔK = 2.04 Å. At this temperature, the crystal is in the C-CDW phase, which is characterized by the star-of-David clusters covering the entire lattice forming a commensurate $(\sqrt{13} \times \sqrt{13})$R13.54° superstructure. Interestingly, while we performed diffraction scans at various nozzle temperatures, the satellite peak is only visible for E_i = 12.6 meV and secondly, we are able to resolve the peak even though it should be rotated with respect to the scanning direction as illustrated in Figure 1D. The latter could be due to a slight azimuthal misalignment of the sample, although we note that Brusdeylins et al. (1989) also observed the peaks arising from the corresponding superstructure, not only in the C-CDW phase but also in the NC-CDW phase at T_S = 340 K.

For $TlBiTe_2$ on the other hand, due to the difficulty associated with the cleavage and the reported likelihood of a patchy termination, we are only able to resolve the specular and a small diffraction peak on one side as shown in the inset of Figure 2B. In general, the intensity scattered into the specular direction is typically by a factor of 10 higher for 1T-TaS_2. As described above, this is sufficient for a determination of the e-ph coupling strength of $TlBiTe_2$ however, it does not permit us to perform any detailed analysis of the $TlBiTe_2$ surface structure and electronic corrugation.

Nevertheless, since a measurement of the angular spread in the specular peak provides an estimate of the surface quality (Farías and Rieder, 1998) and following the approach described in Tamtögl et al. (2017) we can use the measured full-width at half maximum (FWHM) of the specular peak to compare surface order and more specifically the terrace width for both samples.

The peak broadening is proportional to the average domain size, also known as the surface coherence length. As the measured specular width $\Delta\theta_{exp}$ is a convolution of the angular broadening of the apparatus $\Delta\theta_{app}$ and the broadening form the domain size $\Delta\theta_w$, it follows: $\Delta\theta^2_{exp} = \Delta\theta^2_w + \Delta\theta^2_{app}$. The coherence length can then be determined using:

$$l_c = \frac{5.54}{\Delta\theta_w\, k_i\, \cos\vartheta_f} \tag{4}$$

with k_i and ϑ_f as defined beforehand (Farías and Rieder, 1998; Tamtögl et al., 2017).

For 1T-TaS_2, the measured FWHM is typically about 0.04° in ϑ_i-scans, which corresponds to a terrace width of ≈ 500 Å. For $TlBiTe_2$ the FWHM is about 0.05 Å^{-1} in momentum space (inset of Figure 2B) or 0.07° in ϑ_i giving rise to a terrace width of ≈ 200 Å. While STM studies report a Tl island size of the order of 1 − 2 nm and thus much smaller than our result, observed terraces in STM measurements exhibit also widths of about 20 nm (Kuroda et al., 2013; Pielmeier et al., 2015). As the absence of the Tl islands in room temperature STM measurements was attributed to increased mobility of the Tl atoms (Pielmeier et al., 2015), we note that addressing these details and differences would require additional measurements and a more in-depth study.

In summary, we conclude, that as already anticipated, $TlBiTe_2$ is "rougher" and exhibits smaller domain sizes compared to 1T-TaS_2. However, neither of the surface qualities is comparable to some of the binary TIs, where the angular broadening of the specular peak had been reported to be mainly limited by the angular broadening of the apparatus (Tamtögl et al., 2017; Ruckhofer et al., 2019).

3.3 Thermal expansion of 1T-TaS_2

Its unique surface sensitivity makes He diffraction an ideal method to determine the lattice constant of solely the surface layer without any contribution from the underlying layers. From our angular diffraction scans we can thus calculate the surface

lattice constant of 1T-TaS_2 and in a second step the linear thermal expansion coefficient. Following the two-dimensional Laue condition for a hexagonal lattice, the surface lattice constant can be calculated. For T_S = 113 K, we recorded 14 angular scans in $\overline{\Gamma M}$ direction at different incident beam energies resulting in an average lattice constant of a = (3.35 ± 0.03) Å. Similarly, we used eight scans in $\overline{\Gamma M}$ direction for the lattice calculation at T_S = 296 K. From the position of the first order diffraction peaks with respect to the specular peak we thus obtain a surface lattice constant of a = (3.37 ± 0.03) Å at room temperature, which is an increase of roughly 0.6%.

Both values are in good agreement with other experimental studies (scanning tunneling microscopy, LEED, X-ray powder diffraction, surface-enhanced Raman spectroscopy (SERS), and theoretical studies using density functional theory) of the 1T-TaS_2 in-plane lattice parameter (Wilson et al., 1975; Givens and Fredericks, 1977; Sanders et al., 2016; Kratochvilova et al., 2017; Bao et al., 2022).

With these values we can further calculate the in-plane (linear) thermal expansion coefficient (TEC) defined as $\alpha_\parallel = 1/a_0 \cdot \Delta a/\Delta T$, where a_0 is the lattice parameter at T_S = 113 K, Δa the difference between the lattice constant values at different temperatures and ΔT the temperature difference. We obtain a value of

$$\alpha_\parallel = (33 \pm 12) \cdot 10^{-6}\,\mathrm{K}^{-1}.$$

Our value is larger compared to the value that Givens and Fredericks obtained in their X-ray diffraction (XRD) study. As we have only considered two different surface temperatures our result should be treated carefully even though it seems unlikely to be caused by such a large uncertainty and might well be a consequence of the different probing techniques. Table 1 provides a short overview of the thermal expansion coefficients of other transition metal dichalcogenides, which experimental technique had been used, and for which temperature range. Previous studies of TMdCs reported values for the TEC in the range of 5–25 · $10^{-6}\,\mathrm{K}^{-1}$, thus, comparable but slightly smaller than our value (Anemone et al., 2022), which may point toward a particularly weak vdW coupling between the layers.

3.4 Atom-surface interaction and surface electronic corrugation of 1T-TaS_2

As every polarisable object in nature is subjected to the vdW force a fundamental understanding of the force is crucial for any quantitative description and theoretical treatment of molecular adsorption or surface reaction processes and is also of paramount importance for a better design and control of nanoscale devices. Beyond the applications of weak interactions in devices and materials, there are several experimental techniques analyzing nano-structured materials or explicitly using effects occurring from these weak interactions including atomic force microscopy and matter-wave scattering experiments which are probing dispersion forces (Fiedler et al., 2023).

However, in the case of topological nontrivial materials, HAS is the only experimental technique used to date to provide experimental information about the vdW interaction with a topological insulator (Tamtögl et al., 2021b). The latter stresses the need for experimental measurements even more so as, e.g., it is expected that peculiar effects such as the topological magnetoelectric effect (Dziom et al., 2017) cause an unconventional contribution to the vdW potential (Martín-Ruiz and Urrutia, 2018). Before we illustrate the experimental determination of the atom-surface vdW potential of 1T-TaS_2 we will first describe HAS measurements of the step-height distribution in the following.

The surfaces of layered materials such as 1T-TaS_2 are not perfectly flat, rather they are characterized by steps and parallel terraces, e.g., due to defects and the sample preparation process. The step heights and distributions of such periodically modulated surfaces can be calculated and resolved from interference effects in HAS (Farías and Rieder, 1998; Mayrhofer-Reinhartshuber et al., 2013a). As a result of the combination of the He beam being scattered from different terraces, constructive and destructive interference occurs. In a so-called drift measurement, the specular intensity is monitored while the kinetic energy of the incident He beam is changed. In the experiment this can be achieved by changing the nozzle temperature. By modulating the kinetic energy, the phase shift $\Delta\phi$ for the He beam emerging from different terraces is varied. For the specific case of $\vartheta_i = \vartheta_f$ (specular peak) the phase difference of two adjacent terrace levels is given by (Mayrhofer-Reinhartshuber et al., 2013a)

$$\varphi(k_i) = 2hk_i \cos\vartheta_i = h\,\Delta k_z, \tag{5}$$

TABLE 1 Overview of the in-plane thermal expansion coefficients (TEC) of several TMdCs, how they were obtained and for which temperature range. In the case of a negligible TEC the upper limit is noted.

Material	Method	$\alpha_\parallel$ ($10^{-6}\,\mathrm{K}^{-1}$)	T_S range (K)
MoS_2 (Anemone et al., 2018; Anemone et al., 2022)	HAS	≤ 14.0	90–522
$MoSe_2$ (El-Mahalawy and Evans, 1976)	XRD	7.2	293–1073
$PdTe_2$ (Anemone et al., 2022)	HAS	≤ 24.8	90–290
$PtTe_2$ (Anemone et al., 2020)	HAS	≤ 5.6	90–550
TaS_2 (Givens and Fredericks, 1977)	XRD	12.7	138–482
TaS_2 (This work)	HAS	32.9	113–296
WS_2 (Zhang et al., 2016)	SERS	10.3	110–300
WSe_2 (Brixner, 1963; El-Mahalawy and Evans, 1976)	XRD	6.8–11.1	25–600

where h is step height and Δk_z is the change of the wave vector component perpendicular to the surface. For constructive interference, the condition of in-phase scattering $\Delta\phi = 2\pi n$ with an integer value of n must be fulfilled, whereas a half-integer value n leads to destructive interference due to anti-phase scattering. As a result, maxima and minima can be observed in the drift spectrum Figure 4A, where the normalized specular intensity is plotted against the incident wave vector k_i. The measured specular intensity as a function of incident wave vector k_i upon varying the nozzle temperature is plotted for the sample aligned along $\overline{\Gamma M}$ and the crystal being held at room temperature.

As the incident wave vector k_i is varied by changing the nozzle temperature T_N, the He beam intensity scales via $I \propto 1/\sqrt{T_N}$ and the signal has to be corrected for this factor which has been done in Figure 4A. In addition, the intensity decreases also with increasing k_i according to the Debye-Waller attenuation (Ruckhofer et al., 2019). Such a drift spectrum can now be used to determine the step height of the current 1T-TaS_2 sample.

Following a simple theoretical model to describe the periodic intensity modulation which assumes a coherent overlap of plane waves, emerging from different terrace levels, the specular intensity can be calculated with (Tölkes et al., 1997; Mayrhofer-Reinhartshuber et al., 2013a)

$$I(k_i) = I_0\, e^{-2W} \left| \sum_{j=0}^{\infty} a_j e^{-ij\varphi(k_i)} \right|^2. \tag{6}$$

In Equation 6, I_0 is the intensity for a flat surface without steps, $\varphi(k_i)$ the phase shift (see Eq. 5) and a_j the visible fraction of the terrace level j. Eq. 6 has been fitted to the measured drift spectrum in the wave vector range 4.54 Å^{-1} < k_i < 5.41 Å^{-1} and the best fit result is shown in Figure 4 as a blue line with the inset indicating the distribution of the visible terrace fractions. We obtain a surface step height of $h = (6.1 \pm 0.1)$ Å, which is in excellent agreement with the distance between two adjacent TaS_2 layers (Bovet et al., 2003; Li et al., 2019; Kahraman et al., 2020).

As mentioned above, HAS provides direct experimental information about the vdW interaction between an atom and the surface and thus invaluable details about London dispersion forces of vdW layered materials. As a first step to determine the three-dimensional corrugated atom-surface interaction potential of 1T-TaS_2, we follow a further analysis of the drift spectrum. The simple model for interference effects from steps (see Eq. 6) neglects the occurrence of selective adsorption resonances (SARs). These phenomena occur when an incoming helium atom is bound temporarily on the surface due to the attraction of the He-surface interaction potential. A SAR follows from the kinetic condition that the energy of the incident energy E_i equals the kinetic energy of the atom on the surface plus the binding energy ϵ_n of the potential:

$$E_i = \frac{\hbar^2 k_i^2}{2m} = \frac{\hbar^2}{2m}(\mathbf{K}_i + \mathbf{G})^2 + \epsilon_n(\mathbf{K}_i, \mathbf{G}). \tag{7}$$

Such adsorption processes give rise to peaks and dips in the drift spectrum (Tamtögl et al., 2021b). Therefore, these peaks and dips can be used to obtain the bound state energies of the potential. As a first step we concentrate on the laterally averaged atom-surface potential. Each peak/dip at a specific incident wave vector k_i can be associated with a certain bound state energy ϵ_n and reciprocal lattice vector G pair which fulfills the condition given in Eq. (7). In the so-called free atom approximation, ϵ_n ($\mathbf{K}_i$, $\mathbf{G}$) is independent of $\mathbf{K}_i$ and $\mathbf{G}$ (Ruckhofer et al., 2019; Tamtögl et al., 2021b) and thus Figure 4B provides a direct measure of the bound state energies ϵ_n of the laterally averaged potential.

As a next step, we will then model the three-dimensional He-surface interaction potential, whereupon we use the corrugated Morse potential (CMP) due to its algebraic simplicity (Tamtögl et al., 2021b). It consists of two exponentials considering the repulsive and the attractive part of the potential as a function of the lateral position $\mathbf{R}$ on the surface and the distance z from the surface in the following form:

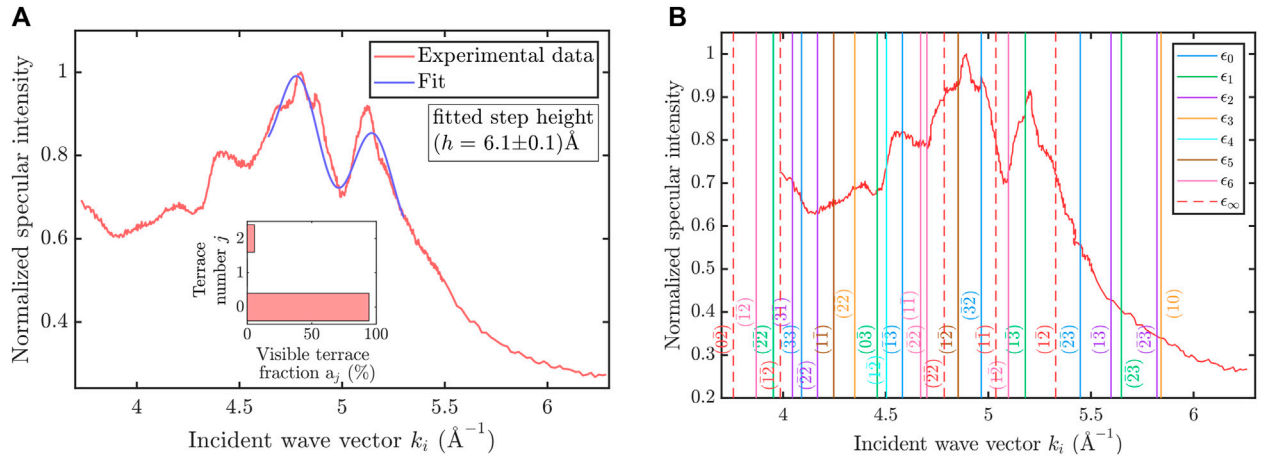

FIGURE 4
(A) Periodic oscillations in the measured specular intensity *versus* incident wave vector k_i provide a measure for the step height distribution of the 1T-TaS_2(0001) sample. Following an analysis upon fitting Eq. 6 (blue curve) to the experimental data points (red) we obtain a step height h = (6.1±0.1) Å for the measurement performed along the $\overline{\Gamma M}$ azimuth while the crystal was kept at a temperature of 296 K **(B)** The position of selective adsorption resonances following an analysis of the same drift spectrum as in **(A)** allows to determinate the laterally averaged atom-surface interaction potential. The vertical colored lines correspond to the different bound-state energies ϵ_n with the dashed red lines illustrating the threshold energy and the corresponding G-vector as a label.

$$V(\mathbf{R},z) = D\left[\frac{1}{\gamma_0}e^{-2\kappa[z-\xi(\mathbf{R})]} - 2e^{-\kappa z}\right]. \quad (8)$$

Here, κ is the stiffness and D the well depth of the potential, $\xi(\mathbf{R})$ the corrugation function, which reflects the periodicity of the crystal surface, and γ_0 is the surface average over $e^{2\kappa\xi(\mathbf{R})}$. The laterally averaged surface potential (i.e., without corrugation in the exponential) of Eq. 8 can be described analytically and the bound state energies are given by

$$\epsilon_n = -D + \hbar\omega\left(n+\frac{1}{2}\right)\left(1-\frac{n+\frac{1}{2}}{2\gamma}\right) \quad (9)$$

with n being a positive integer, $\omega = \kappa\sqrt{2D/m}$ the Debye-frequency and $\gamma = 2D/\hbar\omega$. By fitting Eq. 9 to the ϵ_n-values obtained from the SAR analysis of the drift spectrum we can thus obtain the laterally averaged potential with the well depth and stiffness:

$$D = (8.40 \pm 0.15)\,\text{meV} \quad \text{and} \quad \kappa = (0.45 \pm 0.02)\,\text{Å}^{-1}.$$

The resulting bound state energies and their uncertainties are displayed in Table 2 while in Figure 5A a plot of the laterally averaged potential is shown. The positions of the corresponding SARs in the drift spectrum are displayed as vertical lines in Figure 4B, where each color belongs to one specific bound state energy ϵ_n and the red dashed lines illustrate the threshold energies. The labels next to the lines denote the corresponding reciprocal lattice vector G. For completeness, it should be mentioned that two more analytical bound state energies ϵ_7 and ϵ_8 exist, but they are quite close to zero, that is, to the threshold condition and therefore not displayed in Figure 4B and Table 2. In Figure 5A, the horizontal colored lines represent the first seven analytically calculated bound state energies. We note that SAR measurements are typically obtained with a cooled sample since with increasing temperature inelastic channels give rise to a broadening of the linewidth and may also cause changes from maxima to minima and *vice versa* (Tamtögl et al., 2018; Tamtögl et al., 2021b). Here we use measurements taken at room temperature as the position of the resonances becomes clearer at that temperature. It may be a consequence of the different phases of the cooled sample and the increased likelihood of rest gas adsorption for the latter.

Our value of D is slightly smaller than the value $D = 8.7$ meV from Brusdeylins *et al.* whose value is based on intensity calculations (Brusdeylins et al., 1989) following the hard corrugated wall model together with the Beeby correction and thus does not directly consider scattering from a soft potential resulting in less accuracy compared to the elastic close-coupling method used in the previous works (Sanz and Miret-Artés, 2007; Mayrhofer-Reinhartshuber et al., 2013b). In general compared to other semiconductors, metals, and semimetals, 1T-TaS_2 exhibits one of the "deepest" atom-surface interaction potentials, only surpassed by the graphene/graphite potential (Benedek and Toennies, 2018). At the same time, the stiffness κ is quite close to the value found for the topological insulator Bi_2Se_3 (Ruckhofer et al., 2019; Tamtögl et al., 2021b). With the outermost layer for Bi_2Se_3 being Se, located in the same column of the periodic table just below sulphur, it seems reasonable that the He–TaS_2 potential exhibits a similar stiffness and supports a similar number of bound states.

TABLE 2 Experimentally determined bound state energies ϵ_n for 1T-TaS_2 and corresponding uncertainties upon fitting a laterally averaged Morse potential (Eq. 9) with $D = 8.40$ meV and $\kappa = 0.45$ Å^{-1}.

Bound state	ϵ_n (meV)	$\Delta\epsilon_n$ meV
ϵ_0	7.55	0.15
ϵ_1	5.86	0.13
ϵ_2	4.38	0.11
ϵ_3	3.11	0.08
ϵ_4	2.06	0.06
ϵ_5	1.23	0.03
ϵ_6	0.61	0.01

Following the results of the laterally averaged atom-surface interaction potential we continue with the determination of the three-dimensional atom-surface interaction potential and the corresponding surface electronic corrugation (Tamtögl et al., 2021b; Allison et al., 2022). Following the CMP (Eq. 8), the corrugation $\xi(\mathbf{R})$ for a hexagonal surface such as 1T-TaS_2, can be described by a two-parameter Fourier ansatz,

$$\xi(\mathbf{R}) = \xi(x,y) = \xi_0\left[\begin{array}{c}\cos\left[\frac{2\pi}{a}\left(x-\frac{y}{\sqrt{3}}\right)\right] + \cos\left(\left[\frac{2\pi}{a}\left(x+\frac{y}{\sqrt{3}}\right)\right]\right) \\ +\cos\left(\frac{2\pi}{a}\frac{2y}{\sqrt{3}}\right)\end{array}\right] + h.o., \quad (10)$$

where x and y depict the coordinates in the surface plane and ξ_0 determines the corrugation amplitude. The ansatz above is based on the sixfold symmetry of the topmost surface layer. As the He beam provides an average of the long-range order, we omit the star of David clusters in this description. The corrugation is then typically expressed in terms of the peak-to-peak value $\xi_{pp} = \max(\xi) - \min(\xi)$. With the CMP (Eq. 8) we are able to calculate the diffraction intensities and compare those with the experimentally measured ones to obtain a value for the peak-to-peak corrugation ξ_{pp}.

A theoretical framework to describe the elastic scattering of He atoms from surfaces is the close-coupling (CC) formalism, which is more exact than the hard-wall approximation, but still computationally manageable (Sanz and Miret-Artés, 2007; Allison et al., 2022). The starting point here is the time-independent Schrödinger equation together with the CMP, which contains the Fourier series expansion (Eq. 10) in the exponentials, yielding a set of coupled differential equations for the diffracted waves. These equations are solved for using the CC algorithm, taking into account all open channels and 110 closed channels. The z – boundaries of the integration were set to [−6, 18]. A detailed theoretical treatment and the corresponding equations can be found in several references (Miret-Artés, 1995; Sanz and Miret-Artés, 2007; Mayrhofer-Reinhartshuber et al., 2013b; Kraus et al., 2015), while an implementation of the CC algorithm is available from https://repository.tugraz.at/records/cd0y0-xa478 under the GNU General Public License v3.0.

By comparing the elastic diffraction intensities calculated with the close-coupling algorithm we are able to determine the corrugation of the sample surface (Ruckhofer et al., 2019; Schmutzler et al., 2022). For the measured diffraction intensities we

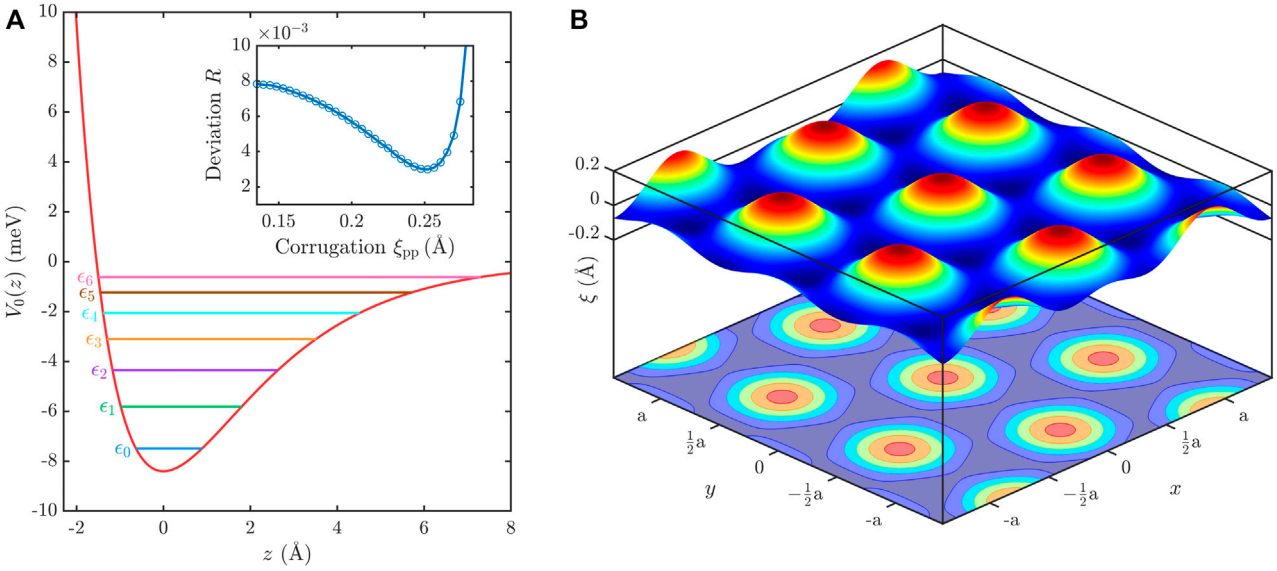

FIGURE 5
(A) Laterally averaged Morse potential for He-TaS_2 with D = 8.40 meV and κ =0.45 Å^{-1} with the first 7 bound state energies ϵ_n. The inset shows the deviation R (Eq. 11) between CC-calculations and the experimental intensities upon varying the corrugation ξ_{pp} with a clear minimum at ξ_{pp} = 0.25 Å. **(B)** Shows a combined three-dimensional and contour plot of the obtained surface electronic corrugation $\xi(x, y)$ as part of the three-dimensional corrugated Morse potential.

used the peak areas instead of the peak height to account for broadening due to the energy spread of the He atoms, angular resolution of the apparatus, and size effects of the crystal surface (Ruckhofer et al., 2019). For the CC calculations, the intensities have been corrected by the Debye-Waller factor, and the values for D and κ from above were kept constant, while the corrugation amplitude ξ_0 (see Eq. 10) was varied between 0.05 and 0.90 Å^{-1}. The best corrugation value ξ_0 is the one that minimises the deviation R between simulated and experimentally obtained diffraction intensities I_G^{sim} and I_G^{exp} given by

$$R = \frac{1}{N}\sqrt{\sum_G \left(I_G^{exp} - I_G^{sim}\right)^2}, \tag{11}$$

with N the number of experimentally measured diffraction scans. As for the calculation of the lattice constants we used in total 22 scans at various incident energies for the optimization process of Eq. 11 to find a global minimum of R as a function of ξ_0. It results in a surface electronic peak-to-peak corrugation (see inset of Figure 5A) of

$$\xi_{pp} = 0.25\ \text{Å},$$

which corresponds to 7.5% of the surface lattice constant a. Figure 5B shows a plot of the best-fit surface electronic corrugation according to Equation 10.

So far, there barely exist any other HAS studies of other TMdCs that determine the electronic corrugation. Anemone et al. studied the 1T-$PtTe_2$ surface and provided a rough estimation of the maximum corrugation amplitude with 0.33 Å (Anemone et al., 2020). It should be mentioned that their estimation is based on the HCW model, which makes a direct comparison difficult. Similarly, various low-index metal surfaces have been studied in atomic beam scattering experiments and revealed a significantly smaller corrugation (Benedek and Toennies, 2018). On the other hand, in comparison to the binary topological insulators and single-element semimetals, which have been studied recently with HAS (Tamtögl et al., 2021b) and analyzed in a similar manner, TaS_2 exhibits a similar surface electronic corrugation.

4 Summary and conclusion

The increasing interest in vdW 2D materials makes 1T-TaS_2 probably one of the best-studied TMdCs and, in fact, 1T-TaS_2 has already been investigated by HAS over 40 years ago. However, these studies were concentrated on a few limited aspects of the system, and theoretical descriptions at that time relied on simplistic models. In contrast, we have reported a detailed helium atom scattering study of the archetypal charge-density wave system and transition metal dichalcogenide 1T-TaS_2. The electron-phonon coupling has been compared with measurements of the 3D topological insulator $TlBiTe_2$. The electron-phonon coupling λ in the C-CDW phase of 1T-TaS_2 has been determined with λ = 0.59 ± 0.12 for 1T-TaS_2 and is thus much larger than the value for $TlBiTe_2$ (λ = 0.09 ± 0.01) which is similar to other semimetal and topological insulator surfaces. In fact, since λ of $TlBiTe_2$ is so close to λ found for Bi_2Te_2Se we conclude that the existence of the Dirac cone alone, as found for both TIs, does not give rise to a significant e-ph coupling.

The large λ of 1T-TaS_2 on the other hand, may be a consequence both of the CDW phase as well as the weak bonding between the individual dichalcogenide layers. The much stronger inter-layer bonding of $TlBiTe_2$ on the other hand, is reflected in the difficulty to cleave the crystals resulting in a very rough surface with a domain size of about 20 nm and overall comparably small scattering intensities. It would also be interesting to establish whether other TMdCs with a vdW layered structure such as 1T-TaS_2 but different bonding between the dichalcogenide layers exhibit a different λ in accordance to the

dependence of λ on the substrate bonding for metal-supported graphene where λ varies between 0.06 and 0.22 (Benedek et al., 2021).

By means of elastic scattering, the structural properties of 1T-TaS_2 have been studied and a linear in-plane thermal expansion coefficient with $\alpha_{\parallel} = (33 \pm 12) \cdot 10^{-6}\ K^{-1}$ has been determined, which is larger than the value from X-ray diffraction and comparable to other TMdCs (Givens and Fredericks, 1977; Anemone et al., 2022). Interference and resonance effects which can be observed upon varying the He beam energy provide further information allowing us to determine the step-height between parallel terraces with $h = (6.1 \pm 0.1)$ Å in accordance with the spacing between the dichalcogenide layers. Based on the mentioned interference effects we are able to determine the three-dimensional atom-surface interaction potential of 1T-TaS_2. Using a corrugated Morse potential, the laterally averaged potential is best described by a well depth $D = (8.40 \pm 0.15)$ meV and a stiffness $\kappa = (0.45 \pm 0.02)$ $Å^{-1}$. Hence 1T-TaS_2 exhibits one of the "deepest" atom-surface interaction potentials compared to other semiconductors/(semi) metals, only surpassed by graphene/graphite which may again be an indication of the "pure" vdW nature of the interlayer bonding. The full three-dimensional potential follows then from a comparison of the diffraction intensities with quantum-mechanical scattering calculations. The optimal agreement is achieved for a surface electronic corrugation with a peak-to-peak value of $\xi_{pp} = 0.25$ Å. While the value is larger than for low-index metal surfaces it is comparable to other semiconductor/semimetal surfaces.

Data availability statement

The raw data supporting the conclusions of this article will be made available by the authors, without undue reservation.

Author contributions

AT provided the experimental concept and MB synthesized the samples and performed additional sample characterization. PM and AR were responsible for the experimental setup and performed the measurements. Data analysis, visualization, and discussion were done by PM, NH, and AT. The manuscript was written by PM and AT. All authors contributed to the article and approved the submitted version.

Funding

This research was funded in whole, or in part, by the Austrian Science Fund (FWF) [P34704] and NAWI Graz. For the purpose of open access, the author has applied a CC BY public copyright license to any Author Accepted Manuscript version arising from this submission. MB acknowledges financial support from the Independent Research Fund Denmark's Sapere Aude program (Grant No. 7027-00077A).

Acknowledgments

We would like to thank G. Benedek, W. E. Ernst, and M. Pusterhofer for their helpful discussions. We would like to thank S. Chandra and C. Felser for providing us with a $TlBiTe_2$ sample.

Conflict of interest

The authors declare that the research was conducted in the absence of any commercial or financial relationships that could be construed as a potential conflict of interest.

Publisher's note

References

Al-Makeen, M. M., Guo, X., Wang, Y., Yang, D., You, S., Yassine, M., et al. (2022). Investigation of the electron–phonon coupling in Dirac semimetal $PdTe_2$ via temperature-dependent Raman spectroscopy. *Phys. Status Solidi RRL* 16, 2200257. doi:10.1002/pssr.202200257

Allison, W., Miret-Artés, S., and Pollak, E. (2022). Perturbation theory of scattering for grazing-incidence fast-atom diffraction. *Phys. Chem. Chem. Phys.* 24, 15851–15859. doi:10.1039/D2CP01013E

Anemone, G., Al Taleb, A., Castellanos-Gomez, A., and Farías, D. (2018). Experimental determination of thermal expansion of natural MoS_2. *2D Mater* 5, 035015. doi:10.1088/2053-1583/aabe4a

Anemone, G., Garnica, M., Zappia, M., Aguilar, P. C., Al Taleb, A., Kuo, C.-N., et al. (2020). Experimental determination of surface thermal expansion and electron–phonon coupling constant of 1T-$PtTe_2$. *2D Mater* 7, 025007. doi:10.1088/2053-1583/ab6268

Anemone, G., Taleb, A. A., Politano, A., Kuo, C.-N., Lue, C. S., Miranda, R., et al. (2022). Setting the limit for the lateral thermal expansion of layered crystals via helium atom scattering. *Phys. Chem. Chem. Phys.* 24, 13229–13233. doi:10.1039/d2cp00758d

Bao, J., Yang, L., and Wang, D. (2022). Influence of torsional deformation on the electronic structure and optical properties of 1T-TaS_2 monolayer. *J. Mol. Struct.* 1258, 132667. doi:10.1016/j.molstruc.2022.132667

Benedek, G., Manson, J. R., and Miret-Artés, S. (2020a). The electron-phonon interaction of low-dimensional and multi-dimensional materials from he atom scattering. *Adv. Mat.* 32, 2002072. doi:10.1002/adma.202002072

Benedek, G., Manson, J. R., and Miret-Artés, S. (2021). The electron-phonon coupling constant for single-layer graphene on metal substrates determined from He atom scattering. *Phys. Chem. Chem. Phys.* 23, 7575–7585. doi:10.1039/D0CP04729E

Benedek, G., Manson, J. R., Miret-Artés, S., Ruckhofer, A., Ernst, W. E., Tamtögl, A., et al. (2020b). Measuring the electron–phonon interaction in two-dimensional superconductors with He-atom scattering. *Condens. Matter* 5, 79. doi:10.3390/condmat5040079

Benedek, G., Miret-Artés, S., Manson, J. R., Ruckhofer, A., Ernst, W. E., and Tamtögl, A. (2020c). Origin of the electron-phonon interaction of topological semimetal surfaces measured with helium atom scattering. *J. Phys. Chem. Lett.* 11, 1927–1933. doi:10.1021/acs.jpclett.9b03829

Benedek, G., Miret-Artés, S. S., Toennies, J. P., and Manson, J. R. (2018). Electron–phonon coupling constant of metallic overlayers from specular He atom scattering. *J. Phys. Chem. Lett.* 9, 76–83. doi:10.1021/acs.jpclett.7b03047

Benedek, G., and Toennies, J. P. (2018). *Atomic scale dynamics at surfaces*. Berlin, Heidelberg: Springer Berlin Heidelberg. doi:10.1007/978-3-662-56443-1

Bovet, M., van Smaalen, S., Berger, H., Gaal, R., Forró, L., Schlapbach, L., et al. (2003). Interplane coupling in the quasi-two-dimensional 1T–TaS_2. *Phys. Rev. B* 67, 125105. doi:10.1103/PhysRevB.67.125105

Brixner, L. H. (1963). X-Ray study and thermoelectric properties of the $W_xT1_{1-x}Se_2$ system. *J. Electrochem. Soc.* 110, 289. doi:10.1149/1.2425734

Brusdeylins, G., Heimlich, C., and Toennies, J. (1989). Helium scattering from the layered compound single crystal surface of 1T-TaS_2 in the temperature region of charge density wave reconstruction. *Surf. Sci.* 211-212, 98–105. doi:10.1016/0039-6028(89)90758-9

Cantini, P., Boato, G., and Colella, R. (1980). Surface charge density waves observed by atomic beam diffraction. *Phys. B+C* 99, 59–63. doi:10.1016/0378-4363(80)90211-9

Chen, Y. L., Liu, Z. K., Analytis, J. G., Chu, J. H., Zhang, H. J., Yan, B. H., et al. (2010). Single Dirac cone topological surface state and unusual thermoelectric property of compounds from a new topological insulator family. *Phys. Rev. Lett.* 105, 266401. doi:10.1103/PhysRevLett.105.266401

Choe, J., Lujan, D., Rodriguez-Vega, M., Ye, Z., Leonardo, A., Quan, J., et al. (2021). Electron-phonon and spin-lattice coupling in atomically thin layers of $MnBi_2Te_4$. *Nano Lett.* 21, 6139–6145. doi:10.1021/acs.nanolett.1c01719

Clerc, F., Battaglia, C., Bovet, M., Despont, L., Monney, C., Cercellier, H., et al. (2006). Lattice-distortion-enhanced electron-phonon coupling and Fermi surface nesting in 1T-TaS_2. *Phys. Rev. B* 74, 155114. doi:10.1103/PhysRevB.74.155114

Coleman, R. V., McNairy, W. W., and Slough, C. G. (1992). Amplitude modulation of charge-density-wave domains in 1T-TaS_2 at 300 K. *Phys. Rev. B* 45, 1428–1431. doi:10.1103/PhysRevB.45.1428

Duong, D. L., Yun, S. J., and Lee, Y. H. (2017). van der Waals layered materials: opportunities and challenges. *ACS Nano* 11, 11803–11830. doi:10.1021/acsnano.7b07436

Dziom, V., Shuvaev, A., Pimenov, A., Astakhov, G. V., Ames, C., Bendias, K., et al. (2017). Observation of the universal magnetoelectric effect in a 3D topological insulator. *Nat. Commun.* 8, 15197. doi:10.1038/ncomms15197

El-Mahalawy, S. H., and Evans, B. L. (1976). The thermal expansion of 2H -MoS_2, 2H-$MoSe_2$ and 2H -WSe_2 between 20 and 800°C. *J. Appl. Crystallogr.* 9, 403–406. doi:10.1107/S0021889876011709

Eremeev, S. V., Bihlmayer, G., Vergniory, M., Koroteev, Y. M., Menshchikova, T. V., Henk, J., et al. (2011). *Ab initio* electronic structure of thallium-based topological insulators. *Phys. Rev. B* 83, 205129. doi:10.1103/PhysRevB.83.205129

Eremeev, S. V., Koroteev, Y. M., and Chulkov, E. V. (2010). Ternary thallium-based semimetal chalcogenides tl-v-vi2 as a new class of three-dimensional topological insulators. *JETP Lett.* 91, 594–598. doi:10.1134/S0021364010110111

Farías, D., and Rieder, K.-H. (1998). Atomic beam diffraction from solid surfaces. *Rep. Prog. Phys.* 61, 1575–1664. doi:10.1088/0034-4885/61/12/001

Fiedler, J., Berland, K., Borchert, J. W., Corkery, R. W., Eisfeld, A., Gelbwaser-Klimovsky, D., et al. (2023). Perspectives on weak interactions in complex materials at different length scales. *Phys. Chem. Chem. Phys.* 25, 2671–2705. doi:10.1039/D2CP03349F

Givens, F. L., and Fredericks, G. E. (1977). Thermal expansion op $NbSe_2$ and TaS_2. *J. Phys. Chem. Solids* 38, 1363–1365. doi:10.1016/0022-3697(77)90008-7

Grimvall, G. (1981). *The electron-phonon interaction in metals*. Amsterdam: North-Holland Pub. Co.

Han, S., Tang, Q., Yuan, H., Luo, Y., and Liu, H. (2023). Effects of electron-phonon coupling on the phonon transport properties of the Weyl semimetals NbAs and TaAs: a comparative study. *J. Materiomics* 9, 520–526. doi:10.1016/j.jmat.2022.12.001

Hein, R. A., and Swiggard, E. M. (1970). Superconductivity in $TlBiTe_2$: a low carrier density (III-V)VI_2 compound. *Phys. Rev. Lett.* 24, 53–55. doi:10.1103/PhysRevLett.24.53

Johannes, M. D., and Mazin, I. I. (2008). Fermi surface nesting and the origin of charge density waves in metals. *Phys. Rev. B* 77, 165135. doi:10.1103/PhysRevB.77.165135

Kahraman, Z., Yagmurcukardes, M., and Sahin, H. (2020). Functionalization of single-layer TaS_2 and formation of ultrathin Janus structures. *J. Mater. Res.* 35, 1397–1406. doi:10.1557/jmr.2020.64

Klanjšek, M., Zorko, A., Žitko, R., Mravlje, J., Jagličić, Z., Biswas, P. K., et al. (2017). A high-temperature quantum spin liquid with polaron spins. *Nat. Phys.* 13, 1130–1134. doi:10.1038/nphys4212

Kratochvilova, M., Hillier, A. D., Wildes, A. R., Wang, L., Cheong, S.-W., and Park, J.-G. (2017). The low-temperature highly correlated quantum phase in the charge-density-wave 1T-TaS_2 compound. *npj Quantum Mater* 2, 42. doi:10.1038/s41535-017-0048-1

Kraus, P., Tamtögl, A., Mayrhofer-Reinhartshuber, F., Apolloner, M., Gösweiner, C., Miret-Artés, S., et al. (2015). Surface structure of Bi(111) from helium atom scattering measurements. Inelastic close-coupling formalism. *J. Phys. Chem. C* 119, 17235–17242. doi:10.1021/acs.jpcc.5b05010

Kumar, A., Kumar, S., Miyai, Y., and Shimada, K. (2022). Temperature-dependent band modification and energy dependence of the electron-phonon interaction in the topological surface state on Bi_2Te_3. *Phys. Rev. B* 106, L121104. doi:10.1103/PhysRevB.106.L121104

Kuroda, K., Ye, M., Kimura, A., Eremeev, S. V., Krasovskii, E. E., Chulkov, E. V., et al. (2010). Experimental realization of a three-dimensional topological insulator phase in ternary chalcogenide tlbise$_2$. *Phys. Rev. Lett.* 105, 146801. doi:10.1103/PhysRevLett.105.146801

Kuroda, K., Ye, M., Schwier, E. F., Nurmamat, M., Shirai, K., Nakatake, M., et al. (2013). Experimental verification of the surface termination in the topological insulator $TlBiSe_2$ using core-level photoelectron spectroscopy and scanning tunneling microscopy. *Phys. Rev. B* 88, 245308. doi:10.1103/PhysRevB.88.245308

Kurosaki, K., Kosuga, A., and Yamanaka, S. (2003). Thermoelectric properties of $TlBiTe_2$. *J. Alloys Compd.* 351, 279–282. doi:10.1016/S0925-8388(02)01038-1

Lai, J.-M., Xie, Y.-R., and Zhang, J. (2021). Detection of electron-phonon coupling in two-dimensional materials by light scattering. *Nano Res.* 14, 1711–1733. doi:10.1007/s12274-020-2943-1

Law, K. T., and Lee, P. A. (2017). 1T-TaS_2 as a quantum spin liquid. *Proc. Natl. Acad. Sci.* 114, 6996–7000. doi:10.1073/pnas.1706769114

Li, Y., Xia, Y., Ekahana, S. A., Kumar, N., Jiang, J., Yang, L., et al. (2017). Topological origin of the type-ii Dirac fermions in $PtSe_2$. *Phys. Rev. Mat.* 1, 074202. doi:10.1103/PhysRevMaterials.1.074202

Li, Y., Xiao, H., Zhou, P., and Cao, J. (2019). Electronic structures of twist-stacked 1T-TaS_2 bilayers. *Phys. Lett. A* 383, 2302–2308. doi:10.1016/j.physleta.2019.04.043

Lin, H., Markiewicz, R. S., Wray, L. A., Fu, L., Hasan, M. Z., and Bansil, A. (2010). Single-Dirac-Cone topological surface states in the $TlBiSe_2$ class of topological semiconductors. *Phys. Rev. Lett.* 105, 036404. doi:10.1103/PhysRevLett.105.036404

Liu, Y., Weiss, N. O., Duan, X., Cheng, H.-C., Huang, Y., and Duan, X. (2016). Van der Waals heterostructures and devices. *Nat. Rev. Mater* 1, 16042. doi:10.1038/natrevmats.2016.42

Lubell, M., and Mazelsky, R. (1965). Thermoelectric properties of the system gete-tlbite$_2$. *Solid-State Electron* 8, 729–733. doi:10.1016/0038-1101(65)90060-2

Manson, J., Benedek, G., and Miret-Artés, S. (2022). Atom scattering as a probe of the surface electron-phonon interaction at conducting surfaces. *Surf. Sci. Rep.* 77, 100552. doi:10.1016/j.surfrep.2022.100552

Martín-Ruiz, A., and Urrutia, L. F. (2018). Interaction of a hydrogenlike ion with a planar topological insulator. *Phys. Rev. A* 97, 022502. doi:10.1103/PhysRevA.97.022502

Mayrhofer-Reinhartshuber, M., Tamtögl, A., Kraus, P., and Ernst, W. E. (2013a). Helium atom scattering investigation of the Sb(111) surface. *J. Phys.: Condens. Matter* 25, 395002. doi:10.1088/0953-8984/25/39/395002

Mayrhofer-Reinhartshuber, M., Kraus, P., Tamtögl, A., Miret-Artés, S., and Ernst, W. E. (2013b). Helium-surface interaction potential of Sb(111) from scattering experiments and close-coupling calculations. *Phys. Rev.* 88, 205425. doi:10.1103/PhysRevB.88.205425

Miret-Artés, S. (1995). Resonant inelastic scattering of atoms from surfaces. *Surf. Sci.* 339, 205–220. doi:10.1016/0039-6028(95)00632-x

National Institute of Standards and Technology (2018). *Innovation unleashed*. Maryland, United States: National Institute of Standards and Technology.

Ngankeu, A. S., Mahatha, S. K., Guilloy, K., Bianchi, M., Sanders, C. E., Hanff, K., et al. (2017). Quasi-one-dimensional metallic band dispersion in the commensurate charge density wave of 1T-TaS_2. *Phys. Rev. B* 96, 195147. doi:10.1103/PhysRevB.96.195147

Osterhoudt, G. B., Wang, Y., Garcia, C. A. C., Plisson, V. M., Gooth, J., Felser, C., et al. (2021). Evidence for dominant phonon-electron scattering in weyl semimetal WP_2. *Phys. Rev. X* 11, 011017. doi:10.1103/PhysRevX.11.011017

Paraskevopoulos, K. M. (1985). Electron effective mass dependence on carrier concentration in $TlBiTe_2$ monocrystals. *Phys. Status Solidi B* 127, K45–K50. doi:10.1002/pssb.2221270156

Pei, C., Huang, P., Zhu, P., Liu, L., Wang, Q., Zhao, Y., et al. (2022). Pressure-induced superconductivity extending across the topological phase transition in thallium-based topological materials. *Cell Rep. Phys. Sci.* 3, 101094. doi:10.1016/j.xcrp.2022.101094

Pielmeier, F., Landolt, G., Slomski, B., Muff, S., Berwanger, J., Eich, A., et al. (2015). Response of the topological surface state to surface disorder in tlbise 2. *New J. Phys.* 17, 023067. doi:10.1088/1367-2630/17/2/023067

Popovich, N., Shura, V., Diakonov, V., Fita, I., and Levchenko, G. (1984). On the superconductivity in $TlBiTe_2$. *Solid State Commun.* 50, 979–981. doi:10.1016/0038-1098(84)90269-2

Rossnagel, K. (2011). On the origin of charge-density waves in select layered transition-metal dichalcogenides. *J. Phys. Condens. Matter* 23, 213001. doi:10.1088/0953-8984/23/21/213001

Ruckhofer, A., Campi, D., Bremholm, M., Hofmann, P., Benedek, G., Bernasconi, M., et al. (2020). Terahertz surface modes and electron-phonon coupling on Bi_2Se_3(111). *Phys. Rev. Res.* 2, 023186. doi:10.1103/PhysRevResearch.2.023186

Ruckhofer, A., Tamtögl, A., Pusterhofer, M., Bremholm, M., and Ernst, W. E. (2019). Helium-surface interaction and electronic corrugation of Bi_2Se_3(111). *J. Phys. Chem. C* 123, 17829–17841. doi:10.1021/acs.jpcc.9b03450

Ruckhofer, A., Benedek, G., Bremholm, M., Ernst, W. E., and Tamtögl, A. (2023). Observation of Dirac charge-density waves in Bi_2Te_2Se. *Nanomaterials* 13, 476. doi:10.3390/nano13030476

Sanders, C. E., Dendzik, M., Ngankeu, A. S., Eich, A., Bruix, A., Bianchi, M., et al. (2016). Crystalline and electronic structure of single-layer TaS_2. *Phys. Rev. B* 94, 081404. doi:10.1103/PhysRevB.94.081404

Sanz, A. S., and Miret-Artés, S. (2007). Selective adsorption resonances: quantum and stochastic approaches. *Phys. Rep.* 451, 37–154. doi:10.1016/j.physrep.2007.08.001

Schmutzler, S. J., Ruckhofer, A., Ernst, W. E., and Tamtögl, A. (2022). Surface electronic corrugation of a one-dimensional topological metal: Bi(114). *Phys. Chem. Chem. Phys.* 24, 9146–9155. doi:10.1039/D1CP05284E

Shimada, T., Ohuchi, F., and Parkinson, B. (1994). Work function and photothreshold of layered metal dichalcogenides. *Jpn. J. Appl. Phys.* 33, 2696. doi:10.1143/jjap.33.2696

Shojaei, I. A., Pournia, S., Le, C., Ortiz, B. R., Jnawali, G., Zhang, F.-C., et al. (2021). A Raman probe of phonons and electron-phonon interactions in the Weyl semimetal $NbIrTe_4$. *Sci. Rep.* 11, 8155. doi:10.1038/s41598-021-87302-y

Singh, B., Lin, H., Prasad, R., and Bansil, A. (2016). Role of surface termination in realizing well-isolated topological surface states within the bulk band gap in $TlBiSe_2$ and $TlBiTe_2$. *Phys. Rev. B* 93, 085113. doi:10.1103/PhysRevB.93.085113

Singh, B., Sharma, A., Lin, H., Hasan, M. Z., Prasad, R., and Bansil, A. (2012). Topological electronic structure and weyl semimetal in the $tlbise_2$ class of semiconductors. *Phys. Rev. B* 86, 115208. doi:10.1103/PhysRevB.86.115208

Sobota, J. A., Teitelbaum, S. W., Huang, Y., Querales-Flores, J. D., Power, R., Allen, M., et al. (2023). Influence of local symmetry on lattice dynamics coupled to topological surface states. *Phys. Rev. B* 107, 014305. doi:10.1103/PhysRevB.107.014305

Spitzer, D. P., and Sykes, J. A. (1966). The Tl_2Te_3-Bi_2Te_3 system. *J. Appl. Phys.* 37, 1563–1566. doi:10.1063/1.1708568

Tamtögl, A., Bahn, E., Sacchi, M., Zhu, J., Ward, D. J., Jardine, A. P., et al. (2021a). Motion of water monomers reveals a kinetic barrier to ice nucleation on graphene. *Nat. Commun.* 12, 3120. doi:10.1038/s41467-021-23226-5

Tamtögl, A., Carter, E. A., Ward, D. J., Avidor, N., Kole, P. R., Jardine, A. P., et al. (2016). Note: a simple sample transfer alignment for ultra-high vacuum systems. *Rev. Sci. Instrum.* 87, 066108. doi:10.1063/1.4954728

Tamtögl, A., Kraus, P., Avidor, N., Bremholm, M., Hedegaard, E. M. J., Iversen, B. B., et al. (2017). Electron-phonon coupling and surface Debye temperature of Bi_2Te_3(111) from helium atom scattering. *Phys. Rev. B* 95, 195401. doi:10.1103/PhysRevB.95.195401

Tamtögl, A., Kraus, P., Mayrhofer-Reinhartshuber, M., Benedek, G., Bernasconi, M., Dragoni, D., et al. (2019). Statics and dynamics of multivalley charge density waves in Sb(111). *npj Quantum Mater* 4, 28. doi:10.1038/s41535-019-0168-x

Tamtögl, A., Mayrhofer-Reinhartshuber, M., Balak, N., Ernst, W. E., and Rieder, K. (2010). Elastic and inelastic scattering of He atoms from Bi(111). *J. Phys. Condens. Matter* 22, 304019. doi:10.1088/0953-8984/22/30/304019

Tamtögl, A., Pusterhofer, M., Bremholm, M., Hedegaard, E. M., Iversen, B. B., Hofmann, P., et al. (2018). A helium-surface interaction potential of Bi_2Te_3(111) from ultrahigh-resolution spin-echo measurements. *Surf. Sci.* 678, 25–31. doi:10.1016/j.susc.2018.02.006

Tamtögl, A., Ruckhofer, A., Campi, D., Bremholm, M., Ernst, W. E., Hofmann, P., et al. (2021b). Atom-surface van der Waals potentials of topological insulators and semimetals from scattering measurements. *Phys. Chem. Chem. Phys.* 23, 7637–7652. doi:10.1039/D0CP05388K

Tölkes, C., Zeppenfeld, P., Krzyzowski, M. A., David, R., and Comsa, G. (1997). Preparation of well-ordered cobalt nanostructures on Au(111). *Phys. Rev. B* 55, 13932–13937. doi:10.1103/physrevb.55.13932

Tsen, A. W., Hovden, R., Wang, D., Kim, Y. D., Okamoto, J., Spoth, K. A., et al. (2015). Structure and control of charge density waves in two-dimensional 1T-TaS_2. *Proc. Natl. Acad. Sci.* 112, 15054–15059. doi:10.1073/pnas.1512092112

Vaskivskyi, I., Gospodaric, J., Brazovskii, S., Svetin, D., Sutar, P., Goreshnik, E., et al. (2015). Controlling the metal-to-insulator relaxation of the metastable hidden quantum state in 1T-TaS_2. *Sci. Adv.* 1, e1500168. doi:10.1126/sciadv.1500168

Wang, Y. D., Yao, W. L., Xin, Z. M., Han, T. T., Wang, Z. G., Chen, L., et al. (2020). Band insulator to Mott insulator transition in 1T-TaS_2. *Nat. Commun.* 11, 4215. doi:10.1038/s41467-020-18040-4

Wilson, J., Salvo, F. D., and Mahajan, S. (1975). Charge-density waves and superlattices in the metallic layered transition metal dichalcogenides. *Adv. Phys.* 24, 117–201. doi:10.1080/00018737500101391

Wilson, J. A., Salvo, F. J. D., and Mahajan, S. (2001). Charge-density waves and superlattices in the metallic layered transition metal dichalcogenides. *Adv. Phys.* 50, 1171–1248. doi:10.1080/00018730110102718

Xu, B., Dai, Y. M., Zhao, L. X., Wang, K., Yang, R., Zhang, W., et al. (2017). Temperature-tunable Fano resonance induced by strong coupling between Weyl fermions and phonons in TaAs. *Nat. Commun.* 8, 14933. doi:10.1038/ncomms14933

Yan, B., Liu, C.-X., Zhang, H.-J., Yam, C.-Y., Qi, X.-L., Frauenheim, T., et al. (2010). Theoretical prediction of topological insulators in thallium-based III-V-VI_2 ternary chalcogenides. *EPL Europhys. Lett.* 90, 37002. doi:10.1209/0295-5075/90/37002

Yu, Y., Yang, F., Lu, X. F., Yan, Y. J., Cho, Y.-H., Ma, L., et al. (2015). Gate-tunable phase transitions in thin flakes of 1T-TaS_2. *Nat. Nanotechnol.* 10, 270–276. doi:10.1038/nnano.2014.323

Zhang, D., Wu, Y.-C., Yang, M., Liu, X., Coileáin, C. Ó., Xu, H., et al. (2016). Probing thermal expansion coefficients of monolayers using surface enhanced Raman scattering. *RSC Adv.* 6, 99053–99059. doi:10.1039/C6RA20623A

Zhang, H., Liu, C.-X., Qi, X.-L., Dai, X., Fang, Z., and Zhang, S.-C. (2009). Topological insulators in Bi_2Se_3, Bi_2Te_3 and Sb_2Te_3 with a single Dirac cone on the surface. *Nat. Phys.* 5, 438–442. doi:10.1038/nphys1270

frontiers | Frontiers in Chemistry

TYPE Original Research
PUBLISHED 06 February 2024
DOI 10.3389/fchem.2024.1355350

OPEN ACCESS

EDITED BY
Luca Vattuone,
University of Genoa, Italy

REVIEWED BY
Mario Rocca,
Università di Genova, Italy
Uwe Burghaus,
North Dakota State University, United States

*CORRESPONDENCE
Anton Tamtögl,
tamtoegl@tugraz.at

RECEIVED 13 December 2023
ACCEPTED 15 January 2024
PUBLISHED 06 February 2024

CITATION
Sabik A, Ellis J, Hedgeland H, Ward DJ, Jardine AP, Allison W, Antczak G and Tamtögl A (2024), Single-molecular diffusivity and long jumps of large organic molecules: CoPc on Ag(100).
Front. Chem. 12:1355350.
doi: 10.3389/fchem.2024.1355350

Single-molecular diffusivity and long jumps of large organic molecules: CoPc on Ag(100)

Agata Sabik[1,2], John Ellis[3], Holly Hedgeland[3], David J. Ward[3], Andrew P. Jardine[3], William Allison[3], Grażyna Antczak[1] and Anton Tamtögl[4]*

[1]Institute of Experimental Physics, University of Wrocław, Wrocław, Poland, [2]Department of Semiconductor Materials Engineering, Wrocław University of Science and Technology, Wrocław, Poland, [3]Cavendish Laboratory, Cambridge, United Kingdom, [4]Institute of Experimental Physics, Graz University of Technology, Graz, Austria

Energy dissipation and the transfer rate of adsorbed molecules do not only determine the rates of chemical reactions but are also a key factor that often dictates the growth of organic thin films. Here, we present a study of the surface dynamical motion of cobalt phthalocyanine (CoPc) on Ag(100) in reciprocal space based on the helium spin-echo technique in comparison with previous scanning tunnelling microscopy studies. It is found that the activation energy for lateral diffusion changes from 150 meV at 45–50 K to ≈100 meV at 250–350 K, and that the process goes from exclusively single jumps at low temperatures to predominantly long jumps at high temperatures. We thus illustrate that while the general diffusion mechanism remains similar, upon comparing the diffusion process over widely divergent time scales, indeed different jump distributions and a decrease of the effective diffusion barrier are found. Hence a precise molecular-level understanding of dynamical processes and thin film formation requires following the dynamics over the entire temperature scale relevant to the process. Furthermore, we determine the diffusion coefficient and the atomic-scale friction of CoPc and establish that the molecular motion on Ag(100) corresponds to a low friction scenario as a consequence of the additional molecular degrees of freedom.

KEYWORDS

surface diffusion, energy dissipation, single-molecule studies, organic thin films, atom-surface sattering, friction

1 Introduction

The self-assembly and growth of aromatic π-conjugated organic molecules adsorbed on metal surfaces is of paramount importance for the fabrication of molecular electronic devices. Controlling the growth of thin films composed of organic molecules implies understanding the interplay between the structure of the film and the dynamics of the molecules on the substrate from the early stages of film deposition. The initial stages of these phenomena involve mass transport where molecular species overcome the energy barrier between two (meta)stable adsorption configurations (Barth et al., 2005). Due to the complex nature of organic molecules, the translational motion on surfaces may be accompanied by rotations or conformational changes (Marbach and Steinruck, 2014). Moreover, for aromatic organic molecules, the interaction with the substrate often occurs via weak van der Waals (vdW) forces and friction may become so low that the molecule exhibits

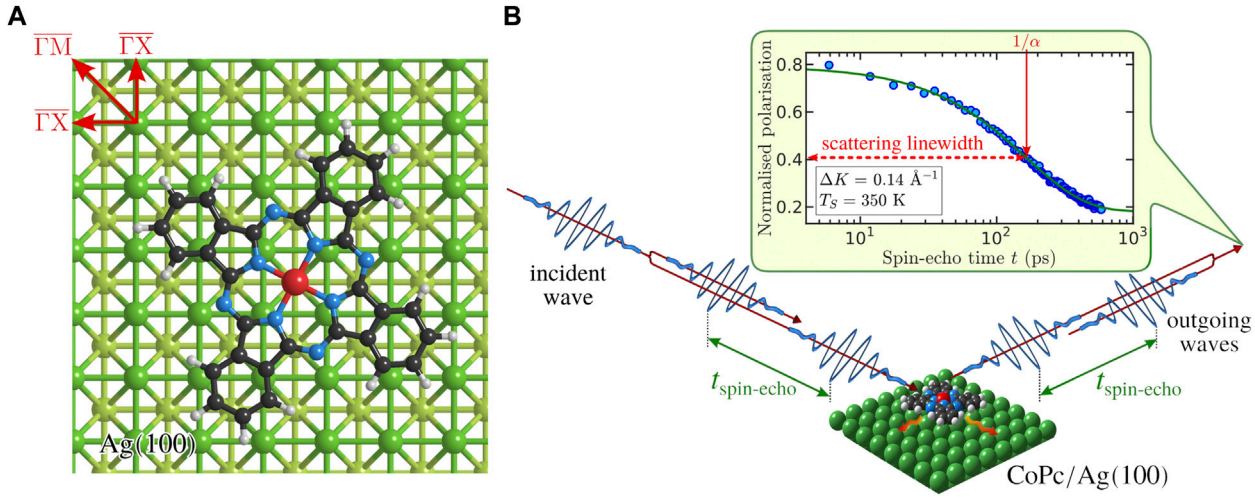

FIGURE 1
(A) Geometry of CoPc ($C_{32}H_{16}CoN_8$) adsorbed on the top-most Ag(100) layer according to (Antczak et al., 2015a). The molecule adsorbs with the central Co atom located at the hollow site. The high-symmetry directions of the Ag(100) surface are illustrated as well. **(B)** Illustration of the helium spin-echo method where two wavepackets scatter with a time difference $t_{spin-echo}$ from the surface, allowing the molecular motion to be interrogated through a loss in correlation, measured via beam polarisation. The top inset shows an exemplary intermediate scattering function (ISF) in terms of normalised polarisation *versus* spin-echo time t (filled circles) which is fitted with a single exponential decay (Eq. 1, solid green line) characterised by the dephasing rate α (scattering linewidth). The logarithmic time axis shows that a single exponential provides a good description of the experimental data.

a diffusive motion in the ballistic regime (Calvo-Almazán et al., 2016). The variety of these processes and possible correlation between those makes the study of surface diffusion challenging (Ferrando and Jardine, 2020). In the traditional view of atomistic surface diffusion, the motion is realised by a random walk of the adatom by crossing a barrier between two neighbouring potential wells: Particles move by hopping from one favourable adsorption site to one of the nearest adjacent sites, following the energetically most favourable route across the potential energy surface (PES). This simple picture holds at low temperatures for a number of systems, specifically for self-diffusion of single atoms across transition metal surfaces (Antczak and Ehrlich, 2007; 2010), but becomes more complex for larger molecules as well as with increasing temperature.

Scanning tunnelling microscopy (STM) allows the observation of these molecular dynamics on surfaces and has been employed as a powerful tool to obtain quantitative information about thermally activated processes, i.e., surface diffusion (Weckesser et al., 1999; Weckesser et al., 2001; Schunack et al., 2002; Kwon et al., 2005; Eichberger et al., 2008; Buchner et al., 2011). From temperature-dependent measurements the activation energy for diffusion, the diffusivity prefactor, and the frequency prefactor or attempt frequency for the rate of barrier crossing can be determined. However, the temperature window accessible to STM investigations is strongly limited to a region where the frequency of molecular jumps is relatively slow in comparison to the time needed for a scan. Here we show that helium-spin echo (HeSE) spectroscopy allows measurements of molecular diffusion at a much higher temperature range. As illustrated in Figure 1B and further described in Section 2, lineshape broadening upon scattering a wave can be used to measure the motion of single molecules down to the relevant picosecond timescales at elevated temperatures. Using HeSE facilitates the collection of data complementary to the existing STM study, allowing measurements of diffusion in a much higher temperature range at coverages comparable to the STM data. The technique also permits measurements in the high coverage regime at elevated temperatures to enable a broader understanding of the adsorbate's surface energetics and the role of molecule-molecule interactions.

The diffusion of phthalocyanine molecules (Pc, $C_{32}H_{16}MN_8$, where M denotes a metal atom) on smooth metal surfaces, such as Ag(100) is one of the representative examples where STM was successfully employed to explore the basic surface diffusion steps. Pcs are good candidate molecules for organic semiconductors as described below and have thus been studied extensively in this context. The characteristic four-leaf feature/shape of the molecule as illustrated in Figure 1A, allows for tracking its diffusion in consecutive STM images (Antczak et al., 2015a). Pcs on Ag(100) are a good model system that allows both STM measurements at cryogenic temperatures and millisecond timescales as well as HeSE measurements at much higher temperatures and picosecond timescales. Most importantly, such a model system has to be stable over a wide temperature range, meaning that any thermal desorption or other thermally induced processes such as molecular decomposition or island creation have to be excluded over the studied temperatures (Kröger et al., 2010). Specifically, we study the motion of cobalt phthalocyanine (CoPc, $C_{32}H_{16}CoN_8$) on Ag(100), where a combination of translational and rotational movements with an activation energy of 0.15 eV was found in STM measurements (Antczak et al., 2015a). However, due to the high mobility of CoPc, the investigated temperature interval was relatively narrow and covers the range from 45 to 50 K. Further, it was shown that above 75 K the molecular jumps are so frequent that it is impossible to recognise where the molecule is in an STM image (Antczak et al., 2017).

The family of Pc molecules is also considered as promising candidate for active layers in electronic devices, e.g., organic solar cells or organic field emission transistors (Wu et al., 2013; Melville

et al., 2015) and recently the properties of Pc on monocrystalline metal surfaces have been widely studied to get a better insight into the performance of electronic devices (Gottfried, 2015). Pcs commonly adsorb with their aromatic plane parallel to the metal surface forming ordered structures, though for most metal-phthalocyanines no island formation is observed in the sub-monolayer regime at room temperature (Kröger et al., 2012; Feyer et al., 2014). CoPc studies have also included its utilisation as a single molecular magnet (Bartolomé et al., 2014; Wang et al., 2021) with possible applications in spintronics (Iacovita et al., 2008) and even quantum computing where the molecules act as single qubits (Warner et al., 2013; Bader et al., 2016). However, while a solid-state quantum computational architecture is likely to take the form of an ordered array assembled on a surface, recent studies have not considered this option (Graham et al., 2017). Finally, the adsorption of CoPc can also be used to manipulate the electronic surface states of a topological insulator (Caputo et al., 2016) and they have been successfully studied in the field of electrocatalysis for electrochemical CO_2 reduction (Feng et al., 2022; Ding et al., 2023) and as possible gas sensors (Bohrer et al., 2007).

Our study illustrates broad agreement for molecular diffusion studied with two different experimental techniques in different temperature regions: STM data taken in real space at low temperature (Antczak et al., 2015a) and HeSE data taken in reciprocal space at a temperature seven times higher. While our results confirm the current understanding of a complex diffusion mechanism over a large temperature window, they illustrate that HeSE is able to observe subtle details such as the occurrence of long jumps at high temperatures and adsorbate interactions. As one may anticipate, there are indeed differences in the molecular motion such as a change of the effective diffusion barrier and the mentioned onset of long jumps with a distinctive motion of the molecules at high temperatures. Hence we show that by combination of STM with HeSE, it is possible to obtain a complete picture of complex diffusion mechanisms over the entire temperature range, from the onset of diffusion to technologically relevant temperatures.

2 Methods

The extension of the existing STM diffusion study of CoPc on Ag(100) to a higher temperature range requires methods that probe the nanometre length scale at an extremely short timescale. Very fast molecular dynamics has been successfully investigated by scattering techniques such as helium atom scattering (Tamtögl et al., 2021; Sacchi and Tamtögl, 2023) or neutron scattering (Tamtögl et al., 2018). The reported measurements were performed on the Cambridge helium-3 spin-echo (HeSE) apparatus where a nearly monochromatic beam of ^{3}He is generated and scattered off the sample surface in a fixed 44.4° source-target-detector geometry. For a detailed description of the apparatus please refer to (Alexandrowicz and Jardine, 2007; Jardine et al., 2009; Holst et al., 2021). Prior to the deposition of CoPc, the Ag(100) substrate was cleaned by several Ar^+ ion sputtering (0.8 keV energy, 10 μA sputtering current) and annealing cycles to 800 K. The quality and cleanliness of the crystal were checked with He diffraction measurements. CoPc was deposited using a home-built Knudsen cell which was filled with crystalline powder (Sigma-Aldrich) and kept at about 620 K while the Ag(100) sample was at 350 K.

Pcs arrange into well-ordered islands on smooth metal surfaces after the so-called critical coverage is reached. In the case of Ag(100) at room temperature, CoPc island creation is detected from around 0.8 monolayer (ML) onward (Wagner et al., 2022a; b). Between critical and ML coverage, the coexistence of mobile molecules in a so-called 2D gas phase with ordered islands was found by photoemission electron microscopy investigations (Wagner et al., 2022a). The molecular 2D gas phase manifests itself as irregular blurring or streaking in STM scan images since mobile molecules at increased sample temperatures result in noise detection by the STM tip (Antczak et al., 2017). The commonly reported superstructure associated with 1 ML of CoPc on Ag(100) is a (5 × 5) superstructure (Sabik et al., 2016). In general, Pcs adsorb with its aromatic plane parallel to flat metal surfaces, and the adsorption geometry of a single CoPc molecule on Ag(100) is presented in Figure 1A. The processes of adsorption can be observed by monitoring the specularly reflected helium signal while dosing CoPc onto the surface. The so-called uptake curve is shown in the Supplementary Material (Adsorption, uptake and coverage calibration). The deposited coverage can then be estimated based on the uptake curve where ML coverage corresponds to the (5 × 5) superstructure (Salomon et al., 2013; 2015; Sabik et al., 2016)). Using a helium scattering cross section of $\Sigma = 1000$ Å^2 for a single CoPc molecule on Ag(100) gives a coverage of 0.11 ML for a specular attenuation of $I_0/2$. Most dynamics measurements were performed at this coverage unless otherwise stated (see Adsorption, uptake and coverage calibration in the Supplementary Material).

A helium spin-echo experiment as shown schematically in Figure 1B, provides direct access to the so-called intermediate scattering function (ISF), $I(\Delta\mathbf{K}, t)$, at a fixed surface parallel momentum transfer $\Delta\mathbf{K}$ specified by the scattering geometry. The measured beam polarisation is proportional to $I(\Delta\mathbf{K}, t)$, which is related to the pair correlation function through a Fourier transform (Jardine et al., 2009; Tamtögl et al., 2020; Tamtögl et al., 2021; Sacchi and Tamtögl, 2023). As illustrated in Figure 1B, due to the motion of the adsorbate on the surface the (auto) correlation determined through the ISF decays with increasing spin-echo time, t. In its basic form, the time dependence follows a simple exponential decay:

$$I(\Delta\mathbf{K}, t) = I_0(\Delta\mathbf{K}, 0) \cdot e^{-\alpha(\Delta\mathbf{K})\cdot t} + C(\Delta\mathbf{K}) \quad (1)$$

with the decay constant (so-called dephasing rate) α and I_0 the amplitude at $t = 0$. As can be seen in a typical ISF in the top inset of Figure 1B, the CoPc data is well represented by a single exponential decay. We note, however, that for other systems and different types of motion occurring on different timescales $I(\Delta\mathbf{K}, t)$ will deviate from the simple form and is better fitted using multiple exponential decays (Jardine et al., 2009).

3 Results

We have performed HeSE measurements after the deposition of a specified amount of CoPc onto the clean Ag(100) substrate (see Section 2). The dynamics of CoPc adsorbed on Ag(100) were extracted from HeSE measurements, via the ISF, $I(\Delta\mathbf{K}, t)$ with a single exponential decay according to Eq. 1. The timescales of molecular motion follow from the dephasing rate α, and the

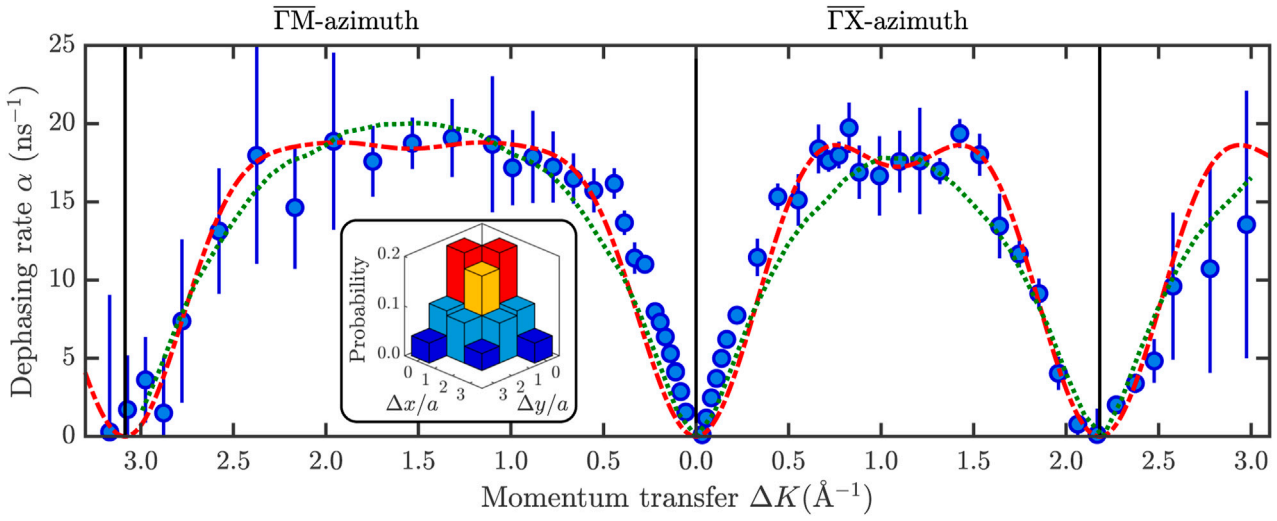

FIGURE 2
Momentum transfer dependence of $\alpha(\Delta\mathbf{K})$ for the diffusion of CoPc on Ag(100) at 350 K and a CoPc coverage of 0.11 ML. The red dash-dotted line shows the Chudley-Elliott model (Eq. 2). The corresponding jump distribution for displacements Δx and Δy in units of the surface lattice constant a, as shown in the inset, illustrates that a significant number of long jumps is present. The green dotted line, according to molecular dynamics simulations, allows a quantitative assessment of the rate of energy transfer between the CoPc molecule and the substrate.

functional dependence of $\alpha(\Delta\mathbf{K})$ *versus* momentum transfer $\Delta\mathbf{K}$ provides details about the diffusive motion and the length scales of the latter in real space. The temperature dependence $\alpha(T)$ reveals the energetic diffusion barriers and can then be directly compared with low-temperature STM data taken in real space.

3.1 Jump diffusion of CoPc on Ag(100)

To determine $\alpha(\Delta\mathbf{K})$ experimentally, HeSE measurements were acquired for a range of $\Delta\mathbf{K}$ values along a selected azimuth by systematically varying the angle of incidence ϑ_i and extracting the dephasing rate α from the resulting exponential decays. The dependence of $\alpha(\Delta K)$ on the momentum $\Delta K = |\Delta\mathbf{K}|$ for the diffusion of CoPc on Ag(100) (T_S = 350 K) is shown in Figure 2 for the two high-symmetry directions of the crystal. For the case that the diffusion of the adsorbate is governed by the interaction of the molecule with a corrugated surface, its motion can be well described by the Chudley-Elliott (CE) model of jump-diffusion (Chudley and Elliott, 1961; Barth, 2000; Jardine et al., 2009; Ferrando and Jardine, 2020). The CE model provides an analytic solution for $I(\Delta\mathbf{K}, t)$ with the dephasing rate α vanishing when the momentum transfer $\Delta\mathbf{K}$ matches a reciprocal surface lattice vector and varying sinusoidally in between. It assumes that a particle rests for a time τ at an adsorption site before it moves to another adsorption site. In the simplest case, this motion happens on a Bravais lattice and the dephasing rate $\alpha(\Delta K)$ becomes:

$$\alpha(\Delta K) = \frac{2}{\tau}\sum_n p_n \sin^2\left(\frac{\Delta\mathbf{K}\cdot\mathbf{l}_n}{2}\right) \qquad (2)$$

where $\mathbf{l}_n$ are the corresponding jump vectors and p_n is the relative probability that a jump to the corresponding site occurs.

Figure 2 shows that the experimental data is best fitted with a CE model (red dash-dotted line, (Eq. 2)) with jumps on the square Ag(100) lattice. The jump distribution is displayed in the inset of Figure 2 and shows a significant fraction of long jumps. The corresponding residence time τ is 0.11 ns with a jump frequency of about 4.6 GHz to one of the nearest neighbour sites. We see already from the significant number of long jumps at 350 K that there is a clear difference to the STM data of the same system by Antczak et al. (2015a) taken at 45–50 K where hardly any long jumps are present. Long jumps are a modification of the simple molecular diffusion picture where jumps occur solely between adjacent sites as mentioned in the introduction: The adsorbate can move across several lattice distances within a single jump, bypassing multiple adjacent sites. Similar to the presented jump distribution here, it was also shown for single-atom diffusion on metals that longer jumps need to be introduced to explain the jump distribution at higher temperatures (Senft and Ehrlich, 1995; Antczak and Ehrlich, 2004) and we will further discuss that in Section 3.4.

Based on the momentum transfer dependence in Figure 2, the CoPc molecule can either jump from hollow to hollow site or from top to top site since only jumps between these adsorption sites give rise to the characteristic minima as shown by the CE model. Bridge sites would give rise to jumps on a square lattice as well, however, the shorter jump vector (compared to jumps between hollow sites) cannot reproduce the momentum transfer dependence of $\alpha(\Delta\mathbf{K})$ as the position of the minima would be further out. On the other hand, from previous combined STM and density functional theory (DFT) studies (Antczak et al., 2015a) it is known that the CoPc molecule adsorbs with the central Co atom located at the hollow site (Figure 1A). Hence we conclude that the hollow site is the favourable adsorption site. As shown by Antczak et al. (2015a), during diffusion the molecule moves over the bridge site while the top adsorption site is the least favourable site (Antczak et al., 2015a) and the HeSE data confirms exactly this type of motion, with the

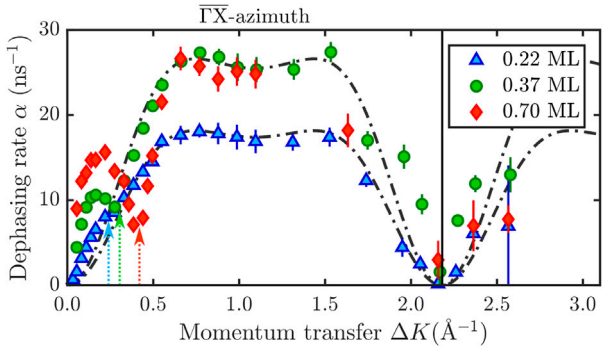

FIGURE 3
With increasing CoPc coverage, adsorbate interactions become evident in the experimental data giving rise to a distinctive peak and dip (illustrated by the arrow) structure in the $\alpha(\Delta K)$ curve at low ΔK which becomes more significant with increasing coverage. The $\alpha(\Delta K)$ curves are shown along $\overline{\Gamma X}$ for T_S = 350 K, with the grey dash-dotted lines from the CE model suggesting that the jump distribution remains the same while only the rate, i.e., amplitude of the model increases with coverage. The lowest coverage (0.11 ML, Figure 2) is not shown here since it is almost identical to the data taken at 0.22 ML.

only exception that at 350 K a high number of multiple or long jumps is present in contrast to the STM data at low temperature. Following the description of atomic-scale motion with the molecule moving or hopping along the surface, the substrate provides the thermal energy for the motion and friction is a direct measure of the molecule-substrate coupling as the rate of energy transfer determines the molecular diffusivity (Barth, 2000; Ala-Nissila et al., 2002; Jardine et al., 2009)—as discussed in Sections 3.3 and 3.4.

We further note that close to $|\Delta\mathbf{K}| = 0$ the experimental data points tend to be slightly above the curve given by the CE model. Such a deviation could be due to adsorbate-adsorbate interactions, however, it is not clearly evident whether it is repeated around the position of the diffraction peaks (vertical lines at about 3 $Å^{-1}$ along $\overline{\Gamma M}$ and 2.2 $Å^{-1}$ along $\overline{\Gamma X}$). Hence it could also be due to a motion of the CoPc molecule perpendicular to the surface (Alexandrowicz and Jardine, 2007).

3.2 Adsorbate interactions and coverage dependence

Repulsive interactions become clearly evident at higher coverages, in particular close to the critical CoPc coverage (Antczak et al., 2017). While there is hardly any difference in the low coverage regimes (Figure 5B), the signature for adsorbate-interactions starts to set in above ≈ 1/4 ML, as shown in Figure 3. A significant change in the shape of the $\alpha(\Delta K)$ curve can be seen as the coverage increases from 0.22 ML to 0.37 ML, and 0.7 ML. For the two lowest coverages (0.11 and 0.22 ML), the deviation from the CE model occurs only close to $|\Delta\mathbf{K}| = 0$ and is not repeated around the position of the diffraction peak, likely due to a motion of CoPc perpendicular to the surface (Alexandrowicz and Jardine, 2007).

With further increasing coverage, i.e., at 0.37 and 0.7 ML, the $\alpha(\Delta K)$ in Figure 3 indicates that the CoPc dynamics is governed by correlated motion where the CoPc motion can no longer be described as isolated self-diffusion. The characteristic shape of the curve, featuring a peak at small ΔK values, followed by a de Gennes narrowing dip (Alexandrowicz and Jardine, 2007; Jardine et al., 2009) (illustrated by the arrows in Figure 3), has been predicted both numerically and analytically for surface diffusion of repulsive particles (Ala-Nissila et al., 2002; Jardine et al., 2009) but has only recently been observed experimentally (Alexandrowicz and Jardine, 2007; Tamtögl et al., 2021). The location of the dip corresponds to a peak in the static structure factor (Serra and Ferrando, 2002), verifies the repulsive nature of the force, and also allows a coverage estimation of the adsorbate (see 1.2 in the Supplementary Information).

While there are fewer data points available at higher coverage, Figure 3 clearly indicates that the jump distribution according to the analytic CE model (grey dash-dotted line) remains the same over the studied coverage regime. Outside the ΔK regions where the repulsive forces are present, the data points are still reproduced by the CE model with the same jump distribution as in Figure 2, the only difference being the overall rate, i.e., the amplitude of the analytic curve. We thus conclude that the jump distribution is not influenced by the coverage and is indeed a pure feature of the increased surface temperature as described in Section 3.3. We note that there seems to be hardly any change in the maximum rate when going from 0.37 ML to 0.7 ML while the position of the de-Gennes dip clearly wanders as expected. The latter may be correlated with the critical CoPc coverage observed at room temperature (Wagner et al., 2022a; b), i.e., where the CoPc molecules are in a 2D gas phase up to around 0.7–0.8 ML and the actual condensation of the 2D ordered structure occurs above 0.8 ML.

Before we attempt to directly compare activated diffusion results with STM measurements, these results show already that the combination of HeSE and STM measurements is extremely useful in investigating complex diffusion mechanisms, including also a large range of different coverages. It remains challenging to observe repulsive interactions with STM and the influence of repulsive forces is typically explored in conjunction with Monte Carlo methods (Trost et al., 1996). Here it was shown recently that repulsive interactions can be made visible by immobilising a fraction of molecules at step edges: Mobile molecules cannot reach the immobilised molecules, leaving behind a span of pristine silver between both due to the repulsive interaction (Antczak et al., 2017). Hence the HeSE measurements are complimentary to the STM measurements, as the former allow us to observe repulsive interactions "directly" during the diffusion process including also high coverage regimes, confirming the presence of repulsive interactions in the diffusion of CoPc on Ag(100) (Antczak et al., 2017).

3.3 Activated diffusion and mass transport at different time-scales

A direct comparison with the diffusivity of CoPc on Ag(100) obtained from real-space STM at low temperatures is easiest to achieve when plotting the HeSE rates in an Arrhenius plot analogous to the analysis of STM data. Therefore, temperature-dependent measurements at a fixed momentum transfer, $\Delta\mathbf{K}$, have been

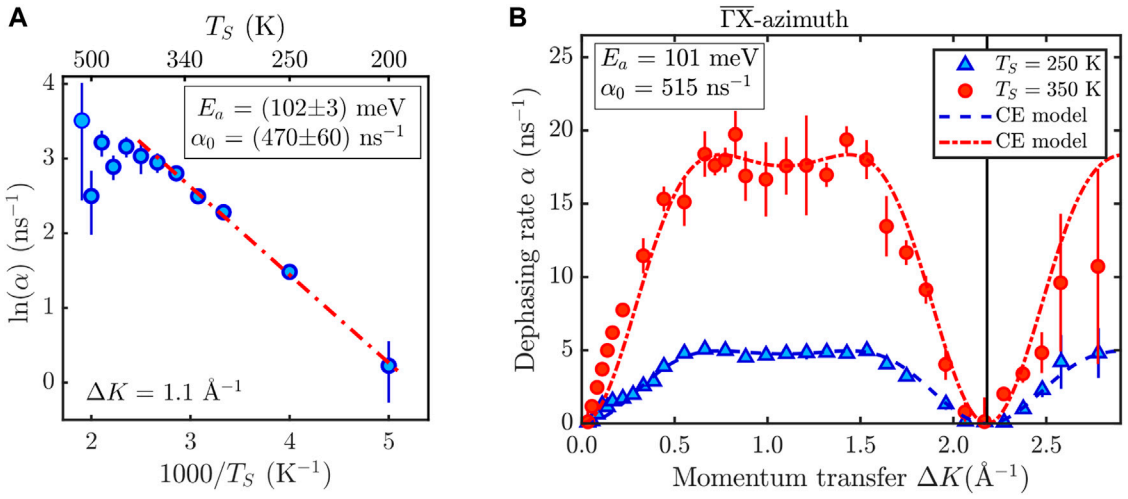

FIGURE 4
(A) Pre-exponential factor α_0 and the activation energy E_a can be determined from an Arrhenius plot at a fixed momentum ΔK over a temperature range of 200 – 500 K. **(B)** Temperature dependence over the whole momentum transfer range along the $\overline{\Gamma X}$-azimuth for a CoPc coverage of 0.11 ML. The dash-dotted and dashed lines show the corresponding CE model according to (2).

performed. For thermally activated processes, Arrhenius' law predicts a temperature dependence of the dephasing rate, α, as:

$$\alpha = \alpha_0 \, e^{-\frac{E_a}{k_B T_S}} \tag{3}$$

where α_0 is the pre-exponential factor describing the jump attempt frequency, E_a is the activation energy for diffusion, k_B the Boltzmann constant and T_S the temperature of the sample surface. Taking the natural logarithm of (Eq. 3) results in a linear relationship between the inverse of the temperature, $1/T_S$, and the natural logarithm of the dephasing rate α.

Figure 4A shows an Arrhenius plot obtained at a fixed momentum transfer ΔK over a wide temperature range from 250 K to about 500 K. We note that in general there is a deviation from the linear behaviour above ≈450 K which is likely to be due to the presence of multiple decays in the ISF. One possible explanation for the bending of the Arrhenius plot at higher temperatures is that with increasing temperature the activation of a metastable adsorption state occurs, located above the ground state with a different rotation of the molecule with respect to the substrate. The latter is, however, beyond the scope of the current study and will not be discussed in detail (Ellis et al., 2024).

The activation energy is then obtained from the slope of the linear fit in Figure 4 whereupon the intercept gives α_0. For the linear fit and the determination of the activation energy, we have excluded the high-temperature points where an obvious deviation from the linear behaviour occurs. From Figure 4A we obtain $E_a = (102 \pm 3)$ meV and $\alpha_0 = (470 \pm 60)$ns^{-1}. The activation energy E_a is similar to the value obtained by STM measurements at low temperatures with 150 meV (Antczak et al., 2015a) but still significantly lower. It illustrates that while the microscopy measurements at 50 K are directly comparable with spin echo measurements in the higher 200–500 K temperature range, the diffusive motion undergoes subtle changes with increasing temperature.

In order to prove the consistency of the determined activation energy E_a across surface length-scales, we have also performed a measurement of the complete momentum transfer dependence along $\overline{\Gamma X}$, at two different temperatures. Figure 4B shows the extracted $\alpha(\Delta\mathbf{K})$ for 250 and 350 K, respectively. The shape of the CE model (dash-dotted and dashed line) is similar for both temperatures, indicating that the hopping motion, including a significant number of long jumps, remains comparable over this temperature range. At the same time, the hopping rate changes with temperature which is expressed in terms of the residence time τ in Eq. 2. We can use the change of the residence time τ with temperature to calculate again the activation energy which has been determined from the Arrhenius plots above. Here $\tau = 4 \cdot 10^{-10}$ s at a sample temperature of 250 K and $\tau = 1.1 \cdot 10^{-10}$ s at 350 K. This gives an activation energy of $E_a = 101$ meV which is consistent with the activation energy determined from the Arrhenius plots.

We can also compare the activation energy with the values found for CuPc on Ag(100) since the diffusion of both CoPc and CuPc on Ag(100) follow the same fashion (Antczak et al., 2015b). However, for the diffusion of CuPc on Ag(100), conflicting values regarding the activation were reported ranging from 30 to 81 meV measured at 140–220 K (Ikonomov et al., 2010; Hahne et al., 2013) and about 200 meV around 75 K (Antczak et al., 2015b). While the first two values were obtained from signal fluctuations of a locally fixed STM tip at higher substrate temperatures, our study illustrates that such a large variation of the activation energy is unlikely to be caused by the increased temperature.

We also note bond formation and clustering at higher temperatures for other Pc molecules in the literature. On the other hand, such an effect would only lead to an immobilising of several molecules and would hence give rise to a decreased number of diffusing molecules. It will thus not have any significant impact on the diffusion of the remaining mobile molecules and as such cannot explain the behaviour in the Arrhenius at high temperature (Ellis et al., 2024).

Finally, the diffusion coefficient D for two-dimensional motion, i.e., tracer-diffusion can be calculated from the hopping rate as determined from the CE model using:

$$D = \frac{1}{4}\langle l \rangle^2 \Gamma \tag{4}$$

where Γ is the hopping rate and $\langle l \rangle$ the mean jump length (Barth, 2000; Jardine et al., 2009; Ferrando and Jardine, 2020). For a hopping rate of $1.9 \cdot 10^{10}$ s^{-1} and a mean jump length of 4.52 Å we obtain a diffusion coefficient of:

$$D = 9.6 \cdot 10^{-10} \text{ m}^2/\text{s},$$

at 350 K. D measured at 350 K corresponds to a prefactor for the diffusivity with $D_0 = 2.7 \cdot 10^{-8}$ m^2/s and is thus much smaller than $D_0 \approx 1 \cdot 10^{-5}$ m^2/s as reported in STM works by Antczak et al. (2015a). While the latter may at first glance appear as a stark discrepancy, it can clearly be related to the reduced effective diffusion barrier E_a obtained at higher temperatures. It further illustrates that for a precise determination of any prefactor D_0, measurements should ideally include also higher temperatures, closer to the extrapolation in the Arrhenius' plot. Thus reports about the fast diffusion of large molecules such as decacyclene and hexa-tert-butyldecacyclene molecules on Cu(110) as observed in STM measurements (Schunack et al., 2002) should also be treated with care, in particular upon extrapolation of the diffusivity to high temperatures.

3.4 Long jumps and atomic-scale friction of CoPc

As shown in the present example, long jumps can dominate high-temperature motion of large organic molecules. While the mechanism of long jumps has been characterised in the case of self-diffusion with field ion microscopy (FIM) on tungsten about 20 years ago (Antczak and Ehrlich, 2005; Antczak, 2006b; a; Antczak and Ehrlich, 2007), the mechanism has hardly been considered for more complex molecules. In the case of metal-atom diffusion following FIM, long jumps are seen as a continuation of single jumps: Detailed analysis of these jumps provides evidence that they still proceed via the lowest potential energy route, but the equilibration of the adatom proceeds in the second or third potential well (Figure 5A), in the case of a double or triple jump, respectively (Antczak and Ehrlich, 2007). As such, long jumps replace a single jump in the atomistic picture and while the total number of jumps follows an exponential increase with temperature, the occurrence of particular jump types does not. For single atom diffusion, long jumps become clearly more important as the temperature increases (Braun and Ferrando, 2002; Pollak and Miret-Artés, 2023) and it has also been suggested that these are a general feature of hydrogen diffusion on close-packed transition metal surfaces at high temperatures (Townsend and Avidor, 2019).

The observation that a large number of long jumps are present at high temperatures already suggests that despite its molecular size, CoPc exhibits a low friction η during diffusion on Ag(100). Moreover, as the analytic CE only tells us the "end" site where the molecule ends up but not the continuation of the molecule in a long jump, a common method to further analyse HeSE data often follows from molecular dynamics (MD) simulations based on solving the Langevin equation (Avidor et al., 2019; Sacchi and Tamtögl, 2023). The Langevin description of dynamics allows a quantitative analysis of the atomic-scale friction η, with η being a direct measure of the coupling between the molecular motion and the heat-bath of the substrate and thus determining the rate of barrier crossing.

In the MD simulations, the interaction of the adsorbed molecule with the substrate atoms is described by a "frozen" potential energy surface (PES, Figure 5A), where the friction coefficient η describes the rate of energy transfer between the molecule and the surface. As one may anticipate for a complex molecule such as CoPc a simple center-of-mass (CoM) MD cannot capture the full details of the diffusion process, however, as shown in Figure 5B the correct jump distribution is reproduced reasonably well with an MD simulation that includes the translational CoM motion and the rotation of the CoPc molecule, in analogy to the low-temperature STM findings by Antczak et al. (2015a).

The potential energy surface used in the simulation is derived from the DFT calculations given in Antczak et al. (2015a) with the exact details described in Molecular dynamics simulation in the Supplementary Material. As illustrated in Figure 5A, the potential consists of a translational part $V(x, y)$ (top panel) and a rotational part, for rotations φ around the C_4 molecular axis perpendicular to the surface (bottom panel, see also Hedgeland et al. (2016)). The latter varies with the adsorption site between hollow (H) sites given by $V_H(\varphi)$, and bridge (B) sites given by $V_B(\varphi)$.

A typical trajectory from an MD simulation with (x, y) and φ *versus* time is shown in the Supplementary Material (Supplementary Figure S2). The momentum transfer dependence $\alpha(\Delta K)$ as extracted from the MD simulation is shown as a green dotted line in Figure 2 as well as in Figure 5B. By varying the friction η under the assumption that the rotational friction is the same as the translational one (see Section 1.3 in the Supplementary Material) we obtain a good fit with the experimental data for

$$\eta = 0.23 \text{ ps}^{-1}.$$

To our knowledge, this is the first report of the atomic scale friction of such a large molecule (The molecular mass of CoPc being 571.46 u whereas previous studies of larger molecules included typically adsorbates with an atomic mass below 100 u) (Jardine et al., 2009; Hedgeland et al., 2016). Friction coefficients have been determined for a wide range of different systems, although most work is concentrated on small adsorbates and in the low-temperature region. The atomic-scale friction η for atomic adsorbates is typically smaller than 1 ps^{-1} (Jardine et al., 2009; Rittmeyer et al., 2016), and only for larger, organic molecules, friction values of e.g., η = 1.8 ps^{-1} for pentacene ($C_{22}H_{14}$) on Cu(110) have been reported (Rotter et al., 2016). On the other hand for benzene (C_6H_6) on Cu(001) a value η = 0.4 ps^{-1} was reported (Hedgeland et al., 2016) when considering both translations and rotations as in the present case. Hence, while one may anticipate increasing friction and thus lower diffusivity for larger molecules, the additional degrees of freedom may impose a different trend, i.e., the diffusivity becomes significantly greater than

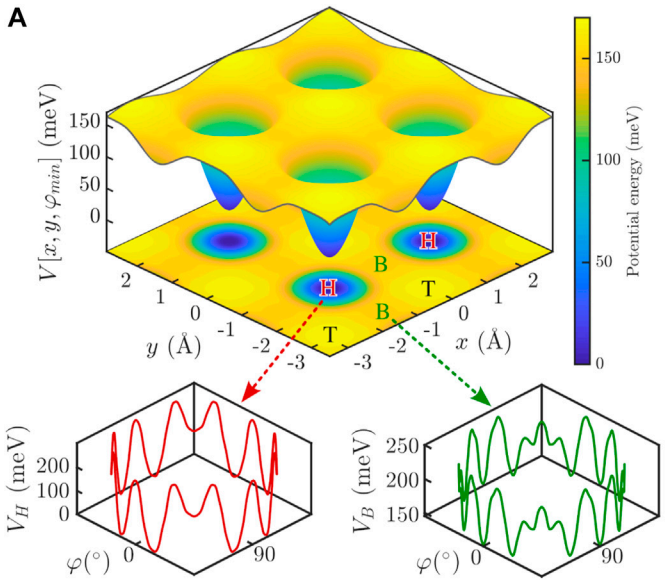

FIGURE 5
(A) Energy landscapes used in the MD Langevin simulations. The upper panels show the lateral potential energy surface (PES) $V(x, y)$, for the minimum rotational energy configuration at each site. The color map extends from the lowest energy (hollow site, H) via the most favourable transition state (bridge site, B), and the highest potential energy site (top site, T). The lower panels show the potential energy as a function of rotation φ around the C_4 molecular axis perpendicular to the surface: The red line on the left is the potential $V_H(\varphi)$ at the hollow site, while the green line on the right is the potential $V_B(\varphi)$ at the bridge site. **(B)** Comparison of the $\alpha(\Delta K)$ curves for the two lowest CoPc coverages together with the green dotted line, according to the MD simulation.

that of a point-like particle with the same mass. In other words, the observed diffusion rate is significantly higher if additional molecular degrees of freedom such as the rotation of the CoPc molecules are included, with the friction $\eta = 0.23$ ps^{-1} for rotations and translations of CoPc upon diffusion over Ag(100). At the same time, as η is the force divided by the mass and the CoPc mass with 571.46 u is very large, we are nevertheless still dealing with very large forces.

In summary, we note that a simple MD that considers both rotations and translations is thus useful to obtain a quantification of the energy transfer rate, even though it cannot capture the full details of the diffusion mechanism of a complex organic molecule over the entire temperature range (Ellis et al., 2024). The observation that an "effective" potential different from the simple geometry of substrate atoms is present is not new and has, e.g., already been observed in the case of atom self-diffusion (Oh et al., 2003)—however it has not been considered for large molecules where the molecular degrees of freedom give rise to a multi-dimensional potential energy surface thus contributing to the "effective" barrier during diffusion.

4 Discussion

We have studied the diffusion of CoPc on Ag(100) using helium spin-echo spectroscopy over a wide temperature and coverage range. Comparison of our data with STM measurements shows broad agreement for data taken at low temperature with STM (Antczak et al., 2015a) and data taken with HeSE in a seven times higher temperature regime. While the diffusion of CoPc still follows a similar route along the potential energy surface, with HeSE we can clearly distinguish the onset of multiple/long jumps with increasing temperature. We thus illustrate the mechanism of long jumps which has been previously characterised by FIM for self-diffusion of tungsten atoms, in the case of large molecular adsorbates on surfaces.

Moreover, the experimentally obtained activation energy for the diffusion of CoPc is significantly lower at high temperatures compared to the barrier obtained in previous STM measurements at cryogenic temperatures (Antczak et al., 2015a). The result illustrates that a precise determination of single-molecular diffusivity measurements and the prefactor D_0 should ideally also include high-temperature data. Previous measurements extrapolating cryogenic STM data over the entire temperature scale and associated high diffusivities should thus be treated with care as mechanistic changes of the molecular motion which can only be observed at high temperatures may be present.

We have further determined the rate of energy transfer between the molecule and the substrate in terms of the atomic-scale friction with $\eta = 0.23$ ps^{-1}. Thus, despite the large molecular size, CoPc/Ag(100) is clearly a low friction scenario and the diffusivity can be understood by including additional molecular degrees of freedom in terms of a combined rotational and translational motion.

Finally, we have illustrated that by the combination of two experimental techniques, HeSE with STM, it is possible to obtain a complete picture of complex diffusion mechanisms and energy dissipation in surface diffusion over the entire temperature range, from the onset of diffusion to technologically relevant temperatures. While STM is capable of providing information in the low-

temperature regime, HeSE can be used to get a better insight into diffusion at higher temperatures as well as at high coverages including the occurrence of long jumps, and adsorbate interactions. The herein presented approach promises also to provide a route by which the factors affecting the underlying structural assembly in organic thin films can be explored and understood at a molecular level.

Data availability statement

The raw data supporting the conclusion of this article is available via: https://doi.org/10.3217/z5d3c-jev61.

Author contributions

AS: Formal Analysis, Investigation, Methodology, Writing–original draft, Writing–review and editing. JE: Conceptualization, Supervision, Writing–review and editing, Formal Analysis, Software, Writing–original draft. HH: Supervision, Writing–review and editing. DW: Supervision, Writing–review and editing. AJ: Supervision, Writing–review and editing. WA: Methodology, Supervision, Writing–review and editing. GA: Conceptualization, Data curation, Investigation, Writing–original draft, Writing–review and editing. AT: Formal Analysis, Funding acquisition, Investigation, Methodology, Visualization, Writing–original draft, Writing–review and editing.

Funding

The author(s) declare financial support was received for the research, authorship, and/or publication of this article. This research was funded in whole, or in part, by the Austrian Science Fund (FWF) [P34704 https://www.doi.org/10.55776/P34704, J3479-N20 https://www.doi.org/10.55776/J3479]. For the purpose of open access, the author has applied a CC BY public copyright licence to any Author Accepted Manuscript version arising from this submission. Supported by TU Graz Open Access Publishing Fund.

Acknowledgments

We would like to thank T. Wagner and P. Zeppenfeld as well as the Johannes Kepler University Linz. AT acknowledges G. Alexandrowicz for helpful discussions. AS acknowledges the Project “Development of the potential and educational offer of the University of Wrocław—the chance to enhance the competitiveness of the University”.

Conflict of interest

The authors declare that the research was conducted in the absence of any commercial or financial relationships that could be construed as a potential conflict of interest.

Publisher’s note

Supplementary material

The Supplementary Material for this article can be found online at: https://www.frontiersin.org/articles/10.3389/fchem.2024.1355350/full#supplementary-material

References

Ala-Nissila, T., Ferrando, R., and Ying, S. C. (2002). Collective and single particle diffusion on surfaces. *Adv. Phys.* 51, 949–1078. doi:10.1080/00018730110107902

Alexandrowicz, G., and Jardine, A. P. (2007). Helium spin-echo spectroscopy: studying surface dynamics with ultra-high-energy resolution. *J. Phys. Cond. Matt.* 19, 305001. doi:10.1088/0953-8984/19/30/305001

Antczak, G. (2006a). Kinetics of atom rebounding in surface self-diffusion. *Phys. Rev. B* 74, 153406. doi:10.1103/PhysRevB.74.153406

Antczak, G. (2006b). Long jumps in one-dimensional surface self-diffusion: rebound transitions. *Phys. Rev. B* 73, 033406. doi:10.1103/PhysRevB.73.033406

Antczak, G., Boom, K., and Morgenstern, K. (2017). Revealing the presence of mobile molecules on the surface. *J. Phys. Chem. C* 121, 542–549. doi:10.1021/acs.jpcc.6b11246

Antczak, G., and Ehrlich, G. (2004). Long jump rates in surface diffusion: W on W(110). *Phys. Rev. Lett.* 92, 166105. doi:10.1103/PhysRevLett.92.166105

Antczak, G., and Ehrlich, G. (2005). Long jumps in diffusion of iridium on W(110). *Phys. Rev. B* 71, 115422. doi:10.1103/PhysRevB.71.115422

Antczak, G., and Ehrlich, G. (2007). Jump processes in surface diffusion. *Surf. Sci. Rep.* 62, 39–61. doi:10.1016/j.surfrep.2006.12.001

Antczak, G., and Ehrlich, G. (2010). *Surface diffusion: metals, metal atoms, and clusters*. Cambridge: Cambridge University Press. doi:10.1017/CBO9780511730320

Antczak, G., Kamiński, W., and Morgenstern, K. (2015b). Stabilizing CuPc coordination networks on Ag(100) by Ag atoms. *J. Phys. Chem. C* 119, 1442–1450. doi:10.1021/jp5103803

Antczak, G., Kamiński, W., Sabik, A., Zaum, C., and Morgenstern, K. (2015a). Complex surface diffusion mechanisms of cobalt phthalocyanine molecules on Ag(100). *J. Am. Chem. Soc.* 137, 14920–14929. doi:10.1021/jacs.5b08001

Avidor, N., Townsend, P., Ward, D., Jardine, A., Ellis, J., and Allison, W. (2019). PIGLE - particles interacting in generalized Langevin equation simulator. *Comput. Phys. Commun.* 242, 145–152. doi:10.1016/j.cpc.2019.04.013

Bader, K., Winkler, M., and van Slageren, J. (2016). Tuning of molecular qubits: very long coherence and spin-lattice relaxation times. *Chem. Commun.* 52, 3623–3626. doi:10.1039/C6CC00300A

Barth, J. (2000). Transport of adsorbates at metal surfaces: from thermal migration to hot precursors. *Surf. Sci. Rep.* 40, 75–149. doi:10.1016/S0167-5729(00)00002-9

Barth, J. V., Costantini, G., and Kern, K. (2005). Engineering atomic and molecular nanostructures at surfaces. *Nature* 437, 671–679. doi:10.1038/nature04166

Bartolomé, J., Monton, C., and Schuller, I. K. (2014). *Magnetism of metal phthalocyanines*. Berlin, Heidelberg: Springer Berlin Heidelberg. doi:10.1007/978-3-642-40609-6_9

Bohrer, F. I., Sharoni, A., Colesniuc, C., Park, J., Schuller, I. K., Kummel, A. C., et al. (2007). Gas sensing mechanism in chemiresistive cobalt and metal-free phthalocyanine thin films. *J. Am. Chem. Soc.* 129, 5640–5646. doi:10.1021/ja0689379

Braun, O. M., and Ferrando, R. (2002). Role of long jumps in surface diffusion. *Phys. Rev. E* 65, 061107. doi:10.1103/PhysRevE.65.061107

Buchner, F., Xiao, J., Zillner, E., Chen, M., Röckert, M., Ditze, S., et al. (2011). Diffusion, rotation, and surface chemical bond of individual 2h-tetraphenylporphyrin molecules on Cu(111). *J. Phys. Chem. C* 115, 24172–24177. doi:10.1021/jp206675u

Calvo-Almazán, I., Sacchi, M., Tamtögl, A., Bahn, E., Koza, M. M., Miret-Artés, S., et al. (2016). Ballistic diffusion in poly-aromatic hydrocarbons on graphite. *J. Phys. Chem. Lett.* 7, 5285–5290. doi:10.1021/acs.jpclett.6b02305

Caputo, M., Panighel, M., Lisi, S., Khalil, L., Santo, G. D., Papalazarou, E., et al. (2016). Manipulating the topological interface by molecular adsorbates: adsorption of Co-phthalocyanine on Bi_2Se_3. *Nano Lett.* 16, 3409–3414. doi:10.1021/acs.nanolett.5b02635

Chudley, C. T., and Elliott, R. J. (1961). Neutron scattering from a liquid on a jump diffusion model. *Proc. Phys. Soc.* 77, 353–361. doi:10.1088/0370-1328/77/2/319

Ding, J., Wei, Z., Li, F., Zhang, J., Zhang, Q., Zhou, J., et al. (2023). Atomic high-spin cobalt(II) center for highly selective electrochemical CO reduction to CH_3OH. *Nat. Commun.* 14, 6550. doi:10.1038/s41467-023-42307-1

Eichberger, M., Marschall, M., Reichert, J., Weber-Bargioni, A., Auwärter, W., Wang, R. L. C., et al. (2008). Dimerization boosts one-dimensional mobility of conformationally adapted porphyrins on a hexagonal surface atomic lattice. *Nano Lett.* 8, 4608–4613. doi:10.1021/nl802995u

Ellis, J., Sabik, A., Jardine, A. P., Antczak, G., and Tamtögl, A. (2024). The range of dynamics: verifying rate theory across 16 orders of magnitude. in preparation

Farías, D., and Rieder, K.-H. (1998). Atomic beam diffraction from solid surfaces. *Rep. Prog. Phys.* 61, 1575–1664. doi:10.1088/0034-4885/61/12/001

Feng, Q., Sun, Y., Gu, X., and Dong, Z. (2022). Advances of cobalt phthalocyanine in electrocatalytic CO_2 reduction to CO: a mini review. *Electrocatalysis* 13, 675–690. doi:10.1007/s12678-022-00766-y

Ferrando, R., and Jardine, A. P. (2020). "Surface diffusion," in *Springer handbook of surface science*. Editors M. Rocca, T. S. Rahman, and L. Vattuone (Berlin, Germany: Springer International Publishing), 45–70. doi:10.1007/978-3-030-46906-1_2

Feyer, V., Graus, M., Nigge, P., Wießner, M., Acres, R., Wiemann, C., et al. (2014). Adsorption geometry and electronic structure of iron phthalocyanine on Ag surfaces: a LEED and photoelectron momentum mapping study. *Surf. Sci.* 621, 64–68. doi:10.1016/j.susc.2013.10.020

Gottfried, J. M. (2015). Surface chemistry of porphyrins and phthalocyanines. *Surf. Sci. Rep.* 70, 259–379. doi:10.1016/j.surfrep.2015.04.001

Graham, M. J., Zadrozny, J. M., Fataftah, M. S., and Freedman, D. E. (2017). Forging solid-state qubit design principles in a molecular furnace. *Chem. Mat.* 29, 1885–1897. doi:10.1021/acs.chemmater.6b05433

Hahne, S., Ikonomov, J., Sokolowski, M., and Maass, P. (2013). Determining molecule diffusion coefficients on surfaces from a locally fixed probe: analysis of signal fluctuations. *Phys. Rev. B* 87, 085409. doi:10.1103/PhysRevB.87.085409

Hedgeland, H., Sacchi, M., Singh, P., McIntosh, A. J., Jardine, A. P., Alexandrowicz, G., et al. (2016). Mass transport in surface diffusion of van der waals bonded systems: boosted by rotations? *J. Phys. Chem. Lett.* 7, 4819–4824. doi:10.1021/acs.jpclett.6b02024

Holst, B., Alexandrowicz, G., Avidor, N., Benedek, G., Bracco, G., Ernst, W. E., et al. (2021). Material properties particularly suited to be measured with helium scattering: selected examples from 2D materials, van der Waals heterostructures, glassy materials, catalytic substrates, topological insulators and superconducting radio frequency materials. *Phys. Chem. Chem. Phys.* 23, 7653–7672. doi:10.1039/d0cp05833e

Iacovita, C., Rastei, M. V., Heinrich, B. W., Brumme, T., Kortus, J., Limot, L., et al. (2008). Visualizing the spin of individual cobalt-phthalocyanine molecules. *Phys. Rev. Lett.* 101, 116602. doi:10.1103/PhysRevLett.101.116602

Ikonomov, J., Bach, P., Merkel, R., and Sokolowski, M. (2010). Surface diffusion constants of large organic molecules determined from their residence times under a scanning tunneling microscope tip. *Phys. Rev. B* 81, 161412. doi:10.1103/PhysRevB.81.161412

Jardine, A., Hedgeland, H., Alexandrowicz, G., Allison, W., and Ellis, J. (2009). Helium-3 spin-echo: principles and application to dynamics at surfaces. *Prog. Surf. Sci.* 84, 323–379. doi:10.1016/j.progsurf.2009.07.001

Kröger, I., Bayersdorfer, P., Stadtmüller, B., Kleimann, C., Mercurio, G., Reinert, F., et al. (2012). Submonolayer growth of H_2-phthalocyanine on Ag(111). *Phys. Rev. B* 86, 195412. doi:10.1103/PhysRevB.86.195412

Kröger, I., Stadtmüller, B., Stadler, C., Ziroff, J., Kochler, M., Stahl, A., et al. (2010). Submonolayer growth of copper-phthalocyanine on Ag(111). *New J. Phys.* 12, 083038. doi:10.1088/1367-2630/12/8/083038

Kwon, K.-Y., Wong, K. L., Pawin, G., Bartels, L., Stolbov, S., and Rahman, T. S. (2005). Unidirectional adsorbate motion on a high-symmetry surface: "walking" molecules can stay the course. *Phys. Rev. Lett.* 95, 166101. doi:10.1103/PhysRevLett.95.166101

Lahee, A., Manson, J., Toennies, J., and Wöll, C. (1987). Helium atom differential cross sections for scattering from single adsorbed CO molecules on a Pt(111) surface. *J. Chem. Phys.* 86, 7194–7203. doi:10.1063/1.452321

Marbach, H., and Steinrück, H.-P. (2014). Studying the dynamic behaviour of porphyrins as prototype functional molecules by scanning tunnelling microscopy close to room temperature. *Chem. Commun.* 50, 9034–9048. doi:10.1039/C4CC01744G

Melville, O. A., Lessard, B. H., and Bender, T. P. (2015). Phthalocyanine-based organic thin-film transistors: a review of recent advances. *ACS Appl. Mat. Interfaces* 7, 13105–13118. doi:10.1021/acsami.5b01718

Oh, S.-M., Kyuno, K., Wang, S. C., and Ehrlich, G. (2003). Step-edge versus interior barriers to atom incorporation at lattice steps. *Phys. Rev. B* 67, 075413. doi:10.1103/PhysRevB.67.075413

Pollak, E., and Miret-Artés, S. (2023). Recent developments in Kramers' theory of reaction rates. *Chem. Phys. Chem.* 24, e202300272. doi:10.1002/cphc.202300272

Rittmeyer, S. P., Ward, D. J., Gütlein, P., Ellis, J., Allison, W., and Reuter, K. (2016). Energy dissipation during diffusion at metal surfaces: disentangling the role of phonons versus electron-hole pairs. *Phys. Rev. Lett.* 117, 196001. doi:10.1103/PhysRevLett.117.196001

Rotter, P., Lechner, B. A. J., Morherr, A., Chisnall, D. M., Ward, D. J., Jardine, A. P., et al. (2016). Coupling between diffusion and orientation of pentacene molecules on an organic surface. *Nat. Mater* 15, 397–400. doi:10.1038/nmat4575

Sabik, A., Gołek, F., and Antczak, G. (2016). Reduction of the low-energy electron reflectivity of Ag(100) upon adsorption of cobalt phthalocyanine molecules. *J. Phys. Chem. C* 120, 396–401. doi:10.1021/acs.jpcc.5b10470

Sacchi, M., and Tamtögl, A. (2023). Water adsorption and dynamics on graphene and other 2D materials: computational and experimental advances. *Adv. Phys. X* 8, 2134051. doi:10.1080/23746149.2022.2134051

Salomon, E., Amsalem, P., Marom, N., Vondracek, M., Kronik, L., Koch, N., et al. (2013). Electronic structure of CoPc adsorbed on Ag(100): evidence for molecule-substrate interaction mediated by Co 3*d* orbitals. *Phys. Rev. B* 87, 075407. doi:10.1103/PhysRevB.87.075407

Salomon, E., Beato-Medina, D., Verdini, A., Cossaro, A., Cvetko, D., Kladnik, G., et al. (2015). Correlation between charge transfer and adsorption site in CoPc overlayers adsorbed on Ag(100). *J. Phys. Chem. C* 119, 23422–23429. doi:10.1021/acs.jpcc.5b05999

Schunack, M., Linderoth, T. R., Rosei, F., Lægsgaard, E., Stensgaard, I., and Besenbacher, F. (2002). Long jumps in the surface diffusion of large molecules. *Phys. Rev. Lett.* 88, 156102. doi:10.1103/PhysRevLett.88.156102

Senft, D. C., and Ehrlich, G. (1995). Long jumps in surface diffusion: one-dimensional migration of isolated adatoms. *Phys. Rev. Lett.* 74, 294–297. doi:10.1103/PhysRevLett.74.294

Serra, A., and Ferrando, R. (2002). An efficient method for computing collective diffusion in a strongly interacting lattice gas. *Surf. Sci.* 515, 588–596. doi:10.1016/S0039-6028(02)02001-0

Tamtögl, A., Bahn, E., Sacchi, M., Zhu, J., Ward, D. J., Jardine, A. P., et al. (2021). Motion of water monomers reveals a kinetic barrier to ice nucleation on graphene. *Nat. Commun.* 12, 3120–3128. doi:10.1038/s41467-021-23226-5

Tamtögl, A., Sacchi, M., Avidor, N., Calvo-Almazán, I., Townsend, P. S. M., Bremholm, M., et al. (2020). Nanoscopic diffusion of water on a topological insulator. *Nat. Commun.* 11, 278. doi:10.1038/s41467-019-14064-7

Tamtögl, A., Sacchi, M., Calvo-Almazán, I., Zbiri, M., Koza, M. M., Ernst, W. E., et al. (2018). Ultrafast molecular transport on carbon surfaces: the diffusion of ammonia on graphite. *Carbon* 126, 23–30. doi:10.1016/j.carbon.2017.09.104

Townsend, P. S. M., and Avidor, N. (2019). Signatures of multiple jumps in surface diffusion on honeycomb surfaces. *Phys. Rev. B* 99, 115419. doi:10.1103/PhysRevB.99.115419

Trost, J., Zambelli, T., Wintterlin, J., and Ertl, G. (1996). Adsorbate-adsorbate interactions from statistical analysis of STM images: N/Ru(0001). *Phys. Rev. B* 54, 17850–17857. doi:10.1103/PhysRevB.54.17850

Wagner, T., Antczak, G., Ghanbari, E., Navarro-Quezada, A., Györök, M., Volokitina, A., et al. (2022a). Standard deviation of microscopy images used as indicator for growth stages. *Ultramicroscopy* 233, 113427. doi:10.1016/j.ultramic.2021.113427

Wagner, T., Antczak, G., Györök, M., Sabik, A., Volokitina, A., Gołek, F., et al. (2022b). Attenuation of photoelectron emission by a single organic layer. *ACS Appl. Mat. Interfaces* 14, 23983–23989. doi:10.1021/acsami.2c02996

Wang, Y., Arabi, S., Kern, K., and Ternes, M. (2021). Symmetry mediated tunable molecular magnetism on a 2D material. *Commun. Phys.* 4, 103. doi:10.1038/s42005-021-00601-8

Warner, M., Din, S., Tupitsyn, I. S., Morley, G. W., Stoneham, A. M., Gardener, J. A., et al. (2013). Potential for spin-based information processing in a thin-film molecular semiconductor. *Nature* 503, 504–508. doi:10.1038/nature12597

Weckesser, J., Barth, J. V., and Kern, K. (1999). Direct observation of surface diffusion of large organic molecules at metal surfaces: PVBA on Pd(110). *J. Chem. Phys.* 110, 5351–5354. doi:10.1063/1.478430

Weckesser, J., De Vita, A., Barth, J. V., Cai, C., and Kern, K. (2001). Mesoscopic correlation of supramolecular chirality in one-dimensional hydrogen-bonded assemblies. *Phys. Rev. Lett.* 87, 096101. doi:10.1103/PhysRevLett.87.096101

Wu, W., Harrison, N. M., and Fisher, A. J. (2013). Electronic structure and exchange interactions in cobalt-phthalocyanine chains. *Phys. Rev. B* 88, 024426. doi:10.1103/PhysRevB.88.024426

Frontiers in Chemistry

Explores all fields of chemical science across the periodic table

Advances our understanding of how atoms, ions, and molecules come together and come apart. It explores the role of chemistry in our everyday lives - from electronic devices to health and wellbeing.

Discover the latest Research Topics

See more →

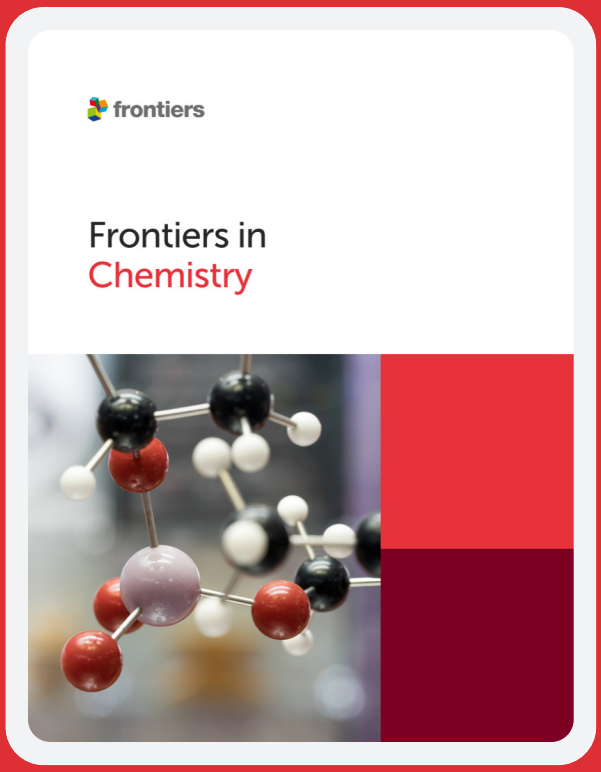

Frontiers

Avenue du Tribunal-Fédéral 34
1005 Lausanne, Switzerland
frontiersin.org

Contact us

+41 (0)21 510 17 00
frontiersin.org/about/contact